



**University of  
Nottingham**  
Biodiscovery Institute

# **Recombinant spider silk protein hydrogels**

Rowan Earlam, MChem

Supervisors: Professor Neil Thomas & Professor Sara Goodacre

Neil Thomas Research Group, School of Chemistry, Biodiscovery  
Institute, University Park, University of Nottingham, NG7 2RD

Thesis submitted to the University of Nottingham for the degree  
of Doctor of Philosophy, March 2021

## COVID-19 Impact statement

Due to the coronavirus pandemic and the resulting first lockdown, the university was shut and access to labs was removed from March 20<sup>th</sup> 2020. The Biodiscovery Institute was opened again from mid July 2020 but I was not able to resume lab work until early August 2020. This was due initially to having a maximum building occupation of 10 % which meant researchers returned in tranches. I was in tranche 2 which could return from the end of July. I was also the lab safety monitor and was therefore heavily involved in the planning and execution of the safe reopening of our labs which took around 2 weeks. As a result of social distancing measures, shift patterns were necessary. This meant that the maximum amount of time you could spend in the lab each day was 7 hours and no weekend working was permitted. Additionally, I was not able to access other buildings where key necessary equipment for analysis was located, until the middle of September.

As a result of the lab closures I was granted an extension which allowed me to continue to work after my initial deadline of September 30<sup>th</sup>. However, this extension was granted on the condition that I modify my research. The original goal of this study was to form NT2RepCT hydrogels and assess them for the functionality and capability in cell culture as 3D scaffolds. Unfortunately, due to a combination of the cell culture suite moving to a new building in the first few months of 2020, which limited access, and then the resultant pandemic, lab closures and shift patterns, it was not possible to perform cell culture experiments. Therefore, this research has shifted to experiments that could be performed in my usual labs which were drug delivery experiments. The pandemic has also had an obvious effect on my mental health and productivity and therefore the resulting thesis should be considered with this frame of reference.

## Abstract

Protein hydrogels are hydrophilic biomaterials that swell and have material properties that resemble biological soft tissue. Hydrogels are appropriate for use in local drug delivery systems due to their extensive porous structure allowing diffusion. Hydrogels prepared from *ex vivo* animal derived proteins bring risk of pathogens and ethical concerns. These issues can be addressed by using recombinantly produced spider silk. Spider silk protein (spidroin) is non-immunogenic, biodegradable and has impressive material properties such as strength and elasticity making it a promising material for hydrogel biomedical applications. In this study the recently reported highly expressing, recombinant mini-spidroin NT2RepCT was processed for the first time into natural protein hydrogels and characterised as a local and controlled drug delivery system.

NT2RepCT self-assembled into physical hydrogels at 2.4 % (w/v) upon incubation at 37 °C in double distilled milli Q (MQ) water Tris, HEPES and CAPS buffers at pH 5.5, 7 and 10. The hydrogel's optical properties, swelling behaviour, pore morphology, nano-fibril structures, stiffness and rheological properties were tunable depending on gelation conditions. It was found NT2RepCT hydrogels formed at pH 10 had increased swelling, high light transmittance and increased stiffness compared to those formed at pH 7 or in MQ water. Glutaraldehyde chemical crosslinking was utilised to increase NT2RepCT hydrogel stiffness.

The effect of hydrogel sample preparation ahead of scanning electron microscopy (SEM) on artefacts and secondary pores was investigated in cryo-SEM, high vacuum SEM and environmental SEM due to hydrogels high water content. It was found that the commonly used plunge freezing in liquid nitrogen technique created the most

artefacts compared to metal mirror (slam) freezing and *in situ* lyophilisation exemplifying the need for careful hydrogel SEM sample preparation.

The NT2RepCT hydrogels formed at pH 10 and in MQ water were injectable and showed shear-thinning properties. These hydrogels were assessed as a controlled drug delivery system and showed pH dependent release of the model drug surrogate rhodamine B. Tyrosine conjugation of 4-(4-(2-azidoethoxy)phenyl)-1,2,4-triazolidine-3,5-dione (PTAD-azide) added a functional handle and the model drug surrogate fluorescein (FAM) was 'clicked' via copper catalyzed azide-alkyne cycloaddition. Improved and controlled release was seen in hydrogels containing conjugated FAM compared to hydrogels containing non-conjugated 'free' FAM.

The properties of the NT2RepCT hydrogels were similar to previously reported natural and recombinant silk hydrogels but without the need for high temperatures, denaturing purification conditions and extensive processing. This study illustrates the diversity and tunability of recombinant minispidroin NT2RepCT hydrogels and demonstrates their suitability as a highly transparent, injectable, pH sensitive and controlled hydrogel drug delivery system.

# Acknowledgments

I would like to take this opportunity to thank my supervisors Professor Neil Thomas and Professor Sara Goodacre for the chance to pursue this PhD.

Huge thanks to the A20 lab members but in particular, Dr David Harvey, Jolanta Beinarovica, Dr Alex Holland and Hannah Betts. You have been incredible, kind and hilarious.

A special appreciation and thanks to Dr Christopher Parmenter and Nicola Weston from The Nanoscale and Microscale Research Centre (nmRC) for their help and advice on hydrogel SEM imaging. Thank you also to the BDI management and technical support team for their continued effort to keep all researchers happy and things running smoothly, despite recent huge challenges.

I cannot thank Dr Mariwan Sayda and Ella Taylor enough for being my best friends and listening to me go on and on about this PhD for the past 4 years, supporting me always. I love you guys; you are my soul mates.

Thank you to my parents Amanda and David and my brother Duncan for caring for me and loving me always.

One more thanks goes to my beautiful cat Kittie who has sat diligently on my laptop and office chair every time I have needed to take a break from writing and for being so perfect and cute.

## Table of contents

COVID-19 Impact statement.....	1
Abstract.....	2
Acknowledgments .....	4
Table of contents.....	5
Abbreviations .....	10
1. Introduction.....	12
1.1. Project background.....	12
1.2. Project objectives .....	13
2. Literature review .....	14
2.1. A brief history of silk.....	14
2.2. Types of spider silk.....	14
2.3. Structure of spider silk.....	15
2.4. How spiders form silk.....	19
2.5. Silk fibroin.....	21
2.6. Why spider silk?.....	22
2.7. Recombinant spider silk expression.....	22
2.8. Recombinant spider silk miniature spidroin design .....	25
2.9. Recombinant spidroins <i>in vivo</i> .....	28
2.10. Industrial interest in recombinant spidroins .....	28
3. General methods .....	29
3.1. Expression and purification of NT2RepCT .....	29
3.1.1. Chemicals and reagents .....	29
3.1.2. Data analysis and statistics.....	29
3.1.3. NT2RepCT protein expression .....	29
3.1.4. NT2RepCT protein purification.....	30
3.1.5. SDS-PAGE .....	31
3.1.6. Protein concentration .....	31
3.1.7. pET22b NT2RepCT plasmid map.....	32
3.2. NT2RepCT purification results .....	32
3.2.1. Higher yields of NT2RepCT in BL21 Rosetta than BL21 ....	32
4. Factors that affect NT2RepCT hydrogel formation .....	34
4.1. Introduction.....	34
4.1.1. Natural and synthetic hydrogels .....	34
4.1.2. Physical, enzymatic and chemical crosslinking of hydrogels..	35

4.1.3.	Factors that affect hydrogel transparency .....	36
4.1.4.	Spider silk protein hydrogels in literature .....	37
4.1.5.	NT2RepCT structure and properties .....	38
4.2.	Methods .....	41
4.2.1.	Physical NT2RepCT hydrogel self-assembly conditions investigated .....	41
4.2.2.	Monitoring hydrogel kinetics at OD <sub>595</sub> .....	42
4.2.3.	Circular Dichroism Spectroscopy.....	42
4.2.4.	Assessing light transmittance of formed heat-induced hydrogels .....	43
4.2.5.	Dynamic Light Scattering (DLS) and Zeta Potential .....	43
4.3.	Results.....	44
4.3.1.	NT2RepCT self assembles into hydrogels at 2.4 % (w/v) at 37 °C	44
4.3.2.	Formation of 2.4 % (w/v) NT2RepCT hydrogel can be monitored at 595 nm .....	44
4.3.3.	Presence of salt, phosphates and media inhibit hydrogel self-assembly.....	45
4.3.4.	NT2RepCT changes conformation with increasing temperature and pH.....	47
4.3.5.	Gelation pH and temperature affected hydrogel appearance .....	50
4.3.6.	NT2RepCT hydrogel self-assembly is closely linked to pH.	53
4.3.7.	Percentage transmission of visible light through hydrogel can be altered by gelation buffer .....	53
4.3.8.	Transparent hydrogels were made in fresh MQ water and 20 mM CAPS pH 10 .....	54
4.3.9.	Gelation time increased in 20 mM CAPS pH 10 .....	55
4.3.10.	DLS and zeta potential .....	56
4.4.	Discussion of the factors that affect hydrogel formation.....	58
4.4.1.	Overview .....	58
4.4.2.	NT2RepCT self-assembles into hydrogels.....	58
4.4.3.	Monitoring hydrogel kinetics at 595 nm only useful for turbid hydrogels .....	59
4.4.4.	Presence of electrolytes inhibitory to heat induced gelation.. .....	59
4.4.5.	NT2RepCT thermal denaturation reflects isolated terminal domains .....	61
4.4.6.	The pH of gelation determines opacity of hydrogel.....	62
4.4.7.	A small change in temperature of gelation affects appearance of hydrogels .....	64
4.4.8.	CAPS10 longer gelation time than MQ hydrogels .....	65

4.4.9.	DLS and zeta potential reflect NT2RepCT temperature and pH dependent behaviour .....	66
4.4.10.	Optically clear NT2RepCT hydrogels .....	67
4.5.	Summary of the factors that affect NT2RepCT hydrogel formation .....	68
5.	Swelling ratios & SEM (Materials characterisation Part A) .....	70
5.1.	Introduction .....	70
5.1.1.	Crosslinking of natural hydrogels .....	70
5.1.2.	Swelling ratios .....	72
5.1.3.	Cryo-SEM, SEM and eSEM .....	73
5.2.	Methods .....	77
5.2.1.	Summary of NT2RepCT hydrogels .....	77
5.2.2.	Glutaraldehyde chemical crosslinking of formed hydrogels	79
5.2.3.	Calculation of swelling ratios .....	79
5.2.4.	Cryo-SEM .....	79
5.2.5.	Focused Ion Beam Scanning Electron Microscopy (FIB-SEM) .....	80
5.2.6.	SEM .....	81
5.2.7.	eSEM .....	81
5.3.	Swelling and SEM Results .....	82
5.3.1.	Opaque hydrogels dissolved in cell culture media at 37 °C	82
5.3.2.	Swelling ratio of opaque hydrogels can be controlled by pH of gelation .....	82
5.3.3.	Opaque hydrogels structural integrity improved when crosslinked with glutaraldehyde .....	84
5.3.4.	Swelling ratios of GA crosslinked opaque hydrogels .....	84
5.3.5.	Hydrogel transparency and swelling .....	87
5.3.6.	Cryo- SEM of MQ 37 O .....	89
5.3.7.	FIB-SEM of MQ 37 O .....	90
5.3.8.	High vacuum SEM GA crosslinked opaque hydrogels .....	92
5.3.9.	High vacuum SEM non-crosslinked MQ 37 T and CAPS10 hydrogels .....	93
5.3.10.	Comparison of SEM/eSEM techniques of GA crosslinked MQ 37 T 1GA and CAPS10 1GA hydrogels .....	95
5.4.	Discussion of swelling behaviour and SEM analysis .....	100
5.4.1.	Overview .....	100
5.4.2.	pH of gelation influences swelling ratio of opaque hydrogels in different swelling solutions .....	100
5.4.3.	Glutaraldehyde chemical crosslinking of NT2RepCT .....	103
5.4.4.	Transparent hydrogels were able to swell more than opaque hydrogels .....	106

5.4.5.	Cryo-SEM and FIB-SEM cryofixation technique is critical	108
5.4.6.	High vacuum SEM of the opaque hydrogels porous structure .....	110
5.4.7.	Artefacts and secondary pores in non-crosslinked transparent hydrogels .....	110
5.4.8.	GA crosslinking in SEM/eSEM .....	112
5.5.	Summary of swelling behaviour and SEM analysis .....	114
6.	Young's modulus and rheology (Materials characterisation Part B) .. .....	117
6.1.	Introduction.....	117
6.1.1.	Mechanobiology .....	117
6.1.2.	Young's modulus .....	119
6.1.3.	Rheology .....	123
6.2.	Materials and Methods .....	127
6.2.1.	Compression testing .....	127
6.2.2.	Rheology .....	127
6.3.	Results.....	128
6.3.1.	Young's modulus .....	128
6.3.2.	Strain sweeps and frequency sweeps of MQ 37 T and CAPS10 hydrogels .....	130
6.3.3.	Assessing viscoelasticity of 1-2.5 % (w/v) NT2RepCT in MQ water and at pH 10.....	133
6.3.4.	Time sweep of MQ 37 T and CAPS10 .....	135
6.4.	Discussion .....	136
6.4.1.	Overview .....	136
6.4.2.	Alkaline pH of gelation increases hydrogel stiffness.....	136
6.4.3.	Gap height alters hydrogel behaviour in rheology .....	138
6.4.4.	Hydrogels form at lower concentrations of NT2RepCT in MQ water than at pH 10.....	140
6.4.5.	Swelling in PBS increases the moduli of MQ 37 T and CAPS10	142
6.5.	Summary of Young's modulus and rheology .....	143
7.	Drug Delivery .....	145
7.1.	Introduction.....	145
7.1.1.	Local drug delivery systems (DDS) .....	145
7.1.2.	Hydrogel DDS applications and targets.....	145
7.1.3.	Controlled release .....	146
7.1.4.	Stimulus responsive 'smart' hydrogels .....	149
7.1.5.	Injectable hydrogels .....	150
7.1.6.	Drug loading .....	151

7.2.	Materials and methods .....	153
7.2.1.	SEM of syringe extruded hydrogels .....	153
7.2.2.	Shear-thinning rheology .....	153
7.2.3.	PTAD azide modification of NT2RepCT .....	154
7.2.4.	Conjugation of fluorescein to NT2RepCT-PTAD-N <sub>3</sub> .....	155
7.2.5.	<i>In vitro</i> release of Rhodamine B from hydrogels .....	156
7.2.6.	<i>In vitro</i> release of fluorescein from encapsulated and conjugated NT2RepCT hydrogels .....	157
7.2.7.	<i>In vitro</i> drug release modelling.....	158
7.3.	Results.....	160
7.3.1.	Hydrogels formed in syringe retained shape upon extrusion. ....	160
7.3.2.	MQ 37 T and CAPS10 non-Newtonian shear thinning behaviour .....	160
7.3.3.	Extruded hydrogels SEM.....	161
7.3.4.	PTAD conjugation small scale and larger scale.....	163
7.3.5.	<i>In vitro</i> release of rhodamine B from hydrogels .....	167
7.3.6.	<i>In vitro</i> release of fluorescein from encapsulated and conjugated NT2RepCT hydrogels .....	170
7.4.	Discussion of NT2RepCT hydrogel drug delivery systems .....	175
7.4.1.	Overview .....	175
7.4.2.	Injectable hydrogels .....	175
7.4.3.	PTAD conjugation .....	177
7.4.4.	<i>In vitro</i> Rhodamine B release .....	182
7.4.5.	<i>In vitro</i> FAM release.....	184
7.4.6.	Kinetic modelling .....	188
7.5.	Summary .....	190
8.	Project conclusions .....	191
9.	Future work .....	193
	References .....	196
	Appendix .....	216

## Abbreviations

2D	Two-dimensional
3D	Three-dimensional
ACN	Acetonitrile
APS	Ammonium peroxydisulfate
BSA	Bovine serum albumin
CAPS	<i>N</i> -cyclohexyl-3-aminopropanesulfonic acid
CD	Circular dichroism
Cryo-SEM	Cryogenic scanning electron microscopy
CT	C terminal
CuAAC	Copper catalyzed alkyne-azide cycloaddition
DDS	Drug delivery system
DLS	Dynamic Light Scattering
DMEM	Dulbecco's Modified Eagle Medium
DMF	Dimethylformamide
ECM	Extracellular matrix
ESEM	Environmental scanning electron microscopy
FAM	Fluorescein
FBS	Fetal bovine serum
FDA	Food and Drug Administration
FIB	Focused Ion Beam
FIB-SEM	Focused Ion Beam scanning electron microscopy
$G'$	Storage modulus
$G''$	Loss modulus
$G^*$	Complex modulus
GA	Glutaraldehyde
$Ga^+$	Gallium cations
GMA	glycerol methacrylate
HEPES	4-(2-hydroxyethyl)-1-piperazineethanesulfonic acid
HEMA	2-hydroxyethyl methacrylate
HRP	Horse radish peroxidase
IV	Intra venous
LCST	Lower critical solution temperature
LN2	Liquid nitrogen
LNS	Liquid nitrogen slush
LVE	Linear viscoelastic
MSC	Mesenchymal stem cells
MQ	Milli Q water
MWCO	Molecular weight cut off
NHS	<i>N</i> -hydroxysuccinimide
NT	N terminal
NIPAAm	Poly( <i>N</i> -isopropylacrylamide)
pAA/pAAm	polyacrylamide
PBS	Phosphate buffered saline
PEG	Poly(ethylene glycol)

PEGdA Poly(ethylene glycol) diacrylate  
pI Isoelectric point  
PTAD 4-(4-(2-Azidoethoxy)phenyl)-1,2,4-triazolidine-3,5-dione  
PVA Poly(vinyl alcohol)  
Q swelling ratio  
R<sup>2</sup> Coefficient of determination  
RFU Relative fluorescence units  
RhB Rhodamine B  
SEM Scanning electron microscopy  
SD Standard deviation  
SDS Sodium dodecyl sulfate  
SOAS Small amplitude oscillatory shear  
Sol-gel solution to gel  
UV Ultraviolet  
UV-VIS Ultraviolet visible

# 1. Introduction

## 1.1. Project background

Spider silk has intrigued humans for millennia, leading to many discoveries and applications. One of the reasons for the continued interest in spider silk is a 'bottom-up' approach to research<sup>1</sup>, seeing a natural material and wanting to understand how it works and what it can be turned into. Spider silk has found uses in many industries, particularly biomedical. Spider silk is distinguished from other natural proteinaceous materials by its strength, extensibility and biocompatibility. By understanding the spider silk proteins modular design, recombinant versions have been created that show different behaviour. One such recombinant protein is called NT2RepCT and was first reported in 2017 by M. Andersson *et al*<sup>2</sup>. NT2RepCT is pH sensitive and highly soluble, and expressed in high yields. NT2RepCT is described in further detail in Section 4.1.5.

Hydrogels are hydrophilic, 3D polymer networks that can swell and absorb large volumes of water without dissolution due to crosslinks<sup>3</sup>. They are a tunable material and suitable for many applications such as cell culture and drug delivery due to their soft material properties which mimic the extra cellular matrix (ECM). Hydrogels are often comprised of *ex vivo* collagen and gelatin which bring the risk of prions, immunological responses and viruses<sup>4</sup>. By forming hydrogels from the recombinant spider silk protein NT2RepCT it is hoped that an impressive, tunable and biocompatible material will be developed that combines the desirable properties of hydrogels with the sought-after properties of spider silk.

## **1.2. Project objectives**

The aim of this PhD research project was to investigate and characterise the formation of recombinant spider silk protein hydrogels formed from NT2RepCT and evaluate their performance as a drug delivery system. The specific research objectives were therefore:

- To construct recombinant NT2RepCT protein hydrogels and investigate factors that affect hydrogel formation.
- To assess the NT2RepCT hydrogel material properties such as swelling ratio, pore size and morphology, Young's modulus and rheological behaviour.
- To examine the NT2RepCT hydrogel potential as a drug delivery system and demonstrate the feasibility of NT2RepCT hydrogels in the field of biomedical science

## 2. Literature review

### 2.1. A brief history of silk

Silk is a natural fibre formed of proteins produced by various invertebrates including spiders<sup>5</sup>, silk worms (*Bombyx mori*)<sup>6</sup>, other insects<sup>7,8</sup> and mussels<sup>9</sup>. Throughout history humans have utilised silk for various uses and the production of silk has had a large influence on human behaviour across the world. The domestication of silk worms, subsequent large volume production of their silk and manufacturing of heavily sought after textiles shaped the historical silk-road trading route<sup>10,11</sup>. Unfortunately, unlike silk worms, spiders are territorial and in some cases cannibalistic and therefore cannot be farmed<sup>12</sup>. Additionally, the volume of silk produced by spiders is considerably less than silk worms and spiders require force reeling to extract silk<sup>13</sup>. Despite these disadvantages, spider silk has been used by humans for hundreds of years for weaponry<sup>14</sup>, fishing nets<sup>15</sup> and bandages<sup>16,17</sup>. The strength, elasticity and toughness of spider silk out competes silk worm silk and other natural fibres<sup>6,18</sup>. Furthermore, the low immunogenicity<sup>19</sup> of spider silk upon implantation has been of great interest and is one of the reasons it has been continuously used and intensely studied.

### 2.2. Types of spider silk

Female orb weaving spiders have 7 different silk glands in their abdomen, each of which produces a different type of silk (Figure 1). These silks' properties vary due to the varied demands required of them. Silk involved in prey capture is glue-like whereas the silk required in egg casing is tough, for protection of the offspring<sup>20</sup>. The most studied spider silk is dragline, which is produced in the major ampullate gland. Dragline silk is used as a safety line in evasion of predators and as the radial spokes in circular webs<sup>15</sup>. It is the strongest of the silks produced by spiders and outcompetes man-made materials such as steel and Kevlar<sup>®</sup> on a weight-to-weight basis due to its impressive extensibility<sup>5,15</sup>.

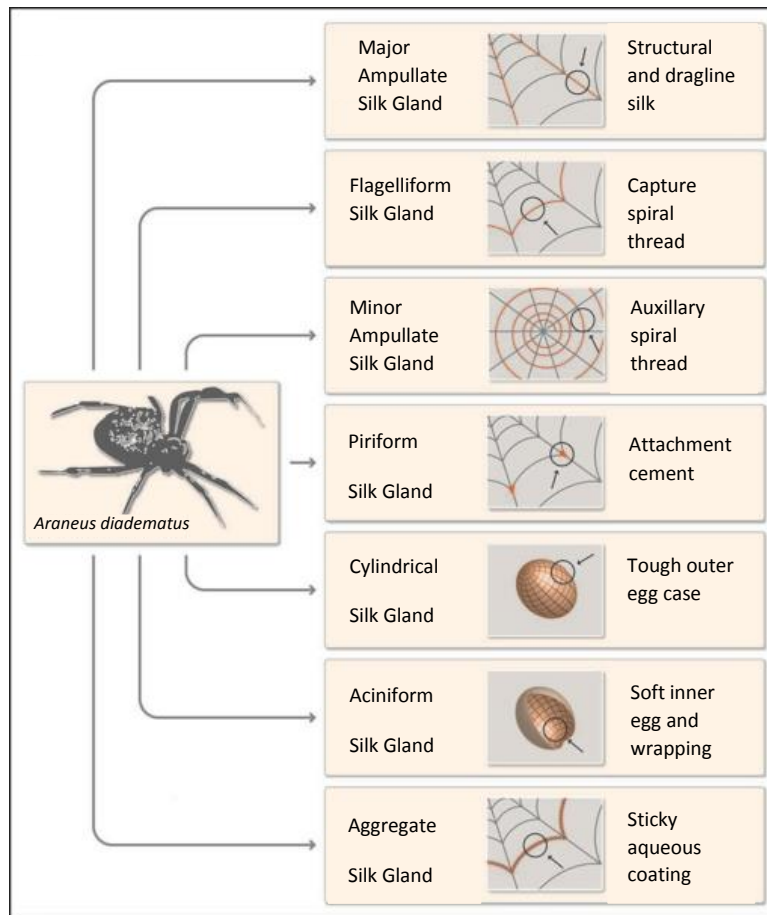


Figure 1: The 7 different types of silk produced in spiders and their uses. Only female spiders can produce silk used in egg casing. Image from: Romer *et al.*<sup>21</sup>

### 2.3. Structure of spider silk

Spider silk is formed mostly of proteins called spidroins. These proteins contain many hydrophobic and non-polar amino acids in short, repetitive polypeptide regions often repeated hundreds of times. These repetitive regions can be over 90 % of the protein composition<sup>21</sup>. This repetitive region is flanked by a non-repetitive N- and C-terminus (Figure 2). Native spider silk proteins are large and can vary in size from between 260<sup>22</sup>-725 kDa<sup>23</sup>. Each spidroin type contains different motifs within the repetitive polypeptide blocks that contribute to the physical attributes of the fibre<sup>24</sup>. Dragline silk is formed of major ampullate silk which comes in two forms: major ampullate silk 1 and 2 (MaSp1 and MaSp2). Both types of major ampullate silk contain

glycine rich regions and poly alanine repeats in the repetitive domain. The two spidroins Masp1 and MaSp2 differ in that MaSp1 contains no proline residues whereas MaSp2 does. Additionally, they have different motifs in the glycine rich regions. MaSp1 contains  $(GA)_n$  and  $(GGX)_n$  motifs, where X = tyrosine, leucine and glutamine<sup>24</sup>. These motifs contribute to the strength of the dragline silk fibre<sup>21</sup>. Whereas MaSp2 contains GPGXX and GPGGQ motifs, where X = glycine, tyrosine or glutamine<sup>25</sup>. These motifs contribute to the extensibility of the dragline silk fibre<sup>21</sup>. In the case of the spider *Araneus diadematus*, dragline silk is formed of MaSp2-like polypeptides. *A. diadematus* fibroin (ADF-1, ADF-3 and ADF-4)<sup>26-27</sup>.

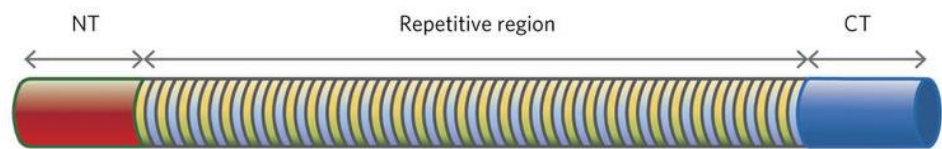


Figure 2: Schematic representation of the structure of major ampullate silk spidroin. The non-repetitive N-terminus is shown in red, the highly repetitive region is shown in alternating blue and yellow to represent the poly-alanine and glycine rich regions. The non-repetitive C-terminus is shown in blue. Image from: Rising *et al.*<sup>28</sup>.

Minor ampullate silk is used by spiders in the auxiliary spiral thread in an orb web and is therefore structural in function, requiring it to be strong but not as extensible as major ampullate spidroins<sup>29</sup>. It is similar to major ampullate silk but contains no proline residues and has a reduced glutamine content<sup>24</sup>. Like major ampullate, minor ampullate is present in two forms, minor ampullate spidroin 1 and 2 (MiSp1 and 2). Minor ampullate spidroins also contain charged amino acids and serine rich spacer regions termed 'spacer' motifs<sup>21,24</sup> (Figure 3). The function of the spacer is currently unknown but there is suggestion that it serves to break the crystalline repetitive

regions and form intra and intermolecular associations through the charged residues present<sup>24</sup>.

	 elastic β-turn spiral GPGXX	 crystalline β-sheet Ala-rich	 3 <sub>1</sub> -helix GGX	 spacer	 NR termini
<b>MaSp1</b>		✓	✓		✓
<b>MaSp2</b>	✓	✓			✓
<b>ADF-3</b>	✓	✓	✓		✓
<b>ADF-4</b>	✓	✓			✓
<b>MiSp1</b>		✓	✓	✓	✓
<b>MiSp2</b>		✓	✓	✓	✓

Figure 3: Structural motifs in major and minor ampullate spidroins. X indicates an amino acid residue that varies depending on the spidroin in question. NR = non repetitive. Adapted from Scheibel. T *et al.*<sup>30</sup>

Upon fibre formation within the repetitive region, poly alanine blocks form into crystalline anti-parallel  $\beta$  pleated sheets and the glycine rich regions form amorphous helical structures<sup>31</sup>. This secondary protein structure gives the formed silk fibre its strength and extensibility<sup>21</sup>. Compared to the variance between silks in the repetitive region, the conserved C terminus (CT)<sup>32</sup> is present in major and minor ampullate spidroins<sup>30,33</sup>. However, there are differences in CT sequence between silk types and spider species<sup>34</sup>. The CT exists as a homodimer with each monomer containing 5  $\alpha$  helices. MaSp and ADF CT domains contain a di-sulfide bridge in the dimer between the single cysteine residue in each monomer<sup>26</sup>. The MiSp CT does not contain a di-sulfide bridge as there are no cysteine residues present in the monomer<sup>35</sup>. However, as seen in Figure 4 there is a very similar structure between the CT of ADF-3 and two MiSp CT dimers.

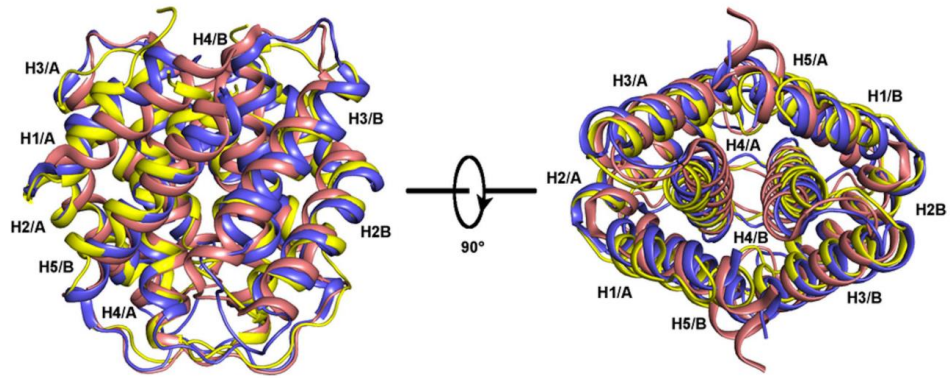


Figure 4: From M. Andersson *et al.*<sup>35</sup> Overlay of 3 CT dimers showing highly conserved structures. “Superposition of MiSp CT structures from *A. ventricosus* (yellow, PDB code 2MFZ) and *N. antipodiana* (blue, PDB code 2M0M) and the ADF-3 CT structure from *A. diadematus* (pink, PDB code 2KHM). Helices are shown as ribbons and labeled H1–H5. The letter A/B indicates the subunit”

Sequence alignment between MaSp and ADF C terminal domains show highly conserved regions including charged residues arginine, aspartic acid and glutamic acid. The charged residues form highly conserved salt bridges which are involved in the C terminal dimer in fibre formation. Compared to the CT, the N terminus (NT) is more highly conserved within both the same spidroin across multiple species but also within different spidroins in the same species<sup>34</sup>. It forms an up-and-down 5  $\alpha$ -helical bundle<sup>36</sup> which is primarily monomeric at neutral pH and physiological salt conditions<sup>37</sup>. The NT of MaSp proteins are highly pH responsive and have a positive and negative poles due to charged residues, leading to the formation of a tightly packed and symmetrical, electrostatic, anti-parallel homodimer (Figure 5) at lower pH<sup>37,38</sup>. In the case of *E. australis* MaSp1 NT domain, dimerisation requires structural conformational changes involving a single tryptophan residue moving from a buried to a solvent exposed site<sup>34</sup>. Additionally, there is a conserved inter-subunit ‘hand-shake interaction’ between D40 and E84 and protonation of 3 highly conserved glutamic acid residues allowing stable

dimer formation<sup>39</sup>. This increased stabilisation of the NT dimer enables fibre formation in the correct part of the spidroin gland within the spider due to decreasing pH throughout the gland. This avoids premature polymerisation of the silk fibre.

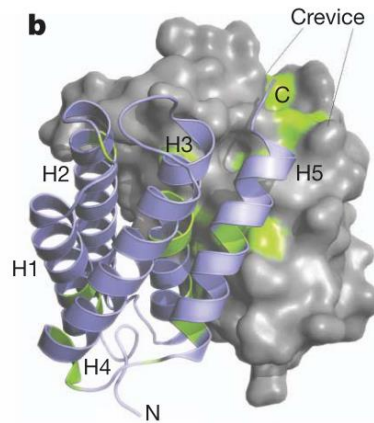


Figure 5: Overall structure of *E. australis* MaSp1 NT homodimer. Subunits A (grey) and B (blue) are shown in surface and ribbon representations, respectively. Strictly conserved residues are highlighted in green. PDB: 3LR2. Image from G. Askarieh et al.<sup>36</sup>

## 2.4. How spiders form silk

Spider silk is produced in spiders by conversion of a highly concentrated silk protein solution called dope, into strong and flexible fibres. Since spiders make a variety of silks, they have different glands for each type of silk produced; dragline silk is made in the major ampullate gland. Spider silk proteins are secreted from epithelial cells lining silk glands. The concentration of silk protein in the first portion of the gland is very high, up to 50% w/v<sup>40</sup>, this is called dope and the proteins exist as micelles to avoid premature aggregation<sup>41,42</sup>. The dope moves along the gland and down a pH gradient<sup>35</sup>, from pH 7.6 to around pH 5.7<sup>6</sup> (Figure 6). The enzyme carbonic anhydrase utilises the increasing pCO<sub>2</sub> along the gland to catalyse the reaction  $\text{H}_2\text{O} + \text{CO}_2 \rightarrow \text{H}^+ + \text{HCO}_3^-$ , decreasing the pH<sup>35</sup>. Additionally, ATPase driven proton pumps<sup>43</sup> help to control and maintain the pH gradient. Ion exchange in the gland with sulfur, potassium and phosphorus pumped into the distal portion of the major ampullate gland while sodium

and chloride ions are removed<sup>44</sup> further aids fibre formation. This is thought to be due to the chaotropic nature of potassium ions, removing the water from the proteins in order for unfolding to occur<sup>44</sup>. The major ampullate gland narrows as it gets closer to the spinnerets at the end from which the fibre is extruded. A combination of shear forces, pH and ion gradients concentrate the dope further and align the silk proteins to form a fibre.

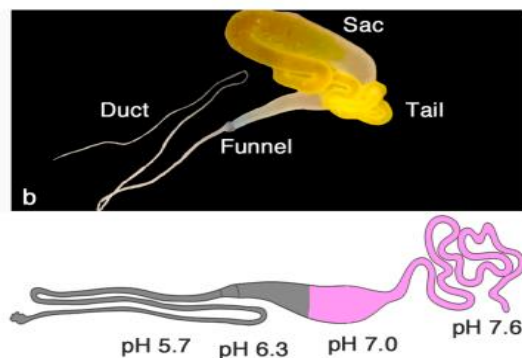


Figure 6: Major ampullate gland (top) labelled and schematic (below) showing pH gradient, moving from pH 7.6 on the right to 5.7 on the left. In the schematic the pink region contains endothelial cells that secrete silk proteins and the grey region has carbonic anhydrase activity. S-shaped duct on the left side of both images. Image from: Andersson *et al.*<sup>35</sup>.

The structure of spider silk proteins also aids the process of fibre formation from the dope; the NT and CT play important regulatory roles in formation of silk. They control the solubility of the protein and regulate the assembly of the proteins into polymer fibres. To form polymeric silk fibres from proteins, the protein monomers must align correctly and dimerize. The spidroin is converted from a primarily alpha helical and random coil conformation<sup>36</sup> to a solid fibre, where  $\beta$  sheets are beginning to form<sup>45</sup>. NT dimerization is pH dependent<sup>36,37</sup> and is used as a control to ensure that fibre formation doesn't happen too early, blocking the gland. At pH greater than 7 the NT

domains exist in an equilibrium between monomers<sup>46</sup> and weakly interacting homodimers<sup>38</sup>. As the pH drops the equilibrium shifts to dimerization and the dimer interactions stabilise<sup>39</sup>. Therefore, as the protein moves along the gland towards the duct, the pH drops and stable NT dimers form with the decreasing pH gradient.

The CT is a homodimer<sup>26</sup> that is highly stable above pH 6. As the protein dope moves along the gland, the drop in pH destabilises the CT dimer. Loss of a salt bridge causes instability in the CT structure, leading to partial unfolding<sup>35</sup>. The CT unfolds into  $\beta$ -amyloid fibrils<sup>35</sup> forming nucleation centres from which polymerisation of the spidroins can occur very rapidly<sup>39,26</sup>. This mechanism has been referred to as 'lock and trigger' with the NT dimer stabilisation forming the lock and the unfolding of the CT as the trigger<sup>35</sup>. This enables rapid polymerisation of the spidroins within a confined and controlled area of the gland.

## 2.5. Silk fibroin

The most characterised and studied silk is produced by the domesticated silkworm *Bombyx mori*. This silk has been used throughout history for textiles, medicine and more recently in biotechnology<sup>47</sup>. Silk is used by the silkworm to make cocoons to protect the pupa in the metamorphosis to a fully-grown moth. Silk worm silk has evolved to be tough<sup>48</sup> compared to strong spider silk. Spider silk must support the weight of the spider and prey whereas silkworm silk should resist attacks by predators trying to eat the cocoons. *B. mori* silk (silk fibroin) consists of a core of fibroin which is made of a heavy chain, a light chain which are connected by a disulfide bridge and a glycoprotein P25. This core is then coated with sericin as it is extruded<sup>48</sup>. Sericin bound to the virgin silk fibroin elicits a strong immune response *in vivo*<sup>49</sup> and therefore needs to be removed during processing of cocoons into silk. However, sericin on its own or combined back with silk fibroin does not cause an immune response<sup>49</sup>. The process of removing sericin, referred to as 'degumming' is a long process that can damage the

structure of the internal fibroin core<sup>50</sup>. Two different methods are employed to remove sericin from the fibroin core: alkaline, using Na<sub>2</sub>CO<sub>3</sub> and enzymatic processing<sup>50</sup>. Silk fibroin has a similar architecture to spidroins. A non-repetitive N and C terminus capping repeated hydrophobic and hydrophobic blocks. The hydrophobic blocks are primarily glycine (GX) repeats where X is alanine, serine or tyrosine. The repetitive hydrophobic blocks create  $\beta$ -sheet crystalline regions which are interspaced with amorphous regions in the repetitive domain<sup>1</sup>.

## **2.6. Why spider silk?**

In addition to spider silk's excellent strength, toughness and elasticity, it induces little immunological response on implantation<sup>19,51,52</sup> and is therefore, an excellent candidate for use in medicinal applications such as tissue engineering or drug delivery. Additionally, spider silk is biodegradable<sup>51</sup>. Native spider silk from *Nephila clavipes* was implanted into a neuronal defect in sheep with no adverse effect and ten months post-surgery axons had regenerated across the defect site indicating that spider silk could support axonal growth *in vivo*<sup>53</sup>. Dragline silk from *Nephila edulis* was investigated as a shallow wound dressing in a sheep model. Capillaries grew into the silk fibre bundles and there was minimal inflammatory response during the healing process. Additionally, the silk was completely degraded in 8 weeks<sup>54</sup>. There is also some evidence that spider silk has a small amount of antimicrobial activity<sup>55</sup>, however, this is more likely to be bacteriostatic rather than bactericidal in nature.

## **2.7. Recombinant spider silk expression**

Unlike silkworms, spiders are aggressive, territorial and can be cannibalistic<sup>30</sup> and cannot be farmed on a large scale. Furthermore, spiders can produce up to seven different types of silk from different spinnerets and therefore collection of pure silk of one type is tricky. Therefore, effort has been made in the past few decades on design and production of recombinant spidroins. Recombinant protein production offers

increased control over the properties, function and batch-to-batch variation compared to naturally derived means. Recombinant spider silks have been produced in insect cells<sup>56</sup>, yeast<sup>57</sup>, plants<sup>58</sup>, bacteria<sup>59</sup>, mammalian cells<sup>60</sup>, transgenic silk worms<sup>61</sup> and even milk from transgenic mice<sup>62</sup> and transgenic goats<sup>63</sup>. Each expression system has its own advantages and disadvantages as summarized in Table 1.

One of the most common expression systems for recombinant spidroins is *E. coli*. This is due to ease of plasmid transformation, the possibility for achieving high cell densities and fast growth kinetics, with doubling times of 20 minutes in optimal conditions<sup>64</sup>. Gram negative *E. coli* can also produce higher levels of the protein of interest compared to Gram positive bacteria due to high expression levels of proteases<sup>65</sup> in the latter. However, Gram-negative *E. coli* release endotoxins from their lipid polysaccharide outer membrane which induce immune responses in humans and animals, even at low concentrations<sup>66</sup>. Endotoxin concentrations can be reduced to acceptable levels using EndoTrap<sup>®</sup> column chromatography<sup>67</sup>, or simple washing steps<sup>67,68</sup>.

Native sized spider silk is difficult to produce in wild type *E. coli*<sup>69</sup> due to its large size<sup>22</sup> and repetitive regions containing many glycine and alanine residues which would quickly exhaust the available residues in the expression host<sup>70</sup>. The high guanine and cytosine content of the mRNA increases the risk of secondary structures forming which impedes transcription leading to pauses or terminations<sup>71</sup>. Despite these challenges, native sized dragline silk spidroins have been produced recombinantly. Increasing the pool of glycyl tRNA has been employed to produce recombinant spidroins based on *N. clavipes* Masp1 with glycine content of up to 44.9 %, of 284.9 kDa<sup>72</sup> and 556 kDa<sup>73</sup> with a 96mer and 192 mer respectively<sup>73</sup>.

Expression system	Silk produced	Proteases	Post translational modification	advantages	disadvantages	notes	REF
Sf9 insect cells with baculovirus	<i>Araneus diadematus</i> recombinant spidroin ADF-4 ADF-3	No	Yes but glycosylation can be different to mammalian	Simultaneously express multiple genes	Small cell volume Expensive media Time consuming cloning procedure	Filamentous structures in cells ADF-4 insoluble expression	56
Yeast <i>Pichia Pastorius</i>	<i>Euprosthenois australis</i> recombinant spidroin Z-4RepCT	Yes	Yes	Protein can be secreted extracellularly	Proteases can cleave protein	Truncation, and glycosylation affected expressed silk function	74
Transgenic potato and tobacco plants	<i>Nephila clavipes</i> recombinant spidroin	No	Yes	Correct protein folding	Lots of space required and long grow times	Expressed silk proteins showed heat resistance	58
Mammalian cells baby hamster kidney cells (BHK)	<i>Araneus diadematus</i> recombinant spidroin ADF-3	No	Yes	Correct protein folding and post translational modifications	High cost of production Culture is susceptible to infection	High solubility of spidroins <i>cf.</i> bacterial expression	60
Bacterial expression <i>E. coli</i>	<i>N. clavipes</i> Masp1 recombinant spidroin	Yes	No	Short culture doubling times Simple culture conditions	Difficulty expressing eukaryotic proteins Inclusion bodies can accumulate protein Endotoxins	Larger spidroins produced by increasing glycyl tRNA pool	73

Table 1: Summary of recombinant expression systems used in spidroin production.

## 2.8. Recombinant spider silk miniature spidroin design

Addition of an affinity tag such as hexa-histidine at the N or C terminus of the recombinant spidroin allows purification by immobilised metal affinity column chromatography (IMAC) (Figure 7). Elution of the his tagged protein is achieved with increasing concentrations of imidazole which out competes the histidine residues for coordination to the immobilised  $\text{Ni}^{2+}$ . Use of hexa histidine tags leads to relatively pure protein in one step from the crude cell lysate. However, the use of transition metal chromatography is not applicable or environmentally friendly on large scale<sup>1</sup>.

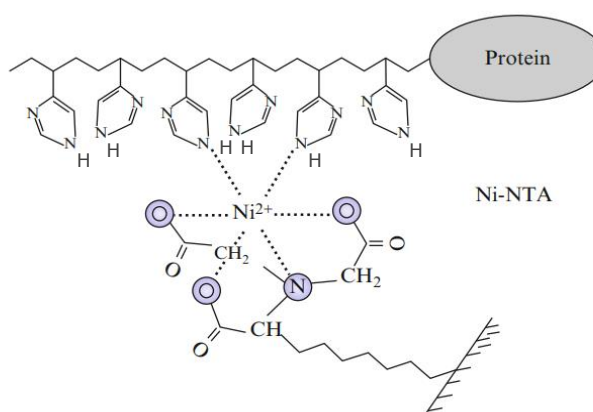


Figure 7: Coordination of hexa histidine affinity tagged protein with Ni-NTA in immobilised metal ion chromatography (IMAC)<sup>75</sup>

The most studied recombinant miniature spidroins are eADF4(C16) and 4RepCT (Table 2). These have been used in many different forms for different applications such as 3D printing<sup>76</sup> and cell culture<sup>77,78</sup>. These two spidroins differ in their design and species origin. The miniature spidroin eADF4(C16) (47.4 kDa) contains 16 repeats of a small glycine rich motif that mimics the repetitive region present in *Araneus diadematus* dragline silk ADF-4<sup>79</sup> with no NT or CT. The spidroin 4RepCT (25 kDa) contains four repeats of the repetitive region and the CT domain of MaSp1 from *E. australis*<sup>80</sup>. The MaSp1 *E. australis* CT domain contains a disulfide bridge and was included to allow instantaneous formation of fibres upon removal of a thioredoxin solubility tag. The

recombinant spidroin MaSp14C is similar in design to 4RepCT in that it contains 4 repeats of the repetitive region and the CT domain but from MaSp1 of *N. clavipes*<sup>81</sup>. It was found that the CT was necessary in the formation of a hydrogel indicating the importance of CT unfolding on polymerisation of macrostructures.

Both the non-repetitive NT and CT were included in the recombinant miniature spidroins NT2RepCT (33 kDa)<sup>2</sup> and N-R<sub>7</sub>-C (~30 kDa)<sup>41</sup>, which contains a N-terminus, 7 repeats of polyalanine and a glycine rich region and a C-terminus from MaSp1 and MaSp2 of *Latrodectus Hesperus*, in an effort to recapitulate native spidroin fiber formation. The NT domains used were both pH sensitive and increased the solubility allowing high expression yields of soluble protein. Fibres were formed by wet spinning in acidic conditions with the introduction of shear force. Both recombinant spidroins were designed in the last 4 years and therefore minimal work has been performed on potential applications. The addition of the pH sensitive spidroin NT domain to increase solubility of other recombinantly produced proteins is marketed by the designers of NT2RepCT at Spiber Technologies AM (Sweden) as SolvNT<sup>1,82</sup>.

Recombinant spider silk	Based on	Size (kDa)	Composition	NT or CT?	Purification method	Yield/L culture	Modifications	Processed into	Reference
<b>eADF4(C16)</b>	<i>Araneus diadematus</i> dragline silk ADF-4	47.4	(n=16) repeats glycine rich motif	None	Thermal purification with denaturing conditions solubilise protein	30 mg	RGD motif (genetic)	Fibres, particles, hydrogels, foams, films, non-woven meshes, 3D printed	83 77,84–88
<b>4RepCT</b>	<i>Euprosthennops australis</i> MaSp1	25	(n=4) repeats glycine rich and polyalanine and CT domain	CT	His tag Ni <sup>2+</sup> affinity chromatography (non-denaturing conditions)	20 mg	RGD motif (chemical) IgG motif (genetic)	Fibres, films, foams, nanomembranes	74,89,78,90–94
<b>MaSp14C</b>	<i>Nephila clavipes</i> MaSp1	26.5	(n=4) repeats of glycine rich and polyalanine and CT domain	CT	His tag Ni <sup>2+</sup> affinity chromatography (non-denaturing conditions)	Not given	None	Hydrogel	81
<b>NT2RepCT</b>	<i>E. australis</i> MaSp1 and <i>Araneus ventricosus</i> MiSp1	33	NT and (n=2) repeats of glycine rich and polyalanine from <i>E. australis</i> MaSp1, CT from <i>A. ventricosus</i> MiSp1	NT and CT	His tag Ni <sup>2+</sup> affinity chromatography (non-denaturing conditions)	125 mg	None	Fibres	2
<b>N-R<sub>7</sub>-C</b>	<i>Latrodectus Hesperus</i> MaSp1 and MaSp2	~30	NT, (n=7) repeats of glycine rich and polyalanine motif, CT	NT and CT	His tag Ni <sup>2+</sup> affinity chromatography (non-denaturing conditions)	420 mg	None	Fibres	41

Table 2: Summary of some of the miniature recombinant spider silk proteins expressed in *E. coli*.

## **2.9. Recombinant spidroins *in vivo***

Various recombinant spider silks have been examined *in vivo* and have been shown to have a very low inflammatory response and are well tolerated. 4RepCT fibres implanted in rats for 7 days supported cell growth and were populated by fibroblast cells with angiogenesis occurring in the centre of the fibre. No multinucleated cells, fibrous capsulation of the fibres or presence of macrophages were seen<sup>52</sup>. A chimeric protein which fuses consensus dragline silk sequences with the antimicrobial peptide Herceptin was implanted in mice with low to mild inflammatory reaction compared to controls<sup>95</sup>. The recombinant spider silk protein AvMaSp-R was investigated *in vitro* and did not induce apoptosis, stimulate macrophages, was non-cytotoxic and therefore deemed to be non-inflammatory<sup>96</sup>. Although more work is needed to determine the suitability of recombinant spidroins for medical applications in terms of inflammation and immune response the published results are promising.

## **2.10. Industrial interest in recombinant spidroins**

Recombinant spider silks have found use in industry with multiple companies focusing on design, production and application of their spidroin technology. AMSilk GmbH (Germany) is a spin out company formed by Professor Thomas Scheibel that uses ADF-4 recombinant silk to form their 'biosteel fiber' which is used in textiles. AMSilk GmbH has also created recombinant silk coated breast implants which induced no immune response or toxicity and reduced capsule thickness and inflammation compared to non-coated<sup>97</sup>. Spiber Technologies AB (Sweden) uses 4RepCT and modified 4RepCT to form fibres, films, foams, coatings for medical applications. Bolt Threads (USA) used larger scale spidroin silk expression in yeast for textiles. Spiber Inc (Japan) have also used their spidroin QMONOS in textile applications to make, among others, ties and a North Face jacket<sup>1</sup>.

## **3. General methods**

### **3.1. Expression and purification of NT2RepCT**

#### **3.1.1. Chemicals and reagents**

Unless otherwise stated, chemical reagents were obtained through commercial sources such as Sigma-Aldrich, Fisher Scientific and New England BioLabs. These materials were used without further purification. Double distilled water was prepared using a Millipore system (MQ water).

#### **3.1.2. Data analysis and statistics**

Data and statistical analysis were performed in either Microsoft Office Excel 2016 or Graph Pad Prism 7 (GraphPad software Inc. San Diego, CA). Data are expressed as mean  $\pm$  standard deviation. Statistically significant differences were determined by either an unpaired student t-test or a two-way analysis of variance (ANOVA) and Tukey post-hoc analysis. Statistical significance was accepted at the  $p < 0.05$  level and indicated in figures as \* $p < 0.05$ , \*\* $p < 0.01$ , \*\*\* $p < 0.001$ , \*\*\*\* $p < 0.0001$ . Protein structures were created in Pymol version 1.7.4.5. Sequencing was performed with SnapGene version 4.0.6.

#### **3.1.3. NT2RepCT protein expression**

Single colonies of BL21 Rosetta (DE3) *E. coli* cells transformed with NT2RepCT pET22b plasmid (Figure 8) on ampicillin (100  $\mu\text{g}/\text{mL}$ ) Lysogeny broth (LB) agar plates were used to inoculate 5 mL sterile LB media with 100  $\mu\text{g}/\text{mL}$  ampicillin. These starter cultures were grown for 16 hours at 37 °C, 180 rpm. Flasks containing 1L autoclaved lysogeny broth (LB) media with 100  $\mu\text{g}/\text{mL}$  ampicillin were inoculated with the 5 mL overnight starter culture using aseptic technique. The 1L cultures were incubated at 30 °C, 200 rpm until  $\text{OD}_{595}$  reached the log phase of growth (0.7-1). Protein expression was induced at 20 °C, 180 rpm using a final concentration of 0.3 mM Isopropyl  $\beta$ -D-1-thiogalactopyranoside (IPTG) for 16 hours.

### 3.1.4. NT2RepCT protein purification

BL21 Rosetta (DE3) *E. coli* cells induced to express NT2RepCT by IPTG were pelleted after expression by centrifugation at 4500 rpm for 10 minutes. The supernatant was discarded, and the cell pellet was re-suspended in 10 mL Buffer A (20 mM Tris, 400 mM NaCl, 40 mM imidazole). The re-suspended cells were lysed using sonication (MSE soniprep 150) for 10 minutes at 15 microns amplitude for 30 seconds bursts and 30 seconds rest at 4 °C. The bacterial lysate was immediately centrifuged at 35,000 x *g* for 30 minutes to pellet cell debris. The supernatant (soluble fraction) was loaded onto a 20 mL IMAC Ni<sup>2+</sup> affinity column (Hi-Trap chelating HP, GE Healthcare) which had been equilibrated with 4 column volumes of Buffer A (20 mM Tris, 400 mM NaCl, 40 mM Imidazole) by peristaltic pump (Econo pump, BioRad), the flow through was collected. The speed did not exceed 2 mL/min. The 20 mL IMAC Ni<sup>2+</sup> affinity column was then transferred to an ÄKTA pure protein purification system (GE Healthcare). Approximately 4 column volumes of 100 % Buffer A (20 mM Tris, 400 mM NaCl, 40 mM Imidazole) at 3 mL/min was run through the column until the absorbance reached <40 mAu. 10% (v/v) Buffer B (200 mM Tris, 400 mM NaCl, 700 mM imidazole) was used to elute contaminating peaks and 30% (v/v) to elute the NT2RepCT into fractions. The percentage of Buffer B was not increased until the absorbance had once again stabilized at ~100 mAu. Fractions that corresponded to a peak in the UV trace (280 nm) were analysed using 15 %SDS PAGE and bromophenol blue staining. PAGERuler Plus Prestained Protein Ladder (Thermo Scientific) was used as a size standard. Fractions that were determined to contain sufficiently pure protein (as determined by SDS PAGE) were dialysed (6-8 kDa MWCO, Molecularporous membrane tubing, Spectra/Por 1) against double distilled milli Q water (MQ) at 4 °C overnight. Dialysed NT2RepCT was flash frozen in liquid nitrogen and lyophilized under vacuum for 48

hours (Micromodulyo 230, Thermo Scientific). Fully lyophilised NT2RepCT was stored at -20 °C until further use.

### 3.1.5. SDS-PAGE

SDS PAGE gels at 15 % (w/v) acrylamide were cast with BioRad mini protean 3 gel kits. Samples to be analysed were combined with 4x SDS loading buffer (400 mM Dithiothreitol (DTT), 200 mM Tris-OH, 8% (w/v) SDS, 40 % (w/v) glycerol and 0.4 % (w/v) bromophenol blue) to obtain a 1x concentration and then boiled at 90 °C for 5 minutes. To separate wells 10 µL each boiled sample was added. All samples were analysed with Thermo Scientific PAGE ruler plus prestain protein ladder. SDS PAGE gels were run at 180V for 10 minutes and then 200V for a further 50 minutes or until the dye front had reached the end of the gel indicating full protein migration. SDS PAGE gels were submerged in MQ water and microwaved on the defrost setting for 5 minutes. This water was discarded and the SDS PAGE gels were submerged in protein stain (GelCode Blue Safe Protein Stain, Thermo Scientific) and microwaved for a further 5 minutes on the defrost setting. The protein stain was removed and the SDS PAGE gel was de-stained for 16-24 hours in MQ water. SDS PAGE gels were imaged using a UV transilluminator on the upper white setting.

### 3.1.6. Protein concentration

Protein concentration was assessed using spectroscopy with a ND-1000 nanodrop spectrophotometer (Thermo Fisher Scientific). The extinction coefficient of NT2RepCT is 18,910 L mol<sup>-1</sup> cm<sup>-1</sup> (calculated by ExPASy ProtParam tool) and the molecular weight of NT2RepCT is 33,278 g mol<sup>-1</sup>. The path length was 1 cm. Concentration of NT2RepCT was calculated by Equation 1:

Equation 1:

$$\text{Concentration} \left( \frac{\text{mg}}{\text{mL}} \right) = \frac{\text{Absorbance}}{18,910 \text{ (L mol}^{-1}\text{cm}^{-1})} \times 33,278 \text{ gmol}^{-1}$$

### 3.1.7. pET22b NT2RepCT plasmid map

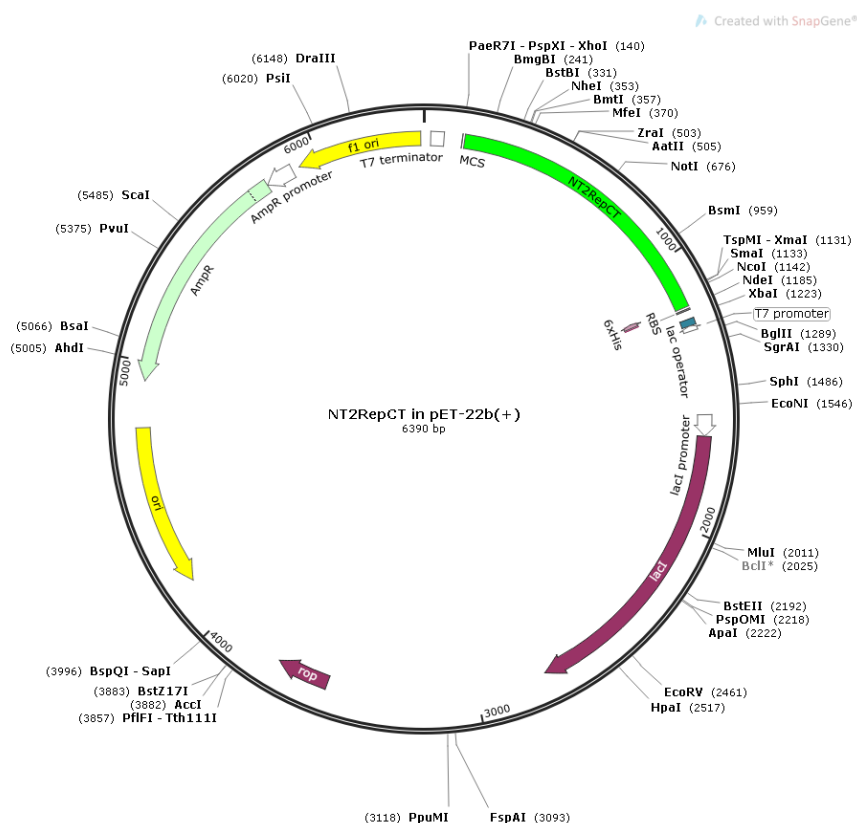


Figure 8: Plasmid map of NT2RepCT in pET-22b(+).

## 3.2. NT2RepCT purification results

### 3.2.1. Higher yields of NT2RepCT in BL21 Rosetta than BL21

The protein expression method described in methods section 3.1.1 and 3.1.4, is based on that described previously by M. Andersson *et al.*<sup>2</sup> however higher yields of 300 mg/L NT2RepCT were achieved. The expression strain BL21 Rosetta (DE3) contains an extra plasmid pRARE which allows for translation of several rare codons. Furthermore, they contain a mutation in the lac permease gene (*lacZY*). However, the gene encoding NT2RepCT in the pET22b vector was codon optimized for *E. coli* expression when it was purchased from ATUM and does not contain any rare codons. Additionally, since no chloramphenicol was used in expression of NT2RepCT, it is likely that the BL21 Rosetta (DE3) lost the pRARE plasmid due to lack of selection pressure

likely forming Tuner BL21 (DE3) derivatives due to the lacZY mutation. This mutation enables uniform and concentration dependent uptake of IPTG allowing homogeneous levels of induction. The increased protein yield in BL21 Rosetta (DE3) is a useful result applicable to other recombinant protein expression. The expression of NT2RepCT was split between soluble and insoluble but as the protein is expressed in high yields it is unnecessary to purify from the insoluble fraction. A 20 mL IMAC Ni<sup>2+</sup> column was used and 40 mM imidazole was used in the loading buffer (Buffer A, 20 mM tris, 400 mM NaCl, 40 mM imidazole). The 20 mL column was not over-loaded with minimal co-elution of NT2RepCT with lower binding contaminants (Figure 9). NT2RepCT dimer interactions and non-specific binding of contaminating proteins to the column were reduced with 400 mM NaCl. Purified NT2RepCT appeared as a single band (Figure 9) at 33 kDa. Equal amounts of NT2RepCT were seen in the insoluble and soluble fraction of the whole cell.

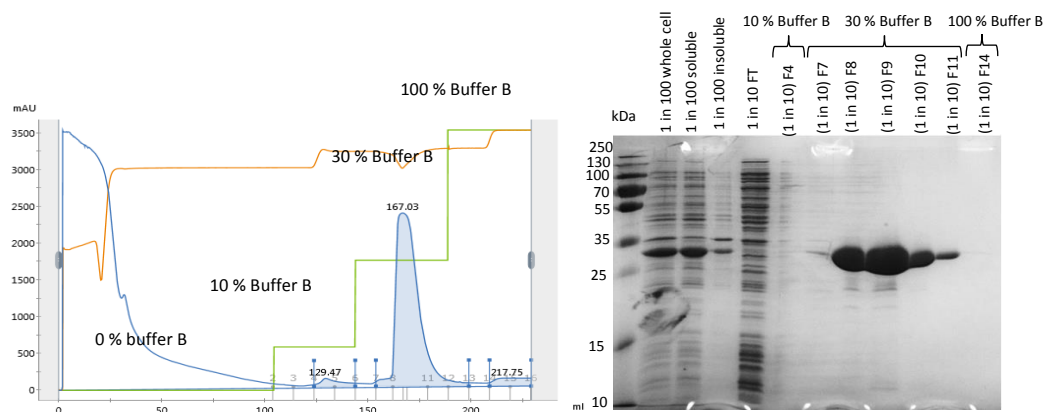


Figure 9: (Left) Purification trace of 2L LB BL21 Rosetta (DE3). Orange line =conductance, Green line = Percentage Buffer B, Blue line = UV absorbance. NT2RepCT eluted from 20 mL Ni<sup>2+</sup> IMAC column with 30 % buffer B. (Right) SDS PAGE gel (15 %) of NT2RepCT purification. Fractions of interest were diluted 10 x, Whole cell, soluble and insoluble fractions were diluted 100 x. The mark in lane 2 (1 in 100 whole cell) is from a tear that occurred during gel handling. FT = Flow through. B = Buffer B.

## **4. Factors that affect NT2RepCT hydrogel formation**

### **4.1. Introduction**

This chapter describes the formation of self-assembling NT2RepCT hydrogels and the conditions under which this occurs. Analysis of NT2RepCT secondary structure in relation to temperature and pH and how this has been exploited to create a range of hydrogels is discussed.

#### **4.1.1. Natural and synthetic hydrogels**

Hydrogels are 3D, crosslinked, hydrophilic polymer networks which swell extensively in water. In the last few decades, many hydrogels have been developed for different biomedical applications. From contact lenses and wound dressings to hygiene products and tissue engineering. However, although patents have been filed, not many hydrogels are commercially available in conventional medicine<sup>98</sup> due to high production costs. Therefore, there is a need for hydrogels that are quick, cheap and easy to produce that have excellent biocompatibility, tunability and specificity.

Hydrogels can be made from synthetic materials such as poly-vinyl alcohol (PVA) and polyethylene-glycol (PEG)<sup>98</sup>. Synthetic hydrogels can be biodegradable<sup>99</sup> or non-biodegradable<sup>100</sup>. They are reproducible in their manufacturing and their properties can be tuned by altering the monomer used, such as by chemically altering functional groups. Synthetic hydrogels also have a longer shelf life due to decreased rate of degradation and are often used to substitute for harder tissues such as bone and cartilage. However, biodegradable synthetic hydrogels can release toxic breakdown products creating systemic side effects<sup>101</sup> and can cause foreign body inflammatory responses particularly if implanted close to adipose tissue<sup>102</sup>. Synthetic hydrogels lack bio-adhesive and bioactive components with poor biocompatibility compared to naturally derived hydrogels<sup>103,104</sup> although this can be a useful property in preventing

unwanted adhesion of tissue post-surgery<sup>105</sup>, particularly for PEG hydrogels due to the low protein adsorption of PEG<sup>106</sup> making it bio-inert. Bioactive and adhesion molecules can be added to synthetic hydrogel networks to increase controlled cell adhesion and proliferation<sup>107,108</sup>.

Natural hydrogels have advantages over synthetic polymers due to their biocompatibility, sustainability and medically relevant degradation rates. Their macromolecular structure is similar to the extra cellular matrix (ECM)<sup>109</sup> due to the topography of proteins, carbohydrates and other natural polymers<sup>104</sup>. Collagen and fibroin are Food and Drug Administration (FDA) approved, clinically tested materials frequently used in hydrogels due to their impressive properties *in vivo*. The components to make natural hydrogels can be physically extracted *ex vivo* from a donor with ethical concerns, batch-to-batch variation and risk of pathogens or can be produced recombinantly removing these risks.

#### **4.1.2. Physical, enzymatic and chemical crosslinking of hydrogels**

Natural hydrogels can be defined by the method in which the cross-links form: physical, enzymatic or chemical. Physical cross-links are transient interactions formed due to entanglement of the monomers and can involve hydrophobic, hydrophilic and ionic interactions<sup>3</sup> in the self-assembling process and are formed from different stimuli, such as temperature, sound and pH. Enzymatic crosslinking takes advantage of the substrate specificity of enzymes to form covalent links between monomers. For example, the use of horse radish peroxidase and hydrogen peroxide to form dityrosine bonds in silk fibroin<sup>110</sup>. Chemically cross-linked hydrogels have permanent, covalent bonds between the monomers forming the polymeric network. Chemical crosslinking can be performed by addition of photoreactive crosslinkers<sup>111</sup>, radical reactions<sup>112</sup> or chemical crosslinkers such as glutaraldehyde<sup>113</sup>. Whilst chemical and enzymatic crosslinking form strong covalent bonds, chemical crosslinking brings benefits such as

fast gelation kinetics and control over degree of crosslinking. However, chemical crosslinkers are often toxic, requiring multiple wash steps to remove residual material, can require non-aqueous media for reactions to proceed and are less environmentally friendly than using physical or enzymatic methods to crosslink<sup>114</sup>. Enzymatic crosslinking however is extremely substrate specific and expensive although it can be used in physiologically relevant conditions, making it useful for injectable hydrogels which crosslink *in situ* under mild conditions<sup>115</sup>. Physical crosslinking is cheap, safe and non-toxic to cells

#### **4.1.3. Factors that affect hydrogel transparency**

Protein hydrogels can be opaque or transparent giving rise to different material properties. Hydrogels are opaque when visible light is absorbed and scattered due to disordered and crystalline structures within the network<sup>116</sup>. Transparent and opaque hydrogels can be used for different purposes: transparency is useful for tissue engineering purposes and imaging whereas opacity is acceptable for drug delivery or implantation. There is some contention in the literature about what causes opaque hydrogels. It has been claimed that opacity is caused by particulate protein aggregation whereas transparency is due to a more stranded architecture<sup>117</sup>. Alternatively, that heterogenous structures within the hydrogel architecture scatter light more than more organized structures<sup>118, 119</sup> causing opacity. However, there are examples of rationally designed and organized crosslinked protein hydrogels which are opaque<sup>120</sup>. It has also been suggested that the degree of  $\beta$ -sheet content and crystallinity within the hydrogel increases opacity<sup>116, 118, 119</sup>. Hydrogels formed of Bovine Serum Albumin (BSA) at pH close to the isoelectric point of the protein were brittle and opaque with more  $\beta$  sheet content, whereas hydrogels formed far from the isoelectric point were transparent with fewer  $\beta$  sheets<sup>121</sup>. Therefore, light

transmittance can be used to understand the architecture within the hydrogel and the structure of the proteins.

#### **4.1.4. Spider silk protein hydrogels in literature**

A larger proportion of the published literature has been focused on silk fibroin hydrogels<sup>122-123</sup>, due to the already extensive research and ready availability. Physical protein hydrogels have been formed from silk fibroin (*Bombyx mori*) by sonication<sup>124,125,126</sup>, thermal gelation<sup>127</sup> and vortexing<sup>123</sup> which range from opaque to transparent depending on the method of gelation and concentration. The sol-gel transition in silk fibroin is associated with an increase in  $\beta$  sheet content<sup>128</sup>. Silk fibroin is an FDA approved biomaterial and elicits low immunological response upon implantation once it is separated from the immunogenic glue-like protein sericin<sup>49</sup>.

There are only a handful of published recombinant spider silk hydrogels as this is an emerging field and therefore there are many opportunities. The first recombinant spider silk protein hydrogel, prepared from C16, a recombinant protein based on the repetitive region from *A. diadematus* dragline silk ADF-4, was reported in 2005. Purification involved denaturing conditions due to insolubility of the spidroin. Transparent, nanofiber based hydrogels self-assembled on the timescale of 48-168 hours and were then stabilized by chemical crosslinking with ammonium peroxydisulfate (APS) catalysed by a ruthenium catalyst, covalently linking tyrosine residues<sup>129</sup>. This recombinant spidroin was developed into eADF4(C16) and was also formed into transparent nanofiber hydrogels at 3% and 7% (w/v). Dialysis against polyethylene glycol (PEG) was also investigated as a method of hydrogel formation although this was difficult to control as above 30% (w/v) the protein began gelling “uncontrollably”. eADF4(C16) hydrogels have since been used for, drug delivery<sup>86</sup> and 3D printing for cell culture purposes by introducing an RGD peptide into the genetic sequence of the protein<sup>76</sup>.

A different method of physical hydrogel self-assembly investigated is heat. Three variations of a soluble recombinant spidroin based on *Nephila clavipes* MaSp1, a C-terminus only (NcCT), a repetitive region (n=4) repeats only (MaSp14) and a combination of the two (MaSp14CT)<sup>81</sup>. The spidroins at 15 % (w/v) were heated from 2 °C to 85 °C and back down to 2 °C. NcCT formed a transparent reversible hydrogel at low temperatures and a translucent irreversible hydrogel above 65 °C whereas MaSp14 did not form a hydrogel at any temperature investigated. MaSp14CT formed an opaque reversible hydrogel at 10 °C and below and did not gel at higher temperatures. Formation of the hydrogels at high temperatures was associated with partial unfolding of protein secondary structure exposing buried hydrophobic amino acid side chains that could interact and stabilize this conformation, whereas at low temperatures increased hydrogen bonding and hydrophobic interactions. NcCT was combined with resilin to create a copolymer hydrogel which had a gelation timescale of hours at 37 °C<sup>130</sup>. A patent<sup>131</sup> has been filed by the inventors of this hydrogel system, indicating the promising prospects of recombinant spider silk protein hydrogels.

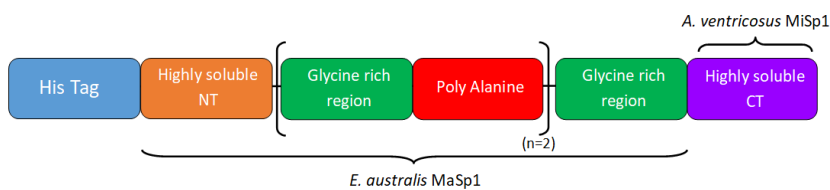
#### **4.1.5. NT2RepCT structure and properties**

NT2RepCT is a chimeric, recombinant spidroin (33 kDa) which was created by combining a highly soluble and pH responsive NT from *Euprosthenoops australis* MaSp1, a short repetitive region from *E. australis* and a highly soluble and pH responsive CT from *Araneus ventricosus* MiSp (Figure 10). The combination of these two highly soluble domains enables this protein to be concentrated to similar concentrations as found in the dope in spider silk glands without precipitating (>500 mg/mL)<sup>2</sup>.

NT2RepCT fibres were formed by extruding highly concentrated protein solution into an aqueous, acidic (pH 3.0-5.5) solution through a narrow capillary. Nearly 1000m of fiber could be produced from 1L of shake flask *E. coli* culture<sup>2</sup>. These fibres were formed from NT2RepCT solution between 100-500 mg/mL by lock and trigger

mechanisms analogous to native silk in silk glands. The recorded toughness for NT2RepCT was 45 MJ/m<sup>3</sup> which is the highest recorded for spun recombinant spider silk.

i.) MGHHHHHMSHTTPWTNPGLAENFMNSFMQGLSSMPGFTASQLDD  
 MSTIAQSMVQSIQSLAAQGRTPNKLQALNMAFASSMAEIAASEEG  
 GGSLSLTKTSSIASAMSN AFLQTTGVVNQPFINEITQLVSMFAQAGMN  
 DVSAGNSGRGQGGYGQGGNAAAAAAAAAAAAAAAAAGQGGQGGY  
 GRQSQGAGSAAAAAAAAAAAAAAAAGSGQGGYGQGGYGQGGYQSGNS  
 VTSGGYGYGTSAAAGAGVAAGSYAGAVNRLSSAEAA SRVSSNIAAIA  
 SGGASALPSVISNIYSGVVASGVSSNEALIQALLELLSALVHVLSSASI  
 GNVSSVGV DSTLN VVQDSV GQYVG



ii.)

Figure 10: i.) Amino acid sequence of NT2RepCT (33 kDa) Light blue = hex histidine purification tag, Orange = NT from *E. australis* MaSp1, Green = glycine rich region (n=3), Red = poly alanine region (n=2), Purple = CT from *A. ventricosus* MiSp1. ii.) Schematic of NT2RepCT in the same colours

The pH sensitivity of the chosen NT and CT is critical to the formation of fibres from NT2RepCT. At pH 7 the *E. australis* MaSp1 NT exists in mainly monomers but as the pH decreases to pH 5.5 the NT forms stable homo dimers (Figure 11) which have strong dipoles<sup>39,36</sup>. At pH 7 *A. ventricosus* MiSp CT as an organized anti-parallel dimer (Figure 11).and the CT unfolds into  $\beta$  sheet amyloid fibrils as pH decreases below 5.5<sup>35</sup>. NT2RepCT shows temperature and pH dependent protein secondary structure. At low temperatures at pH 6-8,  $\alpha$  helical structures dominate with irreversible  $\beta$ -sheets forming as the temperature was increased. At lower pH NT2RepCT became destabilized and aggregated forming fibres in the cuvette. Furthermore, the transition to  $\beta$ -sheet structures occurred at lower temperatures and with a more abrupt transition at lower pH<sup>132</sup>. The self-assembly of NT2RepCT into higher order oligomers

as a result of decreasing pH was captured by electrospray ionization mass spectrometry (ESI-MS). As the pH decreases below 7, NT2RepCT forms non-covalent dimers (Figure 12) with the compact repetitive domain hidden from solvent. The solvent exposed NT and CT dimerize and unfold leading to rapid polymerization and finally fiber formation. MS captured NT2RepCT oligomers up to 12 units. In a previous study, NT2RepCT was shown to form 7-9 nm diameter micelle structures in cryo-EM at pH 5.5 under shear force<sup>2</sup>.

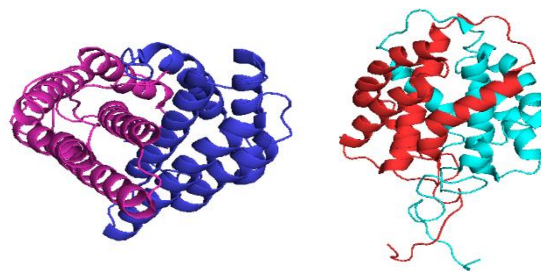


Figure 11: (Left) *E. australis* NT dimer (PDB: 2LTH). Each monomer subunit unit in either pink or purple. (Right) *A. ventricosus* MiSp CT dimer (PDB: 2MFZ). Each monomer subunit in either red or cyan.

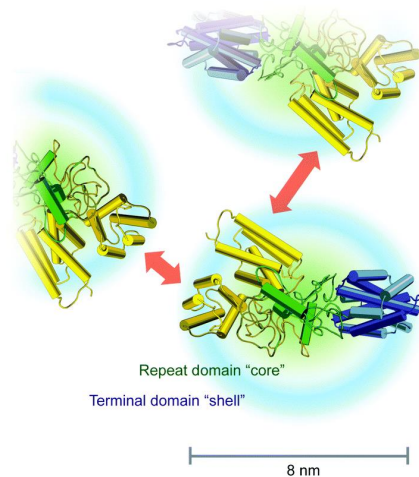


Figure 12: Cartoon of NT2RepCT dimers interacting in fiber self-assembly. The replicate domain (green) creates a condense core that eliminates water whereas the solvent exposed NT (yellow) and CT (blue) create a globular 'shell' with a diameter of ~ 8nm. From: M. Landreh *et al.*<sup>133</sup>

## 4.2. Methods

### 4.2.1. Physical NT2RepCT hydrogel self-assembly conditions investigated

Various concentrations and buffers were used to form NT2RepCT hydrogels (Table 3) to compare previously reported silk hydrogel gelation conditions applicability to NT2RepCT. The pre-gel solutions were then transferred into either 96 well transparent hydrophobic plates (Starstedt) (for absorbance measurements), 1.5 mL Eppendorf or moulds created by removing the top 1 cm of a 1 mL or 5mL graduated, needle free syringe (Leur-lok™, BD Plastipak). The syringe moulds were sealed with Parafilm® (StarLab) to prevent evaporation. Pre-gel solutions were incubated at 37 °C or 40 °C for 16 hours to induce hydrogel formation.

Table 3: Conditions tested that affect NT2RepCT self-assembly hydrogel formation.

<b>NT2RepCT % (w/v)</b>	<b>Buffer</b>	<b>Buffer concentration</b>	<b>Temperature</b>
<b>0.25</b>	MQ water	N/A	37 °C
<b>0.5</b>	MQ water	N/A	37 °C
<b>1</b>	MQ water	N/A	37 °C
<b>2</b>	MQ water	N/A	37 °C
<b>2.4</b>	MQ water	N/A	37 °C
<b>2.4</b>	NaCl (aq)	50, 100, 500 mM	37 °C
<b>2.4</b>	FeCl <sub>3</sub> (aq)	50, 100, 500 mM	37 °C
<b>2.4</b>	CaCl <sub>2</sub> (aq)	50, 100, 500 mM	37 °C
<b>2.4</b>	MgCl <sub>2</sub> (aq)	50, 100, 500 mM	37 °C
<b>2.4</b>	PBS pH 7.4	1x	37 °C
<b>2.4</b>	DMEM	1x	37 °C
<b>2.4</b>	tris pH 4, 7 and 10	20 mM	37 °C & 40 °C
<b>2.4</b>	HEPES pH 4, 7 and 10	20 mM	37 °C
<b>2.4</b>	CAPS pH 10	20 mM	37 °C

#### 4.2.2. Monitoring hydrogel kinetics at OD<sub>595</sub>

The absorbance at 595 nm relating to the turbidity of NT2RepCT heat induced hydrogels was monitored using a TECAN Spark 10M (Spark Control version 1.1). Absorbance measurements were taken every 15 minutes for 16 hours. A 96 well transparent hydrophobic plate (Starstedt) was used and the temperature of 37°C was maintained throughout. Absorbance was normalized to blanks and plotted against time.

#### 4.2.3. Circular Dichroism Spectroscopy

CD spectra were recorded with a Chirascan Plus (Applied Photophysics) equipped with a Quantum Northwest TC 125 temperature controller. Spectra were collected from 180 – 250 nm with a resolution of 1 nm by using a 1 mm path length cuvette. For melt experiment the temperature was increased from 7 °C to 74 °C in smooth ramp mode at a ramp rate of 1 °C per minute. This temperature range was measured at 16 points with 3 acquisitions at each point and a time measurement per point of 0.5 seconds. Lyophilised NT2RepCT was reconstituted in double distilled milli Q water (MQ) at 0.08 mg/mL or at 0.05 mg/mL in 20 mM tris pH 7 or 20 mM CAPS pH 10. Samples were equilibrated at the starting temperature for 5 minutes before measurements. The CD spectra presented represent the accumulation of three measurements and were smoothed by Chirascan software version 4.4.0. CD data are reported in milli degrees (m°) or molar ellipticity (°x cm<sup>2</sup>/dmol).

Conversion from m° to molar ellipticity

Equation 2

$$\text{molar ellipticity } (^\circ \times \text{cm}^2/\text{dmol}) = \frac{m^\circ \times MW (\text{gmol}^{-1})}{10 \times \text{path length (cm)} \times \text{concentration (gL}^{-1}\text{)}}$$

Equation 3

$$\text{molar ellipticity } (^\circ \times \text{cm}^2/\text{dmol}) = \frac{m^\circ \times 33,278 (\text{gmol}^{-1})}{10 \times 0.01 (\text{cm}) \times 0.05 \text{ or } 0.08 (\text{gL}^{-1})}$$

#### 4.2.4. Assessing light transmittance of formed heat-induced hydrogels

Heat induced NT2RepCT hydrogels were formed in a 96 well transparent hydrophobic plate (Starstedt) as described above. Absorbance was measured in triplicate at 400, 500, 600 and 700 nm including blanks and empty wells in a TECAN Spark 10M (Spark Control version 1.1). Absorbance was normalized to blanks. Percentage transmittance (%T) was calculated from absorbance (A) at each wavelength using Equation 4 and Equation 5. Transmittance at each wavelength was compared for hydrogels formed in different buffers.

$$\text{Equation 4: } A = 2 - \log_{10} \left( \frac{1}{T} \right)$$

$$\text{Equation 5: } \therefore \%T = 100(10^{-A})$$

#### 4.2.5. Dynamic Light Scattering (DLS) and Zeta Potential

Dynamic Light Scattering and Zeta potential measurements were performed on a Zetasizer Nano ZS (Malvern Instruments Ltd., UK) using Zetasizer Software version 7.13. Lyophilised NT2RepCT was reconstituted in MQ water, 20 mM tris pH 7 or 20 mM CAPS pH 10 at 1 mg/mL. Each sample was filtered using a Sartorius minisart® 0.22 µm filter before analysis to remove particles and dust. A folded capillary zeta cell DTS1070 cuvette was used. DLS measurements were performed at 25 °C and 37 °C using fresh sample for each experiment. Each sample was measured in 3 replicates of 5 scans. Particle size presented from intensity. Zeta potential was measured at 25 °C.

### 4.3. Results

#### 4.3.1. NT2RepCT self assembles into hydrogels at 2.4 % (w/v) at 37 °C

After 16 hours incubation at 37 °C, only 2.4 % (w/v) NT2RepCT in MQ water formed a translucent hydrogel which resisted gravitational flow after inversion for 40 s (Figure 13). Lower concentrations of NT2RepCT appeared more viscous, particularly 2 % (w/v) NT2RepCT which initially resisted gravitational flow but did not appear to be a hydrogel like 2.4 % (w/v). Compared to the pre-gel solution of 2.4 % (w/v) NT2RepCT, the formed hydrogel was slightly translucent after gelation.

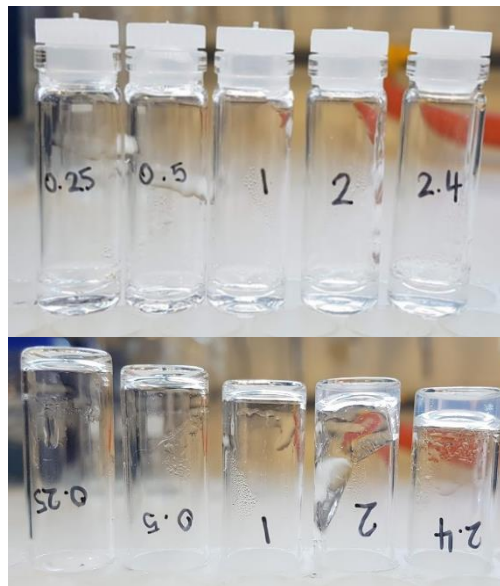


Figure 13: Above: Solutions of NT2RepCT (pre-gel) in MQ water at 0.25, 0.5, 1, 2 and 2.4 % (w/v) in 5 mL glass vials. Below: Those same solutions of NT2RepCT after 16 hours incubation at 37 °C for 16 hours. Vials inverted to show hydrogel formation.

#### 4.3.2. Formation of 2.4 % (w/v) NT2RepCT hydrogel can be monitored at 595 nm

NT2RepCT in MQ water at 2.4 % (w/v) increased in turbidity and opacity as the hydrogel formed (Figure 14). The hydrogels varied from translucent to opaque depending on the vessel they were formed in and the age of the MQ water. This

increase in turbidity was monitored by measuring absorbance at 595 nm over time at 37 °C. The absorbance begins to plateau at 550 minutes (~9.2 hours) associated with a constant turbidity and formation of the translucent to opaque hydrogel.

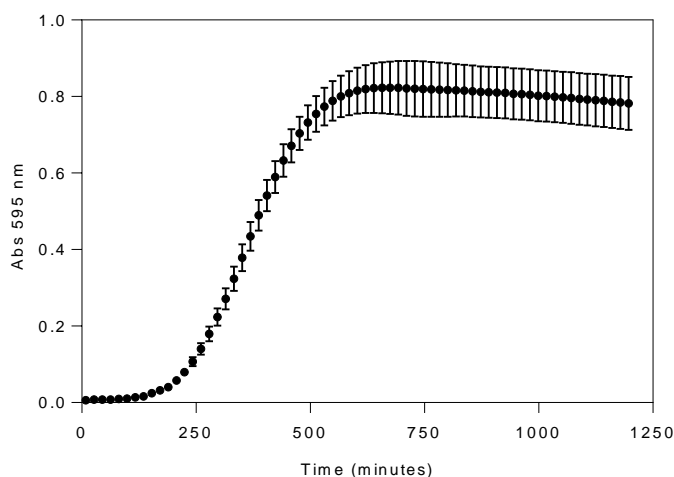


Figure 14: Absorbance at 595 nm over time at 37 °C of 2.4 % (w/v) NT2RepCT in MQ water. (n=3) mean  $\pm$  SD.

#### 4.3.3. Presence of salt, phosphates and media inhibit hydrogel self-assembly

An inhibitory effect was seen on gelation of NT2RepCT hydrogels with phosphate buffered saline (PBS) and cell culture media DMEM supplemented with 10 % (v/v) FBS. aggregated upon heating to 37 °C for 16 hours and formed a globular structure separated from the media (Figure 15). The presence of 50, 100 and 500 mM NaCl, FeCl<sub>3</sub>, CaCl<sub>2</sub> and MgCl<sub>2</sub> prevented self-assembly of NT2RepCT into hydrogels when incubated at 37 °C for 10 hours. All salt conditions caused NT2RepCT to precipitate out of solution upon heating and no hydrogel was formed. Additionally, 100 mM MgCl<sub>2</sub>, 100 mM CaCl<sub>2</sub>, 100 mM and 500 mM FeCl<sub>3</sub> caused immediate precipitation of NT2RepCT at room temperature (20 °C). The samples increased in turbidity over time which was measured by absorbance at 595 nm (Figure 16). A positive control of 2.4 % (w/v) NT2RepCT in MQ water was included as a reference, termed 0 mM [salt]. To test

whether presence of a buffer during hydrogel formation would cancel the inhibiting action of salt 2.4 % (w/v) NT2RepCT in 20 mM tris pH 10.5 + 10 mM NaCl was incubated at 37 °C for 16 hours. No hydrogel formed and NT2RepCT protein precipitated.

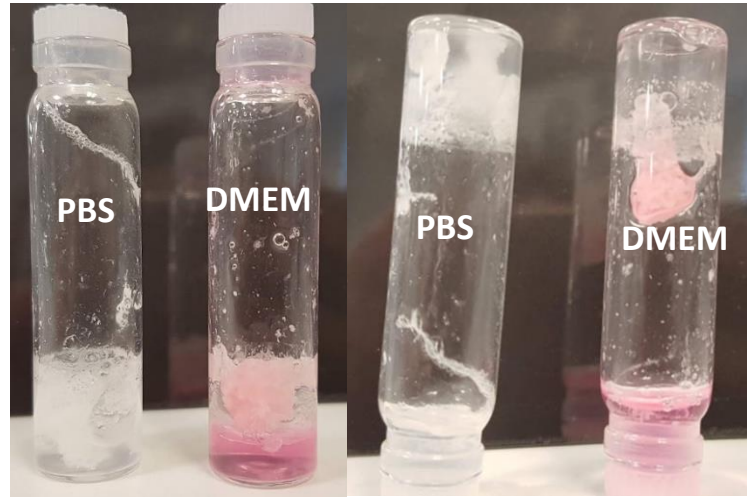


Figure 15: 2.4 % (w/v) NT2RepCT in PBS pH 7.4 and DMEM + 10 % (v/v) FBS after incubation at 37 °C for 16 hours.

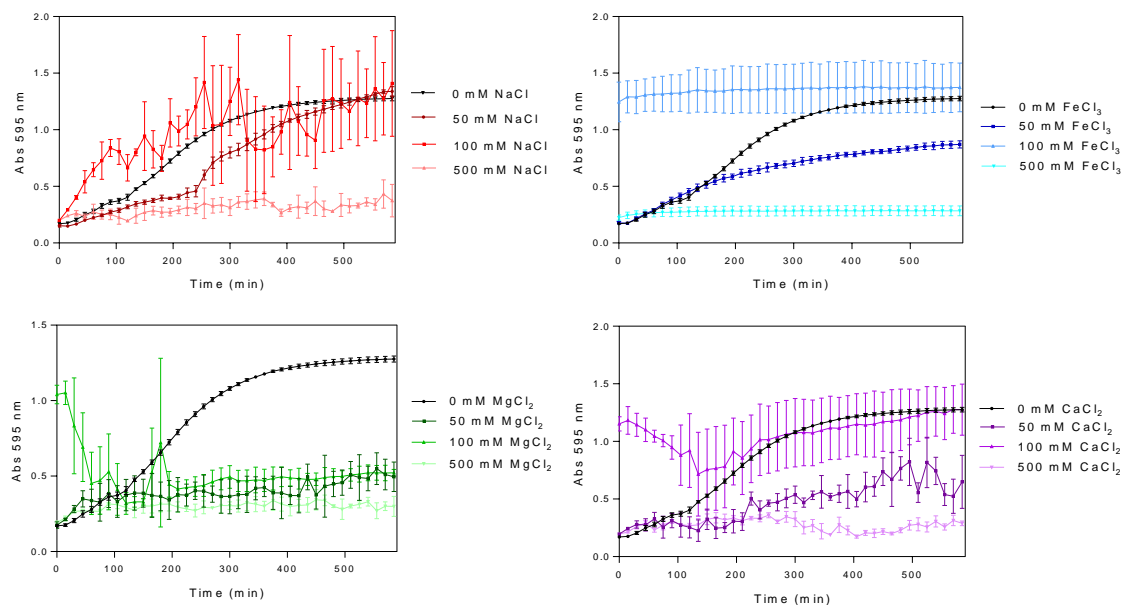


Figure 16: Absorbance at 595 nm of 2.4 % (w/v) NT2RepCT in 0, 50, 100 and 500 mM NaCl (red), FeCl<sub>3</sub> (blue), MgCl<sub>2</sub> (green) or CaCl<sub>2</sub> (purple) over 600 minutes at 37 °C. Black line in all graphs is 0 mM salt (MQ water only). (n=3) mean ± SD.

#### 4.3.4. NT2RepCT changes conformation with increasing temperature and pH

To understand the protein secondary structure of NT2RepCT upon heating, circular dichroism melt experiments were performed. In all conditions tested, NT2RepCT unfolded with increasing temperature. NT2RepCT in MQ water, in 20 mM tris pH 7 or 20 mM CAPS pH 10 (referred to herein as MQ, pH 7 and pH 10) showed not only different melt responses with increasing temperature but different protein conformations at room temperature. MQ shifted from classical  $\alpha$ -helices at low to physiological temperatures to anti-parallel  $\beta$  pleated sheets, shown by a positive band at 195 nm and a negative band at 208 nm<sup>134</sup> at 56 °C and above (Figure 17 MQ).

NT2RepCT in pH 7 shows negative  $\alpha$ -helical bands at 218 and 222 nm but the positive band is at 195 nm not 193 nm. As the temperature increases there was no obvious shift to anti-parallel  $\beta$  pleated sheets as with MQ indicating instead denaturation or a shift to disordered structure as above 210 nm there is low ellipticity (Figure 17 pH 7).

At pH 10 at low and physiological temperatures NT2RepCT exists as primarily  $\alpha$ -helices which decrease in ellipticity with increasing temperature (Figure 17 pH 10). As with pH 7 there is no obvious shift to anti-parallel  $\beta$ -pleated sheets.

Comparing molar ellipticity (MRE), which corrects for sample concentration, at 222 nm showed that MQ was the most  $\alpha$ -helical at the start of the experiment, followed by pH 10 with pH 7 being the least alpha helical (Figure 18). As the temperature increased from 19 to 37 °C, NT2RepCT in MQ had the largest change in MRE at 222 nm due to the shift to anti-parallel  $\beta$ -pleated sheets. pH 7 and pH 10 showed similar change in MRE as the temperature increased to 37 °C indicating the same amount of protein unfolding (Table 4).

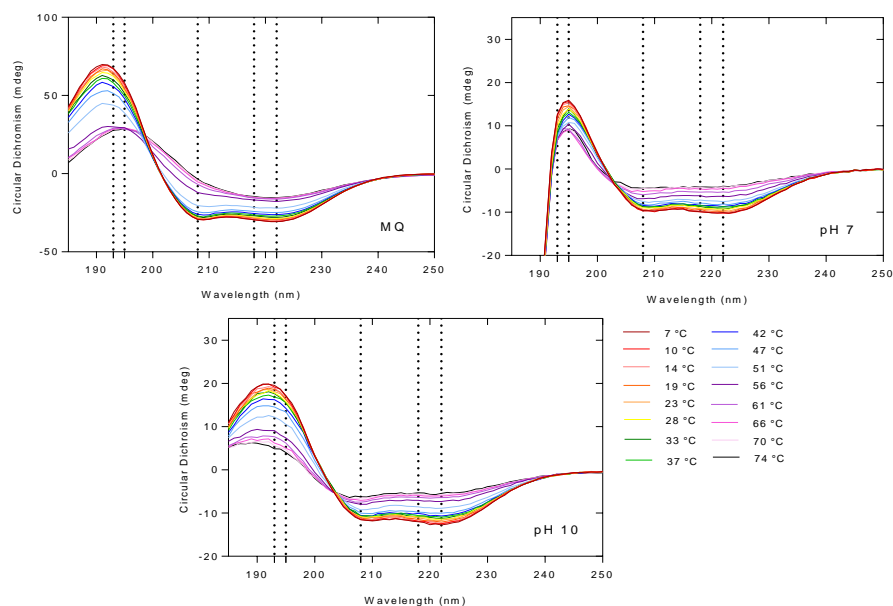


Figure 17: Circular Dichroism of 0.08 mg/mL NT2RepCT in MQ water and 0.05 mg/mL NT2RepCT in 20 mM tris pH 7 and 20 mM CAPS pH 10 at different temperatures. Dotted lines signify expected bands<sup>134</sup> for  $\alpha$  helix (positive band at 193 nm and negative bands at 208 and 222 nm) and anti-parallel  $\beta$ -pleated sheet (positive band at 195 nm and negative band at 218 nm).

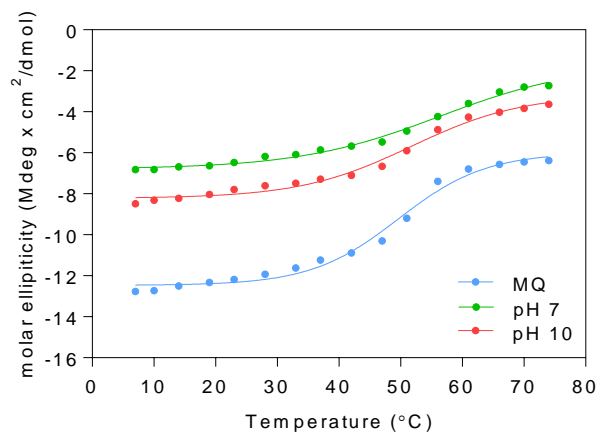


Figure 18: Molar ellipticity ( $\text{Mdeg} \times \text{cm}^2/\text{dmol}$ ) at 222 nm with increasing temperature for NT2RepCT in MQ water (blue), 20 mM tris pH 7 (green) or 20 mM CAPS pH 10 (red). (MQ water = 0.08 mg/mL, pH7 and 10 = 0.05 mg/mL). Solid line represents the best sigmoidal curve fit for visualization.

Table 4: Change in molar ellipticity ( $^{\circ} \times \text{cm}^2/\text{dmol}$ ) (MRE) at 222 nm between 19 and 37  $^{\circ}\text{C}$  for 0.08 mg/mL NT2RepCT in MQ water, and 0.05 mg/mL NT2RepCT in 20 mM tris pH 7 or 20 mM CAPS pH 10.

MRE	MQ ( $\text{M}^{\circ} \times \text{cm}^2/\text{dmol}$ )	pH 7 ( $\text{M}^{\circ} \times \text{cm}^2/\text{dmol}$ )	pH 10 ( $\text{M}^{\circ} \times \text{cm}^2/\text{dmol}$ )
222 nm 19 $^{\circ}\text{C}$	-12	-6.6	-8
222 nm 37 $^{\circ}\text{C}$	-11	-5.9	-7.3
$\Delta$ MRE	1	0.7	0.7

NT2RepCT at pH 7 did not return to the same conformation (pre-melt) when the temperature was decreased to 20  $^{\circ}\text{C}$  after the melt experiment (post-melt) (Figure 19 pH 7). Additionally, when the temperature is lowered ellipticity becomes very negative below 192 nm. At pH 10, the  $\alpha$ -helix negative bands at 208 and 222 nm are very similar post-melt and the spectra overlap (Figure 19 pH 10).

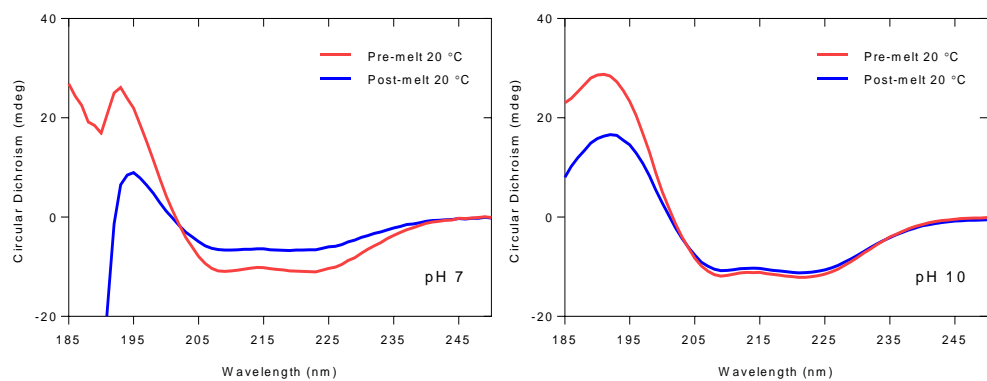


Figure 19: CD spectra of 0.05 mg/mL NT2RepCT in either 20 mM tris pH 7 or 20 mM CAPS pH 10. Red line = CD spectra recorded at 20  $^{\circ}\text{C}$ , Blue line = The same sample after heating in melt experiment from 7-74  $^{\circ}\text{C}$  with heating of 1  $^{\circ}\text{C}/\text{min}$  and then cooled back down to 20  $^{\circ}\text{C}$ . Spectra shown are accumulation of 10 scans smoothed in Chirascan software.

### 4.3.5. Gelation pH and temperature affected hydrogel appearance

The effect of pH in the pre-gel solution buffer determined the opacity and appearance of the formed NT2RepCT hydrogel after incubation at 37 °C for 10 hours (summarized in Table 5). At pH 4 in both tris and HEPES, 2.4 % (w/v) NT2RepCT immediately precipitated out of solution and formed white, opaque hydrogels upon heating to 37 °C for 10 hours. The absorbance at 595 nm increased slightly over the time of the experiment for 20 mM tris pH 4 and initially decreased slightly for 20 mM HEPES pH 4. However, since both pH 4 pre-gel solutions were already turbid due to protein precipitation, 595 nm absorbance could not monitor hydrogel formation (Figure 20).

Table 5: Appearance of NT2RepCT pre-gel solution and hydrogel formed in either 20 mM tris pH 4, 7 and 10, 20 mM HEPES pH 4, 7 and 10 or 20 mM CAPS pH 10. Hydrogels were formed by incubation at 37 °C for 10 hours

<b>Buffer</b>	<b>pH 4</b>	<b>pH 7</b>	<b>pH 10</b>
<b>20 mM Tris</b>	Cloudy liquid	Clear liquid	Clear liquid
<b>20 mM HEPES</b>	Cloudy viscous liquid	Clear liquid	Clear liquid
<b>AFTER INCUBATION AT 37 °C for 16 hours</b>			
<b>20 mM Tris</b>	White opaque hydrogel	White opaque hydrogel	Transparent hydrogel
<b>20 mM HEPES</b>	White opaque hydrogel	White opaque hydrogel	Translucent white hydrogel

At pH 7, 2.4% (w/v) NT2RepCT formed a clear, pre-gel solution with no protein precipitation. After heating to induce hydrogel self-assembly both pH 7 buffer

conditions formed white opaque hydrogels. Absorbance at 595 nm for 20 mM tris pH 7 and 20 mM HEPES pH 7 both increased in the same sigmoidal shape as hydrogels formed in MQ water (pH 5.5) but reached a plateau in a shorter time period and with higher absorbance than MQ water hydrogel. 20 mM tris pH 7 had a steeper gradient and reached constant absorbance at 595 nm faster than 20 mM HEPES pH 7.

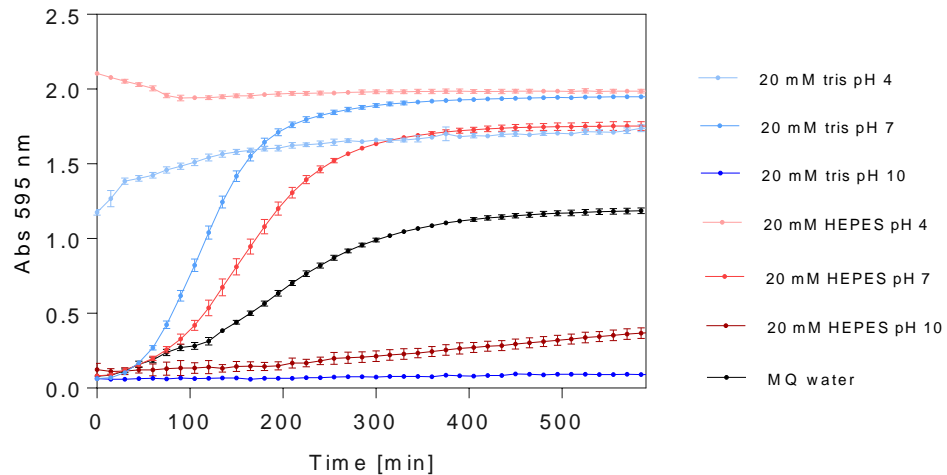


Figure 20: Absorbance at 595 nm over time measured at 37 °C of 2.4 % (w/v) NT2RepCT in 20 mM tris pH 4, 7 and 10 and 20 mM HEPES pH 4, 7 and 10. A control of 2.4 % (w/v) NT2RepCT in MQ water was included. (n=3) mean  $\pm$  SD.

At pH 10, 2.4 % (w/v) NT2RepCT formed a clear pre-gel solution, again with no protein precipitation in both buffer types (20 mM tris or 20 mM HEPES). After heating to induce hydrogel self-assembly, the 20 mM tris pH 10 hydrogels appeared transparent and the 20 mM HEPES pH 10 hydrogels were translucent. Absorbance at 595 nm did not increase over time for 20 mM tris pH 10 as the hydrogels were transparent and there was no apparent increase in turbidity. There was a slow increase in absorbance at 595 nm for 20 mM HEPES pH 10, due to the translucent appearance of the hydrogels. However, this increase in absorbance did not follow a sigmoidal shape like the hydrogels formed in either MQ water or at pH 7.

Increasing the temperature of hydrogel formation from 37 °C to 40 °C during the 16 hour incubation gelation period affected the morphology in different ways depending on the buffer the pre-gel solution was in (Figure 21). In hydrogels formed in MQ water, increasing the temperature meant the hydrogel could not hold its shape as well and appeared softer. Upon ejection from the syringe mould the hydrogel spread slightly and did not have as defined edges as the 37 °C MQ water hydrogel. This was also the case for hydrogels formed in 20 mM tris pH 7, although both 37 °C and 40 °C formed very soft, opaque white hydrogels. Interestingly, for hydrogels formed in 20 mM tris pH 10, increasing the temperature from 37 to 40 °C improved the apparent structural integrity and the formed hydrogel had smoother edges. Therefore, only hydrogels formed in 20 mM tris pH 10 improved when the temperature to induce hydrogel formation was increased by 3 °C. The hydrogels appeared to have similar levels of transparency regardless of temperature of incubation.

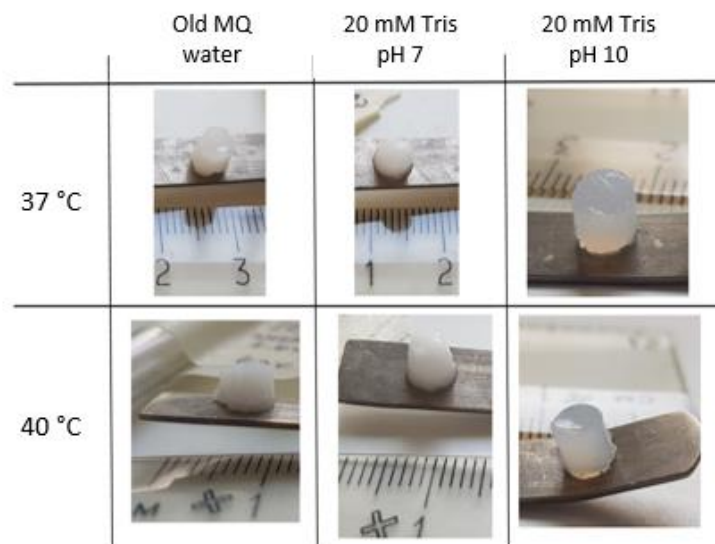


Figure 21: 2.4 % (w/v) NT2RepCT hydrogels formed in MQ water, 20 mM tris pH 7 or 20 mM tris pH 10 at 37 or 40 °C. (incubated for 16 hours) Hydrogels shown next to ruler with 1 cm measurements for scale.

#### 4.3.6. NT2RepCT hydrogel self-assembly is closely linked to pH

Hydrogels formed in tris or HEPES buffers originally prepared at pH 10 two weeks or more prior to hydrogel formation were soft and opaque in appearance. Hydrogels formed in 20 mM CAPS pH 10 were transparent. Additionally, hydrogels prepared in fresh MQ water were transparent compared to those prepared in older MQ water stored in plastic 20 mL universal containers (Figure 22).

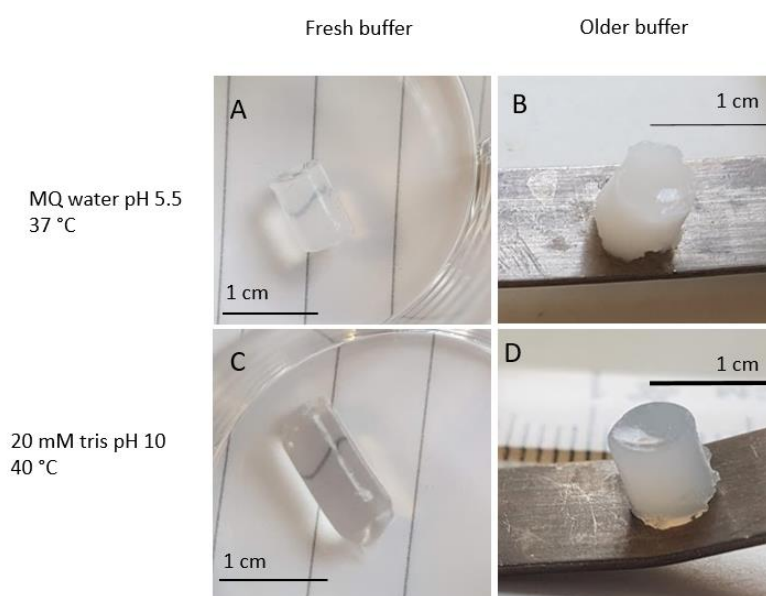


Figure 22: Differences in transparency of 2.4 % (w/v) NT2RepCT hydrogels formed in fresh and old buffers. A = 2.4 % (w/v) NT2RepCT in fresh MQ water incubated for 16 hours at 37 °C. B = 2.4 % (w/v) NT2RepCT in old MQ water incubated for 16 hours at 37 °C. C = 2.4 % (w/v) NT2RepCT in fresh MQ water incubated for 16 hours at 37 °C. D = 2.4 % (w/v) NT2RepCT in old 20 mM tris pH 10 incubated for 16 hours at 40 °C. Scale bar = 1 cm.

#### 4.3.7. Percentage transmission of visible light through hydrogel can be altered by gelation buffer

NT2RepCT hydrogels at 2.4 % (w/v) were formed by incubation at 37 °C for 16 hours in: fresh (< 1 day) MQ water, old (>2 weeks in plastic 20 mL universal tube), fresh 20 mM tris pH 10, old 20 mM tris pH 10, fresh 20 mM HEPES pH 10, 20 mM tris pH 7

and 20 mM CAPS pH 10. Percentage transmission was calculated from absorbance at 400, 500, 600 and 700 nm as described in methods (Section 4.2.4) (Figure 22). Fresh MQ water, 20 mM tris pH 10 and 20 mM HEPES pH 10 had high transmittance, over 75 % for all wavelengths tested. Old MQ water and 20 mM tris pH 7 showed very low transmittance of visible light. Old 20 mM tris pH 10 had higher transmittance than old MQ water but not as high as fresh 20 mM tris pH 10. 20 mM CAPS pH 10 showed high transmittance > 90%.

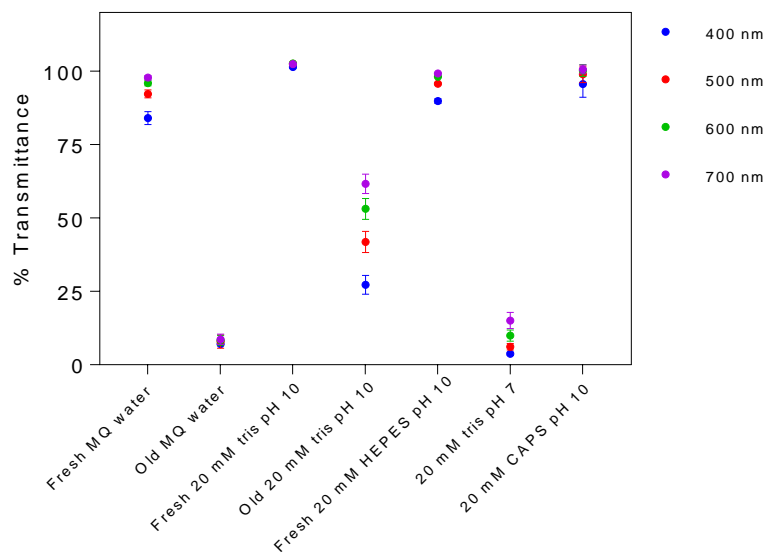


Figure 23: Percentage transmittance at 400 (blue), 500 (red), 600 (green) and 700 (purple) nm of 2.4 % (w/v) NT2RepCT hydrogels prepared in either fresh or older buffers by incubation at 37 °C for 16 hours. (n=3) mean  $\pm$  SD.

#### 4.3.8. Transparent hydrogels were made in fresh MQ water and 20 mM CAPS pH 10

Three batches (N=3) of 2.4 %(w/) NT2RepCT in either fresh MQ water or 20 mM CAPS pH 10 were formed in a 96 well plate by incubation at 37 °C for 16 hours from 3 different purifications of NT2RepCT. The three batches of 20 mM CAPs pH 10 had over 90 % transmission in all wavelengths tested with no significant difference at 700, 600

and 500 nm (Figure 24). However, there was  $P < 0.05$  statistical difference between batch 1 and 3 at 400 nm. Hydrogels formed in fresh MQ water were less reproducible than those formed in 20 mM CAPs pH 10 with significant differences ( $P < 0.0001$ ) at all wavelengths between batch 2 and the other batches. Batch 1 and batch 3 were only significantly different at 400 ( $P < 0.0001$ ) and 500 nm ( $P > 0.05$ ). However, there was still high transmittance above 90 % at 500 nm and over 80 % at 400 nm.

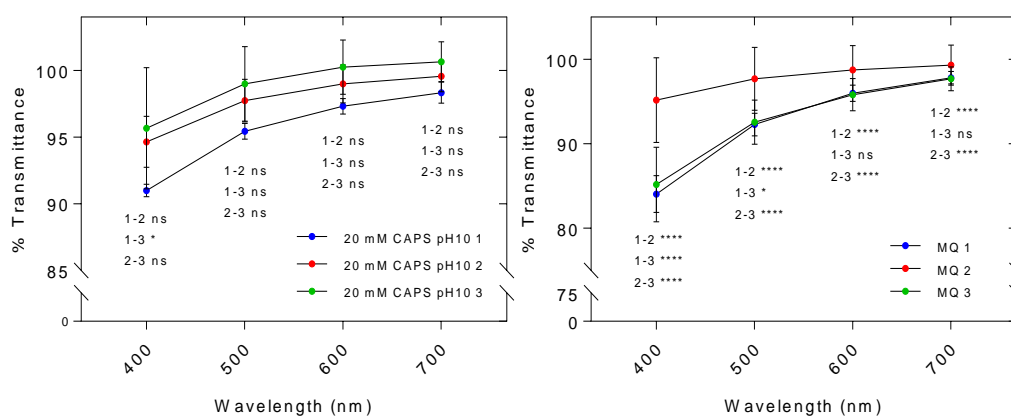


Figure 24: Percentage transmittance for 3 different batches of 2.4 % (w/v) NT2RepCT hydrogels incubated for 16 hours at 37 °C in either 20 mM CAPS pH 10 (above) or fresh MQ water (below). Each replicate numbered 1 to 3. Percentage transmittance each hydrogel batch ( $n=3$ ) mean  $\pm$  SD. Significance between each batch: 1-2 comparing batch 1 to 2, 1-3 comparing batch 1 to 3, 2-3 comparing batch 2 to 3. (ns not significant,  $*p < 0.05$ ,  $****p < 0.0001$ )

#### 4.3.9. Gelation time increased in 20 mM CAPS pH 10

Inversion tests to determine gelation point were used for MQ 37 T and CAPS10 hydrogels (formed in fresh MQ water and 20 mM CAPs pH 10). At the beginning of the experiment both MQ 37 T and CAPS10 flowed and were liquids. After 2 hours incubation at 37 °C, MQ 37 T had formed a self-supporting translucent hydrogel but CAPS10 was still liquid although the viscosity had increased. CAPS10 increased in

viscosity over time and at 6 hours was very viscous but was still flowing slowly. At 6.5 hours CAPS10 formed a self-supporting hydrogel that did not flow (Figure 25).

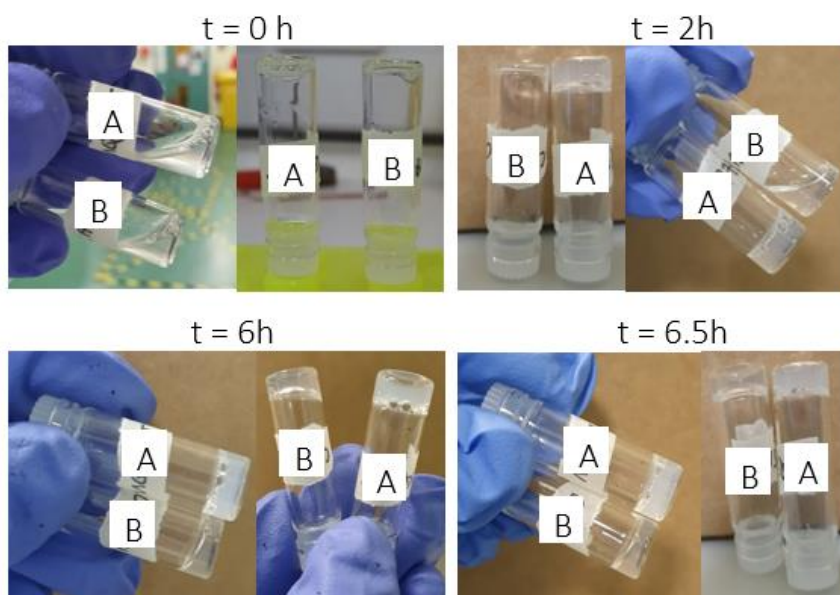


Figure 25: Inversion test to determine gelation time for MQ 37 T (A) and CAPS10 (B) hydrogels at 37 °C. MQ 37 T (A) formed a hydrogel in 2 hours but CAPS10 (B) took 6.5 hours to form.

#### 4.3.10. DLS and zeta potential

DLS measurements showed an increase in average particle diameter with increasing temperature from 25 °C to 37 °C for all conditions of NT2RepCT. Additionally, at 37 °C the diameter of the particle increased with every replicate of the 5 scans due to protein aggregation. There was also increasing polydispersity and protein aggregation for NT2RepCT in MQ water at 25 °C (Figure 26).

The zeta potential varied depending on the solution surrounding NT2RepCT. NT2RepCT in MQ water had a zeta potential of  $-14.03 \pm 0.72$  mV, in pH 7 the zeta potential was  $-5.23 \pm 0.82$  mV and at pH 10 the zeta potential was  $-23.7 \pm 1.39$  mV.

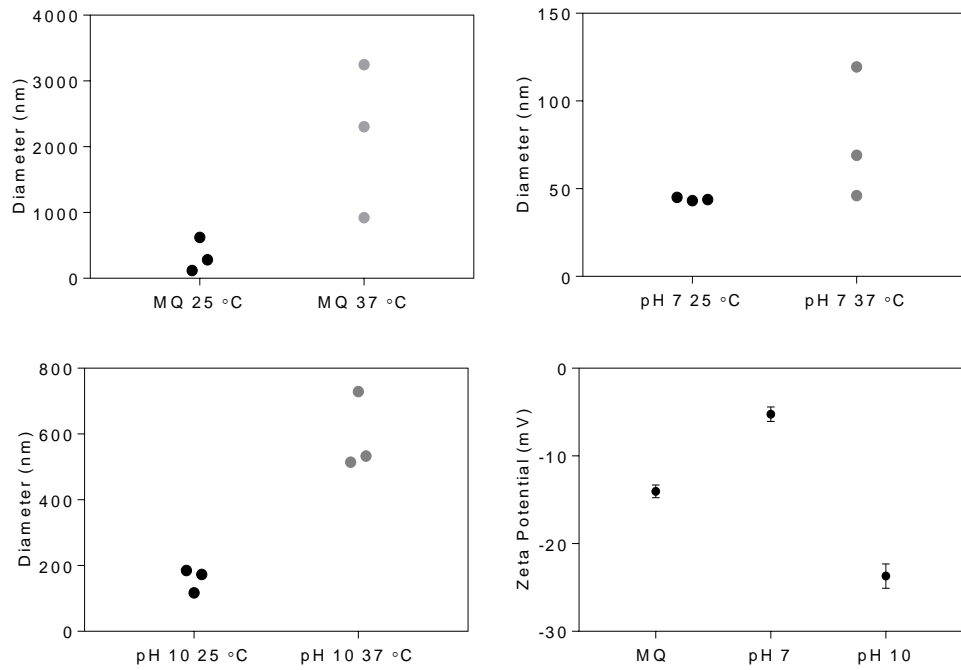


Figure 26: DLS and Zeta Potential of 0.8 mg/mL NT2RepCT in MQ water, 20 mM tris pH 7 or 20 mM CAPS pH 10. (Black circles = measured at 25 °C, Grey circles = measured at 37 °C) A = Diameter of NT2RepCT in MQ, B = NT2RepCT in 20 mM tris pH 7, C = NT2RepCT in 20 mM tris pH 10 and D = Zeta potential of NT2RepCT at 25 °C in MQ water, 20 mM tris pH 7 and 20 mM CAPS pH 10. DLS measurements shown as 3 separate repetitions of 5 scans. Zeta potential shown as (n=3) mean  $\pm$  SD.

## **4.4. Discussion of the factors that affect hydrogel formation**

### **4.4.1. Overview**

It was the aim of this chapter to determine whether NT2RepCT could form natural hydrogels from thermal stimulus and what effects this would have on hydrogel appearance and optical properties. By investigating how the secondary structure of NT2RepCT changed and understanding the pH and temperature dependence of the protein behavior, this could be utilized to form different hydrogels. It was shown that pH of gelation is a driving factor in the mechanism of hydrogel self-assembly.

### **4.4.2. NT2RepCT self-assembles into hydrogels**

The minimum concentration for NT2RepCT to self-assemble into a self-supporting hydrogel structure was found to be 2.4 % (w/v). Published silk physical hydrogels, prepared with silk fibroin or recombinant spider silk, have been made in the range of 0.6-15% (w/v)<sup>81,112,119,126</sup>. The recombinant spider silk eADF4(C16) was prepared at 3 % (w/v) for cell culture purposes<sup>76</sup>. For comparison, one of the lowest concentration self-supporting physical hydrogels reported was made from a 6 kDa protein motif YajC-CT at 0.4 mg/mL or 0.04 % (w/v)<sup>128</sup> by thermal gelation at 90 °C. Matrigel, which forms physical hydrogels at 37 °C and above is shipped frozen at concentrations between 0.8-1.2 % (w/v) and can be used at 100% or lower concentrations depending on assay type<sup>135,136</sup>. Collagen I hydrogels in cell culture on average range from 0.3-3 % (w/v) with many below 1 % (w/v)<sup>137</sup>.

Material properties, appearance, protein secondary structure and functionality of the published silk hydrogels varied with protein concentration indicating a relationship between the former and the latter. At 2 % (w/v), NT2RepCT formed a very viscous solution that was not self-supporting and flowed after inversion so could not be termed a hydrogel by that test. However, inversion tests are a very rudimentary method for analysis and results can vary depending on the diameter of the

container<sup>138</sup>. Rheology to assess the magnitude of storage ( $G'$ ) and loss modulus ( $G''$ ) in the linear viscoelastic region (LVE) during a frequency sweep would give a better understanding of the material properties, in addition to other rheological tests<sup>139</sup>. Rheology and other mechanical testing of NT2RepCT hydrogels are discussed in Section 6.3.2.

#### **4.4.3. Monitoring hydrogel kinetics at 595 nm only useful for turbid hydrogels**

If a hydrogel is opaque or translucent, the gelation kinetics can be monitored over time, as the hydrogel becomes more opaque. Turbidity at 595 nm is related to the optical density and light scattering in a solution. Turbidity has been used as a method of tracking gelation kinetics with silk fibroin (measured at 590 nm)<sup>119</sup>, the recombinant spidroin eADF4(C16) (measured at 570 nm)<sup>112</sup>, eMaSp1 (measured at 570 nm)<sup>140</sup> and a recombinant spidroin NcCT-resilin construct (measured at 350 nm). In the case of NT2RepCT, for the opaque hydrogels formed at pH 7 or older buffers differences in turbidity/optical density over time can be seen.

#### **4.4.4. Presence of electrolytes inhibitory to heat induced gelation**

NT2RepCT is an extremely soluble protein with many charged residues and has dimer-monomer interactions depending on pH and salt<sup>39</sup>. There are many salt bridges, ionic interactions and hydrophobic interactions that occur within NT2RepCT dimerization and subsequent oligomerization. As NT2RepCT unfolds with increasing temperature, further charged residues and patches are exposed in addition to hydrophobic patches and residues.

Chaotropic and kosmotropic ions destabilize and stabilize protein structure in water respectively. Chaotropic agents disrupt hydrogen bonding, weakening the hydrophobic effect, solubilizing hydrophobic interactions and therefore destabilizing hydrophobic aggregates<sup>141</sup>. This can cause the protein to unfold, denature and

precipitate. Kosmotrophic agents on the other hand stabilize hydrogen bonding of proteins in water, contributing to stable hydrophobic aggregates and intermolecular interactions.  $\text{Ca}^{2+}$  and  $\text{Mg}^{2+}$  are chaotrophic agents whereas  $\text{Na}^+$  is kosmotrophic.  $\text{Fe}^{3+}$  is not classified as chaotrophic or kosmotrophic, it is a large ion with high charge density. Interestingly, none of the salts and therefore chaotrophic/kosmotrophic cations promoted NT2RepCT hydrogel formation, they were inhibitory to the process and at all concentrations caused protein precipitation and no hydrogel formation. Due to the chaotrophic nature of  $\text{Ca}^{2+}$  and  $\text{Mg}^{2+}$ , this is understandable as hydrophobic interactions in hydrogel formation would be disrupted. NaCl is used in protein purification to prevent dimer formation, which is likely key in hydrogel formation, particularly at low pH. Since all salts were tested in MQ water and pH is not altered by addition of salt, NT2RepCT would dimerize and unfold at 37 °C (as shown in Section 4.3.4) but the presence of salts would affect protein interactions and therefore inhibit hydrogel formation. The same inhibitory effect was also seen for DMEM and PBS. DMEM is a complex mixture of electrolytes, including calcium chloride and sodium chloride at 1.8 mM and 109.5 mM respectively. In addition to these salts, DMEM also contains other components which likely disrupt NT2RepCT hydrogel formation. PBS contains 100 mM phosphate buffer, 27 mM KCl and 137 mM NaCl.

In comparison to NT2RepCT, the recombinant spidroin eADF4(C16) had faster gelation and more opaque in the presence of DMEM. Furthermore, addition of DMEM or  $\text{CaCl}_2$  improved the mechanical properties of formed hydrogels despite no significant differences in bulk morphology or protein secondary structure<sup>142</sup>. The absence of a NT or CT in eADF4(C16) might explain this different response to DMEM, chaotrophic and kosmotrophic cations. The highly soluble NT and CT of NT2RepCT are highly likely to be involved in hydrogel formation, creating a more complex system and mechanism of gelation than for the 16 repeats of eADF4(C16).

FeCl<sub>3</sub> also had an inhibitory effect on hydrogel formation, with NT2RepCT precipitating immediately at room temperature before incubation at 37 °C. This could be due to the high concentrations used. Silk fibroin incubated with Fe(III) at pH 5.7 at 37 °C overnight formed opaque greenish hydrogels. However, the highest concentration tested was 10.7 mM. It was found that Fe(III) promoted formation of  $\beta$  sheets<sup>118</sup>.

Therefore, NT2RepCT hydrogels cannot be self-assembled directly into cell culture appropriate media. Additionally, the gelation is on too long a timescale for cell seeding and the cells would likely fall to the bottom and not be evenly distributed.

#### **4.4.5. NT2RepCT thermal denaturation reflects isolated terminal domains**

The different changes in NT2RepCT protein secondary structures with increasing temperature and pH is a useful attribute that can be exploited to form protein hydrogels, particularly a shift to  $\beta$ -sheet structures with increasing temperature, which has been seen previously with other recombinant spidroins<sup>81,140</sup>. Presence of  $\beta$ -sheets has been shown to be a prominent feature in physically crosslinked protein hydrogels<sup>112,124</sup>. Indeed,  $\beta$ -sheets were critical in formation silk fibroin hydrogels and led to irreversible hydrogel formation above 15 % gelation<sup>128</sup>. Like NT2RepCT, silk fibroin contains glycine rich regions but it lacks polyalanine repeats<sup>90</sup>. The crystalline,  $\beta$ -sheet polyalanine replicates in natural spider silk contribute to formation of strong fibres<sup>2,6,30</sup>.

The temperature and pH dependent behavior of whole NT2RepCT in this study was similar to published behavior of the isolated terminal domains *E. australis* MaSp1 NT<sup>39</sup> and *A. ventricosus* MiSp1 CT<sup>35</sup> and whole NT2RepCT<sup>132</sup>. The thermal degradation of NT2RepCT in MQ water (pH 5.5) reflected that of the isolated CT at pH 5.5 and NT2RepCT at pH 6.0, a shift from  $\alpha$ -helical to anti-parallel  $\beta$ -sheets.

In all three conditions studied there was a decrease in CD signal with increasing temperature likely due to aggregation and precipitation of NT2RepCT as has been seen previously<sup>132</sup>. The differences seen in NT2RepCT secondary structure at pH 7 in this study where disordered structures were seen compared to that reported by T. Arndt *et al.*<sup>132</sup> where irreversible  $\beta$ -sheet formation was seen is most likely due to poor CD signal.

As with isolated NT and CT at around neutral pH, NT2RepCT was also able to refold somewhat to the pre-melt structure. The thermal denaturation behavior at pH 10 is very similar to pH 7 but NT2RepCT refolds to  $\alpha$ -helical structures to a higher degree than at neutral pH. Unfortunately, the post-melt structural analysis of NT2RepCT in MQ was not performed, unlike NT2RepCT in pH 7 and pH 10. However, it is expected that NT2RepCT would behave the same as isolated CT and would not be able to refold to  $\alpha$ -helical structures after  $\beta$ -sheets had formed.

However, NT2RepCT in MQ was recorded when the CD lamp had fewer hours of usage and the instrument was more in use therefore giving better quality data due to continual purging of the system with nitrogen gas. Due to large change in conformation, NT2RepCT hydrogels cannot be sterilized by autoclaving as this will change and alter properties of hydrogels with the temperature rise to 120 °C. Therefore, sterilization by 0.22  $\mu$ m filtration before hydrogel formation is necessary if the hydrogel was to be implanted or injected into the body.

#### **4.4.6. The pH of gelation determines opacity of hydrogel**

Although poor buffer choice is usually detrimental to experimental set up, in this study it shows the importance of pH on hydrogel appearance and formation. At alkaline pH 10, NT2RepCT forms clear, transparent hydrogels. At neutral pH 7 the hydrogels formed are opaque and white. In pH 5.5 freshly decanted MQ water from the Millipore filtration machine, the hydrogels are clear. However, if that water has

become carbonated or is slightly impure, the pH will shift closer to pH 7, and this will affect the hydrogels optical properties. This was seen when the pH of older MQ water was tested with universal indicator paper. Clearly HEPES and tris buffers are not capable of maintaining pH 10 for long periods, unlike CAPS buffer (See Figure 27 for pKa values). This is due to pH drift and limited buffering capacity of these buffers at pH 10. Furthermore, tris buffer has significant pH drift with temperature<sup>143</sup>

This is exemplified in Figure 22 where fresh MQ water and 20 mM tris pH 10 form clear hydrogels and solutions older than 2 weeks form opaque to translucent hydrogels. At more neutral pH, NT2RepCT dimerizes and loses  $\alpha$ -helical structure as the temperature increases and does not full refold upon cooling. This could lead to inhomogeneous structures within the hydrogel that lead to light scattering and opaqueness<sup>116</sup>. It is not clear what state NT2RepCT is in at pH 10, whether monomer or dimer, X-ray crystallography has been performed at lower pH. Unfortunately, the crystal structure of NT2RepCT at pH 10 is outside of the scope of this research and therefore only speculation can be conveyed without more evidence. At pH 10, nearly all acidic amino acid side chains, and amines will be deprotonated<sup>118</sup>, this could cause more electrostatic repulsion due to increased net negative charge. This would reduce protein aggregation leading to more organized structures and less light scattering. This would not be the case for MQ water, a different mechanism of hydrogel formation would occur due to unfolding of CT and a shift to  $\beta$  sheet, not to mention a different charge state of NT2RepCT. Hydrogel formation is a complicated process which is different at different pH and in the presence of impurities. A comparison of pore size and morphology at different pH is discussed in further chapters in addition to comparisons of material properties between opaque and clear hydrogels.

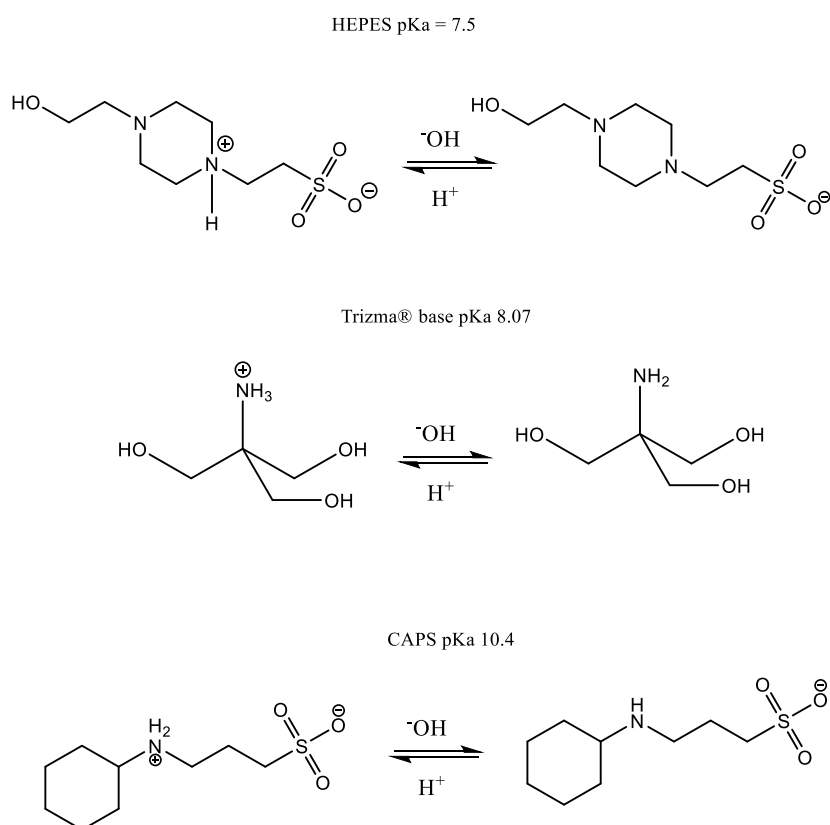


Figure 27: Dissociation and pKa values of the biological buffers HEPES, tris and CAPS.

#### 4.4.7. A small change in temperature of gelation affects appearance of hydrogels

Despite the temperature difference being only 3 °C, there are slight differences in appearance between hydrogels formed at 37 and 40 °C. The increase in temperature introduces more energy into the system increasing the rate of protein collisions and aggregation for all buffer conditions. It should be mentioned that in Figure 21 the hydrogels are all opaque to translucent and were formed in buffers older than 2 weeks and therefore might behave differently with changes in temperature than clear hydrogels formed at more alkaline (CAPS pH 10) or pH 5.5 (fresh MQ water) conditions. NT2RepCT hydrogels formed in MQ water or 20 mM tris pH 7 at 40 °C were less self-supporting than those formed at 37 °C. The 3 °C increase relates to a slight increase in unfolding of secondary structure which has likely prevented homogenous hydrogel formation and promoted a weaker hydrogel architecture. From MRE at 222 nm (Figure

18) pH 7 has the least  $\alpha$ -helical structure. Hydrogels formed in 20 mM Tris pH 10 appeared improved by the 3 °C increase. Despite Tris being a poor buffering system, the pH is likely to be higher than those formed in 20 mM tris pH 7. This higher pH has created a translucent hydrogel with less light scattering than older MQ water or 20 mM tris pH7. This likely means there is a possibly a more homogenous structure which has been accentuated by the higher temperature. As a result of this experiment it was decided that only MQ water formed at 37 °C and the hydrogels formed at pH 10 at the 37 °C and 40 °C would be taken forward for material testing. The other 3 hydrogels would be too soft to work with as they would break upon very slight mechanical loading and transfer between cell culture plate wells would be incredibly difficult. A comparison of Young's modulus of pH 10 hydrogels formed at the two temperatures is discussed in Chapter 5 to confirm the visual differences seen.

#### **4.4.8. CAPS10 longer gelation time than MQ hydrogels**

To investigate the effects of gelation pH on hydrogel kinetics a simple inversion test was used. Monitoring optical density at 595 nm was not a suitable technique for transparent gelation kinetics. Inversion tests work on the principle that a viscous liquid will flow but a viscoelastic hydrogel will not and is a commonly used qualitative technique<sup>81,118, 130,144</sup>. Both pre-gel solutions containing 2.4 % (w/v) NT2RepCT in either fresh MQ water or 20 mM CAPS pH 10 flowed from the bottom of the tube to the top upon inversion and with tilting of the tube at time zero. A self-supporting hydrogel was formed after 2 hours at 37 °C in MQ water but the gelation time was 3-fold longer for 20 mM CAPS pH 10. The inversion test used monitored the initial self-supporting hydrogel stage, it is very likely that further crosslinking and stabilization of material properties of the hydrogel continues after this. A qualitative and more accurate technique used to monitor gelation kinetics is rheology, where a pre-gel solution's storage and loss modulus are monitored after gelation is initiated<sup>139</sup>.

The slowing of gelation kinetics in 20 mM CAPS pH 10 is likely a result of the minimal changes in NT2RepCT protein secondary structure with increasing temperature as seen in CD (Section 4.3.4) and increased electrostatic repulsion. At pH 10, NT2RepCT is negatively charged due to deprotonation of acidic groups. Not only is pH 10 much more alkaline than the pI of NT2RepCT at 4.26 (Calculated by Protparameter), but all N terminal histidine amine groups are deprotonated as their pKa are around 9. In ultra-pure MQ water, which is around pH 5.5, the overall negative charge is less and therefore there is less electrostatic repulsion leading to faster gelation. This was seen in silk fibroin hydrogels crosslinked by the Fenton reaction which crosslinks tyrosine by a redox pair of hydrogen peroxide and ferrous iron. The silk fibroin Fenton crosslinked hydrogels formed at pH 9.2 showed increased gelation time and increased light transmittance compared to those formed at pH 5.7 due to increased electrostatic repulsion since silk fibroin was negatively charged at pH 9.2<sup>118</sup>. NT2RepCT in MQ water at 37 °C showed an unfolding of  $\alpha$  helical secondary structure and a shift towards  $\beta$  pleated sheets. This unfolding, exposing previously hidden ionized and hydrophobic amino acids in NT2RepCT leads to more rapid gelation.

#### **4.4.9. DLS and zeta potential reflect NT2RepCT temperature and pH dependent behaviour**

NT2RepCT aggregated under all pH conditions (MQ, pH 7 and pH 10) when the temperature increased from 25 to 37 °C. The aggregation in MQ and pH 7 at room temperature is expected as seen in ESI-MS<sup>133</sup>, however all reported diameters were greater than 7-9 nm as seen in Electron Microscopy<sup>2</sup>. As DLS calculates hydrodynamic radius by diffusion of the particle and reported values are from intensity, the results cannot be directly compared to diameters calculated from different techniques. Relative increases in aggregation with increasing temperature per scan were largest for MQ, followed by pH 10 and then pH 7. At pH 5.5, fibrils are forming as the

NT2RepCT forms high order oligomers, this is accelerated by increased Brownian motion due to temperature rise. NT2RepCT particle size in pH 7 and pH 10 increased about two-fold as temperature increased.

Perhaps of more significance is the zeta potential of NT2RepCT at different pH. Zeta potential is a measure of the charge repulsion/attraction of the slipping plane between particles and the bulk solution, measured from the electrophoretic mobility. The pI of NT2RepCT is 4.26, therefore at all tested conditions NT2RepCT is net negatively charged. It would be expected that pH 7 would aggregate the most followed by MQ and then pH 10 the least. However, despite a zeta potential closest to 0 at pH 7, NT2RepCT particle size is smallest and shows least aggregation per replicate at 25 °C. Only at alkaline pH does the zeta potential of whole NT2RepCT reflect that of *E. asutralis* MaSp1 NT which was determined between pH 2-10 by G. Askarieh *et al.*<sup>36</sup>. At pH 6.5, NT zeta potential is ~-15 mV and decreases to -20 mV at pH 10. The repetitive region and CT contain many charged residues which could affect zeta potential.

#### **4.4.10. Optically clear NT2RepCT hydrogels**

Transparent hydrogels formed in 20 mM CAPS pH 10 were more reproducible than hydrogels formed in fresh MQ water with only statistically significant variation at 400 nm. This difference is likely due to the inability of MQ water to buffer. Small impurities would affect the pH, since the hydrogels were not prepared under a flame there is some risk of contamination. There will also be batch to batch differences in the purification process. Despite efforts to use the same conditions there will be differences in buffers, temperature, yield of NT2RepCT etc. It is likely these carry through into the hydrogel preparation and since MQ water cannot shield these differences like a buffer would, it leads to differences in the hydrogel appearance and potentially microstructure since NT2RepCT is pH sensitive. It seems this has less of a

downstream impact in hydrogels prepared in 20 mM CAPS pH 10 due to its buffering capacity.

The transmittance of 2.4 % (w/v) NT2RepCT in 20 mM CAPS pH 10 and MQ water is high compared to published silk fibroin hydrogels. Silk fibroin molecular weight was decreased by alkaline hydrolysis causing an increase transmittance of visible light with lower molecular weight. However, even after 180 minutes, the longest hydrolysis time they reported, the highest transmittance at 700 nm was only 80 % and decreased to ~30 % with shorter wavelengths<sup>116</sup>. The authors proposed that the average cluster size that forms the polymeric silk fibroin chains was about 400 nm in diameter, causing the absorption of light at this wavelength. Other published silk (fibroin or recombinant spidroin) hydrogels have not reported specific transparency between 400-700 nm but are described as 'transparent' although it is not clear what their metric of testing is<sup>126,129,76,130</sup>.

#### **4.5. Summary of the factors that affect NT2RepCT hydrogel formation**

The aim of this chapter was to determine whether the recombinant mini spidroin NT2RepCT could be formed into protein hydrogels. It was found that at concentrations of 2.4 % (w/v) NT2RepCT self-assembled into self-supporting, physically crosslinked hydrogels after incubation at 37 °C in various buffers. Depending on the buffer chosen to form the hydrogels in, the light transmittance, appearance and gelation time could be controlled.

An assessment of the behaviour of NT2RepCT in three different conditions, pure MQ water, at pH 7 and at pH 10 was performed with circular dichroism. In pure MQ water there was a shift to  $\beta$ -pleated sheets, at pH 7 there was an unfolding to a disordered structure, whereas at pH 10 there was little change from the original  $\alpha$ -helical structure. These structure changes were exploited to form NT2RepCT hydrogels with

different properties. It was found that pH had a profound impact on the visual appearance of the hydrogel and gelation kinetics. At pH 10, optically transparent and reproducible hydrogels were formed after 6.5 hours incubation at 37 °C. An investigation into buffering capacity of tris, HEPES and CAPS found that the better the buffering capacity at pH 10 the more optically transparent the hydrogel formed. At pH 10 there is likely a large net negative surface charge on NT2RepCT which leads to increased electrostatic repulsion between protein molecules. Combined with the  $\alpha$ -helical protein secondary structure, this likely led to an organized and homogenous structure. Dynamic light scattering (DLS) assessment of the zeta potential at pH 10 was determined to be  $-23.7 \pm 1.39$  mV, suggesting stability against aggregation.

In MQ water that had been freshly dispensed from the Millipore water purification system at pH 5.5, optically transparent hydrogels were formed within 2 hours. However, if the MQ water used was not fresh the pH increased to  $\sim 7$  which led to opaque hydrogels with low optical transparency. The zeta potential of NT2RepCT in MQ water was  $-14.03 \pm 0.82$  mV suggesting less resistance to aggregation than at pH 10. Hydrogels formed at pH 7 were opaque, soft and unstable. This was due to the combination of a zeta potential of  $-5.23 \pm 0.72$  mV and an increasingly disordered protein secondary structure leading to aggregated and non-homogenous hydrogel architecture.

It was found that presence of metal salts, cations and phosphates prevented NT2RepCT hydrogel formation indicating that these hydrogels could not be formed *in situ*. Therefore, the hydrogels would need to be formed outside the body and then implanted or injected to the site of action.

The next chapter discusses the swelling characteristics and pore morphology of the hydrogels created in this chapter and how the gelation conditions can control hydrogel behaviour.

## **5. Swelling ratios & SEM (Materials characterisation Part A)**

### **5.1. Introduction**

The material properties of a hydrogel are controlled and affected by many factors such as the degree of crosslinking, the nature of those crosslinks, the monomer concentration, the nature of the monomer, presence of ions and temperature. Characterisation of hydrogel properties can be achieved through a variety of techniques such as SEM, rheology and calculating the swelling ratios. Each technique has its limitations and therefore to properly characterize hydrogels a variety of techniques is required to gather information about their structure and composition. Once these are understood, the hydrogels functionality and behaviour can be manipulated to make the hydrogel suitable for different applications. This chapter is split into 2 parts and investigates qualitatively and quantitatively the material properties of the hydrogels described in Chapter 4 and discusses the different factors involved in controlling these properties: Part A examines the hydrogel swelling ratios and morphology through SEM. Part B examines the hydrogel material properties through Young's modulus and rheology.

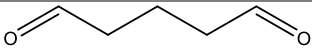
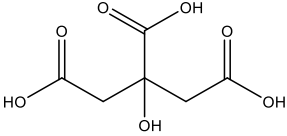
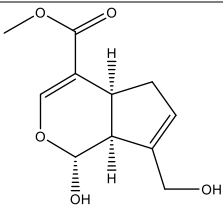
#### **5.1.1. Crosslinking of natural hydrogels**

Hydrogel network crosslinking can be categorised into two groups, chemical and physical. Chemical crosslinks are permanent covalent bonds and physical crosslinks are transient bonds due to chain entanglement, hydrophobic and hydrophilic bonding<sup>3</sup>. This crosslinking can be intra- and intermolecular leading to highly interconnected and porous three-dimensional networks. Chemical crosslinking is often used to stabilize hydrogels derived from natural materials to improve material properties. It decreases the degradation rate and increases mechanical properties such as stiffness. Crosslinking can be initiated by addition of a crosslinking agent or by activation of UV

sensitive crosslinking functional groups on the monomer. The addition of a crosslinking agent elicits less control over crosslinking density and homogeneity compared to activating functional groups on the monomer but is easier and sometimes cheaper. Unfortunately, chemical crosslinking is often toxic to cells and care needs to be taken to remove any excess/residual crosslinker to avoid toxicity.

Four chemical crosslinkers commonly used in hydrogels are glutaraldehyde<sup>114</sup> (GA), carbodiimide<sup>145</sup>, citric acid<sup>146</sup> and genipin<sup>114,147,148</sup>. Each crosslinker has advantages and disadvantages as summarized in Table 6. GA has been used frequently in the literature to crosslink a variety of natural materials into biocompatible hydrogel scaffolds including: silk<sup>149</sup>, chitosan-gelatin blends<sup>150</sup>, gelatin<sup>151</sup> and chitosan<sup>152</sup>.

Table 6: Summary of chemical crosslinkers commonly used in hydrogels

Chemical crosslinker	Crosslinks (functional group)	Advantage	Disadvantage
 Glutaraldehyde	ε-amine of lysine  amine  hydroxyl	Cheap  Readily available  High crosslinking degree	Toxic  Difficult to remove residual  Can introduce a yellow colour
 Carbodiimide	Amines  Carboxylic acids  hydroxyl	Easy removal  Minimal toxicity	Expensive  Low crosslinking degree
 Citric acid	Hydroxyl	Cheap  Non-toxic  Provides pendant functional groups for bioconjugation	High temperatures needed for crosslinking
 Genipin	Primary amines	Naturally derived  Low toxicity	Expensive  Can introduce blue colour

### 5.1.2. Swelling ratios

One of the defining characteristics of a hydrogel is its ability to swell in aqueous buffers or media without dissolution due to crosslinks. Swelling occurs due to osmotic pressure differences between the hydrogel and the surrounding media and is affected by many factors such as: the ionic composition and pH of the media, the number of hydrophilic or ionisable moieties within the hydrogel polymer backbone, temperature and the degree of crosslinking. Protein hydrogels are ionic due to the presence of charged amino acid side chains, the NT and CT. Therefore, when a hydrogel is swelling in solution there are three components of the Gibbs free energy of the system.

$$\text{Equation 6: } \Delta G_{total} = \Delta G_{elastic} + \Delta G_{mixing} + \Delta G_{ionic}$$

The total free energy  $\Delta G_{total}$  is an equilibrium of the elastic forces  $\Delta G_{elastic}$  from the crosslinked chains, the energy of enthalpic mixing  $\Delta G_{mixing}$  and the energy from the ionic interactions within the hydrogel  $\Delta G_{ionic}$  and between the hydrogel and the swelling solution<sup>153,154</sup>. The elastic forces promote contraction as the network is stretched and enthalpic mixing promotes swelling as the solution enters the hydrogel network. The ionic contribution can also shift the equilibrium swelling of the system from ionic shielding or promotion of water entry into the system and can affect enthalpic mixing.

Hydrogels are complex systems, particularly protein hydrogels which contain a mixture of amorphous, crystalline, stranded and aggregated areas due to differences in protein secondary and tertiary structure. Models that predict hydrogel swelling make many assumptions and are based on gaussian distribution of strands with homogenous crosslink distribution<sup>117</sup>. In most of the published literature a simple equation (Equation 7) is used to calculate the swelling ratio Q by relating the weights of the swollen  $W_{(s)}$  and dry  $W_{(d)}$  hydrogel. This method assumes the same density of the hydrogel material throughout. The same ratios can be used to calculate the

volumetric swelling ratio  $Q_v$  by substituting the weights of swollen and dry hydrogels with the volume  $V_{(s)}$  and  $V_{(d)}$  respectively to give Equation 8.

$$\text{Equation 7: } Q = \frac{W_{(s)} - W_{(d)}}{W_{(d)}}$$

$$\text{Equation 8: } Q_v = \frac{V_{(s)} - V_{(d)}}{V_{(d)}}$$

For hydrogels that will be implanted into the body for drug delivery or as a scaffold it is important to characterize the swelling ratio to understand the volume change upon swelling and therefore the drug release rate and how swelling can influence the material properties. Swelling ratio was increased in hydrogels prepared from silk fibroin that had undergone increasing lengths of alkaline hydrolysis, decreasing the molecular weight of the fibroin due to increased space between the silk fibroin network chains<sup>116</sup>. Silk that had been processed via alkaline hydrolysis for 10 minutes had a swelling ratio of  $\sim 40$  whereas 90 minutes of alkaline hydrolysis increased the swelling ratio 2-fold to  $\sim 80$ . As the swelling ratio increased, the elastic character of the hydrogel decreased. It was suggested that the lower molecular weight increased the space available for water molecules to enter in the swelling process<sup>116</sup>.

Generally, swelling will reduce a hydrogel's material properties but there have been efforts to decouple this relationship. A non-swelling hydrogel was prepared from tetra-armed hydrophilic and thermoresponsive synthetic polymers which retained high resistance to deformation and controllable gelation time. Opposing forces of swelling and deswelling within the hydrogel maintained the volume and prevented mechanical hysteresis or failure to tolerate a continual manual load<sup>155</sup>.

### **5.1.3. Cryo-SEM, SEM and eSEM**

Hydrogels are porous materials and suitable for 3D cell culture and drug delivery as these pores allow diffusion of nutrients, small drug molecules, oxygen and waste products such as urea and CO<sub>2</sub>. The size, distribution and frequency of the pores

determines how effective diffusion is within the hydrogel and is controlled by protein concentration, the method of gelation and the number of crosslinks. Pores can be visualised by scanning electron microscopy (SEM). Hydrogels contain a large amount of water and poor sample freezing before lyophilisation can introduce crystalline ice and artefacts<sup>156</sup> and pores can collapse upon drying leading to images that do not accurately reflect the native hydrogel structure<sup>157</sup>. Furthermore, although SEM can provide sub-micron resolution, images captured are within one tiny area of the hydrogel and do not reflect the potentially heterogenous nature of the material.

Cryo-SEM operates at cryogenic temperatures and hydrogel sample freezing is ideally performed to avoid formation of crystalline ice polymorphs which can disrupt the structure of the hydrogel. Vitreous or amorphous ice forms when water molecules transition from liquid to solid state with little change to their molecular arrangement and is therefore the ideal ice polymorph for hydrogel cryo-SEM analysis<sup>158</sup>. Vitreous ice can transition into crystalline ice polymorphs when the temperature is raised in an irreversible process. It is therefore paramount in cryo-SEM to form and preserve vitreous ice in a process known as cryo-fixation through a delicate balance of temperature and pressure. However, even in ideal circumstances, vitreous ice is only formed to depths of 10-20  $\mu\text{m}$  into the sample<sup>158</sup>.

Methods of cryo-fixation include plunge freezing in liquid nitrogen slush (LNS)<sup>156,158,159</sup>, high pressure freezing<sup>158,160</sup> and metal mirror freezing<sup>159</sup>, also called slam freezing. LNS has a lower freezing temperature of -210 °C than liquid nitrogen at -196 °C and is formed by holding liquid nitrogen under vacuum<sup>161</sup>. Additionally, the Leidenfrost effect which occurs in liquid nitrogen plunge freezing due to an insulating layer of water vapour between the sample and the liquid nitrogen, does not occur in LNS plunge freezing<sup>161</sup>. High pressure freezing reduces ice crystal nucleation in the sample<sup>158</sup>. The sample is carefully sandwiched in the sample carrier and space is filled

by a cryoprotective filler material and frozen in liquid nitrogen under high pressures which prevents an increase in volume in the sample upon freezing. A similar principle is applied in metal mirror or slam freezing but at lower pressures and requires no careful sample placement or filler material. A gold coated copper metal disk is cooled to liquid nitrogen temperatures and the sample is placed into a plastic ring which is punched or slammed into this cooled disk. Due to the thin layer used inside the disk, rapid freezing is achieved due to efficient heat transfer out of the sample and into the metal disk. Focused ion beam (FIB) SEM can be used to mill into the sample surface under cryogenic conditions. A stream of gallium ions is used to cut into the surface at an angle, creating a window into the sample which can be observed by the SEM beam<sup>162</sup>. FIB-SEM has been used for hydrogel pore visualisation by lyophilising the milled hydrogel to remove water from the pores<sup>159</sup> and is commonly used in the life sciences field<sup>161</sup>. Although cryo-SEM and FIB-SEM can produce highly detailed and potentially accurate images of hydrogel systems, these techniques are less high throughput than regular SEM. Additionally, the sample preparation can be time consuming and tricky and therefore these techniques are less commonly used than high vacuum SEM.

High vacuum SEM requires lyophilised and water free samples that are coated with a conductive metal such as gold or platinum to prevent charging of the sample by the electron beam, to prevent thermal damage and to increase the secondary electron signal creating higher resolution images. However, many samples can be prepared and analysed at the same time and once lyophilised and heavy metal coated, can be kept at room temperature making SEM imaging quick and higher throughput compared to cryo-SEM or eSEM. Plunge freezing in liquid nitrogen or at -80 °C and lyophilisation is the most commonly used sample preparation technique for hydrogels<sup>163,140-81</sup> due to ease of use, reduced cost, no need for specialised equipment and higher throughput

nature. However, it is therefore common to see hydrogels in the literature showing a typical honey-comb crystalline ice structure<sup>160</sup> or authors mentioning cracking and shrinking of hydrogel samples after lyophilisation<sup>163</sup>. The prevention of artefacts and secondary pores caused by the electron beam or sample preparation was investigated in glycerol methacrylate (GMA) and 2-hydroxyethyl methacrylate (HEMA) hydrogels<sup>156</sup>. It was found that there was a relationship between the swelling ratio, hydrogel stiffness and the resistance to SEM artefacts and secondary pores with stiffer hydrogels with lower swelling ratios fairing better than softer hydrogels with larger swelling ratios<sup>156</sup>.

Environmental SEM (eSEM) can be used to visualise hydrogels in their native state<sup>156</sup> by controlling vapour pressure and temperature to prevent pore collapse. *In situ* eSEM freeze drying<sup>164</sup> can also be performed which monitors and controls the extent of lyophilisation to prevent disturbance to the hydrogel structure. SEM is a powerful technique, but images should be assessed with caution considering the sample composition, SEM preparation and imaging conditions.

## 5.2. Methods

### 5.2.1. Summary of NT2RepCT hydrogels

Various NT2RepCT hydrogel gelation conditions such as temperature, buffer and pH were investigated and assessed for swelling ratio and by SEM as summarised by Table 7 to Table 9

Table 7: NT2RepCT hydrogel codes and gelation conditions for non-crosslinked opaque NT2RepCT hydrogels. All hydrogels prepared at 2.4 % (w/v).

Hydrogel code	Buffer	pH	Temperature (°C)	Appearance	Chemical Crosslinking
<b>MQ 37 O</b>	MQ water	~7	37	Opaque	None
<b>MQ 40 O</b>	MQ water	~7	40	Opaque	None
<b>t7 37 O</b>	20 mM tris pH 7	7	37	Opaque	None
<b>t7 40 O</b>	20 mM tris pH 7	7	40	Opaque	None
<b>t10 37 O</b>	20 mM tris pH 10	10	37	Opaque	None
<b>t10 40 O</b>	20 mM tris pH 10	10	40	Opaque	None

Table 8: NT2RepCT hydrogel codes and gelation conditions for 1 % (v/v) Glutaraldehyde (GA) crosslinked opaque 2.4 % (w/v) NT2RepCT hydrogels.

<b>Hydrogel code</b>	<b>Buffer</b>	<b>pH</b>	<b>Temperature (°C)</b>	<b>Appearance</b>	<b>Chemical Crosslinking</b>
<b>MQ 37 O</b> <b>1GA</b>	MQ water	~7	37	Opaque	1 % (v/v) GA
<b>MQ 40 O</b> <b>1GA</b>	MQ water	~7	40	Opaque	1 % (v/v) GA
<b>t7 37 O</b> <b>1GA</b>	20 mM tris pH 7	7	37	Opaque	1 % (v/v) GA
<b>t7 40 O</b> <b>1GA</b>	20 mM tris pH 7	7	40	Opaque	1 % (v/v) GA
<b>t10 37 O</b> <b>1GA</b>	20 mM tris pH 10	10	37	Opaque	1 % (v/v) GA
<b>t10 40 O</b> <b>1GA</b>	20 mM tris pH 10	10	40	Opaque	1 % (v/v) GA

Table 9: NT2RepCT hydrogel codes and gelation conditions for non-crosslinked transparent 2.4 % (w/v) NT2RepCT hydrogels.

<b>Hydrogel code</b>	<b>Buffer</b>	<b>pH</b>	<b>Temperature (°C)</b>	<b>Appearance</b>	<b>Chemical Crosslinking</b>
<b>MQ 37 T</b>	MQ water	5.5	37	Transparent	None
<b>HEPES T</b>	20 mM HEPES pH 10	10	37	Transparent	None
<b>CAPS10</b>	20 mM CAPS pH 10	10	37	Transparent	None

### 5.2.2. Glutaraldehyde chemical crosslinking of formed hydrogels

Pre-formed heat induced opaque NT2RepCT hydrogels were transferred from the syringe moulds either directly into 3-5 mL of 1 % (v/v) glutaraldehyde (GA) in MQ water (called not pre-swelled) or into 20 mL MQ water to remove tris (called pre-swelled) and then into 3-5 mL of 1-2 % (v/v) glutaraldehyde (GA) in MQ water for in wells of a 24 well plate. Crosslinking was performed at 20 °C for 6 hours in the fume hood. After crosslinking the GA hydrogels were transferred into 20 mL MQ water for 16 hours and then into a further 20 mL of MQ water for another 16 hours to remove excess GA. GA crosslinked hydrogels were stored in MQ water at +4 °C until further use.

### 5.2.3. Calculation of swelling ratios

NT2RepCT hydrogels (crosslinked not pre-swelled or pre-swelled or non-crosslinked) were placed into excess swelling media (MQ water, PBS or DMEM + 10 % (v/v) FBS) at either 20 or 37 °C for 24 hours. Swollen hydrogels were carefully removed from swelling media and gently blotted with a Kimwipe™ to remove excess swelling media and weighed on a 5 decimal point balance. The swollen hydrogels were then dried at 20 °C for 24 hours in a desiccator containing calcium chloride. Once dried the hydrogels were re-weighed and the swelling ratio (Q) was calculated by:

$$\text{Equation 7: } Q = \frac{W_{(s)} - W_{(d)}}{W_{(d)}}$$

Where  $W_{(s)}$  is the weight of the swollen hydrogel and  $W_{(d)}$  is the weight of the dry hydrogel. Each hydrogel type and swelling condition were measured in triplicate (n=3).

### 5.2.4. Cryo-SEM

The opaque NT2RepCT MQ water hydrogel MQ 37 O was prepared for cryo-SEM by pipetting 5 µL non-swollen, as prepared hydrogel into rivets with 3 mm diameter opening which were fastened to the cryo-SEM sample holder at room temperature. The sample holder was then transferred into liquid nitrogen slush at -210 °C using a PP3010 Prepdek™ workstation to immediately freeze the hydrogel sample. After

freezing, the sample holder was transferred into the PP3010 Prepdek™ cryo-SEM sample preparation chamber at -190 °C under vacuum. The frozen hydrogel sample was fractured with a cold scalpel to reveal the inner porous structure. The temperature of the sample preparation chamber was raised to -90 °C to sublime water from the pores for 10 minutes. The temperature was then lowered to -135 °C and the hydrogel surface was sputter coated with a thin layer of conductive platinum. The coated sample was then transferred under high vacuum into the cryo-SEM (FEI Quanta 200 3D dual beam SEM) microscope chamber and onto the sample stage. Images were captured at an accelerating voltage of 5 kV.

### **5.2.5. Focused Ion Beam Scanning Electron Microscopy (FIB-SEM)**

The opaque NT2RepCT MQ water hydrogel MQ 37 O was prepared for FIB-SEM by pipetting 5 µL of non-swollen, as prepared hydrogel into a small plastic ring that was attached via double sided copper tape to a magnetic backed sponge. Metal mirror freezing (slam freezing) was used to rapidly freeze the hydrogel sample using a Leica Reichert MM08 E. The frozen sample was rapidly transferred into liquid nitrogen at -190 °C and attached to the cryo-SEM sample holder whilst still in liquid nitrogen using a PP3010 Prepdek™ workstation. The sample holder was then transferred under vacuum into the PP3010 Prepdek™ cryo-SEM sample preparation chamber which was at -190 °C. The temperature of the sample preparation chamber was raised to -135 °C and the hydrogel was then sputter coated with a thin layer of conductive platinum. The temperature was decreased to -190 °C and the coated sample was transferred under vacuum to the cryo-SEM (FEI Quanta 200 3D dual beam SEM) microscope chamber and onto the sample stage. Prior to milling hydrogel cross-sections with FIB-technology, samples were coated and compacted with platinum using the gas injector to improve the strength of the surface during the milling process. Areas were then chosen to mill and by drawing a rectangle of defined dimensions. The sample stage

was tilted to 54° so the FIB beam would hit the sample perpendicular to the cross-sectional cutting area. A stream of Gallium (Ga<sup>+</sup>) ions at beam currents of 50 pA–1 nA cut into the sample to a depth of 10 µm and were cleaned up with successive milling along one edge to give a clean surface. The temperature in the SEM chamber was then raised to -90 °C to for 40 minutes to sublime the sample and reveal the porous structure. Images of the milled cross-section were performed at a sample stage tilt angle of 45 ° to see into the milled area. Images were taken at an accelerating voltage of 10 kV.

### **5.2.6. SEM**

NT2RepCT hydrogels were freeze dried for SEM by 2 methods, flash freezing or metal mirror freezing. Flash frozen hydrogels were prepared by plunging small sections of swollen hydrogel into liquid nitrogen. They were then lyophilized for 24 hours at -60 °C at 0.1 mbar. Metal mirror freezing used a Leica reichert MM08 E. Approximately 5 µL hydrogel sample was placed onto double sided copper tape before freezing and then lyophilized at -90 °C and 0.1 mbar for 24 hours. Lyophilized NT2RepCT hydrogel samples were mounted on carbon tape and sputter coated with a thin layer of either platinum (120s) or gold (90s) and observed using JEOL-JSM-6490 SEM with an accelerating voltage of 10 kV.

### **5.2.7. eSEM**

NT2RepCT hydrogels were observed in FEI Quanta 650 eSEM (environmental SEM) at 10 kV at low vacuum with two sample preparation methods, *in situ* freeze drying and metal mirror (slam) freezing. For *in situ* freeze drying, a portion of swollen hydrogel was placed on the Peltier stage at 2 °C at 89 % humidity. The temperature was dropped inside the eSEM to -10 °C, 56 % humidity at 270 Pa. Auxiliary nitrogen gas was used to remove water vapor, and the temperature was dropped to -18 °C at 220 Pa. Images were collected with an acceleration voltage of 10 kV. For samples prepared by metal

mirror (slam) freezing, approximately 5  $\mu$ L sample was placed on double sided copper tape and frozen using a Leica reichert MM08 E metal mirror freezer. The frozen sample was quickly transferred into the Peltier stage of the eSEM to minimize frost formation. Images were collected at -18 °C in low vacuum mode with pressure of 130 Pa and an acceleration voltage of 10 kV.

### **5.3. Swelling and SEM Results**

#### **5.3.1. Opaque hydrogels dissolved in cell culture media at 37 °C**

NT2RepCT opaque hydrogels formed in old MQ water (MQ 37 O and MQ 40 O), 20 mM tris pH 7 (t7 37 O and t7 40 O) or old 20 mM tris pH 10 (t10 37 O and t10 40 O) did not maintain their structural integrity and dissolved within 30 minutes when placed into either PBS or DMEM + 10 % (v/v) FBS at 37 °C.

#### **5.3.2. Swelling ratio of opaque hydrogels can be controlled by pH of gelation**

All non-crosslinked opaque 2.4 % (w/v) NT2RepCT hydrogels swelled in DMEM + 10 % (v/v) FBS (referred to from here-in as DMEM) or MQ water at 20 °C. Only MQ 37 O and t10 40 O showed significant differences ( $P < 0.001$ ) in swelling between the two buffers as determined by an unpaired students t-test (Figure 28). The opaque hydrogel MQ 37 O swelled 222 % more in DMEM than in MQ water whereas t10 40 O swelled 260 % more in DMEM than MQ water. When directly comparing the swelling in MQ water, t10 40 O swelled significantly ( $P < 0.001$ ) 130 % more in MQ water than MQ 37 O (Figure 29). The opposite was the case when directly comparing the swelling in DMEM in which MQ 37 O swelled significantly ( $P < 0.01$ ) 409 % more than t10 40 O in the same buffer (Figure 29). The other opaque hydrogels swelled to a similar degree in MQ water or DMEM with hydrogels containing tris (t7 37 O, t7 40 O and t10 37 O) measured as having a swelling ratio Q of 12-20 in both buffers. NT2RepCT hydrogels

formed in MQ water at 40 °C (MQ 40 O) swelled more with Q of  $36.6 \pm 13.6$  in MQ water and  $44.8 \pm 10.8$  in DMEM at 20 °C. These high standard deviations reflect the extremely soft nature of this hydrogel. It was difficult to manipulate the swollen hydrogels without damaging them and this likely led to loss of material and higher errors compared to other hydrogel types.

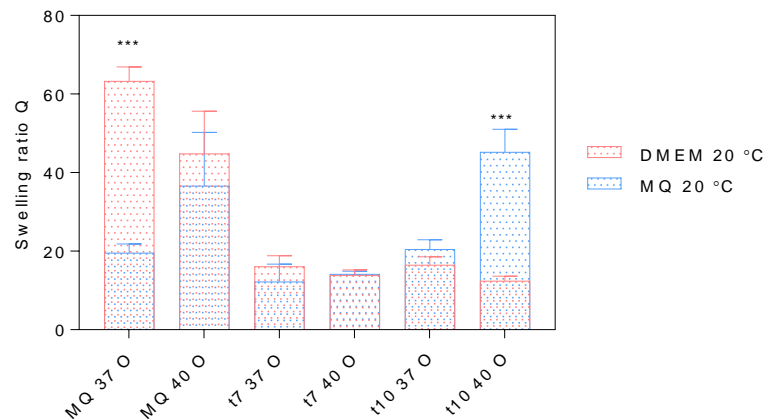


Figure 28: Swelling ratio (Q) of non-crosslinked opaque NT2RepCT hydrogels at 20 °C in DMEM (pink bars) or MQ water (blue bars). Unpaired students t-test \*\*\* P<0.001. (n=3) error bars represent SD.

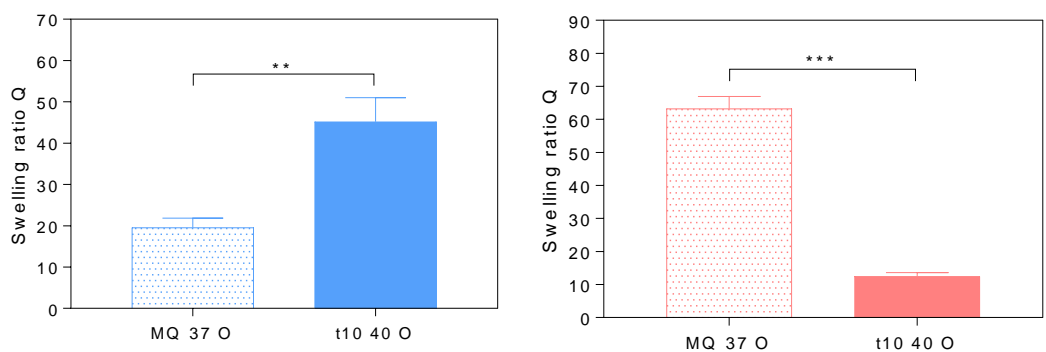


Figure 29: (Left) Swelling ratio (Q) in MQ water at 20 °C of the opaque hydrogels MQ 37 O (blue dots) and t10 40 O (blue filled). (Right) Swelling ratio (Q) in DMEM at 20 °C of the opaque hydrogels MQ 37 O (pink dots) and t10 40 O (pink filled). Unpaired students t-test \*\* P<0.01, \*\*\* P<0.001 (n=3) ± SD

### 5.3.3. Opaque hydrogels structural integrity improved when crosslinked with glutaraldehyde

Due to the dissolution of opaque NT2RepCT hydrogels in cell culture appropriate media at 37 °C, 1 % (v/v) glutaraldehyde (GA) was used to chemically crosslink and stabilize the hydrogel structure. Upon crosslinking the hydrogels appeared stiffer (Figure 30) and were able to hold their shape compared to non-crosslinked. Additionally, the GA crosslinked hydrogels swelled and did not dissolve in DMEM + 10 % (v/v) FBS at 37 °C.



Figure 30: Opaque NT2RepCT 2.4 % (w/v) MQ water hydrogel crosslinked with 1 % (v/v) glutaraldehyde. Scale bar = 1 cm.

### 5.3.4. Swelling ratios of GA crosslinked opaque hydrogels

Opaque NT2RepCT hydrogels to be GA crosslinked were either pre-swollen in MQ water (to remove any tris present which would be crosslinked by GA) and then placed in 1 % (v/v) GA or immediately placed in 1 % (v/v) GA. Hydrogels pre-swollen before crosslinking are referred to as pre-swollen and hydrogels that were not pre-swollen before crosslinking are referred to as not pre-swollen.

The swelling ratio in MQ water at 20 °C only showed significant decreases in swelling ratio when the hydrogels were pre-swollen before GA crosslinking in MQ 37 O 1GA, t10 37 O 1GA hydrogels with a decrease of 21 % and 39 % respectively. The swelling ratio was significantly increased by 150 % in t10 40 O 1GA when the hydrogel was pre-swollen before crosslinking. The other opaque GA crosslinked hydrogels showed no

differences in swelling ratio between pre-swollen and not pre-swollen treatments in MQ water at 20 °C with Q between 25-50 (Figure 31). Overall, the 1 % (v/v) GA crosslinked opaque hydrogels swelled more in MQ water at 20 °C than the non-crosslinked opaque hydrogels.

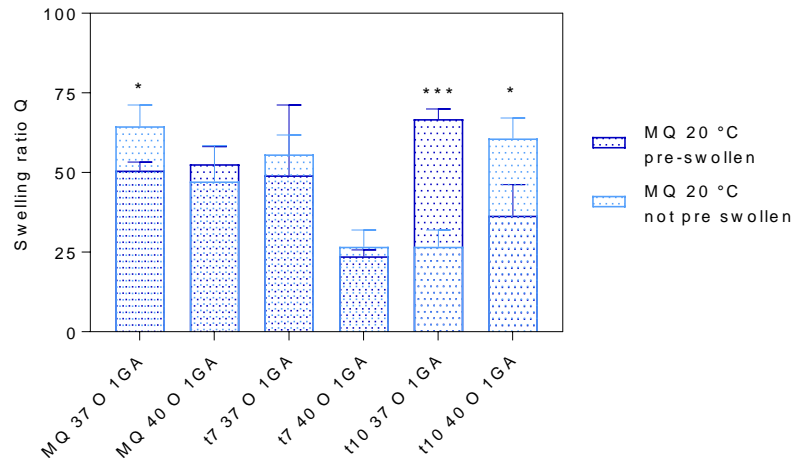


Figure 31: Swelling ratio (Q) of 1 % (v/v) GA crosslinked NT2RepCT hydrogels at 20 °C in MQ water. Hydrogels were either pre-swollen in MQ water before GA crosslinking or not pre-swollen. Dark blue dots = pre-swollen, light blue dots = not pre-swollen. (n=3) Error bars show SD. Unpaired students t-test \*P<0.05, \*\*\* P<0.005.

Except for t7 37 O 1GA which increased its swelling ratio by 70 % when the hydrogel was pre-swollen before GA crosslinking, the swelling ratios in DMEM at 20 °C were not significantly different whether the hydrogels were pre-swollen or not pre-swollen with Q 10-30 (Figure 32). Overall, the 1 % (v/v) GA crosslinked opaque hydrogels had similar swelling ratios in DMEM at 20 °C to the non-crosslinked opaque hydrogels.

At 37 °C in DMEM there were no significant differences in swelling between pre-swelling and not pre-swelling for any of the 1 % (v/v) GA crosslinked opaque hydrogels with Q = 15-30 (Figure 33). Additionally, the swelling ratios for all pre-swollen or not

pre-swollen hydrogels was not affected by increasing the temperature of DMEM from 20 °C to 37 °C.

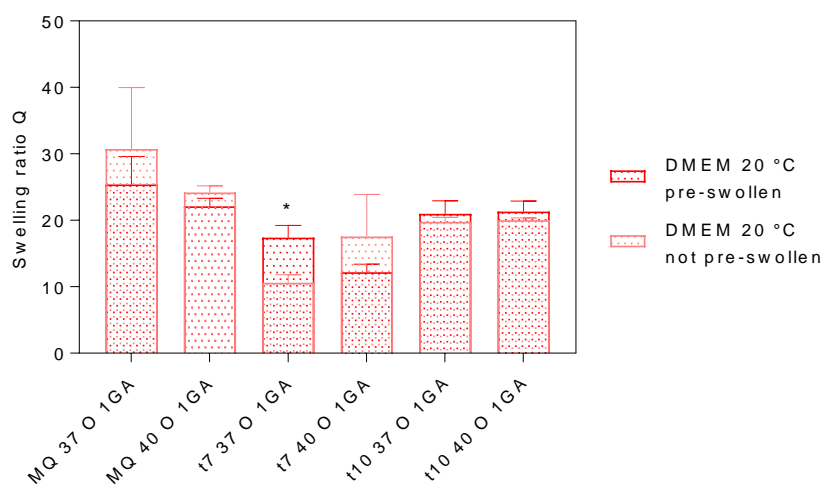


Figure 32: Swelling ratio (Q) of 1 % (v/v) GA crosslinked NT2RepCT hydrogels at 20 °C in DMEM. Hydrogels were either pre-swollen in MQ water before GA crosslinking or not pre-swollen. Red dots = pre-swollen, pink dots = not pre-swollen. (n=3) Error bars show SD. Unpaired students t-test \*P<0.05.

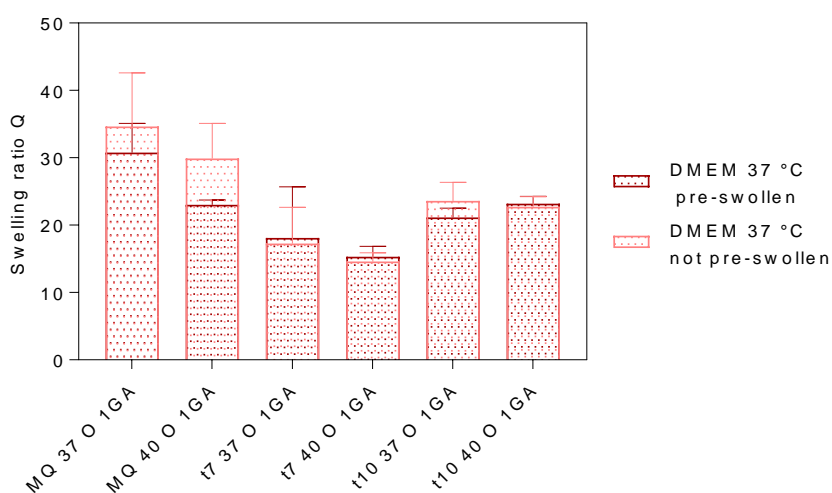


Figure 33: Swelling ratio (Q) of 1 % (v/v) GA crosslinked opaque NT2RepCT hydrogels in DMEM at 37 °C. Hydrogels were pre-swollen in water before GA crosslinking (maroon) or not pre-swollen (pink). (n=3) error bars represent SD.

### 5.3.5. Hydrogel transparency and swelling

Transparent hydrogels formed in fresh MQ water or 20 mM CAPS pH 10 had higher swelling ratios than opaque hydrogels. When swollen in MQ water at 20 °C MQ 37 T swelled 183 % more compared to MQ 37 O (Figure 34). Comparing NT2RepCT hydrogels formed in least to most appropriate pH 10 buffer (Tris, HEPES and CAPS), the Q increases with increasing buffering capacity. Using HEPES instead of tris resulted in a 154 % increase in swelling. If CAPS was used instead of HEPES the swelling increased by a further 61 % or a 307 % increase compared to tris buffer (Figure 35).

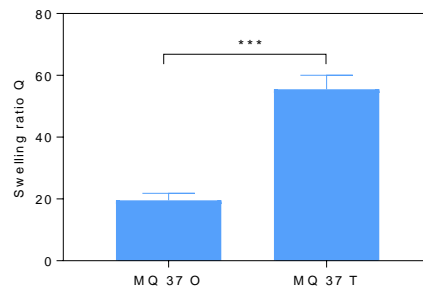


Figure 34: Swelling ratio (Q) in MQ water at 20 °C of non-crosslinked opaque and transparent NT2RepCT hydrogel formed in MQ water at 37 °C. Unpaired students t-test \*\*\* P<0.001. (n=3) error bars represent SD.

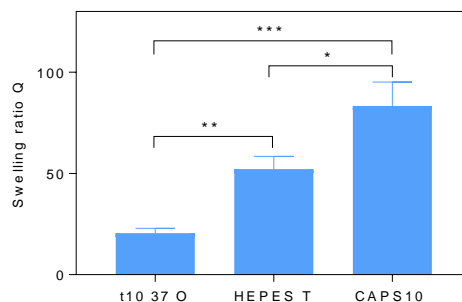


Figure 35: Swelling ratio (Q) in MQ water at 20 °C of NT2RepCT hydrogels formed in either old 20 mM tris pH 10 (opaque), fresh 20 mM HEPES pH 10 (clear) or 20 mM CAPS pH 10. Unpaired students t-test \* $P < 0.05$ , \*\* $P < 0.01$ , \*\*\* $P < 0.001$ . (n=3) error bars represent SD.

NT2RepCT transparent hydrogels formed in 20 mM CAPs pH 10 (CAPS10) swelled significantly more (50 % increase) than hydrogels formed in fresh MQ water (MQ 37 T) (Figure 36). However, the opposite was the case in PBS. Comparing swelling at 37 °C of MQ 37 T and CAPS10 in PBS at 3 different pH: 5, 6.45 and 7.6, at all pH MQ 37 T swelled significantly more than CAPS10 (Figure 37). There was no significant difference in swelling for MQ 37 T across the different PBS pH tested. This was the same for CAPS10.

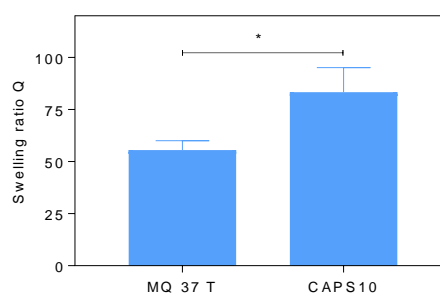


Figure 36: Swelling ratio (Q) of transparent 2.4 % (w/v) NT2RepCT hydrogels formed in MQ water (MQ 37 T) or 20 mM CAPS pH 10 (CAPS10) swollen in MQ water at 20 °C. (n=3)  $\pm$  SD (\* =  $P < 0.05$ )

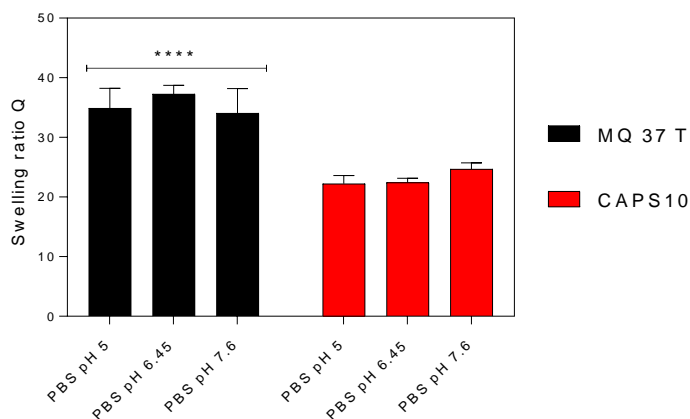


Figure 37: Swelling ratio (Q) of transparent NT2RepCT hydrogels formed in MQ water (MQ 37 T) (black bars) or 20 mM CAPS pH 10 (CAPS10) (red bars) at 37 °C swollen in 1 x PBS pH 5, 6.45 or 7.6 at 37 °C. (n=3)  $\pm$  SD. (one-way ANOVA \*\*\*\* P<0.0001)

### 5.3.6. Cryo- SEM of MQ 37 O

The opaque NT2RepCT hydrogel MQ 37 O was imaged using Cryo-SEM. The hydrogel was flash frozen in liquid nitrogen slush and manually cut with a scalpel to reveal the inner porous structure. Across the sublimed hydrogel surface pores of different shapes and sizes were observed. In areas towards the middle of the hydrogel (Figure 38 B) sample in the rivet, the pores were larger (6-12  $\mu$ m), directional and rectangular in shape. Pores at the edge of the hydrogel rivet were rounder, smaller (1-3  $\mu$ m) and no directionality was observed (Figure 38 A). Inefficient and slow sample freezing in the middle of the hydrogel sample led to formation of hexagonal ice crystal artefacts whereas at the edge where freezing was efficient and fast likely a more accurate representation of the hydrogel porous structure.

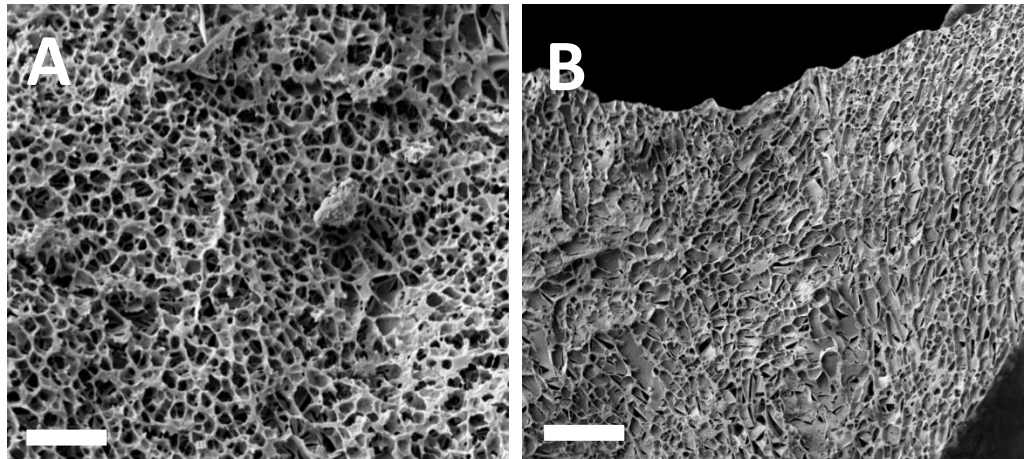


Figure 38: Representative Cryo-SEM images of the opaque MQ water NT2RepCT hydrogel MQ 37 O. A) MQ 37 O hydrogel porous structure after sublimation Image taken at edge of hydrogel in the rivet. Scale bar = 10  $\mu\text{m}$ . B) Same hydrogel MQ 37 O in a different area showing crystalline ice pore artefacts that are long and directional due to inefficient freezing and fracturing with scalpel. Image taken at middle of hydrogel in the rivet Scale bar = 50  $\mu\text{m}$

### 5.3.7. FIB-SEM of MQ 37 O

Focused Ion Beam (FIB) SEM was used to mill into the opaque NT2RepCT hydrogel MQ 37 O after metal mirror (slam) cryo-fixation of the hydrogel. The  $\text{Ga}^+$  beam was used to cut areas 10  $\mu\text{m}$  wide and maximum 5  $\mu\text{m}$  deep. After milling and before sublimation the cut face was smooth with minimal texture (Figure 39 A). As the temperature was raised and held at  $-90\text{ }^\circ\text{C}$ , water began to sublime from the surface revealing small pores across the cut face (Figure 39 B). After 40 minutes sublimation a textured and heterogenous structure was revealed (Figure 39 C) with pores between 200 nm – 1.2  $\mu\text{m}$ . Pore sizes were calculated by the SEM imaging software. The pores were not uniformly distributed and there were areas of white NT2RepCT hydrogel with no pores. The dimpled and uneven surface of the cut face indicates the presence of

underlying structure with light grey to white hydrogel and black indicating voids or pores where water has sublimed.

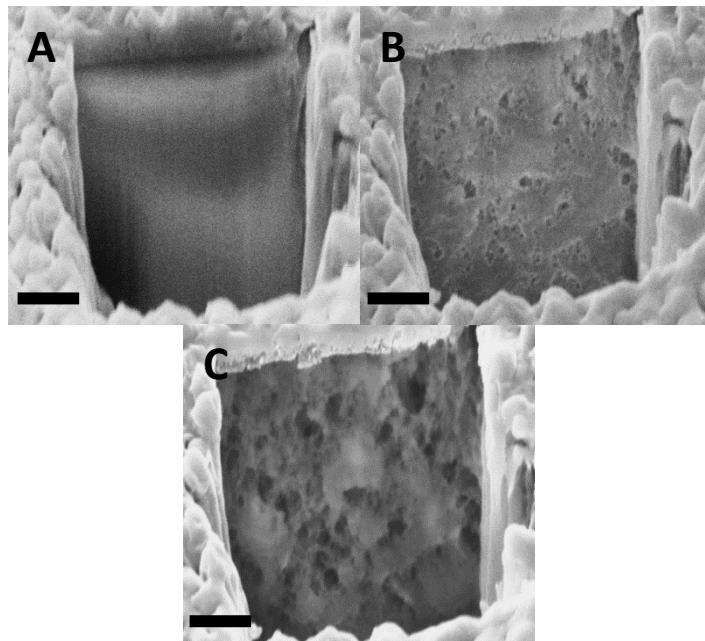


Figure 39: Representative FIB-SEM images of opaque NT2RepCT hydrogel MQ 37 O before, during and after 90 minutes of sublimation at -90 °C. A) area milled by the FIB gallium ion beam before sublimation B) same area after 15 minutes of sublimation C) same area after 40 minutes sublimation. Scale bars: 3  $\mu\text{m}$  (A-C).

### 5.3.8. High vacuum SEM GA crosslinked opaque hydrogels

Chemical crosslinking with GA was used to stabilize the hydrogel network structure in the opaque NT2RepCT hydrogels MQ 37 O 1GA, t37 O 1GA and t40 O 1GA.

MQ 37 O 1GA hydrogel (Figure 40 A) showed structures that appeared collapsed and with small pores (1-2.5  $\mu\text{m}$ ) and less porosity compared to t10 37 O 1GA and t10 40 O 1GA hydrogels which had very similar structures with small, interconnected networks of pores that range from 1-20  $\mu\text{m}$  (Figure 40 B & C). There were areas of honey-comb crystalline ice formation deeper into the hydrogel.

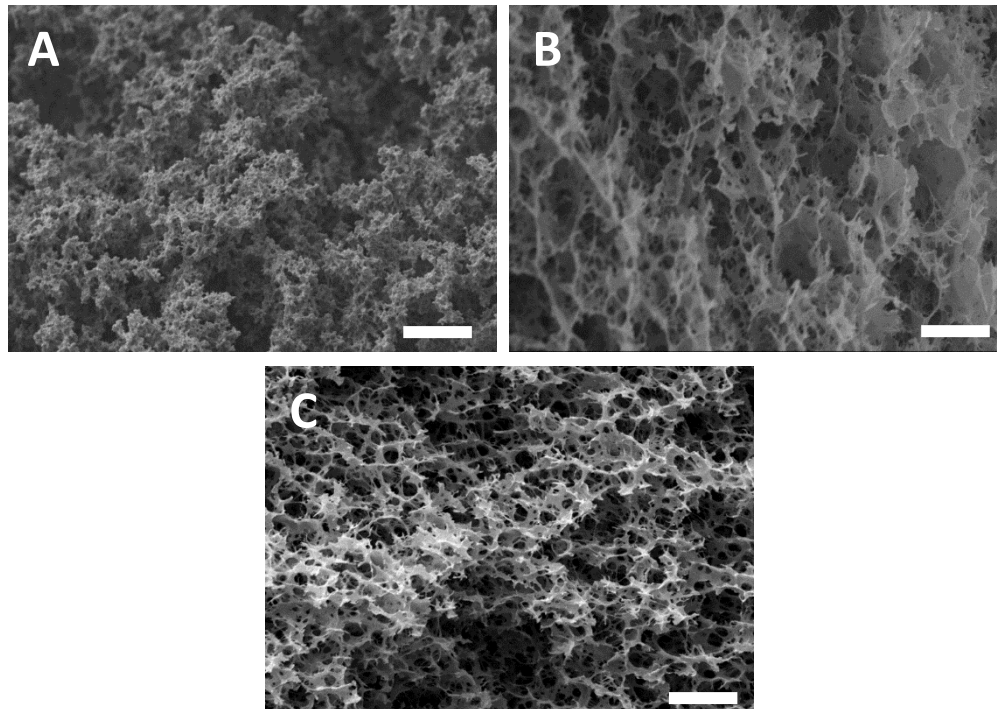


Figure 40: Representative SEM images of plunge frozen and freeze dried 1 % (v/v) GA crosslinked opaque hydrogels A =MQ 37 O 1GA, B = t37 O 1GA, C = t40 O 1GA. Acceleration voltage = 10 kV, scale bars = 10  $\mu\text{m}$

### **5.3.9. High vacuum SEM non-crosslinked MQ 37 T and CAPS10 hydrogels**

The transparent NT2RepCT hydrogels MQ 37 T and CAPS10 were imaged using high vacuum SEM with no chemical crosslinking. Ahead of lyophilisation two freezing techniques were employed, plunge freezing in liquid nitrogen and metal mirror (slam) freezing. MQ 37 T (Figure 41 A&B) and CAPS10 (Figure 41 C&D) hydrogels prepared for SEM by plunge freezing and lyophilisation contained a wide range of pore sizes and shapes. Presence of honey-comb hexagonal pores were seen in both samples with smaller less angular pores in small areas. The larger pores were directional and orientated along one axis. Additionally, there were cracks and large voids present as a result of the plunge freezing and lyophilisation process.

The other sample preparation technique metal mirror (slam) freezing ahead of lyophilisation created a meshed fibrous and torn structure in MQ 37 T (Figure 42 A&B) with no visible pores. CAPS10 hydrogels prepared by metal mirror (slam) freezing and lyophilisation formed a textured, non-porous surface morphology with large smooth homogenous areas (Figure 42 C&D). The areas of texture in CAPS10 suggested fibre like structures but not to the same extent as in MQ 37 T.

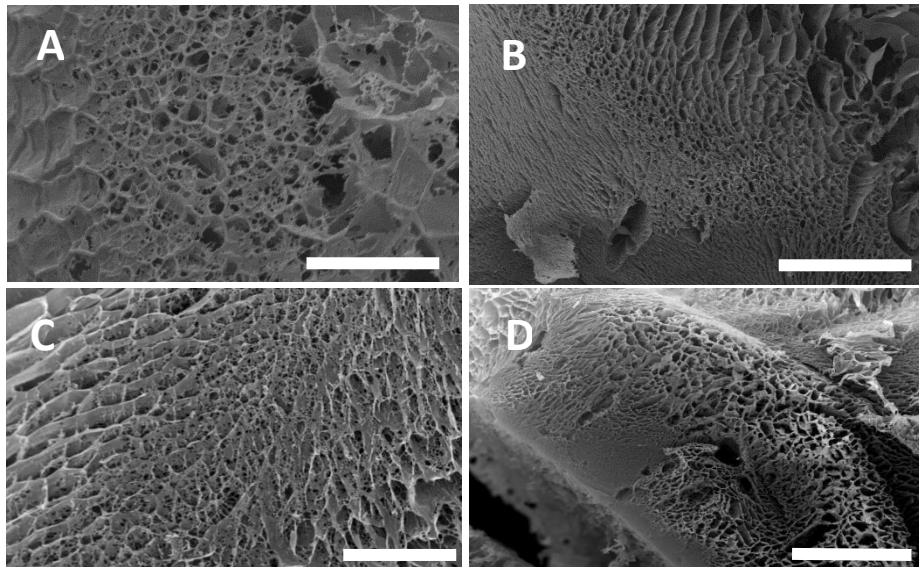


Figure 41: Representative images of MQ 37 T (A & B) and CAPS10 (C & D) non-crosslinked hydrogels imaged by SEM after plunge freezing and lyophilisation. Imaged at 15 kV acceleration voltage. Scale bars: A = 10  $\mu\text{m}$ , B = 100  $\mu\text{m}$ , C = 10  $\mu\text{m}$ , D = 100  $\mu\text{m}$

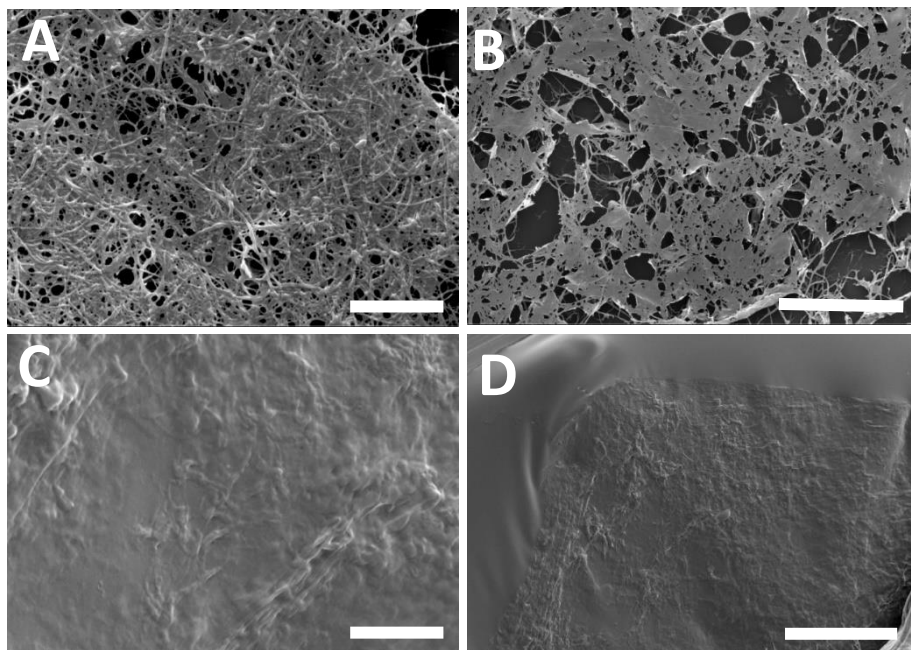


Figure 42: Representative images of MQ 37 T (A & B) and CAPS10 (C & D) non-crosslinked hydrogels imaged by SEM after slam metal mirror freezing and lyophilisation. Imaged at 10 kV acceleration voltage. Scale bars: A = 10  $\mu\text{m}$ , B = 30  $\mu\text{m}$ , C = 10  $\mu\text{m}$ , D = 50  $\mu\text{m}$

### **5.3.10. Comparison of SEM/eSEM techniques of GA crosslinked MQ 37 T 1GA and CAPS10 1GA hydrogels**

The transparent hydrogels MQ 37 T and CAPS10 were crosslinked with 1 % (v/v) GA. A comparison of two SEM techniques: high vacuum SEM and low vacuum eSEM was performed. The hydrogels for high vacuum SEM were prepared by plunge freezing in liquid nitrogen for a direct comparison to the non-crosslinked transparent hydrogels MQ 37 T and CAPS10. For eSEM the 1 % (v/v) GA crosslinked hydrogels were either metal mirror (slam) frozen and imaged under low vacuum or the hydrogels were placed into the eSEM sample chamber wet and by controlling the temperature and vapour pressure were *in situ* lyophilised.

In the plunge frozen and lyophilised high vacuum SEM images of MQ 37 T 1GA (Figure 43 A & B) and CAPS10 1GA (Figure 43 C&D) there were larger pores of diameter 4-25  $\mu\text{m}$  and smaller pores of sub-micron diameter. Within the pores of MQ 37 T 1GA and CAPS10 1GA plunge frozen SEM were extensive fibril structures which were not seen in the eSEM images or in the non-crosslinked MQ 37 T and CAPS10 hydrogels prepared for SEM by liquid nitrogen plunge freezing and lyophilisation (Figure 41- Figure 42). Crystalline ice in honey-comb structures were seen in all 1 % GA (v/v) MQ 37 T 1GA and CAPS10 1GA hydrogels prepared for high vacuum SEM by plunge freezing in liquid nitrogen (Figure 44 A-D).

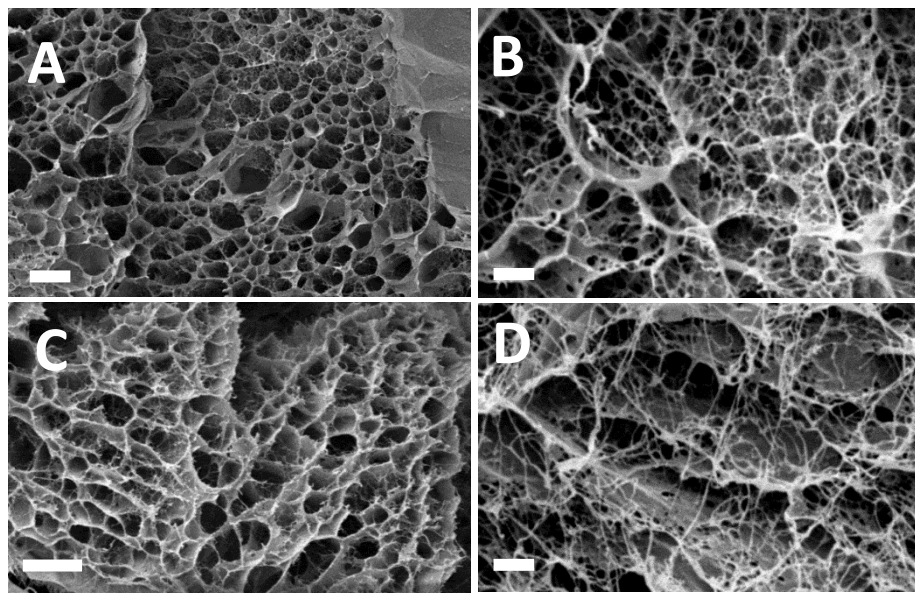


Figure 43: Representative high vacuum, liquid nitrogen plunge freeze and lyophilised SEM images of pores and fibrils of 1 % (v/v) GA crosslinked hydrogels MQ 37 T 1GA (A & B), CAPS10 1GA (C & D) hydrogels. Scale bars: A) 20  $\mu\text{m}$ , B) 2  $\mu\text{m}$  C) 10  $\mu\text{m}$ , D) 2  $\mu\text{m}$ .

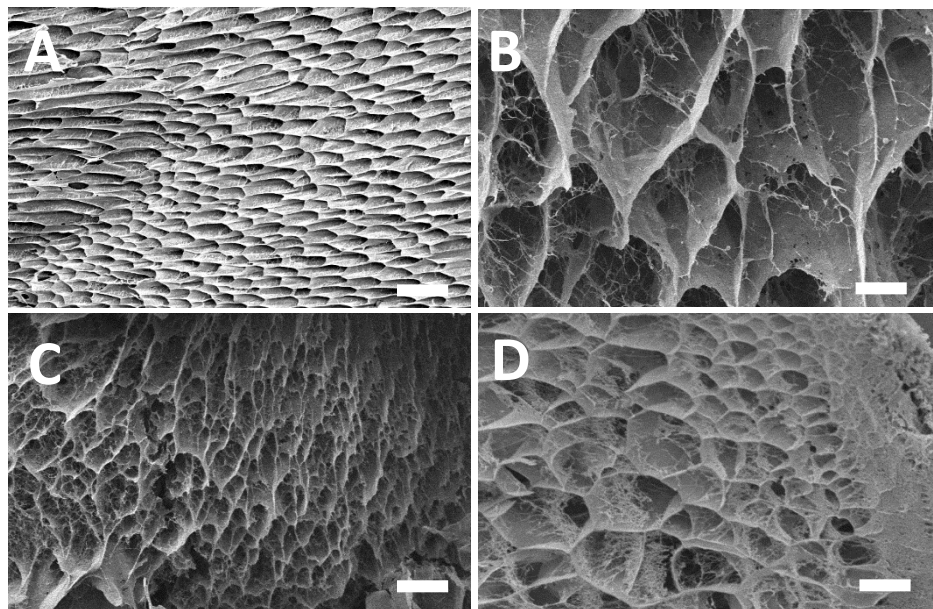


Figure 44: Examples of crystalline ice honey-comb structures and fibrils in 1% (v/v) GA crosslinked NT2RepCT hydrogels prepared for SEM by plunge freezing in liquid nitrogen. A & B) CAPS10 1GA C & D) MQ 37 T 1GA. Scale bars: A & C) 50  $\mu\text{m}$ , B & D) 10  $\mu\text{m}$ .

Low vacuum eSEM immediately after metal mirror (slam) freezing led to extensive porous networks for MQ 37 T 1GA (Figure 45 A-C) and CAPS10 1GA (Figure 45 D-F). As with high vacuum SEM, there was a large range of pore sizes with some areas showing larger (3-12  $\mu\text{m}$ ) pores and other areas with much smaller pore sizes (sub 1  $\mu\text{m}$ ). This is best seen in Figure 45 E. In the areas with larger pores, the walls between pores were thicker and the pores were more circular in shape in CAPS10 1GA than MQ 37 T 1GA (Figure 45 A & D). The smaller pores did not show this feature (Figure 45 C & F). It is likely the larger pores are an artefact from the hydrogel eSEM sample preparation and visualisation. Particularly in MQ 37 T 1GA, hexagonal shapes were etched into the surface of the hydrogel (Figure 45 B).

Lyophilising the hydrogels *in situ* in the eSEM chamber led to a porous network with multiple layers visible. The initial eSEM images in the native wet state of MQ 37 T 1GA and CAPS10 1GA showed a flat surface with little texture (Figure 46 A & D). After the *in situ* lyophilisation process extensive porous structures were seen for both hydrogels (Figure 46 B & E). MQ 37 T 1GA (Figure 46 C) showed more extensive pore structure than CAPS10 1GA (Figure 46F). Pore size ranged from 2-9  $\mu\text{m}$  and no smaller pores were seen as in the metal mirror (slam) frozen eSEM, additionally the walls between the pores were thicker in CAPS10 1GA than MQ 37 T 1GA.

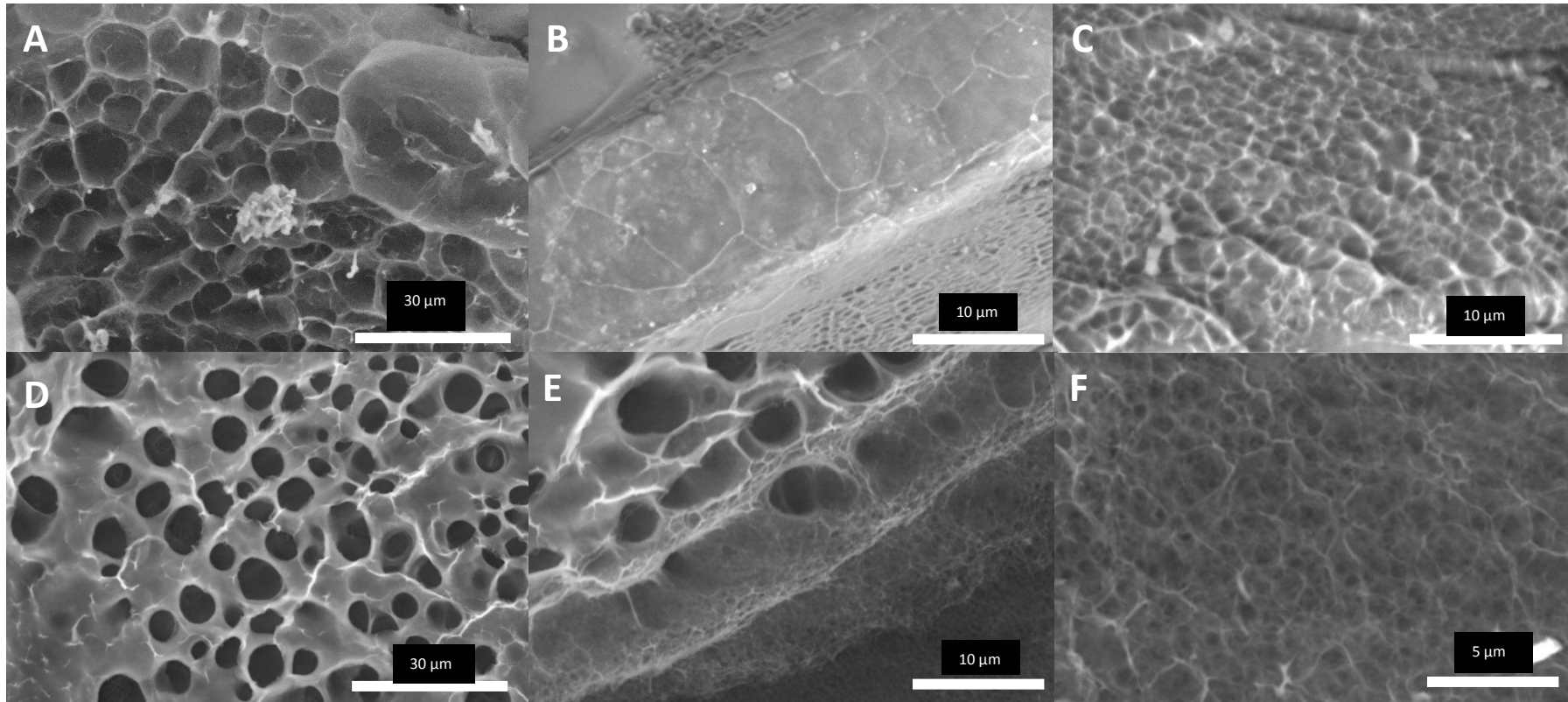


Figure 45: Representative low vacuum eSEM images of metal mirror (slam) frozen MQ 37 T 1GA and CAPS10 1GA. A – C) MQ 37 T 1GA, D – F) CAPS10 1GA.

A mixture of larger (3 – 12 μm) pores and very small (sub 1 μm) pores were seen Scale bars: A) 30 μm B) 10 μm C) 10 μm D) 30 μm E) 10 μm F) 5 μm.

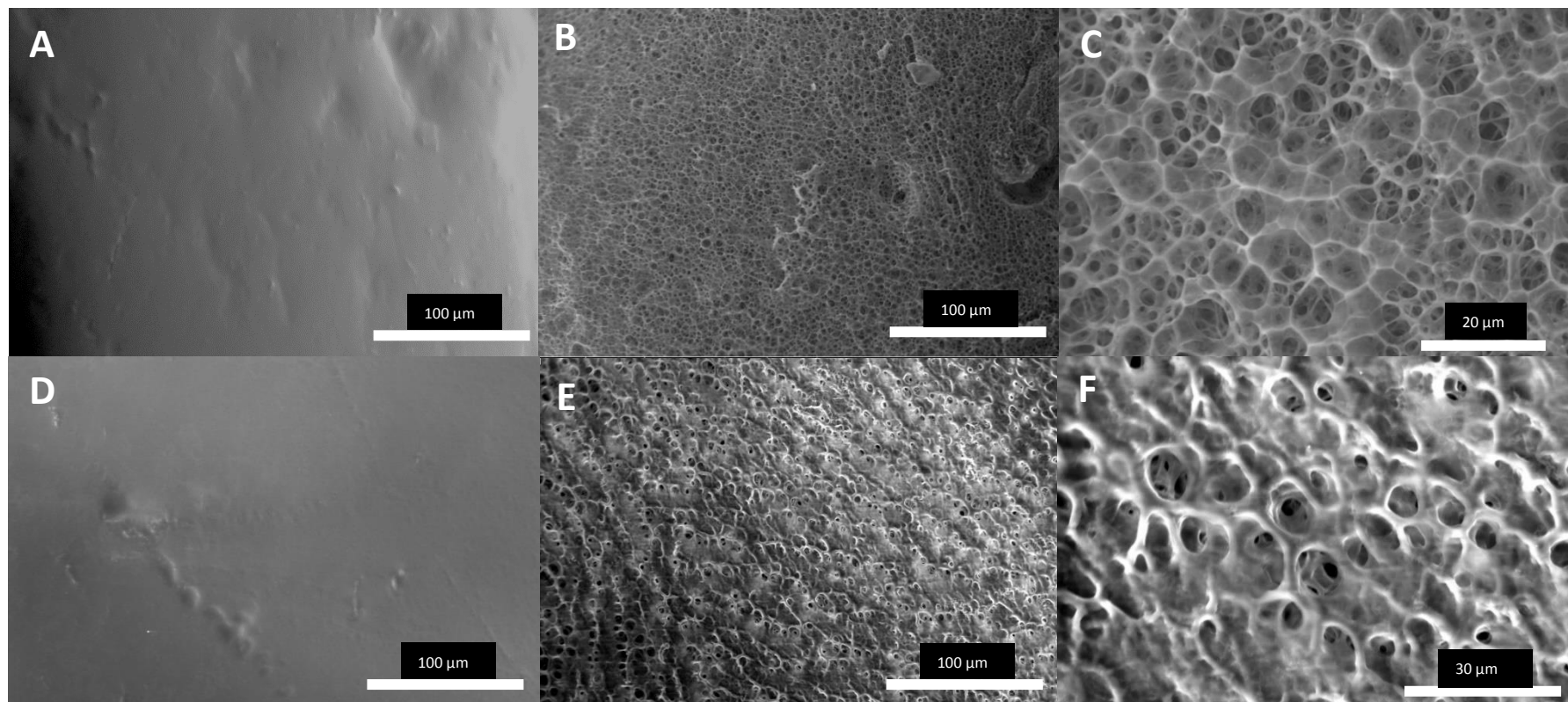


Figure 46: Representative *in situ* lyophilisation eSEM images of MQ 37 T 1GA and CAPS10 1GA. A) MQ 37 T 1GA wet native state B-C) MQ 37 T 1GA after *in situ* lyophilisation, D) CAPS10 1GA wet native state, E-F) CAPS10 1GA after *in situ* lyophilisation. Scale bars: A) 100 µm B) 100 µm C) 20 µm D) 100 µm E) 100 µm F) 20 µm.

## **5.4. Discussion of swelling behaviour and SEM analysis**

### **5.4.1. Overview**

The aim of this chapter was to assess the swelling ratios and pore morphology of the hydrogels created in the previous chapter. Glutaraldehyde (GA) crosslinking was used to stabilize the opaque hydrogels, preventing them from dissolving in cell culture buffer DMEM and PBS at 37 °C. A clear difference in swelling ratio was seen between the opaque and transparent hydrogels, particularly the hydrogels formed at pH 10 which had significant increases in swelling ratio the closer to pH 10 the hydrogel was formed. Four SEM techniques were investigated to visualise the porous structure of the hydrogels, cryo-SEM, FIB-SEM, high vacuum SEM and eSEM. Additionally, different hydrogel SEM sample preparations and GA chemical crosslinking were examined in an attempt to preserve hydrogel architecture and reduce the formation of crystalline ice polymorphs and artefacts.

### **5.4.2. pH of gelation influences swelling ratio of opaque hydrogels in different swelling solutions**

The opaque hydrogels MQ 37 O, MQ 40 O, t7 37 O, t7 40 O, t10 37 O and t10 40 O could not swell in DMEM or PBS at 37 °C and dissolved within 30 minutes. However, they could swell in MQ water and DMEM at 20 °C. In the previous chapter it was found that NT2RepCT could not form hydrogels in either PBS or DMEM at 2.4 % (w/v) when incubated at 37 °C for 16 hours, forming an aggregate of precipitated protein upon heating. The combination of the salt, cations, phosphates and sugars in DMEM disrupted hydrogen-bonds and intermolecular interactions involved in forming the hydrogel network. This process was accelerated by heat leading to protein unfolding. It is likely that the opaque hydrogels would dissolve in DMEM or PBS at 20 °C over longer time periods than 24 hours. Long term swelling stability experiments to determine hydrogel mass loss should be performed for all NT2RepCT hydrogels. This

temperature dependent instability was not seen in the transparent hydrogels MQ 37 T and CAPS10 although these were swollen in PBS and not DMEM due to planned cell culture experiments being cancelled and drug delivery in PBS being performed instead. Transparent hydrogel swelling and a comparison to opaque hydrogel swelling is discussed in section 5.3.5.

The swelling behaviour of hydrogels can impact its applications and the ability to control the swelling leads to tunable and potentially 'smart' materials. Swelling of protein hydrogels at different pH is dictated by the isoelectric point (pI) of the protein. If the pH is greater than the pI, the protein will accrue surface negative charge due to ionization of acidic amino acid side chains. It follows that if the pH is less than the pI, the protein will accrue overall positive charge due to ionization of basic amino acid side chains. If the pH is equal to the pI, the protein will have no net charge and be neutral. An increase in protein surface charge, whether positive or negative leads to increased electrostatic repulsion between the protein chains of the hydrogel. This increases the hydrophilicity of the hydrogel leading to increased swelling due to increased uptake of water molecules<sup>154,144</sup>.

By increasing the pH and temperature of gelation to pH 10 and 40 °C, t10 40 O swelled significantly more in water than MQ 37 O. However, in DMEM t10 40 O swelled significantly less than MQ 37 O. In fact, the presence of tris at pH 7 or 10 at either 37 °C or 40 °C led to less swelling in DMEM than hydrogels formed with no buffer in MQ water as seen in Section 5.3.2.

MQ 37 O swells less in MQ water than t10 40 O because the pH of pure MQ water is around 5.5 and this is close to the isoelectric point of NT2RepCT of 4.26. Additionally, there is no buffering capacity. Therefore, there is minimal surface charge and minimal electrostatic repulsion within the MQ 37 O hydrogel<sup>153</sup>. Consequently, there is little swelling as the hydrophilicity of the hydrogel is low. However, in DMEM which is

buffered to  $\sim$  pH 7, the pH  $>$  pI and MQ 37 O becomes ionized leading to increased overall negative charge and increased electrostatic repulsion and swelling. Whereas, for t10 40 O which was formed in 20 mM tris pH 10, the pH was already greater than pI of NT2RepCT. The protein had a large amount of negative surface charge with increased electrostatic repulsion between chains. When swelled in MQ water which contains no ions to mask the overall negative surface charge and no buffering capacity, the pH is around the same pH of gelation. Water enters the t10 40 O hydrogel as it has higher hydrophilicity and swells more in MQ water than MQ 37 O. When t10 40 O is swollen in excess DMEM at pH 7, which contains many cations these form electrostatic bonds to the negatively charged groups which decreases electrostatic repulsion and increases electrostatic attraction. The overall ionization state of t10 40 O is decreased in addition to the pH decreasing to  $\sim$ 7 leading to a net neutrally charged protein which has less hydrophilicity compared to at a higher pH, this in turn leads to decreased swelling in DMEM compared to MQ 37 O.

The t10 40 O hydrogel also had an increased temperature of gelation (40 °C vs 37 °C) which led to increased NT2RepCT unfolding and secondary structure change. This potentially exposed previously hidden anionic amino acids such as tyrosine and lysine, with pKa of 10.07 and 10.79 respectively, and this could have accentuated the swelling response. Hence, t10 40 O swells 2-fold more in MQ water than t10 37 O likely due to increased ionization of residues that are buried in t10 37 O. In MQ 40 O swelling in both MQ water and DMEM are high due to solvent exposed residues and greater  $\beta$ -sheet content at 40 °C.

In the case of t7 37 O and t7 40 O which were formed at pH 7, NT2RepCT has less overall negative surface charge compared to those formed at higher pH (t10 37 O and t10 40 O). Therefore, when swollen in either MQ water or DMEM, there is little difference in swelling between the two swelling solutions. In MQ water t7 37 O and

t7 40 O remain at ~ pH 7 and with minimal electrostatic repulsion swells little. When swollen in DMEM, once again the pH in the hydrogel is pH 7 and so the hydrogels swell the same amount as in MQ water.

Other protein hydrogels exhibit pH sensitive swelling behaviours due to the isoelectric point of the protein. Gelatin and albumin undergo conformation changes from a linear form to an  $\alpha$ -helical structure which is stabilized by hydrogen bonding at certain pH<sup>153</sup>. Hybrid hydrogels formed from collagen and silk fibroin showed pH sensitive reversible gelation at pH 4 due to increased electrostatic repulsion between the protein chains<sup>145</sup>.

### **5.4.3. Glutaraldehyde chemical crosslinking of NT2RepCT**

GA is one of the cheapest and readily available chemical crosslinkers. GA primarily crosslinks  $\epsilon$ -amine group of lysine but can also crosslink other functional groups such as amines, phenols, thiols and imidazoles<sup>165</sup>. The exact mechanism of GA crosslinking is not yet fully understood although intensive research has been carried out<sup>165,166</sup>. GA can exist in 13 different forms, monomeric and polymeric which depend on pH, concentration and temperature<sup>167</sup>. It has been suggested that GA exists as the monomeric dialdehyde, as a cyclic hemiacetal or as a cyclic hemiacetal oligomer<sup>166</sup> in acidic conditions (Figure 47). GA crosslinking was performed in MQ water which is slightly acidic at pH 5.5. There is contention in the literature about the mechanism of GA crosslinking with suggestions of Schiff bases and Michael additions. Schiff bases are the expected reactive species formed upon nucleophilic attack by the  $\epsilon$ -amine of lysine (Figure 48) but these are unstable in acidic conditions and break down to reform the amine and aldehyde<sup>166</sup>. Another suggestion is a combination of a Schiff base for one lysine amine and an anti-Markownikoff reaction on another lysine amine by the same polymeric form of glutaraldehyde<sup>165</sup>. A 6 membered ring crosslink was formed

between lysine and arginine residues in barnase trimer, a bacterial RNase crosslinked with GA<sup>167</sup>.

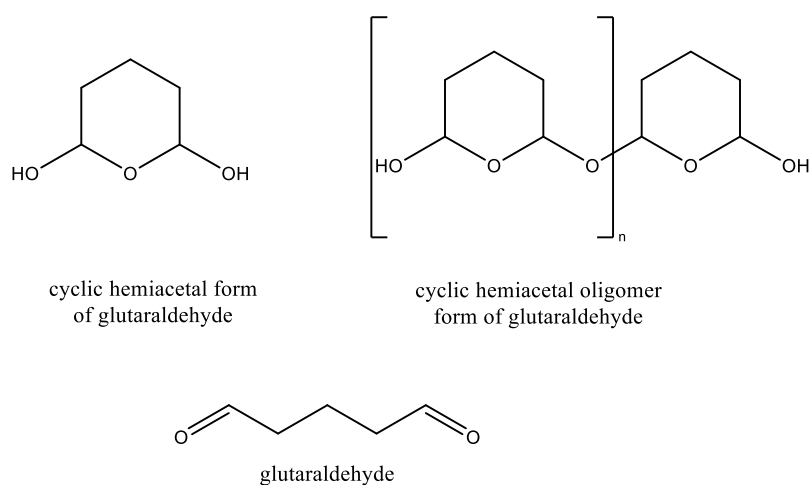


Figure 47: The forms of glutaraldehyde in acidic conditions. Adapted from I. Migneaul *et al.*<sup>166</sup>.

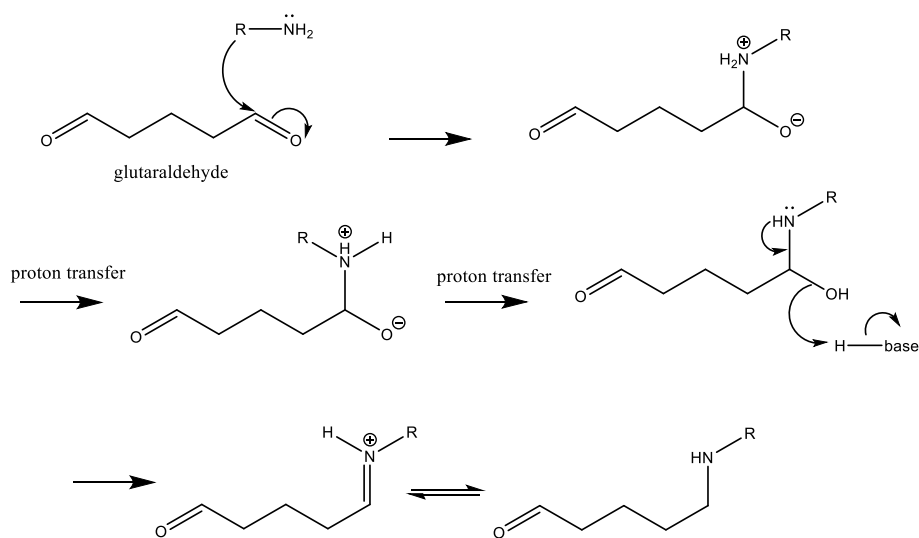


Figure 48: Expected lysine and glutaraldehyde reaction via a Schiff base.

Glutaraldehyde is a suitable chemical crosslinker for NT2RepCT since the protein contains 2 lysine residues which are 27 residues apart and both found on the NT (Figure 49). In addition, NT2RepCT contains 52 serines and 5 arginine residues which could also be involved in the GA crosslinking due to the amine containing R groups.

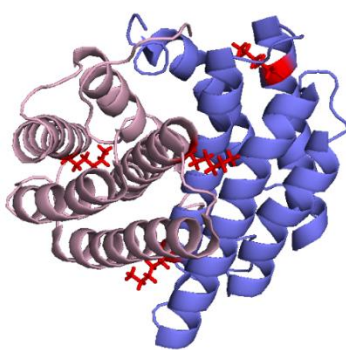


Figure 49: NT2RepCT *E. australis* NT dimer with lysine shown (red) each dimer in different colour (purple and pink) for clarity (PDB: 2LTH). NT2RepCT NT exists as a dimer in acidic conditions.

After GA crosslinking the opaque hydrogels were able to swell in DMEM at 37 °C (Section 5.3.4) with no dissolution as the chemical, covalent crosslinking stabilizing the hydrogel network. Since the NT2RepCT hydrogels t7 37 O, t7 40 O, t10 37 O and t10 40 O contained tris that would also be crosslinked by GA, hydrogels were either pre-swollen in MQ water before GA crosslinking to remove tris or were GA crosslinked not pre-swollen, still containing tris. Pre-swelling in MQ water before GA crosslinking would alter the hydrogel network. Therefore, a difference in swelling ratio was seen between pre-swollen and not pre-swollen hydrogels in MQ water at 20 °C with significant differences seen in MQ 37 O 1GA, t10 37 O 1GA and t10 40 O 1GA. In the crosslinking process the hydrogels were submerged in an excess of 1 % (v/v) GA in MQ water at ~ pH 5.5 which is close to the pI of NT2RepCT leading to overall slight negative surface charge. In hydrogels containing tris (not pre-swollen) the buffering capacity might have resisted to some degree this pH change and maintained the hydrogels closer to their original pH during crosslinking. When the opaque 1 % (v/v) GA crosslinked hydrogels were swollen in DMEM at 20 °C and 37 °C there was minimal

difference in swelling between pre-swollen and not pre-swollen treatments. This suggests whatever phenomena that caused the differences when swollen in MQ water were masked by presence of cations and salts in DMEM reducing swelling.

All the 1 % (v/v) GA crosslinked opaque hydrogels swelled more in MQ water at 20 °C than the non-crosslinked opaque hydrogels with  $Q = 25-60$  compared to  $Q = 12-40$  in the non-crosslinked. This increase in  $Q$  in MQ water is likely related to both increased stability of the hydrogel network allowing increased stretch and capacity of the network before dissolution and increased hydrophilicity from polymeric GA crosslinking. The differences in  $Q$  between the different 1 % (v/v) crosslinked opaque hydrogels were decreased compared to the non-crosslinked suggesting that GA crosslinking made all the opaque hydrogels similar in crosslinking degree and structure.

#### **5.4.4. Transparent hydrogels were able to swell more than opaque hydrogels**

The pH of gelation has a large impact on the swelling ability of the NT2RepCT hydrogels, particularly at pH 10. CAPS10 has a better buffering capacity at pH 10 than tris or HEPES. This means NT2RepCT in CAPS pH 10 has more net surface negative charge due to deprotonation of N terminal histidine  $\text{NH}_3^+$  to  $\text{NH}_2$  and potential deprotonation of the acidic amino acids lysine and tyrosine. Therefore, CAPS10 has the highest swelling ratio in MQ water, followed by HEPES10 and the least seen in t10 40 O (Figure 35). This is because tris and HEPES would not maintain pH 10 and with a lower pH there would be less net surface charge and therefore less electrostatic repulsion.

MQ 37 T was prepared with freshly decanted, ultra-pure MQ water MQ 37 O was prepared with older MQ water. The new pH was more neutral and closer to pH 7 as measured by universal indicator paper. Therefore, in MQ 37 O unfolding to a

disordered protein secondary structure would occur upon heating as seen in the CD results at pH 7. There is also the possibility of plasticisers and other contaminants in the old MQ water leading to possible protein precipitation and aggregation. It is at this point unknown why MQ 37 O forms an opaque and minimally swelling hydrogel. A study of the pH dependent swelling of opaque and transparent hydrogels made from egg white or whey protein isolate suggested that opaque hydrogels were particulate in microstructure, whereas transparent hydrogels had a stranded architecture that had increased swelling ability due to increased elastic character. The particulate hydrogels were described as rigid with little room for expansion in swelling<sup>117,121</sup>.

The transparent hydrogels MQ 37 T and CAPS10 followed the same swelling response in PBS as the opaque non-crosslinked hydrogels in DMEM. MQ 37 T swelled significantly more in PBS at all pH (5, 6.45 and 7.6) than CAPS10 (Figure 37). PBS contains disodium hydrogen phosphate, potassium dihydrogen phosphate, potassium chloride and sodium chloride. These salts could mask the negatively charged groups in CAPS10 reducing the hydrophilicity and swelling compared to MQ 37 T. It was expected that the different pH of PBS would lead to different swelling ratios. MQ 37 T should swell the least in PBS pH 5 if electrostatic repulsion was the only factor, followed by increased swelling as the pH increases due to increased ionization of NT2RepCT. However, NT2RepCT undergoes a conformational change at pH 5.5 and below<sup>2</sup> leading to unfolding of the CT into  $\beta$ -amyloid like fibrils. This unfolding could have contributed to the increased swelling. The same swelling ratio was also seen in CAPS10 at all PBS pH suggesting that electrostatic interactions are not the only factor involved in swelling.

Recombinant spider silk hydrogels are a relatively new field and although a handful have been published, very few discuss swelling behaviour. The only published swelling data so far seems to be for the recombinant spidroin eADF4(C16). At 3-7 % (w/v),

hydrogels which were chemically crosslinked at tyrosine residues by APS and ruthenium and showed a 5 to 10-fold increase in volume when swollen in tris/HCl buffer at pH 7.5. Since swelling ratios of NT2RepCT hydrogels were calculated by weight it is difficult to make a comparison to crosslinked eADF4(C16) hydrogels swelling since the specific density of NT2RepCT is unknown. However, a comparison to silk fibroin hydrogels can be made. Silk fibroin hydrogels formed by sonication at 3 % (w/v) had a swelling ratio of around 40 in PBS pH 7.4. This is similar to MQ 37 T swollen in PBS pH 7.6 where  $Q = 34 \pm 4.1$  and slightly higher than CAPS10 swollen in PBS pH 7.6 where  $Q = 24.7 \pm 1.0$ . Compared to other natural hydrogels prepared from 1.2 mg/mL collagen ( $Q = \sim 3$ ) or 1-2 % hyaluronic acid ( $Q = \sim 7-8$ )<sup>168</sup>, all NT2RepCT hydrogels swelled 2 to 10-fold more in PBS or DMEM.

#### **5.4.5. Cryo-SEM and FIB-SEM cryofixation technique is critical**

Preparing high water content systems for cryo-SEM depends on efficient and fast freezing to achieve cryo-fixation. Using liquid nitrogen slush (LNS) which is around -210 °C and small sample volume was hoped to achieve this. However, an increase in pore size (6-12  $\mu\text{m}$ ) and rectangular shape of pores was seen in MQ 37 O hydrogels towards the middle of the hydrogel sample that was frozen in liquid nitrogen slush. At the edge of the rivet, the hydrogel pores were smaller (1-3  $\mu\text{m}$ ) and more circular in shape (Figure 38). Furthermore, a directionality of the rectangular pores was seen, potentially from the manual cutting and fracturing of the frozen hydrogel sample by the scalpel in the sample preparation chamber of the SEM. The scalpel was controlled by a stick on the outside of the chamber, creating a long lever effect and was difficult to use in a controlled manner.

This difference in pore size is related to slower freezing towards the middle of the sample in the rivet leading to artefacts and larger pores due to crystalline ice disrupting the hydrogel structure. This change in pore size was seen for high water content

alginate hydrogels prepared for cryo-SEM by plunge freezing in LNS. The pore size increased the deeper into the hydrogel and further away from edge of hydrogel the images were taken<sup>158</sup> due to hexagonal ice expanding and displacing the alginate polymer network within the hydrogel. Whereas at the edge of the hydrogel sample, <20  $\mu\text{m}$  depth, efficient heat transfer and rapid freezing formed vitreous ice. Therefore, the smaller pores at the edge of the rivet are more likely to be close to the actual hydrogel architecture. Multiple techniques are required to image and analyse hydrogel pores in their native state since all sample preparation techniques have the risk of altering the sample. To try to improve the freezing rate, metal mirror (slam) freezing was employed. Although these cryofixation method operate at liquid nitrogen temperatures of -190 °C which is warmer than LNS at -210 °C, the thin layer created by the slam freezer could increase the freezing rate. The metal rivets were 3 mm in diameter and vitreous freezing only occurs within the first 20  $\mu\text{m}$ <sup>158</sup> maximum. The slam freezer creates a layer  $\sim$ 0.5 mm thick which is the height of the plastic ring used to hold the sample. A comparison of cryo-SEM using slam freezing was not performed as FIB-SEM was favoured although this comparison should be performed Due to the cryo-SEM being in high demand to maximise the bookable slots available, FIB-SEM was used to visualise the metal mirror (slam) frozen MQ 37 O hydrogel. During the water sublimation process a porous network was revealed with larger pores seen at the end of the sublimation process (Figure 39). Voids containing subliming water were dark grey to black and areas of hydrogel were light grey to white. The milled area was not coated in conductive platinum and therefore the high energy electron beam likely charged the area and caused local structural collapse and secondary pores through freeze-etching<sup>156</sup>. FIB-SEM has been previously used to successfully visualise pores of a hydrogel over 20 minutes sublimation although the type of hydrogel and its formation were not discussed<sup>159</sup>. The pore sizes revealed in the initial 15 minutes of

the sublimation process and at the end were smaller than those seen in LNS cryofixation SEM which ranged from 1-3  $\mu\text{m}$  with no nanometer scale pores. Due to the intensive sample preparation process required and low throughput nature of cryo-SEM, high vacuum SEM and eSEM were utilised to try to visualise the pores of NT2RepCT hydrogels.

#### **5.4.6. High vacuum SEM of the opaque hydrogels porous structure**

The opaque hydrogels formed in MQ water, 20 mM tris pH10 at 37 °C and 40 °C were crosslinked with 1 % (v/v) GA (MQ 37 O 1GA, t10 37 O 1GA and t10 40 O 1GA) to stabilize and chemically fix their internal architecture and were therefore swollen ahead of freezing and lyophilisation. Non-crosslinked opaque hydrogels were not analysed by SEM since these were not taken forward after swelling experiments.

MQ 37 O 1GA had a greatly different morphology compared to non-crosslinked MQ 37 O analysed by cryo-SEM with minimal porous structure observed (Figure 40). This could be an artefact of GA crosslinking or plunge freezing in liquid nitrogen. Both t10 37 O 1GA and t10 40 O 1GA appeared similar in the captured SEM images with interconnected pores between 1 and 20  $\mu\text{m}$ . Areas of crystalline ice were present in the hydrogels due to inefficient freezing with liquid nitrogen plunge freezing. Furthermore, lyophilisation at -60 °C and 0.1 mbar might have caused any vitreously frozen ice to change to a crystalline polymorph of ice upon heating<sup>158</sup>. Interestingly, no fibrillar structure was seen in MQ 37 O 1GA, t10 37 O 1GA or t10 40 O 1GA but was seen in MQ 37 T 1GA and CAPS10 1GA as discussed in the following section.

#### **5.4.7. Artefacts and secondary pores in non-crosslinked transparent hydrogels**

The transparent NT2RepCT hydrogels MQ 37 T and CAPS10 porous structure was examined initially non-crosslinked using high vacuum SEM. A comparison of liquid nitrogen plunge freezing and metal mirror (slam) freezing was performed on the PBS

swollen hydrogels before lyophilisation and sputter coating. Large, crystalline ice honey-comb pores were seen in addition to cracks and tears in the plunge frozen MQ 37 T and CAPS10. There were some areas of smaller pores close to the surface, but these were infrequent (Figure 41). The swollen MQ 37 T and CAPS10 had high swelling ratios (Q) of 60-100 % and were soft with Young's modulus less than 1 kPa (discussed in the materials characterisation section 6.4.2). This combination of factors is more likely to be susceptible to artefacts and crystalline ice formation which pushes aside the hydrogel material, creating pores<sup>156,158</sup>. In plunge freezing a chunk of swollen hydrogel was frozen and took 1-2 seconds to freeze. Metal mirror (slam) freezing was then investigated on the same PBS swollen, non-crosslinked hydrogels MQ 37 T and CAPS10. Interestingly, although MQ 37 T was torn and fractured due to the freezing and lyophilisation process, it had very fibrous in structure with lots of crossed fibrils (Figure 42 A), similar to those seen in collagen hydrogels<sup>169,170</sup> or silk fibroin-4RepCT silk mats<sup>90</sup>. A textured surface was also seen in CAPS10 metal mirror (slam) frozen although to a lesser extent than MQ 37 T. The presence of fibrils in MQ 37 T could be explained by the unfolding of the CT dimer into  $\beta$ -amyloid like fibrils at pH 5.5 and below and the slam freezing process introduces compressional force into the sample, deforming it to the shape of the ring. Fibres are formed in NT2RepCT at acidic pH and with shear force<sup>2</sup> which is a directional force not compressional. Since the same fibril structure was not seen to the same extent in CAPS10, pH of gelation could be a factor, although the CAPS10 hydrogel sample was not as thin in the plastic ring as MQ 37 T and no tears were seen. In a hydrogel prepared from  $\beta$ -lactoglobulin, fibrils were expected due to a similar unfolding to amyloid like fibrils seen in NT2RepCT and were only seen with efficient freezing<sup>171</sup>.

#### 5.4.8. GA crosslinking in SEM/eSEM

To improve the mechanical properties and minimise artefact formation<sup>156</sup>, the transparent hydrogels MQ 37 T and CAPS10 were crosslinked with 1 % (v/v) GA. If crystalline ice did form, it was hoped that stronger crosslinks within the hydrogel could minimise the damage caused, although ice is very destructive and can damage concrete<sup>172</sup>. Glutaraldehyde (GA) chemical fixation has been used in eADF4(C16) hydrogels before freezing at -80 °C and lyophilisation for SEM although in all images, crystalline ice was present with a typical honey-comb structure but to a lesser extent as the concentration of eADF4(C16) increases which in turn increases the crosslink density and stiffness<sup>112</sup>. Crosslinking of alginate scaffolds with GA before SEM altered the surface morphology creating a smoother appearance over 24 hours and no crystalline ice was seen<sup>173</sup>.

Overall, for the 1 % (v/v) GA crosslinked hydrogels MQ 37 T 1GA and CAPS10 1GA across the two SEM techniques and three SEM sample preparation methods both hydrogels had an extensive and interconnected porous structure. However, a wide range of pore sizes were seen and therefore artefacts were not eliminated. High vacuum liquid nitrogen plunge freezing SEM showed the most crystalline ice compared to eSEM. This finding contributes to the evidence that liquid nitrogen plunge freezing is not an efficient freezing method due to the Leidenfrost effect, despite it being used extensively in the literature for the SEM imaging of hydrogels<sup>1,157,174</sup>. Low vacuum eSEM operates at -18 °C which leads to freeze-etching of the hydrogel surface<sup>156</sup> and irreversible changing of amorphous ice to a crystalline polymorph.

Interestingly, in the high vacuum SEM images fibril like structures were seen inside the pores of both MQ 37 T 1GA and CAPS10 1GA and throughout the entire lyophilised hydrogel (Figure 43). More investigation is needed to conclude whether the fibrils are an artefact of sample processing or are native structures. Atomic force microscopy can

been used to monitor fibril formation in hydrogels<sup>175,128</sup>. Formation of nano-fibrils is not out of the question for NT2RepCT hydrogels and is seen at the air-liquid interface of solutions of the recombinant spidroin 4RepCT<sup>176,177</sup>. 4RepCT shares the repetitive domain with NT2RepCT although 4 repeats not 2 and contains the CT from *E. australis* which contains a disulphide bridge. Fibrils have not been seen in other reported recombinant spider silk hydrogels.

To compare the hydrogel architecture seen in MQ 37 T 1GA and CAPS10 1GA high vacuum SEM, environmental SEM (eSEM) was employed. This technique can image samples in their hydrated state leading to more accurate representations. Furthermore, no coating or sample preparation is needed. However, as with cryo-SEM this technique is low throughput with only one sample being able to be analysed in the eSEM at a time. Additionally, the resolution is much lower than cryo-SEM or SEM which operate under vacuum as presence of water vapour and nitrogen in the sample chamber to control hydration state interfere with the electron beam<sup>164</sup>.

In the native, hydrated state both MQ 37 T 1GA and CAPS10 1GA showed smooth surfaces with minimal texture and no pores visible (Figure 46 A & D). It is possible that the hydrogels form with a film around the entire outside surface but this smooth surface observation is likely a layer of water<sup>156</sup> since surface pores became visible in the *in situ* lyophilisation process.

The only pore sizes seen in *in situ* lyophilisation eSEM were 4-30  $\mu\text{m}$  with no sub 1  $\mu\text{m}$  pores seen as in low vacuum eSEM and high vacuum SEM. The freezing temperature in this process was -10 °C and then reduced to -18 °C with water vapour and pressure controlled to prevent instant lyophilisation. In MQ 37 T 1GA, the pores are less regular in shape than CAPS10 1GA in addition to being more numerous and having thinner pore walls (Figure 46 C & F). If these pores are artefacts, then due to the reduced material properties of MQ 37 T compared to CAPS10 (material properties

are discussed in the following chapter) CAPS10 was likely able to resist secondary pore formation more than MQ 37 T. Another factor could be the initial hydrogel structure before 1 % (v/v) GA crosslinking. If MQ 37 T contains more nano-fibril structures due to unfolding of the CT into  $\beta$ -amyloid like fibrils compared to CAPS10, these small pores between fibrils could be smaller and more numerous than pores in a primarily alpha helical protein secondary structure at pH 10. Therefore when ice crystal formation does occur, there are more nucleation points and more water containing pores to be filled with crystalline ice, pushing the pore walls aside<sup>164</sup>. This difference in pore wall thickness was not seen in high vacuum SEM or in the smaller pores in the low vacuum eSEM therefore it could also be due to differences in hydration state between the two hydrogels.

## **5.5. Summary of swelling behaviour and SEM analysis**

As expected, the different hydrogels formed in Chapter 4 showed different swelling characteristics and morphologies in SEM analysis. The opaque hydrogels MQ 37 O, MQ 40 O, t7 37 O, t7 40 O, t10 37 O and t10 40 O dissolved in DMEM and PBS at 37 °C and were therefore not suitable for further experiments involving these physiological buffers. However, these hydrogels could swell in MQ water and DMEM at 20 °C. The opaque hydrogels MQ 37 O and t10 40 O showed opposite swelling behaviour in MQ water and DMEM at 20 °C. This swelling behaviour is because of increased or decreased electrostatic repulsion within the hydrogels leading to altered hydrophilicity and water entry. In t10 40 O swollen in MQ water the electrostatic repulsion within the hydrogel is higher than MQ 37 O and therefore t10 40 O swells significantly more. However, in DMEM MQ 37 O swells more due to the ionic shielding occurring in t10 40 O and the increased negative charge in MQ 37 O as  $\text{pH} > \text{pI}$ . This is a good example of how gelation conditions can affect hydrogel behaviour and

illustrates the potential for smart hydrogels that alter their behaviour in response to a stimulus.

GA crosslinking was used to improve the swelling behaviour of the opaque hydrogels with an increase in swelling seen in MQ water compared to the non-crosslinked. This chemical crosslinking prevented hydrogel dissolution at 37 °C exemplifying the increased strength of crosslinking.

In the previous chapter, Chapter 4, it was discovered that NT2RepCT hydrogels with high light transmittance and slower gelation times were formed the closer the pH was to pH 10. This pH dependence also affects hydrogel swelling. The swelling ratio (Q) of NT2RepCT hydrogels increased the closer the pH of gelation was to pH 10. The transparent hydrogel CAPS10 swelling ratio Q in MQ water at 20 °C was 307 % higher than the opaque hydrogel t10 40 O. A higher swelling ratio was also seen in the transparent hydrogel MQ 37 T compared to MQ 37 O indicating a relationship between light transmittance and swelling.

Hydrogel morphology was assessed by four different SEM techniques and five sample preparation methods to reduce the impact crystalline ice artefacts. Cryo-SEM and FIB-SEM of the opaque NT2RepCT hydrogel MQ 37 T revealed an interconnected porous network. However, artefacts and crystalline ice were created in the sample preparation although less so in metal mirror (slam) freezing.

High vacuum SEM revealed inter-connected porous networks in the opaque 1 % (v/v) GA crosslinked hydrogels MQ 37 O 1GA, t10 37 O 1GA and t10 40 O 1GA. The images of the non-crosslinked MQ 37 T and CAPS10 hydrogels did not reveal any porous structure in either plunge freezing or metal (mirror) slam freezing. Therefore, 1 % (v/v) GA crosslinking was used to preserve hydrogel porous architecture in MQ 37 T and CAPS10. Extensive fibril like structures were seen throughout MQ 37 T 1GA and CAPS10 1GA but were not present in MQ 37 O 1GA, t10 37 O 1GA or t10 40 O 1GA.

These fibril structures were also not seen in the eSEM imaging of MQ 37 O 1GA and CAPS10 1GA suggesting they may be an artefact of sample preparation.

It was found that crystalline ice and artefacts could not be avoided but they could be mitigated. The most commonly used high vacuum SEM sample preparation technique of plunging in liquid nitrogen created extensive honey-comb crystalline ice artefacts and secondary pores in all hydrogels.

Low vacuum eSEM metal mirror (slam) frozen and *in situ* lyophilisation eSEM of MQ 37 T 1GA and CAPS10 1GA revealed extensive porous networks. Low vacuum eSEM of MQ 37 T 1GA and CAPS10 1GA metal mirror (slam) frozen showed small sub 1  $\mu\text{m}$  pores and pores 2-9  $\mu\text{m}$ . *In situ* lyophilisation of MQ 37 T 1GA and CAPS10 1GA did not show sub 1  $\mu\text{m}$  pores but revealed an extensive inter-connected crosslinked porous network.

Although all the SEM analysis revealed porous networks, it is unwise to draw too many conclusions from the results. Differences in pore morphology were seen between the 1 % (v/v) GA crosslinked opaque hydrogels and the transparent hydrogels but the effect of GA crosslinking on the hydrogel architecture is unknown.

The following chapter discusses the mechanical characterisation by compression testing and rheology of the 1 % (v/v) GA crosslinked opaque hydrogels MQ 37 O 1GA, t10 37 O 1GA and t10 40 O 1GA and the non-crosslinked transparent hydrogels MQ 37 T and CAPS10.

## 6. Young's modulus and rheology (Materials characterisation Part B)

### 6.1. Introduction

This chapter is the second part of the characterization of NT2RepCT hydrogels focusing on their material properties and resistance to stress and deformation. Analysis of Young's modulus is performed with compression testing and rheology is used to investigate the hydrogel's flow after deformation. The effect of gelation pH and temperature on the NT2RepCT hydrogel's material property is discussed.

#### 6.1.1. Mechanobiology

Many human tissue cells, except for red blood cells and cells of the immune system, do not survive in a suspension or in a fluid, they require a matrix to not only attach to, but to receive signals from. They adhere to and additionally pull on their surrounding environment, whether this is other cells or the extracellular matrix (ECM). These actions can affect cell morphology via the cytoskeleton, processes within the cell and morphology of ion-channels<sup>178,179</sup>. Therefore, it is not only cell signals that affect how cells behave, but their environment too. In order to culture cells *in vitro* as close to physiological conditions as possible, it is important to create artificial cell matrices that reflect the ECM in terms of stiffness and attachment points<sup>180</sup>.

In addition to the ECM material properties influencing intracellular processes in differentiated cells, it can also determine the fate of undifferentiated naïve cells. Undifferentiated mesenchymal stem cells (MSCs) cultured on 2D collagen coated polyacrylamide (pAA) hydrogels of different stiffness as measured by the Young's modulus (E), committed to neuronal, myoblast or osteoblast differentiation depending on E of the matrix. MSCs cultured on hydrogels with E of 0.1-1 kPa underwent differentiation to neuronal cells, when E was 8-17 kPa they became myoblastic and when E was 25-40 kPa they differentiated to osteoblasts<sup>181</sup>. The

stiffness ranges of were chosen to reflect the Young's modulus of brain tissue, muscle and stiffer collagenous ECM. Culture media could alter to a certain degree the fate of the MSCs but soluble growth factors in addition to matrix stiffness was the driving factor for differentiation.

When comparing 2D and 3D cell culture, the extra dimension adds a layer of complexity and further reflects *in vivo*. The relationship between matrix stiffness and cell morphology/differentiation is not linear as in 3D cultures the cells are limited by their ability to push back and deform against the matrix<sup>182</sup>.

Comparing hydrogels with another biomaterial, sponges showed differences in cell morphology. Sponges have larger and more interconnected pores than hydrogels<sup>183</sup>, allowing faster rates of diffusion. The extracellular environment impacts the cell morphology and phenotype, altering the cytoskeleton and cell proliferation. In a comparison between chitosan sponges and hydrogels, chondrocytes adopted different shapes depending which matrix they were cultured in. Chondrocytes cultured in the large porous, hard environment of the sponges adopted spindle shape, whereas those cultured in the hydrogel were round. Additionally, the cells cultured in the sponges distributed unevenly in small clusters as compared to in the hydrogel where they distributed homogeneously<sup>183</sup>.

Characterizing an implanted biomaterial's material properties is also important for drug delivery as they can act as both a scaffold and a drug delivery platform. Understanding the limits of the material and how it will respond to pressure from its surrounding environment ensures it will not fracture or collapse, releasing a large concentration of loaded drug due to increased surface area. Furthermore, matching material properties of the implanted biomaterial, with the surrounding tissue ensures no mismatch<sup>184,168</sup> which can exert undue stress and pressure on these tissues. This can lead to scarring, injury and patient discomfort<sup>1</sup>.

### 6.1.2. Young's modulus

The stiffness and elasticity of biomaterials are important properties to characterise since they will affect material handling, tissue compatibility and potentially the responsiveness to stimuli. Young's modulus  $E$  (Pa) or the elastic modulus is a measure of the materials resistance to elastic deformation under load. It is a measure of stiffness.  $E$  relates force per unit area (stress) to proportional deformation (strain) along a single axis (Figure 50) and is calculated by Equation 9, Hooke's law.

Equation 9: 
$$E = \frac{\sigma}{\epsilon} = \frac{\frac{F}{A}}{\frac{\Delta L}{L_0}} = \frac{FL_0}{A\Delta L}$$

Hooke's law where  $\sigma$  = uniaxial stress,  $\epsilon$  = strain,  $F$  = force (compression or extension),  $A$  = cross-sectional surface area perpendicular to the applied force,  $\Delta L$  = change in length (positive if extension and negative if compression),  $L_0$  = original length.

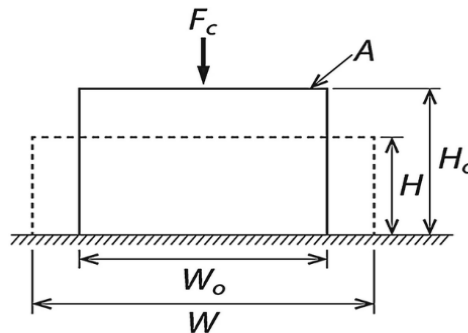


Figure 50: From D. Lee *et al.*<sup>185</sup>. Measurement of elastic moduli by compression. Deformation of sample under compressive force  $F_c$  applied along one axis perpendicular to  $A$ .  $A$  = cross sectional sample area,  $H_0$  = original sample height,  $H$  = sample height after compression.  $W_0$  = original sample width,  $W$  = sample width after compression. The height of the sample decreases whilst the width increases under compressive force. The normal stress ( $\sigma$ ) and strain ( $\epsilon$ ) of the sample are defined as  $\sigma = F_c/A$  and  $\epsilon = (H_0-H)/H_0$ .

Experimentally, Young's modulus can be calculated from the initial linear portion of a stress vs strain curve which can be from compression or extension of the material. In compression it represents how much the material will deform before plastic/permanent deformation, non-reversible shape change, occurs under compressive load. On the stress vs strain curve this is where the response is no longer linear and is called the yield point or yield strength. After this point the material will either distort until it is flat and completely compressed or will deform until it breaks.

The Young's modulus of tissues in the body varies from very stiff bones<sup>186</sup> at 20-40 MPa to very soft neuronal tissue<sup>187</sup> at 100-400 Pa (Table 10). The Young's modulus of a hydrogel can be controlled, much like swelling ratio, by monomer concentration and degree of crosslinking. Increasing the concentration of eADF4(C16) silk protein from 3 to 7 % (w/v) led to a 200-fold increase in Young's modulus of the hydrogels<sup>112</sup>. Additionally, ruthenium catalysed chemical crosslinking of these hydrogels with APS further increased the Young's modulus 3-fold compared to the non-crosslinked. The authors suggested that increasing the protein concentration and introducing chemical crosslinking decreased mobility of nanofibrils within the hydrogel leading to an increased stiffness of the network<sup>112</sup>. This large range, 0.2-110 kPa, of Young's moduli meant that eADF4(C16) hydrogels have been utilised for different applications from bioprinting to 3D cell culture<sup>188</sup>. Silk fibroin hydrogels formed by sonication showed a linear increase in Young's modulus as the protein concentration was increased from 1 to 8 % (w/v)<sup>126</sup>. While all hydrogels formed had a Young's modulus in the range of neural cells and tissues the authors suggested that a hydrogel that was too soft would lead to quicker diffusion of growth factors which led to reduced growth factor immobilisation which negatively affected neurite outgrowth. However the findings showed that this applied in a small range of stiffness, as the 8 %

(w/v) hydrogels supported less neural outgrowth than the 4 % (w/v) in their *in vitro* experiments<sup>126</sup>.

Compared to natural hydrogels, synthetic hydrogels generally show more favourable material properties including larger Young's modulus<sup>189</sup>. This is related to the strong covalent crosslinking involved in synthetic hydrogels, since physically crosslinked, natural hydrogels rely primarily on weak intermolecular interactions and hydrogen bonding. Furthermore, the pore size and crosslink density can be more controlled in synthetic hydrogels creating a homogenous material and ability to increase the Young's modulus without the need to increase monomer concentration as is the case with protein hydrogels. A 4-arm PEG crosslinker was added to PEGDA hydrogels leading to an increased local crosslink density which increased the Young's modulus by 1.7-fold to 400 kPa<sup>190</sup>. The Young's modulus also increased 10-fold to 3500 kPa by reducing the molecular weight of the PEGDA from 10 kDa to 3.4 kDa. This increase in Young's modulus was caused by a smaller mesh size in the lower molecular weight PEGDA which is equivalent to the chain length between crosslinks<sup>190</sup>.

Polyethylene glycol (PEG), poly(2-hydroxyethyl methacrylate) (polyHEMA) and poly(acrylamide) (PAAm) are commonly used materials for synthetic hydrogels used in biomedical applications<sup>189</sup>. Hydrogels for biomedical applications must be biocompatible and while PEG and polyHEMA are, PAAm monomers are cytotoxic<sup>191</sup>. Natural protein hydrogels have the added benefit of a morphology and topology that is more like the ECM than synthetic hydrogels and can be easily functionalised with integrin binding sites. Furthermore, protein hydrogels are often more biodegradable than synthetic hydrogels.

Table 10: Young's modulus (kPa) of tissues in the body and published hydrogels

Material	Young's modulus (kPa)	Ref
Bone (cortical)	20–40 x10 <sup>6</sup>	186
Skin	1.28–1.03 x10 <sup>3</sup>	192
Nerve	150-300	184
Soft cartilage	100	187
Heart	10-15	193
Brain	0.1-0.4	187
Fat	0.017	187
Matrigel™ (at 37 °C)	0.45	194
1.2 mg/mL type-1 collagen hydrogel	0.3	168
1 % (w/v) HA (>1.2 MDa) hydrogel	0.1	168
1-8 % (w/v) silk fibroin hydrogels	4-33	126
eADF4(C16) 3-7 % (w/v) hydrogel crosslinked/non-crosslinked	0.2-110	140
R4C and R48 <i>N. clavipes</i> spider silk CT and resilin hydrogels	0.1-1	130
Composite PEG and Hyaluronic acid UV- crosslinked hydrogels	1-12	102
Collagen-polyacrylamide interpenetrating network hydrogels	12-32	195

### 6.1.3. Rheology

Another method of hydrogel characterisation is rheology which analyses a materials flow after deformation (change in size or shape of material) from shear force (force applied perpendicular to materials surface) (Figure 51). The hydrogel sample is placed between two parallel plates and sinusoidal shear force is introduced by rotation of the upper plate at a certain frequency of oscillation. This creates shear deformation within the hydrogel material as the top section moves past neighbouring sections within the hydrogel. The applied stress is called shear stress  $\tau$  and is equal to the shear force  $F_s$  which has units of N, divided by the shear area  $A$  which has units of  $m^2$  giving shear stress  $\tau$  with the units Pa (Equation 10).

Equation 10: 
$$\text{Shear stress } \tau = \frac{F_s (N)}{A (m^2)} = Pa$$

Shear strain ( $\gamma$ ) is quantified by the angle ( $\theta$ ) (Figure 51). If  $\theta$  is small, then  $\gamma$  can be calculated by the ratio between the lateral displacement of the hydrogels top surface ( $L$ ) to the height of the hydrogel ( $H_0$ ) and therefore this unit is dimensionless and is often represented as a percentage (Equation 11).

Equation 11: 
$$\text{Shear strain } (\%) \gamma = \frac{L}{H_0}$$

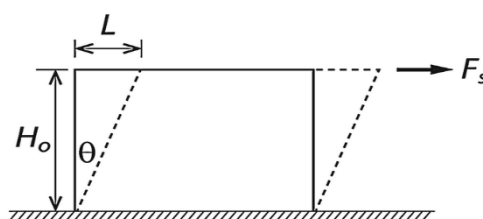


Figure 51: Deformation of a hydrogel by shear force ( $F_s$ ) The bottom of the hydrogel is fixed whilst the top is displaced by length ( $L$ ) in the direction of shear force ( $F_s$ ). The height ( $H_0$ ) remains the same throughout the shear deformation. The angle ( $\theta$ ) is used to calculate shear strain. Diagram from D. Lee *et. al.*<sup>185</sup>.

Due to the rotational oscillation of the upper plate, shear strain when plotted against time is a sine curve, with amplitude  $\gamma_A$ . The counter force in the lower plate is also measured and this is called the shear stress ( $\tau$ ). When the angle  $\theta$  is small, i.e. there is only small deformation to the hydrogel, shear stress is also a sine curve when plotted against time, with amplitude  $\tau_A$ . In a hydrogel, which is a viscoelastic material there is a delay between the movement of the upper plate, the shear strain sine wave, and the response from the lower plate, the shear stress sine wave, putting them out of phase (Figure 52). The phase shift is called  $\delta$  and is  $0^\circ$  for an ideally elastic material and  $90^\circ$  for an ideally viscous flowing material and between these two extremes for a viscoelastic material such as a hydrogel. The complex shear modulus  $G^*$  is the difference between the amplitude of the shear stress  $\tau_A$  and the amplitude of the shear strain  $\gamma_A$  sine curves (Equation 12) and describes the entire viscoelastic behaviour of the material.

Equation 12: 
$$\text{Complex modulus } G^* = \frac{\tau_A}{\gamma_A}$$

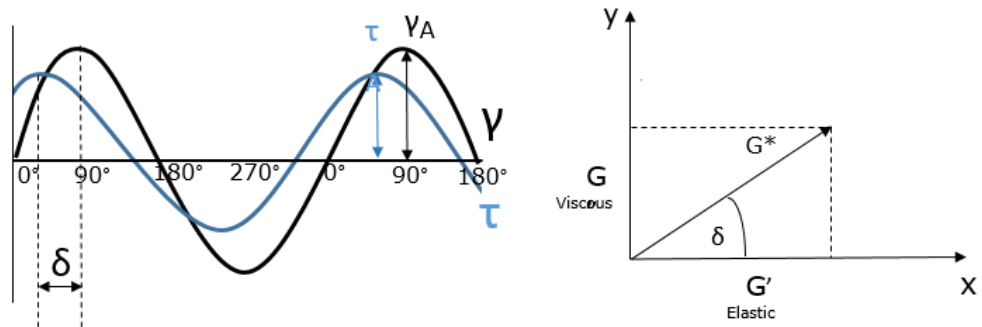


Figure 52: (Left) For a viscoelastic material, the sine waves of shear strain  $\gamma$  (black) and shear stress  $\tau$  (blue), show a phase shift of the angle  $\delta$  due to the time lag between the applied strain and measured stress response. (Right) A vector diagram of  $G^*$  complex modulus of viscoelastic response.

By plotting  $G^*$  as a vector and then placing the phase angle shift  $\delta$  below it, this signifies the position of the x axis and then the y axis is drawn perpendicularly up from the x axis (Figure 52). The portion of the  $G^*$  complex modulus vector is projected along the x axis is termed the storage modulus  $G'$  (Pa) and represents the elastic portion of the modulus response. The portion of  $G^*$  vector that is projected onto the y axis is the loss modulus  $G''$  (Pa) which is the viscous portion of the viscoelastic response.  $G'$  is the energy stored within the hydrogel system. The deformation induced by shear stress stretches and elongates the internal polymer structure of the hydrogel creating elastic potential energy and when the stress is removed this energy is used to bring the polymer chains back into their original shape.  $G''$  measures the viscous component, i.e. the liquid in the system. It is a measure of the friction caused within the hydrogel during deformation. Friction creates heat and this heat energy dissipates throughout the system and is lost. Hydrogels are characterised in rheology by  $G' > G''$  which is due to the crosslinks that prevent the hydrogel structure from dissolving which means there is a greater contribution to  $G^*$  from the elastic component than the viscous component.

Typically small amplitude oscillatory shear (SOAS)<sup>139</sup> rheology is used for hydrogels and the storage and loss modulus are investigated within the linear viscoelastic (LVE) region. Within this region the deformation is not permanent to the system and it can recover within the time scale of the next measurement. The moduli in the LVE region are independent of the amplitude of deformation. The most common rheological experiments to characterise hydrogel behaviour are time sweeps, frequency sweeps and strain sweeps<sup>139</sup>. Time sweeps analyse the stability of the hydrogel over time at constant strain and frequency. They can be used to analyse the equilibrium modulus and monitor the solution to hydrogel (sol-gel) transition as the elastic behaviour increases and then dominates leading to  $G' > G''$ . Strain sweeps are performed at a

constant frequency but throughout a range of strain (amplitude of oscillation). By monitoring  $G'$  and  $G''$ , the yield point and flow point can be determined by the end of the LVE region<sup>196</sup>. These provide information about the limits of the crosslinking, at what strain the crosslinks will begin to break and at what strain the hydrogel will show more viscous behaviour and flow. Frequency sweeps are performed at constant strain but over a range of frequencies (speed of oscillation) and provide information about the frequency dependence of the moduli. At low frequencies this simulates slow motion on long time scales or the material at rest, whereas high frequencies simulate fast motion on short time scales.

Rheology was used to assess the change in material properties of silk fibroin hydrogels which had tyrosine residues crosslinked by the enzyme horse radish peroxidase (HRP). By increasing the fibroin molecular weight and concentration, the storage modulus also increased indicating increased elasticity. It was found that the hydrogels were all frequency independent and able to withstand strains of up to 100 % before plastic (permanent) deformation<sup>110</sup>. This resistance to plastic deformation at high strain is unusual in physically crosslinked hydrogels and is likely a result of the enzymatic crosslinking. Physically crosslinked hydrogels made of agarose, collagen, fibrin, Matrigel™ or methylcellulose were resistant to deformation up to 10-15 % strain<sup>139</sup>. Outside the LVE at higher strains, the loss modulus rapidly increased to the flow point and the storage modulus decreased as the network was fractured and deformed. The resistance to strain deformation was improved in a free radical polymerised poly(*N*-isopropylacrylamide) (NIPAAm) based hydrogel by the addition of lignin<sup>196</sup> which also increased the range of the LVE region by 10-fold to 100 % strain. Addition of lignin also improved the storage modulus with respect to increasing frequency by 4-fold to 4 kPa indicating increased robustness of the crosslinked network.

## **6.2. Materials and Methods**

### **6.2.1. Compression testing**

Compression testing of NT2RepCT hydrogels was performed on a TA.HDplus Texture Analyser (Stable Micro Systems) with a 32 mm diameter compression upper platen and a stationary lower platen. Hydrogels were cast in 1 mL flat plunger syringes with removed discharge orifice. The casting setup was sealed with parafilm. Non-crosslinked, transparent hydrogels MQ 37 T and CAPS10 and GA crosslinked, opaque hydrogels MQ 37 O 1GA, t10 37 O 1GA and t10 40 O 1GA were swollen at 20 °C in PBS pH 7.2 for 24 hours before measurement. The opaque and non-crosslinked hydrogels MQ 37 O, t10 37 O and t10 40 O were measured non-swollen. The hydrogel cylinders were sliced into 1.5-2 mm slices with a scalpel and the height and diameter of each were measured before analysis with a caliper. Unconfined compression testing was performed at 20 °C. The pre-test speed was 1 mm/s and the test speed was 0.5 mm/s. The trigger force was set to 0.049 N and strain was 30 %. Analysis was performed in replicates of 5-8. The Young's modulus for each type of hydrogel was calculated from the gradient of the initial linear portion (5-10 % strain) of each sample's stress-strain profile using linear regression in Graphpad Prism 7.04.

### **6.2.2. Rheology**

Rheological assessment was performed on an Anton Parr MCR 301 Rheometer with 8mm plate-plate geometry and a gap height of 0.5 or 1 mm. A Peltier hood attachment was used to prevent sample evaporation and maintain temperature of 37 °C. Strain sweeps were performed at 1 – 100 % strain at a constant shear rate of 1 1/s. Frequency sweeps were performed at 0.01-100 1/s with a constant strain of 5 %. Lyophilised NT2RepCT was reconstituted to 2.4 % (w/v) in either MQ water (MQ 37 T) or 20 mM CAPS pH 10 (CAPS10), termed the pre-gel solution. Hydrogels were cast in moulds as previously described. Once formed, the hydrogels (MQ 37 T and CAPS10) were gently

ejected into 3 mL of PBS and swollen for 24 hours at 20 °C. Strain sweeps and frequency sweeps were performed on PBS swollen hydrogels. Time sweeps were performed at constant strain of 5 % and constant frequency of 1 Hz on both swollen and non-swollen NT2RepCT hydrogels. One hydrogel sample was used for each measurement. Each hydrogel sample was carefully trimmed to size (12 mm to 8 mm diameter) with a plastic spatula after the chosen gap height was reached. A sample size of 3 was used for each experimental group. Results shown are averages ( $n=3$ )  $\pm$  SD.

## **6.3. Results**

### **6.3.1. Young's modulus**

The non-crosslinked opaque hydrogels MQ 37 O, t10 37 O and t10 30 O were compressed non-swollen. The Young's modulus significantly increased with increasing pH and temperature of gelation. MQ 37 O Young's modulus was  $298 \pm 83$  Pa whereas the hydrogel t10 37 O Young's modulus was  $1297 \pm 266$  Pa, an increase of 335 %. The hydrogel t10 40 O Young's modulus was  $1896 \pm 267$  Pa an increase of 46 % compared to t10 37 O (Figure 53). Unfortunately, the opaque, non-crosslinked hydrogels could not be analysed swollen in PBS because they were too soft to cut with the scalpel and did not retain a circular shape or flat surface.

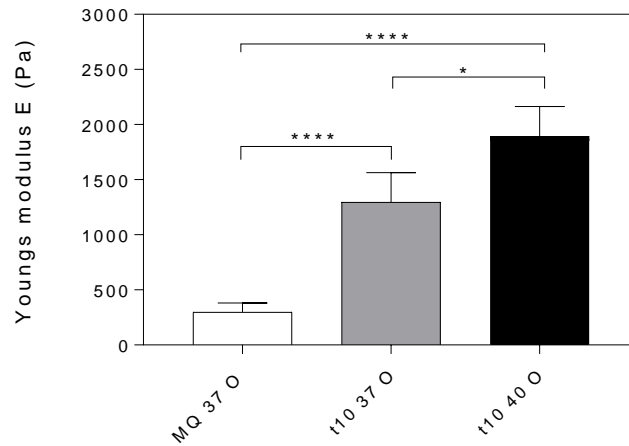


Figure 53: Young's modulus of opaque non-swollen, non-crosslinked 2.4 % (w/v) NT2RepCT hydrogels MQ 37 O, t10 37 O and t1040 O. Measured at 20 °C. (n=5)  $\pm$  SD (Unpaired students t-test \*P<0.01,\*\*P<0.005,\*\*\*\*P<0.0001)

Interestingly, the differences in Young's modulus in the 1 % (v/v) GA crosslinked opaque hydrogels was not as significant as in the non-crosslinked. The calculated Young's modulus (E) for opaque, 1 % (v/v) GA crosslinked hydrogels MG 37 O 1GA and t10 37 O 1GA were similar at  $235.6 \pm 80$  Pa and  $256.8 \pm 59$  Pa respectively (Figure 54). The Young's modulus of t10 40 O 1GA was significantly increased by 77 % to  $454.7 \pm 110$  Pa compared to t10 37 O 1GA. Opaque, swollen, 1 % (v/v) GA crosslinked hydrogels were measured to have a higher Young's modulus than the non-crosslinked, swollen, transparent hydrogels MQ 37 T and CAPS10 (Figure 55). CAPS10 was significantly stiffer than MQ 37 T with a Young's modulus of  $211 \pm 76$  Pa and  $105 \pm 53$  Pa respectively.

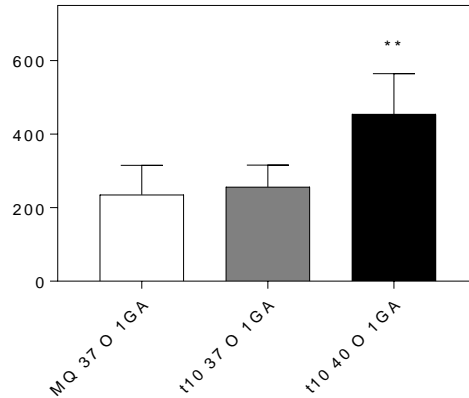


Figure 54: Young's modulus of opaque 1 % (v/v) GA crosslinked 2.4 % (w/v) NT2RepCT hydrogels swollen in PBS for 24 hours. Measured at 20 °C. (n=5) ± SD (\*\*P<0.005) (P = 0.0049)

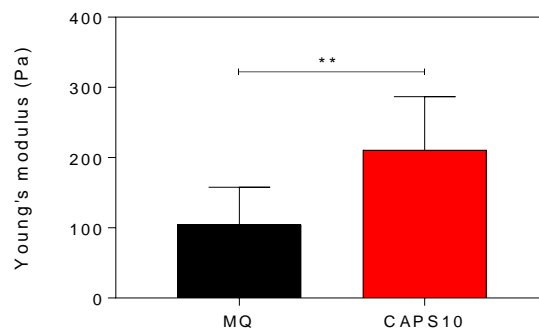


Figure 55: Young's modulus of transparent 2.4 % (w/v) NT2RepCT hydrogels formed with either MQ or 20 mM CAPS pH 10. Hydrogels swollen in PBS for 24 hours. Measured at 20 °C. (n=8) ± SD. (\*\*P<0.005)

### 6.3.2. Strain sweeps and frequency sweeps of MQ 37 T and CAPS10 hydrogels

Strain tests were performed between 1-100 % strain with a constant frequency of 1 Hz to determine the storage ( $G'$ ) and loss ( $G''$ ) modulus in the LVE region and the LVE limit of MQ 37 T and CAPS10 PBS swollen hydrogels. A comparison of 2 different gap heights, 0.5 and 1 mm was performed (Figure 56). The LVE in the strain sweeps for MQ 37 T and CAPS10 at 0.5 mm and 1 mm are both in the same range (1-~10 % strain).

However, the storage modulus  $G'$  of CAPS10 was 136 % greater than  $G'$  of MQ 37 T at 0.5 mm and 1 mm gap height. The loss modulus  $G''$  was 183 % greater in CAPS10 than in MQ 37 T at 0.5 mm. Though, this increase in loss modulus  $G'$  between CAPS10 and MQ 37 T was less pronounced at 1 mm gap height at only 123 % (Table 11).

The flow point where  $G' < G''$ , at which the system has more of a liquid component than a viscous component was greater for MQ 37 T hydrogels than CAPS10. At 0.5 mm gap height CAPS10 flow point was 21.4 % less than MQ 37 T but at 1 mm gap height this percentage difference was decreased to 11.1 %.

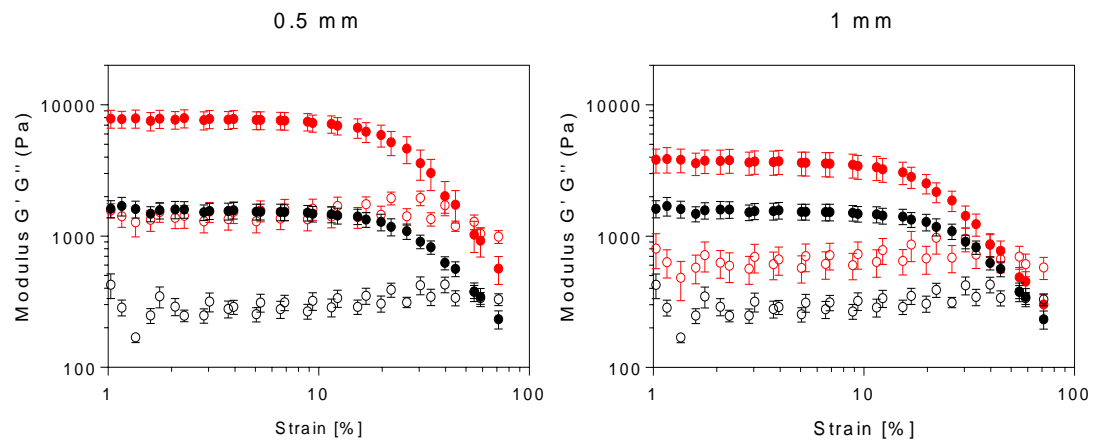


Figure 56: Strain sweep of MQ 37 T and CAPS10 hydrogels at 0.5 mm gap height and 1 mm gap height. Hydrogels swollen in PBS pH 7 for 24 hours before measurement. Measured at 37 °C. Frequency = 1 Hz, strain 0.1-100 %. Closed symbols ( $G'$ ), open symbols ( $G''$ ) Black = MQ 37 T, Red = CAPS10 (n=3)  $\pm$  SD

Table 11: Strain LVE storage ( $G'$ ) and loss ( $G''$ ) modulus (Pa) and strain failure point (% strain) of swollen MQ 37 T and CAPS10 hydrogels at 0.5 and 1 mm gap height. (n=3) average  $\pm$  SD.

	<b>MQ 37 T</b>	<b>CAPS10</b>	<b>% difference (increase/decrease)</b>
<b><math>G'</math> 0.5 mm (Pa)</b>	3259 $\pm$ 60	7699 $\pm$ 169	+ 136 %
<b><math>G''</math> 0.5 mm (Pa)</b>	507 $\pm$ 61	1439 $\pm$ 119	+ 183 %
<b><math>G' &lt; G''</math> flow point (% strain)</b>	70	55	- 21.4 %
<b><math>G'</math> 1 mm (Pa)</b>	1560 $\pm$ 55	3677 $\pm$ 124	+ 136 %
<b><math>G''</math> 1 mm (Pa)</b>	288 $\pm$ 54	643 $\pm$ 79	+ 123 %
<b><math>G' &lt; G''</math> flow point (% strain)</b>	45	40	- 11.1 %

After the LVE region of strain was determined, frequency sweeps were performed between 0.1-100 Hz to determine the LVE region of frequency and the frequency dependence of the storage and loss modulus. A constant strain of 5 % was used as this was within the LVE for both MQ 37 T and CAPS10 as determined by the strain sweeps. Again, a comparison of 2 different gap heights was performed, 0.5 and 1 mm.

At both gap heights analysed, MQ 37 T and CAPS10 showed the same moduli dependence to increasing frequency (Figure 57) but that moduli was of greater magnitude at 0.5 mm as was the case in the strain sweeps. At low frequencies the loss modulus  $G''$  for both MQ 37 T and CAPS10 was very low and increased as the frequency increased until 0.2 Hz where  $G''$  is approaching  $G'$  before decreasing again and stabilising at 1 Hz. This was the case for both 0.5 and 1 mm gap height. The storage modulus  $G'$  slowly increased with increasing frequency up to 30 Hz at 0.5 mm gap

height for both MQ 37 T and CAPS10 and up to 25.7 Hz at 1 mm. At these frequencies the viscoelastic behaviour was lost as the loss modulus  $G''$  equalled the storage modulus  $G'$  and as the frequency increased to 100 Hz,  $G'$  rapidly increased and  $G''$  rapidly fell as the hydrogel became elastic.

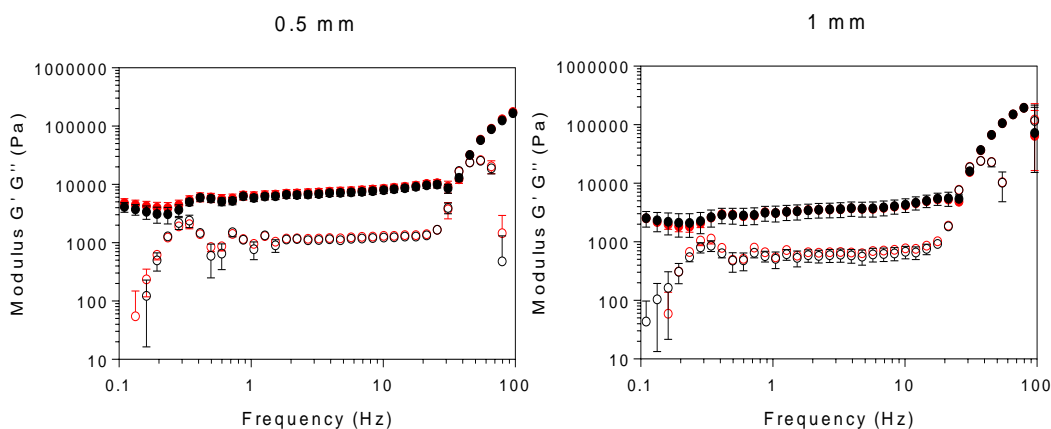


Figure 57: Frequency sweep of MQ 37 T and CAPS10 hydrogels at 0.5 mm (Left) and 1mm (Right) gap height. Hydrogels swollen in PBS pH 7 for 24 hours before measurement. Measured at 37 °C. Frequency = 0.1-100 Hz, strain 5 %. Closed symbols ( $G'$ ), open symbols ( $G''$ ) Black = MQ 37 T, Red = CAPS10 (n=3)  $\pm$  SD

### 6.3.3. Assessing viscoelasticity of 1-2.5 % (w/v) NT2RepCT in MQ water and at pH 10

To determine the concentration at which hydrogel behaviour could be measured, i.e.  $G' > G''$ . Lyophilised NT2RepCT was reconstituted in either MQ water or 20 mM CAPS pH 10 at 1, 1.5, 2 and 2.5 % (w/v). The gelation time was 18 hours at 37 °C. Time sweeps at constant strain of 5 % and constant frequency of 1 Hz for 60 seconds were performed on each hydrogel type. The strain and frequency used reflect the LVE region for MQ 37 T and CAPS10 hydrogels. Additionally, a qualitative assessment of the physical appearance of the different concentrations examined was performed (Table 12).

Table 12: Physical appearance of 1-2.5 % (w/v) NT2RepCT in MQ water or 20 mM CAPS pH 10 after 18 hours incubation at 37 °C

<b>% (w/v) NT2RepCT</b>	<b>MQ water</b>	<b>20 mM CAPS pH 10</b>
1	Very soft hydrogel	Slightly viscous liquid
1.5	Hydrogel	Viscous liquid
2	Hydrogel	Soft hydrogel
2.5	Hydrogel	hydrogel

All concentrations tested in MQ water formed a hydrogel with the visual rigidity increasing as the concentration increased. However, for those formed in 20 mM CAPS pH 10, a hydrogel was only formed at 2 and 2.5 % (w/v) NT2RepCT with viscous liquids formed at 1 and 1.5 % (w/v) NT2RepCT. The results of the time sweeps reflected this as typical hydrogel behaviour ( $G' > G''$ ) was observed for all concentrations of NT2RepCT in MQ water but only for 2 and 2.5 % (w/v) for 20 mM CAPS pH 10 (Figure 58). At all concentrations tested, the initial rheological measurements (0-10 s) were not stable but began to stabilize after this time point, albeit with sinusoidal variation of  $G'$  and  $G''$  which was more pronounced at the lower concentrations tested. In all samples, the moduli of MQ water hydrogels was greater than the moduli for those formed in 20 mM CAPS pH 10.

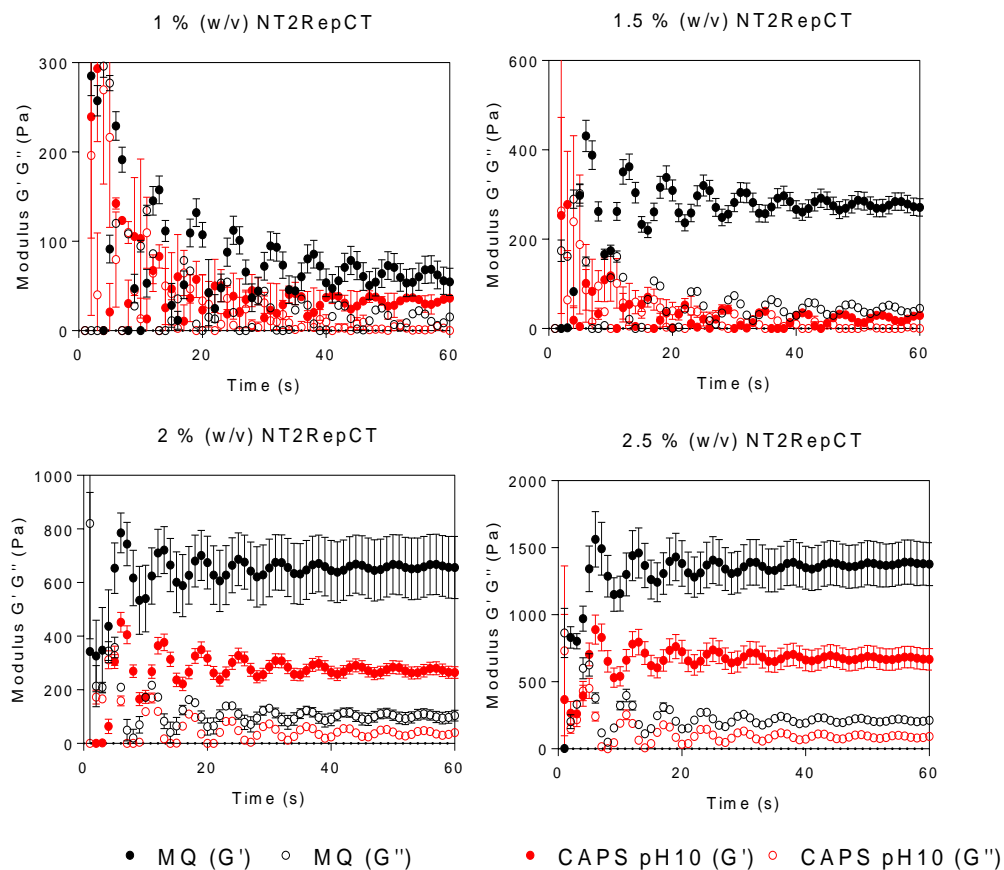


Figure 58: Time sweeps of 1-2.5 % (w/v) NT2RepCT after incubation in either MQ water (MQ) or 20 mM CAPS pH 10 (CAPS pH 10) for 18 hours at 37 °C. Closed symbols = Storage modulus G', Open symbols = Loss modulus G''. Black = MQ water, Red = 20 mM CAPS pH 10. Constant strain of 5 % and frequency of 1 Hz, gap height 1 mm, measured at 37 °C (n=3) ± SD

### 6.3.4. Time sweep of MQ 37 T and CAPS10

A time sweep of MQ 37 T and CAPS10 hydrogels that had been swollen in PBS was performed at constant 5 % strain and constant frequency of 1 Hz as determined by the LVE region in the strain and frequency sweeps (Figure 59). As expected, for both swollen hydrogels, the storage modulus G' was greater than the loss modulus G'', indicating presence of a hydrogel. However, the moduli took 5 s to stabilize and the initial readings had large errors, particularly MQ 37 T although there was no sinusoidal behaviour. The moduli of MQ 37 T were of greater magnitude than CAPS10.

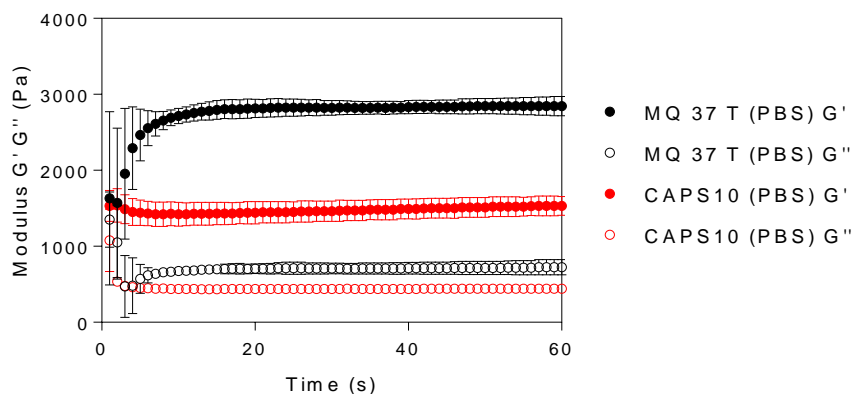


Figure 59: Time sweep of MQ 37 T and CAPS10 hydrogel that had been swollen in PBS for 24 hours. Closed symbols = Storage modulus  $G'$ , Open symbols = Loss modulus  $G''$ . Black = MQ water, Red = CAPS pH 10. Constant strain of 5 % and frequency of 1 Hz, gap height 1 mm, measured at 37 °C (n=3)  $\pm$  SD

## 6.4. Discussion

### 6.4.1. Overview

The aim of this chapter was to assess the material properties of NT2RepCT hydrogels, particularly their resistance to deformation. Compression testing was used to investigate the effects of pH and temperature of gelation and it was found that hydrogels formed at pH 10 were significantly stiffer than those formed in MQ water. Rheology was utilized to probe the viscoelastic behaviour of MQ 37 T and CAPS10 hydrogels and evaluate minimum NT2RepCT concentration to show viscoelastic hydrogel behaviour. Interestingly MQ 37 T hydrogels were found to have superior storage and loss modulus at constant strain and frequency but CAPS10 hydrogel behaved more elastically with variable strain.

### 6.4.2. Alkaline pH of gelation increases hydrogel stiffness

Assessing the Young's modulus of hydrogels is an important test to carry out when the intended purpose of the hydrogels is implantation into a body tissue or for culturing cells. The non-crosslinked, opaque hydrogels MQ 37 O, t10 37 O and t10 40 O were

only able to be analysed non-swollen and therefore cannot be directly compared to the swollen 1 % (v/v) GA crosslinked opaque hydrogels or the transparent hydrogels MQ 37 T or CAPS10. After swelling in PBS 7.2 the non-crosslinked opaque hydrogels were extremely soft and difficult to manipulate. Attempts to cut the swollen hydrogel cylinder with a scalpel and transfer to the measuring plate of the compression testing instrument resulted in crushed, non-uniform shapes which were not suitable for this type of analysis. Use of atomic force microscopy to measure the Young's modulus would be more suited to these samples and is an investigation that should be performed in the future. The non-swollen opaque, non-crosslinked hydrogels Young's modulus could be increased significantly by changing the gelation buffer from MQ water to 20 mM tris pH 10. The Young's modulus and resistance to deformation could be further increased by increasing the gelation conditions from 37 °C to 40 °C (Figure 53). In the literature often the authors do not specify whether the Young's modulus is determined in swollen or non-swollen hydrogels. Since swelling increases the pore and mesh sizes and depending on the swelling buffer, can increase charge repulsion in the hydrogel networks, this will clearly affect the material properties.

The measured Young's modulus for the swollen opaque and GA crosslinked hydrogels MQ 37 O 1GA, t10 37 O 1GA and t10 40 O 1GA were in the range of 200-500 Pa. Interestingly, it was only t10 40 O 1GA that was significantly stiffer and more resistant to deformation (Figure 54). MQ 37 O 1GA and t10 37 O 1GA had very similar Young's modulus despite visually appearing to have different stiffness and having significantly different swelling ratios when swollen in MQ water.

In the transparent hydrogels, increasing the pH of gelation increased the measured Young's modulus with CAPS10 having a greater E than MQ 37 T. At pH 10, NT2RepCT is primarily alpha helical and undergoes little secondary structure conformational change with increasing temperature as analysed by CD as seen in Chapter 4. The

differences in Young's modulus can also be explained by considering the lower swelling ratio of CAPS10 compared to MQ 37 T in PBS (Figure 37). Furthermore, CAPS10 hydrogels appear less porous than MQ 37 T hydrogels as imaged by SEM and eSEM (Figure 43 and Figure 45) which could contribute to the greater resistance to compression deformation. All the swollen hydrogels examined by unconfined compression testing were in the stiffness range of brain tissue<sup>187</sup> and similar to Matrigel™<sup>194</sup>. Compared to published silk hydrogels, the NT2RepCT hydrogels had Young's modulus in the same range as low concentration eADF4(C16) hydrogels<sup>140</sup> and hydrogels based on the CT of *N. clavipes*<sup>130</sup>. However, compared to silk fibroin hydrogels which have a high  $\beta$  sheet content they were softer<sup>126</sup>.

Due to the need for GA crosslinking, which is toxic and difficult to remove, the 1 % (v/v) GA opaque hydrogels were not taken forward for further materials testing or into assessment of drug delivery capabilities in the following chapter.

### **6.4.3. Gap height alters hydrogel behaviour in rheology**

Rheological analysis of the swollen transparent hydrogels MQ 37 T and CAPS10 was performed to probe the material properties. Strain sweeps and frequency sweeps were performed to determine the linear viscoelastic region (LVE) limit. Ideally, a pre-gel solution is used so that the hydrogel is formed between the plates, therefore the hydrogel architecture is not compressed and put under stress before rheological analysis. Pre-formed hydrogels can be analysed by rheology, but care must be taken to not overly compress and therefore disrupt and potentially destroy crosslinks, pores and other delicate components. Unfortunately, due to a combination of long gelation times and presence of a hex-histidine purification tag which temporarily damaged the copper alloy of the rheometers measuring geometry leaving black residue during long holds at 37 °C, this was not possible for NT2RepCT hydrogels. This also meant that gelation kinetics of NT2RepCT hydrogels could not be performed by monitoring the

growth of  $G'$  from pre-gel solution. A TEV protease cleavage site was introduced between the hex-histidine tag and NT2RepCT and expressed in high yield but due to time constraints, no hydrogels were formed from the cleaved, hex-histidine tag free NT2RepCT. Please see Appendix for expression of TEVNT2RepCT.

An 8 mm diameter flat geometry was chosen due to limited volumes of sample available and the diameter of the hydrogel casting syringes which were 12 mm. Larger sample geometries and smaller gap heights are known to give more accurate results due to increased magnitude of the torque created in measurements. This increased torque increases the rheometers ability to resolve the phase angle between the stress and strain waves<sup>139</sup>. Two different gap heights were investigated to analyse the difference in moduli response.

In all experiments on formed hydrogels, as expected  $G'$  was larger than  $G''$  within the LVE limit signifying the presence of a hydrogel. In strain sweep experiments an arbitrary frequency of 1 Hz was chosen which was later determined to be within the LVE region in the frequency sweep for both MQ 37 T and CAPS10 hydrogels. In the strain sweep, both MQ 37 T and CAPS10 showed linear behaviour with constant moduli as strain was increased between 1 and 10 % strain at both gap heights investigated. At both 0.5 mm and 1 mm (Figure 56) gap height strain sweep experiments, CAPS10 was determined to have a larger  $G'$  and  $G''$  than MQ 37 T. Additionally, the ratio between  $G'$  and  $G''$  was greater in CAPS10 than MQ 37 T indicating more elastic character. However, this ratio difference decreased at 1 mm gap height. In addition to increasing the magnitude of the moduli, the yield point, increased with a smaller gap height. At 0.5 mm the hydrogels showed greater resistance to deformation compared to 1 mm. This could be due to increased contact between the hydrogel sample and the analysis geometry, leading to reduced sample slippage which can affect the results<sup>197</sup>. However, since the hydrogel was already

deformed at 0.5 mm the internal structure could be more resistant to deformation due to increased elastic behaviour due to compression<sup>139</sup> pushing water out of the pores.

Despite CAPS10 moduli being greater than MQ 37 T, the flow point ( $G' = G''$ ) at both gap heights was at a higher strain for MQ 37 T than CAPS10. This suggests that while CAPS10 had more elastic character and resistance to deformation the crosslinks were more brittle. However, at 1 mm gap height, the difference in flow point was less pronounced between the two hydrogels. The greater storage modulus  $G'$  of CAPS10 can be explained by considering the differences in pore morphology as seen in eSEM (Figure 45) between CAPS10 and MQ 37 T. The walls between the pores were thicker in CAPS10 which could contribute to the greater resistance to deformation.

Next, frequency sweeps were performed at 5 % strain which was determined to be within the LVE limit in the performed strain sweeps. Decreasing the gap height had less of an impact on the magnitude of the measured moduli than in the strain sweep experiments. At both gap heights tested, MQ 37 T and CAPS10 hydrogels displayed the same frequency dependent behaviour of the moduli. The storage modulus  $G'$  plateaued between 0.1 and 25-30 Hz, depending on the gap height, whereas the loss modulus  $G''$  was only stable between 1 Hz and the glass transition frequency. At low frequencies the loss modulus had large errors due to low torque being generated and the measurements being below the phase angle separate on detection limit of the rheometer<sup>139</sup>.

#### **6.4.4. Hydrogels form at lower concentrations of NT2RepCT in MQ water than at pH 10**

A further investigation into the lowest concentration to form a self-supporting hydrogel was undertaken by performing time sweeps. NT2RepCT in either MQ water or 20 mM CAPS pH 10 at 1, 2.5, 2 and 2.5 % were incubated for 18 hours at 37 °C.

Previously in Chapter 4 the lowest concentration that passed the inversion test was 2.4 % (w/v) in MQ water after incubation for 16 hours at 37 °C in glass tubes. Inversion tests are qualitative and results can vary depending on the tubes dimensions<sup>138</sup>. This could explain the difference seen when the hydrogels were cast in plastic syringe moulds with larger diameters.

Every MQ water NT2RepCT concentration formed self-supporting hydrogels by visual inspection with the edges of the hydrogel appearing sharper with increasing concentration. On the other hand, in 20 mM CAPS pH 10 only at 2 and 2.5 % (w/v) formed self-supporting hydrogels. Viscous liquids were formed at 1.5 % (w/v) and 1 % (w/v). At 2.4 % (w/v) hydrogels formed in 20 mM CAPS pH 10 had slower gelation kinetics than those formed in MQ water, taking 6.5 hours to pass inversion test whereas MQ water hydrogels took 2 hours. Therefore, the presence of CAPS and a more alkaline pH 10 slows hydrogel formation. It is possible that 1 and 1.5 % (w/v) NT2RepCT in 20 mM CAPS pH 10 would form a hydrogel but on a longer time scale than 18 hours. This needs to be investigated.

The time sweeps for all incubated NT2RepCT in both buffers at the concentrations were unstable until 10-20 seconds into the time sweep with the time to stability decreasing as the concentration increased. MQ water hydrogels from 1.5-2.5 % (w/v) NT2RepCT all showed viscoelastic behaviour as  $G'$  was 3-fold greater than  $G''$ . The 20 mM CAPS pH 10 hydrogels showed viscoelastic behaviour at 2 and 2.5 % (w/v) but  $G'$  was only 1.5 to 2-fold greater than  $G''$ . In all samples the magnitude of  $G'$  increased with increasing concentration of NT2RepCT as the resistance to deformation and elastic character increased with increasing crosslinking. Additionally, the hydrogels formed in MQ water showed greater  $G'$  and  $G''$  than those formed in 20 mM CAPS pH 10 at all concentrations of NT2RepCT. This increase in  $G'$  is common with increasing protein concentration<sup>140,110,198,129</sup>

Sinusoidal  $G'$  and  $G''$  were seen for all samples suggesting that the strain and frequency selected should be altered in future analysis as these were suitable for PBS swollen MQ 37 T and CAPS10, which also could explain the low  $G'$  seen. The initial readings non-linearity and then more linear behaviour suggest that application of the shear strain and frequency was causing rearrangement of the hydrogel architecture, creating a more viscoelastic response which was seen less as the concentration increased.

#### **6.4.5. Swelling in PBS increases the moduli of MQ 37 T and CAPS10**

A comparison time sweep of PBS swollen MQ 37 T and CAPS10 hydrogels was performed at constant 5 % strain and constant frequency of 1 Hz. There was no observed sinusoidal behaviour of the moduli over time as seen in the unswollen 1-2.5 % (w/v) NT2RepCT hydrogels.

Interestingly, despite MQ 37 T and CAPS10 hydrogels being formed at 2.4 % (w/v) and being swollen in PBS, the storage and loss modulus were 2-fold greater than those measured in the non-swollen 2.5 % (w/v) hydrogels formed in MQ water and 20 mM CAPS pH 10. The increase in the storage modulus  $G'$  could be explained by increased contact of the rheometer geometry with the swollen sample and reduced friction due to a greater volume of water, or from increased charge interactions between chains due to ionization with components of PBS. At the pH of formation, hydrogels formed in MQ water contain NT2RepCT that is unfolding to  $\beta$  sheets and at pH 10 NT2RepCT is still primarily  $\alpha$  helical with slight unfolding with increasing temperature. Introduction of excess PBS pH 7.2 in swelling would increase the pH of the MQ water hydrogels and decrease the pH of the 20 mM CAPS pH 10 hydrogels. It is not known what happens to NT2RepCT with changing pH and this is something that should be investigated in the future. Potentially this change in pH affects NT2RepCT secondary

structure. The increase in the loss modulus  $G''$  is expected since MQ 37 T and CAPS10 were swollen and contained more water to dissipate energy than the unswollen hydrogels.

Addition of monovalent and bivalent cations included in gelation increased the material properties of eADF4(C16) hydrogels<sup>142</sup>. The authors suggested that increased physical crosslinking induced by these cations was responsible. NT2RepCT does not form hydrogels in the presence of salts as the protein precipitates. However, once the hydrogel is formed and PBS is added. This improves the moduli suggesting a positive interaction is occurring increasing the elasticity and resistance to deformation. More work is required to understand this phenomenon.

## **6.5. Summary of Young's modulus and rheology**

Examining the material properties of hydrogels is important to understand how the material will perform and how its resistance to deformation can be controlled.

The opaque hydrogels MQ 37 O, t10 37 O and t10 40 O showed an increase in Young's modulus with increasing pH and temperature illustrating how hydrogel material properties can be tuned. Upon crosslinking with 1 % (v/v) GA the stark differences in Young's modulus were reduced possibly due to increased homogeneity between the hydrogels. However, the hydrogel formed at 40 °C at alkaline pH, t10 40 O 1GA was still the stiffest compared to t10 37 O 1GA and MQ 37 O 1GA.

The same trend was seen in the transparent hydrogels MQ 37 T and CAPS10 with CAPS10 having a significantly increased Young's modulus. This gives further evidence that hydrogels formed closer to pH 10 have superior properties.

Rheology is an important technique in the field of hydrogels since they are viscoelastic materials. As evidenced here, experimental set up is critical to gaining accurate readings. The magnitude of the moduli could be increased with a smaller gap

height due to increased strain in the hydrogel system. It is therefore important to ensure experimental set up is suitable for the systems being investigated.

CAPS10 hydrogel showed a greater moduli response with increasing strain compared to MQ 37 T although the flow point was greater in MQ 37 T hydrogels. Both MQ 37 T and CAPS10 showed the same frequency dependence of the moduli suggesting that despite the differences in behaviour, they have a similar crosslinking architecture due to being formed of the same protein at the same concentration.

It was also found that NT2RepCT would form hydrogels at lower concentrations in MQ water than in 20 mM CAPS pH 10. The minimum concentration to form a hydrogel as assessed by rheological time sweeps where  $G' > G''$  was 2 % (w/v) in 20 mM CAPS pH 10 but 1 % (w/v) in MQ water. This difference could be attributed to the different protein secondary structure shift and charge state of NT2RepCT in these two buffers.

The opaque and GA crosslinked hydrogels were not carried forward for further materials testing or as drug delivery systems due to the toxicity of GA. However, GA crosslinking was utilised to stabilize the extruded hydrogel architecture in high vacuum SEM as it was in Chapter 5.

The next chapter, chapter 7 discusses MQ 37 T and CAPS10 hydrogels as a drug delivery system and an assessment of their shear-thinning behaviour is reported.

# 7. Drug Delivery

## 7.1. Introduction

This chapter investigates the application of the NT2RepCT MQ 37 T and CAPS10 hydrogels as a controlled drug delivery system. Their shear-thinning properties and injectability is examined and the release of two model drug surrogates, Rhodamine B (RhB) and fluorescein (FAM) is assessed. Conjugation of FAM to NT2RepCT was explored as a model to improve and prolong drug release from the hydrogel.

### 7.1.1. Local drug delivery systems (DDS)

Compared to conventional, systemic drug delivery such as intravenous (IV) injection and oral routes, local drug delivery systems (DDS) reduce the risk of side effects and systemic toxicity as the drug is delivered directly to the site of action. This means a lower concentration can be administered to achieve a therapeutic effect as there is minimal distribution throughout the body, contrast to the distribution of IV and oral drug administration<sup>199</sup>. Additionally, conventional routes often require repeated doses, and this can lead to reduced patient compliance.

Hydrogels are an emerging class of local drug delivery systems<sup>200</sup> due to their tuneable characteristics, hydrophilicity and swelling ability. This allows encapsulation and delivery of hydrophilic drugs, cells and other bioactive components and therapeutic agents into the body. Furthermore, hydrogel material properties can mimic ECM making them suitable for implantation. Other types of DDS include films<sup>88</sup>, particles<sup>201 202</sup>, nano-particles<sup>203</sup>, foams<sup>204</sup> and fibres<sup>205</sup>.

### 7.1.2. Hydrogel DDS applications and targets

Hydrogel DDS are suitable for many different applications and targets, from arthritis<sup>206</sup>, cancer therapy<sup>207</sup>, growth factor delivery<sup>208</sup>, wound care<sup>209</sup>, infectious disease treatment<sup>210</sup> to ophthalmic care<sup>211</sup>. It is important that the material used for the hydrogel is non-immunogenic, biocompatible to the specific tissue, has favorable

mechanical properties and is biodegradable, so that surgery is not required to remove the hydrogel DDS. The biodegradation rates should be in line with new tissue growth. There are many published journal articles on recombinant protein hydrogel DDS, however very little progress on commercialization of these materials has occurred due to high cost of production<sup>212</sup>. Most on-market hydrogel DDS are made from either synthetic and biocompatible polymers such as polyethylene-glycol (PEG) or polyvinyl alcohol (PVA), polysaccharides (alginate, cellulose or hyaluronic acid) or from *ex vivo* collagen and gelatin<sup>213</sup>. The materials often used have decades of research behind them and have been extensively tested for safety and are FDA approved which can be a barrier for new biomaterials<sup>1</sup>. However, there is need for innovative hydrogel DDS made of new biomaterials such as spider silk which is non-immunogenic, biodegradable and a diverse material that can be functionalised.

### **7.1.3. Controlled release**

Drug delivery systems such as hydrogels often have multiphasic release of the drug. Upon placement into the body or diffusion buffer there is an initial fast rate of release termed 'burst release' where a significant percentage of loaded drug moves out of the hydrogel, followed by a slower rate of release as the system stabilizes. Burst release can have negative consequences as an initial higher dose of the drug is released, potentially leading to side effects as the local systemic toxicity threshold is reached. Additionally, burst release reduces the effective lifetime of the controlled delivery device and can require more frequent administrations. Burst release is also disadvantageous if the drug to be delivered has a short-half-life *In vivo* and rapid clearance from the body, leading to wasted drug and a higher cost<sup>214</sup>. However, burst release can be beneficial depending on the application and drug used. Rapid pain relief and wound treatment can benefit from initial burst release to quickly reduce pain, followed by a slower release to maintain and support gradual healing of the wound<sup>214</sup>.

In cases where rapid release of the drug would have negative consequences, a slower and more sustained release profile is desirable. Therefore, there has been significant effort to control the release of drugs from hydrogel systems<sup>199</sup> and to have sustained release over a long time period. Burst release of the model drug rhodamine B was controlled in *Bombyx mori* hydrogels by addition of silk nanoparticles<sup>215</sup>. Another method for controlling burst release is surface diffusion control, using a less permeable film to coat the hydrogel<sup>216</sup>.

The mechanism of release of a physically encapsulated drug within a hydrogel network is diffusion based and is greatly controlled by steric hindrance due to the ratio between the drug and the hydrogel mesh size which is the space between the polymer chains (Figure 60). One method of decreasing hydrogel mesh size is by increasing the monomer concentration. The release rate of BSA from recombinant spideroin eADF4(C16) hydrogels was decreased by increasing the concentration of eADF4(C16). BSA release was decreased from ~100 % release after 10 hours at 3 % (w/v) eADF4(C16) to ~40 % release at 5 % (w/v) eADF4(C16)<sup>86</sup>.

A loaded drug that is smaller than the mesh size will have a quicker rate of release with fast diffusion out of the network than a drug that is about the same size as the mesh size which will be affected by steric hindrance. If the loaded drug is larger than the mesh size, for example a large biomacromolecule, which will be effectively immobilised in the hydrogel network. Release of this drug will be as a result of either hydrogel network degradation by the local environment, by swelling of the hydrogel which will increase the network pore size, or by deformation of the network physically pushing out the drug<sup>217</sup>. Degradation of the hydrogel network and swelling can be tuned by the factors in hydrogel design, such as presence of protease cleavage sites, monomer concentration and crosslinking density.

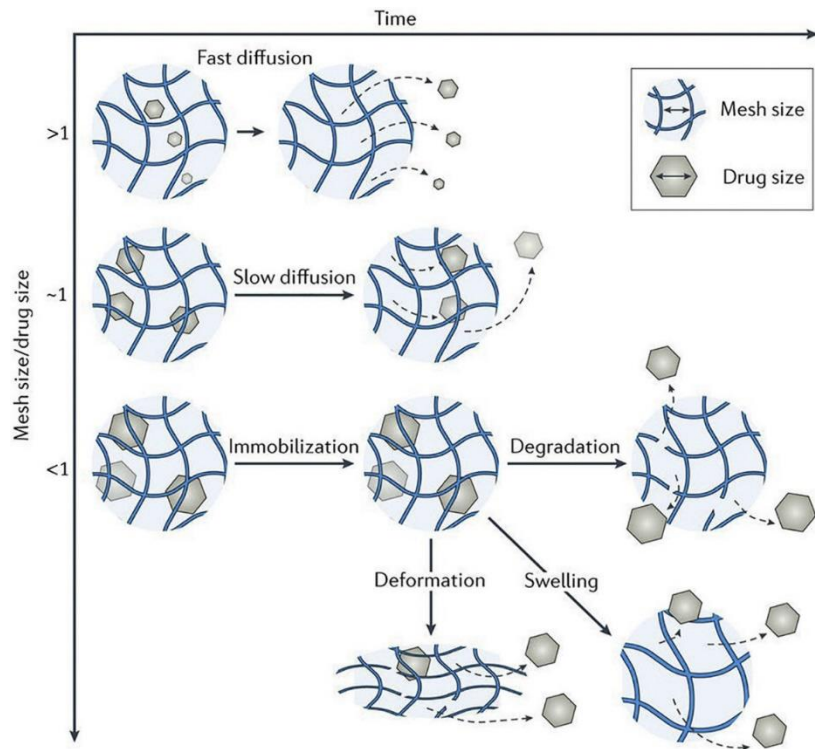


Figure 60: The hydrogel drug diffusion release rate is controlled by ratio between the hydrogel mesh size and the drug size<sup>217</sup>. Drugs smaller than the mesh size have fast rates of diffusion. Diffusion rate decreases as the drug size increases as steric hindrance becomes more important. Dashed lines show the path of the released drugs.

Other rate controlling processes<sup>218</sup> in hydrogel drug delivery systems are the heterogeneity of pore structure and changes in pH which influence hydrogel-drug interactions, as strong adsorption of drug molecule to hydrogel network will decrease rate of release. Minimal stirring or movement of the surrounding media leads to an undisturbed, higher concentration of drug surrounding the hydrogel which inhibits further release of the drug from the hydrogel into the media<sup>217</sup>. Stirring or constantly refreshing the media then this can speed up drug release due to improved sink conditions better representing the *in vivo* environment. Temperature can also affect

release rate, not only due to increased random movement of particles but changes in swelling in stimulus responsive hydrogels.

#### **7.1.4. Stimulus responsive 'smart' hydrogels**

Disease states can elicit changes in pH and temperature within the body, for example acidic pH in the extracellular tumour environment or wounds and increased temperature of infection<sup>153</sup>. Additionally, different tissues and organs in the body exist at different physiological pH for example the stomach, the gastrointestinal tract and the blood. Hydrogels that are stimulus responsive can change their swelling ratio and therefore volume and pore size in response to its local environment pH or temperature. This leads to changes in drug release rate allowing controllable and targeted release.

Drugs can either be physically entrapped in the hydrogel network or covalently bound to it. Diffusion of physically entrapped drugs out of the hydrogel network can be controlled by environmental pH and temperature changes, whereas release of covalently bound drugs can be controlled by light or presence of certain enzymes which will break down the hydrogel network or cleave a labile bond releasing the drug.

Hydrogels that show increased/decreased swelling in response to pH are due to ionisable groups within the hydrogel network polymer. In the case of protein hydrogels, the proteins isoelectric point (pI) dictates the swelling response with reduced swelling at pH = pI and increased swelling at pH less than or greater than pI due to increased electrostatic repulsion<sup>153</sup>. A chemically crosslinked hydrogel formed of chitosan and sodium alginate<sup>144</sup> showed pH sensitive release of BSA with greatly reduced cumulative release at pH 1.2 than pH 7.4. This was due to significantly increased swelling at pH 7.4 compared to pH 1.2 which increased pore sizes reducing the steric hindrance and allowing BSA to diffuse out of the hydrogel. This altered swelling and therefore drug release would allow an orally administered hydrogel to

have a slow rate of release in the stomach but an increased rate of release in the intestine for a more targeted release. A keratin methacrylic acid hydrogel showed similar pH responsive BSA release<sup>219</sup> which was explained by increased polymer-BSA interactions at low pH due to positive ionisation of BSA and negative ionisation of a carboxyl group on the hydrogel, whereas at physiological pH the interaction was weaker and the BSA was released from the hydrogel.

Thermoresponsive hydrogels which can alter their swelling or sol-gel transition around 37 °C have been used in biomedical applications. One of the most common synthetic materials is poly(N-isopropylacrylamide) (PNIPAAm) which undergoes a conformational shift due to changes in hydrophobicity and hydrophilicity to a lower critical solution temp (LCST)<sup>153</sup> leading to gelation. Hybrid hydrogels of PNIPAAm and natural materials such as peptides and chitosan have been designed for thermoresponsive drug delivery of antibacterial peptides<sup>175</sup> and BSA<sup>220</sup>.

### **7.1.5. Injectable hydrogels**

Injectable hydrogels can be implanted without anaesthesia and are not an invasive surgery and are therefore more economical and have improved patient outcomes. Additionally, injectable hydrogels can mould to the shape of the cavity or defect which restores tissue continuity, reducing risk of stress on surrounding tissues and stress from the tissues onto the hydrogel<sup>221</sup>. Injectable hydrogels can either undergo a sol-gel transition *in vivo* or pre-formed hydrogels can be administered, providing they are shear-thinning and have rapid recovery of their elastic modulus. Hydrogels that crosslink *in situ* must have rapid gelation times, on the order of minutes so that there is minimal loss from the injection site or leakage to surrounding tissues and dilution into the blood which would reduce the hydrogel volume and potentially lead to toxicity depending on the hydrogel pre-gel components<sup>200</sup>. Furthermore, the gelation must not be negatively affected by the local *in vivo* environment. The crosslinking can

be initiated by enzymes or by non-toxic photoactivated chemical crosslinkers (eg. NHS esters), which are more expensive crosslinking mechanisms but offer greater control over the hydrogel<sup>222</sup>. Compared to injecting *in situ* gelling hydrogels, the effect of the *in vivo* environment on gelation is not a factor for injectable pre-formed hydrogels and this means hydrogels with slower gelation kinetics can be used.

Shear-thinning hydrogels flow like low-viscosity fluids with increasing shear rates involved in injection but then rapidly recover their material properties with the removal of shear force<sup>200,217</sup>. Self-assembling hydrogels with reversible physical crosslinks form due to dynamic competition between attractive forces such as hydrophilic and hydrophobic interactions, hydrogen bonding, electrostatic attraction, and repulsive forces such as electrostatic repulsion. These individual forces are weak and easily broken but together are strong enough to form a stable network and prevent the hydrogel from dissolving. These interactions are not fixed like covalent bonds and therefore can be dissociated due to shear-forces leading to shear-thinning behavior. Rapid recovery of these interactions creates shear-thinning hydrogels<sup>200</sup>.

#### **7.1.6. Drug loading**

Drug loading of the hydrogel DDS can either be by permeation, entrapment or by covalent bonding (Figure 61). In permeation the hydrogel is formed and then swollen in a solution containing the drug which diffuses into the hydrogel. In entrapment the drug is added to the pre-gel solution and gelation is initiated, physically entrapping the drug within the hydrogel network. Drugs can also be added to the hydrogel by a covalent bond before gelation. Permeation is only suitable for small, hydrophilic drugs, loading can take multiple days and loading efficiency can be low with wasted drug in the swelling solution. Additionally, permeation is slower than entrapment or covalent bonding. However, covalent bonding can alter the drugs or biomacromolecules activity and potentially inactivate them. Entrapment and covalent bonding methods

can be suitable for biomacromolecules or hydrophobic drugs. Typically, hydrogels that are loaded by permeation methods have higher degrees of burst release than entrapment or covalent bonding since there will be more drug directly on the surface of the hydrogel<sup>223</sup>.

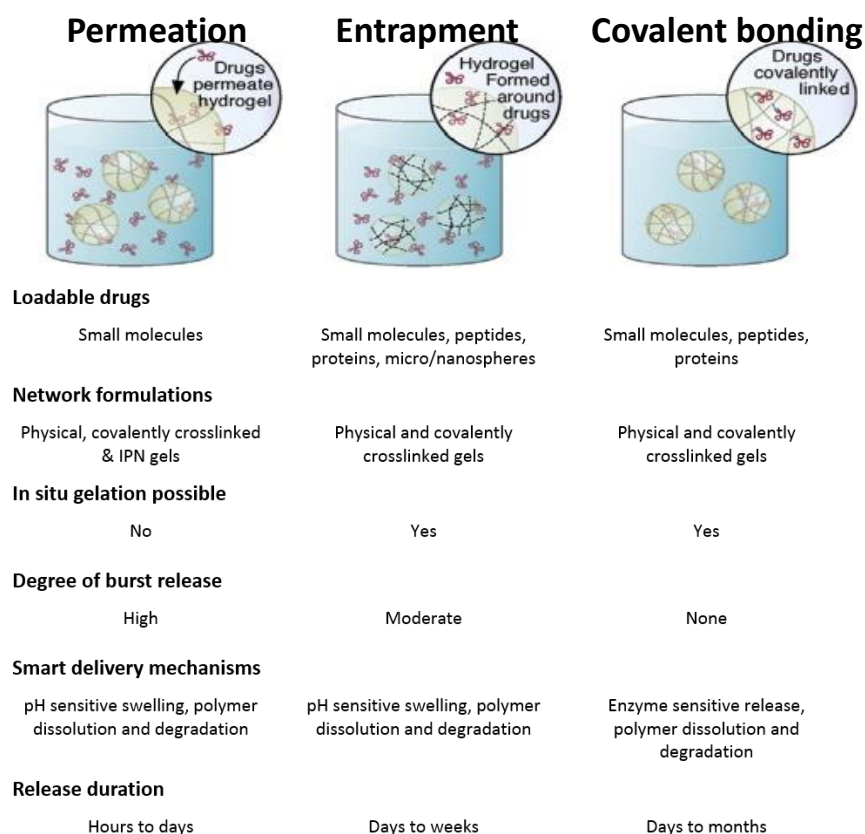


Figure 61: Three different drug loading strategies for hydrogels: Permeation, entrapment and covalent bonding. From N. Bhattarai *et al.*<sup>223</sup>

To avoid burst release, drug loading by a covalent bond can be utilised. Covalent bonds were investigated as a novel method of conjugating antibiotics to the recombinant spider silk 4RepCT. This method utilised an *E. coli* methionine auxotroph, the non-natural L-azidohomoalanine as a methionine analogue and copper catalysed alkyne-azide cycloaddition (CuAAC), also known as click-chemistry. This chemical modification could be instigated pre-film<sup>78</sup> and post fibre formation making it an incredibly flexible method of drug incorporation. *In vitro* testing of the antibiotic

functionalised silk fibres of 4RepCT showed excellent antimicrobial activity<sup>91</sup>. This method of covalently linking drugs to the silk protein could be utilised in hydrogels.

In the case of protein hydrogels, the amino acid sequence can be truncated directly to enzymes<sup>84</sup>, integrin binding sites<sup>77</sup> or other bioactive biomacromolecules. However, this can change the folding of the protein and affect its activity and care should be taken.

## **7.2. Materials and methods**

### **7.2.1. SEM of syringe extruded hydrogels**

NT2RepCT hydrogels were prepared by aliquoting 300  $\mu$ L 2.4 % (w/v) NT2RepCT in MQ water (MQ 37 T) or 20 mM CAPS pH 10 (CAPS10) into a 0.5 mL syringe and incubating at 37 °C for 16 hours. The set hydrogels MQ 37 T and CAPS10 were extruded through a 16 G needle either into 1 % (v/v) GA or into MQ water ahead of preparation for SEM. After 6 hours of crosslinking in 1 % (v/v) GA at 20 °C, which was used to stabilize the structure for SEM, the crosslinked hydrogels were washed with excess MQ water and were gently transferred into the lid of a 50 mL centrifuge tube. The non-crosslinked MQ water swollen hydrogels were also gently transferred into the lid of a 50 mL centrifuge tube and were flash frozen by submerging the lid into liquid nitrogen. The hydrogels were then lyophilised for 24 hours. Lyophilised NT2RepCT hydrogel samples were mounted on carbon tape and sputter coated with a thin layer of conductive platinum. Hydrogels were observed and images captured with a JEOL-JSM-6490 SEM and an accelerating voltage of 10 kV.

### **7.2.2. Shear-thinning rheology**

Rheological assessment was performed on an Anton Parr MCR 301 Rheometer with 8mm plate-plate geometry and a gap height of 1 mm. A Peltier hood attachment was used to prevent sample evaporation and maintain temperature of 37 °C. Viscosity as

a function shear rate was performed between 0.1-100 (1/s). Rheological assessments were performed on swollen, pre-formed hydrogels. MQ 37 T and CAPS10 hydrogels were prepared in 5 mL syringe moulds as previously described. Once formed, the hydrogels MQ 37 T and CAPS10 were gently ejected into 3 mL of PBS and swollen for 24 hours at 20 °C. One hydrogel sample was used for each measurement. Each hydrogel sample was carefully trimmed to size (12 mm to 8 mm diameter) with a plastic spatula after the chosen gap height was reached. A sample size of 3 was used for each experimental group. Results shown are averages ( $n=3$ )  $\pm$  SD.

### 7.2.3. PTAD azide modification of NT2RepCT

PTAD azide reaction performed at 89.6  $\mu$ L scale in DMF and Na Phosphate buffer as described by H. Ban *et al.*<sup>224</sup> and at 1 mL scale in DMF or acetonitrile and Na Phosphate buffer or Tris buffer. For 89.6  $\mu$ L scale: 4-(4-(2-azidoethoxy)phenyl)-1,2,4-triazolidine-3,5-dione (PTAD-N<sub>3</sub>) and 1,3-Dibromo-5,5-dimethylhydantoin (Dibromantin) (both Sigma-Aldrich) were prepared in dry DMF at 6 mM. Equal volumes (10  $\mu$ L) of PTAD-N<sub>3</sub> and Dibromantin were combined in an Eppendorf to oxidise the PTAD-N<sub>3</sub> and vortexed to give a cherry red colour. This mixture was kept on ice. To an Eppendorf containing 70  $\mu$ L of a 1 mg/mL NT2RepCT in 100 mM Na Phosphate buffer pH 7.4, 5 aliquots of 3.92  $\mu$ L of the freshly prepared activated PTAD-N<sub>3</sub> were added with a fresh pipette tip every 2 seconds. This was prepared in 6 replicates. After 25 minutes at 20 °C the reactions were purified using Zeba™ Spin Desalting Columns, 7k MWCO, 0.5 mL (Thermo Fischer Scientific). Each column was used to purify 2 PTAD-N<sub>3</sub> NT2RepCT conjugation reactions. The flow through containing PTAD-N<sub>3</sub> NT2RepCT were collected and combined and stored at 4 °C ahead of conjugation to fluorescein alkyne in a copper catalyzed azide-alkyne cycloaddition reaction (CuAAC). For 1 mL scale: 4-(4-(2-azidoethoxy)phenyl)-1,2,4-triazolidine-3,5-dione (PTAD-N<sub>3</sub>) and 1,3-Dibromo-5,5-dimethylhydantoin (Dibromantin) (both Sigma-Aldrich) were prepared in either dry

DMF or acetonitrile (ACN) at 6 mM. Equal volumes (300  $\mu$ L) of PTAD-N<sub>3</sub> and Dibromantin were combined in a glass vial to oxidise the PTAD-N<sub>3</sub> and vortexed to give a cherry red colour. This mixture was kept on ice. To a glass vial containing 1 mL of a 1 mg/mL NT2RepCT in 100 mM Na Phosphate buffer pH 7.4 or 20 mM Tris pH 8, 5 aliquots of 56  $\mu$ L of the freshly prepared activated PTAD-N<sub>3</sub> were added with a fresh pipette tip every 2 seconds. After 25 minutes at 20 °C the reactions were transferred into dialysis tubing (6-8 kDa MWCO, Molecularporous membrane tubing, Standar RC Tubing, Spectra/Por 1) and dialysed against 1 L of 20 mM Tris pH 8 for 4 hours, refreshing the dialysis buffer after 2 hours. The dialysed PTAD-N<sub>3</sub> NT2RepCT were transferred into tubes and stored at + 4 °C ahead of conjugation to fluorescein alkyne in a copper catalysed click reaction (CuAAC)

#### **7.2.4. Conjugation of fluorescein to NT2RepCT-PTAD-N<sub>3</sub>**

CuAAC was performed at 1 mL scale: 500  $\mu$ L of PTAD-N<sub>3</sub> NT2RepCT was reacted with 50 mM fluorescein alkyne (FAM), 50 mM CuSO<sub>4</sub>, 50 mM Tris(benzyltriazolylmethyl)amine (THPTA), 50 mM CaSO<sub>4</sub> and 50 mM sodium ascorbate in a 20 mM Tris pH 7.5 buffer. The reaction was dialysed (6-8 kDa MWCO, Molecularporous membrane tubing, Standar RC Tubing, Spectra/Por 1) against 1L of 20 mM Tris pH 8 for 4 hours, refreshing the dialysis buffer after 2 hours. Unconjugated NT2RepCT was compared to conjugated NT2RepCT-FAM by analysis on a 15 % SDS PAGE gel. Negative controls to examine autofluorescence, non-covalent interactions of FAM and NT2RepCT and to evaluate the success of CuAAC reaction were included. The transilluminator UV light setting on Syngene G:Box (GeneFlow Limited) at 800 ms was used to capture fluorescence of the conjugated NT2RepCT-FAM and unbound FAM before staining of the gel with Gelcode™ Blue Safe Protein Stain according to manufacturer's instructions.

### **7.2.5. *In vitro* release of Rhodamine B from hydrogels**

Rhodamine B was used as a model polar, hydrophilic model drug surrogate to investigate the effect of pH on drug release from NT2RepCT hydrogels. Rhodamine B was dissolved in MQ water to reach a concentration of 0.5 mg/mL. Lyophilised NT2RepCT was reconstituted in either MQ water or 20 mM CAPS pH 10 to a concentration of 26.7 mg/mL. Hydrogels containing rhodamine B were prepared by combining 90  $\mu$ L 26.7 mg/mL NT2RepCT in MQ water or 20 mM CAPs pH 10 with 10  $\mu$ L of 0.5 mg/mL rhodamine B to give a final NT2RepCT concentration of 24 mg/mL and a final rhodamine B concentration of 0.05 mg/mL. Hydrogels of volume 100  $\mu$ L were cast in individual wells of a 24 well plate, creating a ring shape. Gelation was performed by incubation at 37 °C for 16 hours (overnight), the plate was wrapped in tin foil to protect the samples from light. Release of rhodamine B was initiated by addition of 1 mL of PBS at pH 5.5, 6.45 or 7.4 at 37 °C. At certain time intervals, 200  $\mu$ L PBS buffer was removed and transferred into wells of a 96 well black, clear bottom plate (Corning®) and replaced by 200  $\mu$ L fresh, pre-warmed PBS at the appropriate pH. The concentration of rhodamine B was quantified by measuring the fluorescence with an ultraviolet-visible (UV-VIS) spectrophotometer (Tecan Spark 10M) using an excitation wavelength of 533 nm and emission wavelength of 627 nm. A standard curve was created at each PBS pH to account for the pH dependent fluorescence change of RhB, and the equation of each line was used to calculate rhodamine B concentrations from fluorescence at the specific pH. Cumulative release of rhodamine B was calculated by Equation 13.

Equation 13:

$$\text{Cumulative release \%} = \frac{V_a C_i + \sum_1^{n-1} V_w C_i}{m_0} \times 100$$

Where  $V_a$  is the volume of the PBS aliquot removed,  $C_i$  is the concentration of rhodamine B at time  $i$ ,  $n$  is the displacement time,  $V_w$  is the volume of PBS in the well containing the hydrogel and  $m_0$  is the total mass of rhodamine B in the hydrogel. Blanks of each PBS buffer and NT2RepCT hydrogels containing no rhodamine B were used to account for any background fluorescence. Statistical significance was determined by unpaired students t-test. The final data are presented as mean  $\pm$  SD (n=3).

### **7.2.6. *In vitro* release of fluorescein from encapsulated and conjugated NT2RepCT hydrogels**

A comparison of the release of FAM alkyne that was covalently bound and FAM alkyne that was encapsulated in the hydrogel network was performed. NT2RepCT hydrogels with covalently bound FAM alkyne were prepared in MQ water and 20 mM CAPS pH 10. These samples were called PTAD-FAM MQ and PTAD-FAM CAPS10. For PTAD-FAM MQ and PTAD-FAM CAPS10, 100  $\mu$ L containing 24.95 mg/mL NT2RepCT and 0.05 mg/mL NT2RepCT-PTAD-FAM in either MQ water or 20 mM CAPS pH 10 respectfully, were aliquoted into wells of a Corning™ 96-well clear bottom black polystyrene microplate.

Hydrogels containing 0.65  $\mu$ g FAM alkyne encapsulated, non-covalently in the network were prepared. These samples were called FAM MQ and FAM CAPS10. For FAM MQ and 1FAM CAPS10, 100  $\mu$ L containing 24 mg/mL NT2RepCT and  $6.5 \times 10^{-3}$  mg/mL FAM alkyne in either MQ water or 20 mM CAPS pH 10 respectfully, were aliquoted into wells of a Corning™ 96-well clear bottom black polystyrene microplate. Control wells containing 100  $\mu$ L of 24 mg/mL NT2RepCT with no FAM alkyne and empty wells were included to account for background fluorescence. For each sample and control the hydrogels were prepared in replicates of five. Gelation was performed by incubation at 37 °C for 16 hours (overnight), the plate was wrapped in tin foil to protect the

samples from light. Release of FAM alkyne was initiated by addition of 250  $\mu\text{L}$  PBS pH 7 at 37  $^{\circ}\text{C}$ . At certain time intervals, 100  $\mu\text{L}$  PBS buffer was removed and transferred into wells of a 96 well black, clear bottom plate (Corning<sup>®</sup>) and replaced by 100  $\mu\text{L}$  fresh, pre-warmed PBS. The concentration of FAM alkyne was quantified by measuring the fluorescence with an ultraviolet-visible (UV-VIS) spectrophotometer (Tecan Spark 10M) using an excitation wavelength of 494 nm and emission wavelength of 521 nm. A standard curve was created, and the equation of the line used to calculate FAM concentrations from fluorescence. Cumulative release of FAM alkyne was calculated by the Equation 14.

Equation 14:

$$\text{Cumulative release } (\mu\text{g}) = V_a C_i + \sum_{1}^{n-1} V_w C_i$$

Where  $V_a$  is the volume of the PBS aliquot removed,  $C_i$  is the concentration of FAM at time  $i$ ,  $n$  is the displacement time and  $V_w$  is the volume of PBS in the well containing the hydrogel. The final data are presented as mean  $\pm$  SD ( $n=5$ ).

### 7.2.7. *In vitro* drug release modelling

Release of rhodamine B and FAM alkyne from NT2RepCT hydrogels was examined using four mathematical models of drug release:

Zero-order kinetic Equation 15:

$$\frac{M_t}{M_{\infty}} = kt$$

First-order kinetic Equation 16:

$$\ln\left(\frac{M_t}{M_{\infty}}\right) = kt$$

Higuchi kinetic Equation 17:

$$\frac{M_t}{M_{\infty}} = kt^{\frac{1}{2}}$$

Korsmeyer-Peppas kinetic Equation 18:

$$\frac{M_t}{M_\infty} = kt^n$$

Where  $M_t$  is the total amount of drug released at time  $t$ ,  $M_\infty$  is the total amount of drug to be released,  $k$  is the kinetic constant and  $n$  is the diffusivity exponent.

The cumulative release data of rhodamine B and FAM alkyne up to 60% release<sup>225</sup>, was fitted to the mathematical models and the  $R^2$  for each was calculated and used to determine goodness of fit. For the zero order, first order and Higuchi model the data was plotted and analysed in Graphpad Prism 7.04. Linear regression analysis was used to find  $R^2$  and  $k$ . For the Korsmeyer-Peppas model, the data was analysed and fit to the model using non-linear regression analysis utilising the Microsoft Office Excel 365 solver functionality to minimise the sum of the squared difference between the data and the model, subject to the constraints that  $k$  and  $n$  were greater than or equal to zero. The data analysis correlation function was used to calculate  $R^2$ . The diffusivity exponent release mechanism of the Korsmeyer-Peppas model was assessed with the criteria summarised in Table 13.

Table 13: Summary of drug release mechanisms indicated by the diffusivity exponent  $n$  calculated by the Korsmeyer-Peppas equation for a slab shaped material. Values and indications from M. Lobo *et al.*<sup>225</sup>

<b>n</b>	<b>Indication</b>
<b>&lt;0.5</b>	Quasi-Fickian diffusion
<b>=0.5</b>	Fickian diffusion
<b>0.5&lt;n&lt;1</b>	Anomalous transport, a combination of diffusion and swelling
<b>&gt;1</b>	Case II transport (zero order kinetics due to swelling)

## 7.3. Results

### 7.3.1. Hydrogels formed in syringe retained shape upon extrusion

To test the recovery of MQ 37 T and CAPS10 hydrogels after deformation, the hydrogels were cast in a 0.5 mL syringe with a 16 G needle attachment. Both MQ 37 T and CAPS10 were hand-extruded from the needle in a slow and controlled manner onto a Petri dish in a wiggling line (Figure 62). Once extruded the hydrogels did not visibly lose their extruded shape for the duration of the experiment (5 h). The extruded hydrogels were transparent.

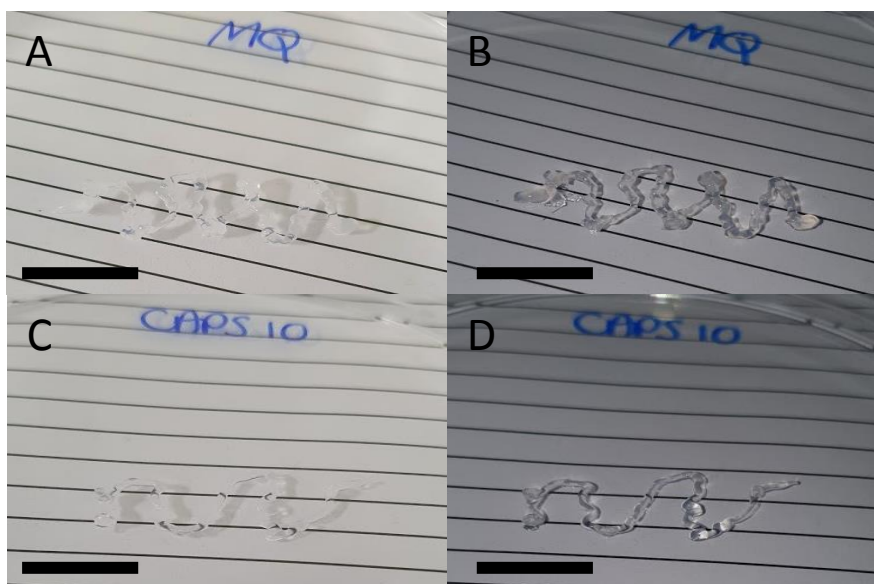


Figure 62: Injectable MQ 37 T and CAPS10 hydrogels. Hydrogels cast in 0.5 mL syringe with 16 G needle. Hand extruded into an empty Petri dish placed on-top of lined paper to show transparency and for clearer images. Photos taken with and without flash. A) MQ 37 T (no flash), B) MQ 37 T (flash), C) CAPS10 (no flash), D) CAPS10 (flash). Scale bar = 1 cm

### 7.3.2. MQ 37 T and CAPS10 non-Newtonian shear thinning behaviour

The shear-thinning properties of MQ 37 T and CAPS10 were assessed by measuring viscosity as a function of shear rate between 0.1 and 100 (1/s). Viscosity decreased semi-linearly with increasing shear rate indicating that the hydrogels were shear

thinning and showed non-Newtonian behaviour (Figure 63). At 0.1 (1/s) shear rate and at each shear rate increase measured, CAPS10 was more viscous than MQ 37 T.

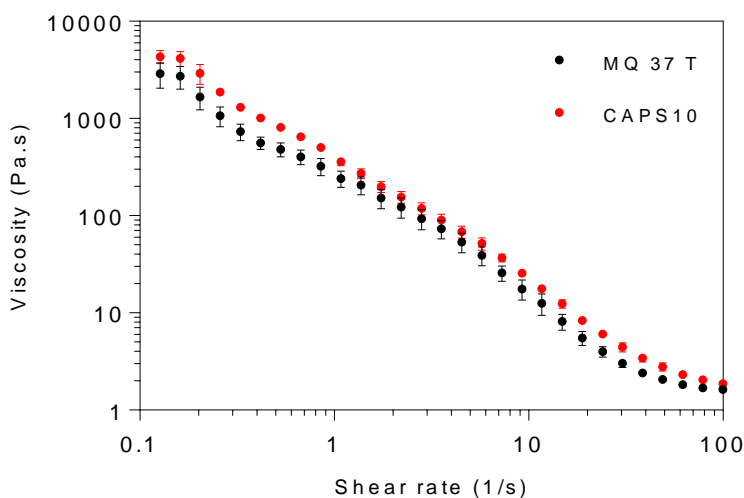


Figure 63: Viscosity as a function of shear rate. Shear-thinning behavior of MQ 37 T (black) or CAPS10 (red). Hydrogels swollen in PBS pH 7 for 24 hours. Measured at 37 °C. Shear rate measured between 0.1 and 100 (1/s), gap height 1 mm. (n=3) ± SD

### 7.3.3. Extruded hydrogels SEM

To investigate the effect of shear force of injection extrusion on the hydrogel internal porous structure, SEM was utilised. MQ 37 T and CAPS10 hydrogels were formed in 0.5 mL syringes and extruded either directly into 1 % (v/v) GA or into MQ water. Non-crosslinked extruded hydrogels, termed 'syringe no GA', appeared textured with angular 10 µm pores in CAPS10 syringe no GA but no visible pore structure in MQ 37 T syringe no GA. This textured appearance was not seen in MQ 37 T syringe 1 GA or CAPS10 syringe 1 GA (Figure 64). The pores in the 1 % (v/v) GA crosslinked syringed hydrogels were smaller and have directionality along an axis. Furthermore, there were areas of smooth, flat, lamellar like surfaces in both the 1 % (v/v) GA crosslinked syringed hydrogels but more extensively in MQ 37 T syringe 1GA (Figure 65).

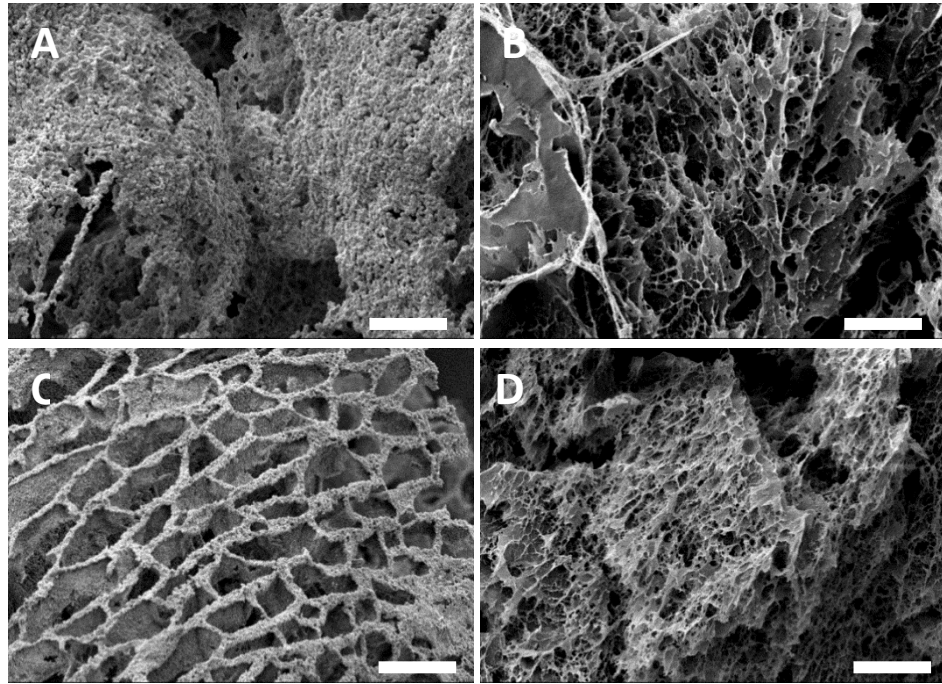


Figure 64: Comparison SEM images of MQ 37 T and CAPS10 hydrogels after being extruded from a 16 G needle with and without glutaraldehyde crosslinking. A = MQ 37 T No GA, B = MQ 37 T 1 GA, C = CAPS10 no GA, D = CAPS10 1GA. All scale bars 10  $\mu\text{m}$

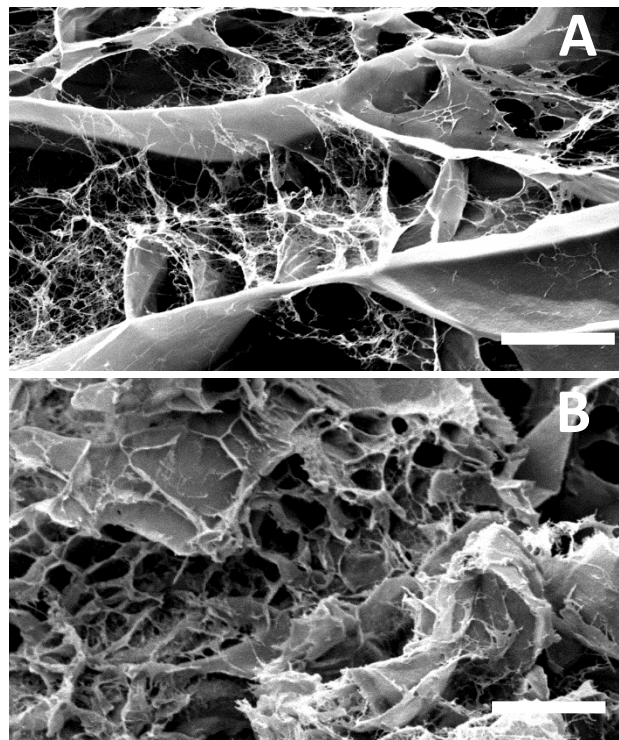


Figure 65: SEM images of MQ 37 T 1GA and CAPS10 1GA injected hydrogels.

A = MQ 37 T 1GA, B = CAPS10 1GA. Scale bars = 10  $\mu\text{m}$ .

### 7.3.4. PTAD conjugation small scale and larger scale

Initially, the exact procedure for bioconjugation of PTAD azide to tyrosine residues from H. Ban *et al.*<sup>224</sup> was performed at small scale (89.6  $\mu$ L) using dry DMF and 100 mM Na Phosphate buffer pH 7.4. The reaction was performed in 5 replicates simultaneously and after removal of unreacted reaction components using 0.5 mL Zeba™ spin 7k MWCO desalting columns, the NT2RepCT-PTAD azide products were combined. CuAAC was performed the following day to click fluorescein alkyne (FAM alkyne) to NT2RepCT-PTAD azide. The success of the reaction was visualized with an SDS PAGE gel (Figure 66) comparing non-processed NT2RepCT as a control, NT2RepCT + PTAD azide reaction product and NT2RepCT-PTAD azide FAM alkyne CuAAC reaction product. After the dye front had reached the bottom of the SDS PAGE gel, it was immediately imaged using 800 ms exposure of UV light. Only lane 4 containing NT2RepCT-PTAD azide FAM alkyne CuAAC reaction product fluoresced with 2 areas showing most intense fluorescence: A band at 33 kDa corresponding with the expected molecular weight of NT2RepCT and a band at the dye front due to diffusion of fluorescein during running of the SDS PAGE gel. Since the NT2RepCT protein band in the unstained, UV light exposed image of the SDS PAGE gel has localized, intense fluorescence but the control NT2RepCT in lanes 2 and 3 do not means there is no autofluorescence of NT2RepCT at 800 ms exposure.

After capturing fluorescence, the SDS PAGE gel was stained to visualize protein bands and imaged again using white light. In the stained image there is a protein band at the expected molecular weight of 33 kDa in all lanes, with additional higher molecular weight protein bands present in NT2RepCT-PTAD azide in Lane 3 and NT2RepCT-PTAD azide FAM alkyne CuAAC in Lane 4. The band size of the NT2RepCT protein band decreases between lane 2 and lane 4, due to loss of protein during the reactions and transfer between vessels. Additionally, the center of the NT2RepCT

protein band increases in molecular weight during the conjugation reactions further suggesting successful conjugation, however since the NT2RepCT band is so large in Lane 2 it bulges out and appears at lower molecular weight than is expected.

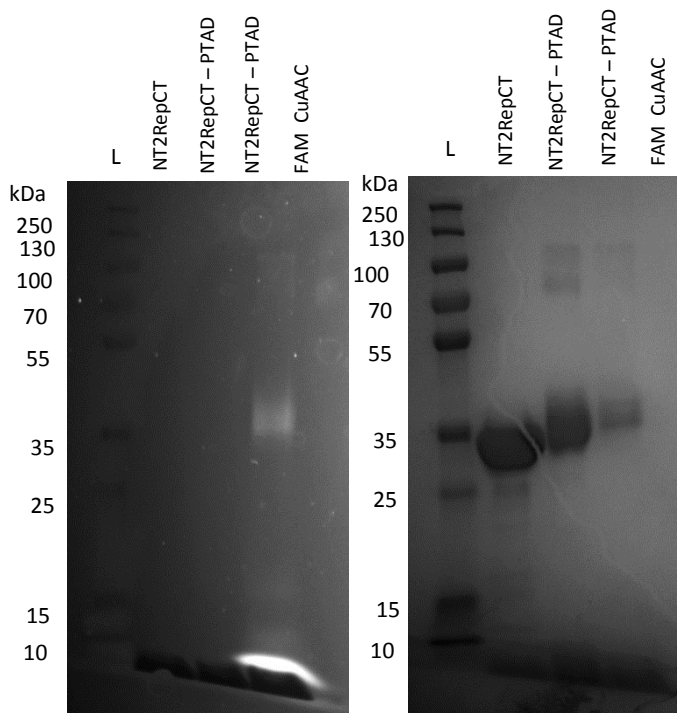


Figure 66: SDS PAGE analysis of successful small-scale conjugation of FAM alkyne and NT2RepCT, both images are of same SDS PAGE gel. Left: SDS PAGE gel before staining with 800 ms exposure to visualise FAM alkyne Right: Same SDS PAGE gel stained with Gelcode blue safe stain to visualise protein bands. Lane 1: Protein ladder 10-250 kDa. Lane 2: 1 mg/mL NT2RepCT. Lane 3: 1 mg/mL NT2RepCT after tyrosine PTAD azide reaction product after Zeba™ spin 7 kDa MWCO desalting column clean up. Lane 4: NT2RepCT-PTAD azide FAM alkyne CuAAC reaction product. The SDS PAGE gel ripped during processing.

Next, larger reaction volumes and the effect of acetonitrile and 20 mM Tris pH 8 in the conjugation were investigated. Additionally, dialysis was used to remove unreacted reaction components instead of Zeba™ spin 0.5 mL desalting columns.

Lyophilised NT2RepCT was reconstituted in either 100 mM Na Phosphate pH 7.4 or 20 mM Tris pH 8 at 1 mg/mL. PTAD-N<sub>3</sub> and the activator were prepared at 6 mM in either dry DMF or acetonitrile. The four combinations (Na phosphate + DMF, Tris + DMF, Na phosphate + acetonitrile and Tris + acetonitrile) were prepared at the same volume with 5 x 56 µL of the 3 mM PTAD-N<sub>3</sub> + activator (in dry DMF or acetonitrile) added to 1 mL of 1 mg/mL NT2RepCT (in Na/phosphate or Tris buffer) on ice. After 25 minutes each reaction condition was transferred into a separate dialysis tubing and dialysed against 20 mM Tris pH 8. After dialysis the CuAAC reaction of NT2RepCT-PTAD azide and FAM alkyne was performed as described above. Again, SDS PAGE was used to determine FAM-alkyne conjugation, with exposure of 800 ms UV-light.

Negative controls included indicated that no autofluorescence of NT2RepCT or any of the NT2RepCT-PTAD-N<sub>3</sub> occurred, as the lanes containing these controls (Figure 67 lanes A-F) showed no fluorescent protein bands, whereas in the stained SDS PAGE gel image there is protein present. However, the negative control to determine whether there are non-covalent interactions between FAM alkyne and NT2RepCT (Figure 67 lane F) showed a fluorescent band. To determine whether NT2RepCT-PTAD-N<sub>3</sub> would bind to FAM alkyne and to assess the success of the CuAAC reaction, a negative control containing NT2RepCT-PTAD-N<sub>3</sub>, FAM alkyne and all CuAAC reaction components minus copper under the same reaction conditions of CuAAC was included (Figure 67 lane G). As with the other negative controls, no fluorescent protein band was seen, and the FAM alkyne migrated with the dye front. In all samples containing FAM alkyne, whether CuAAC samples or the controls, were prepared at the same concentration of FAM alkyne and all unbound FAM alkyne migrated with the dye front to the bottom of the gel. However, some FAM alkyne had covalently bound in the CuAAC reactions as there was still a fluorescent protein band (Figure 67 lanes H to K).

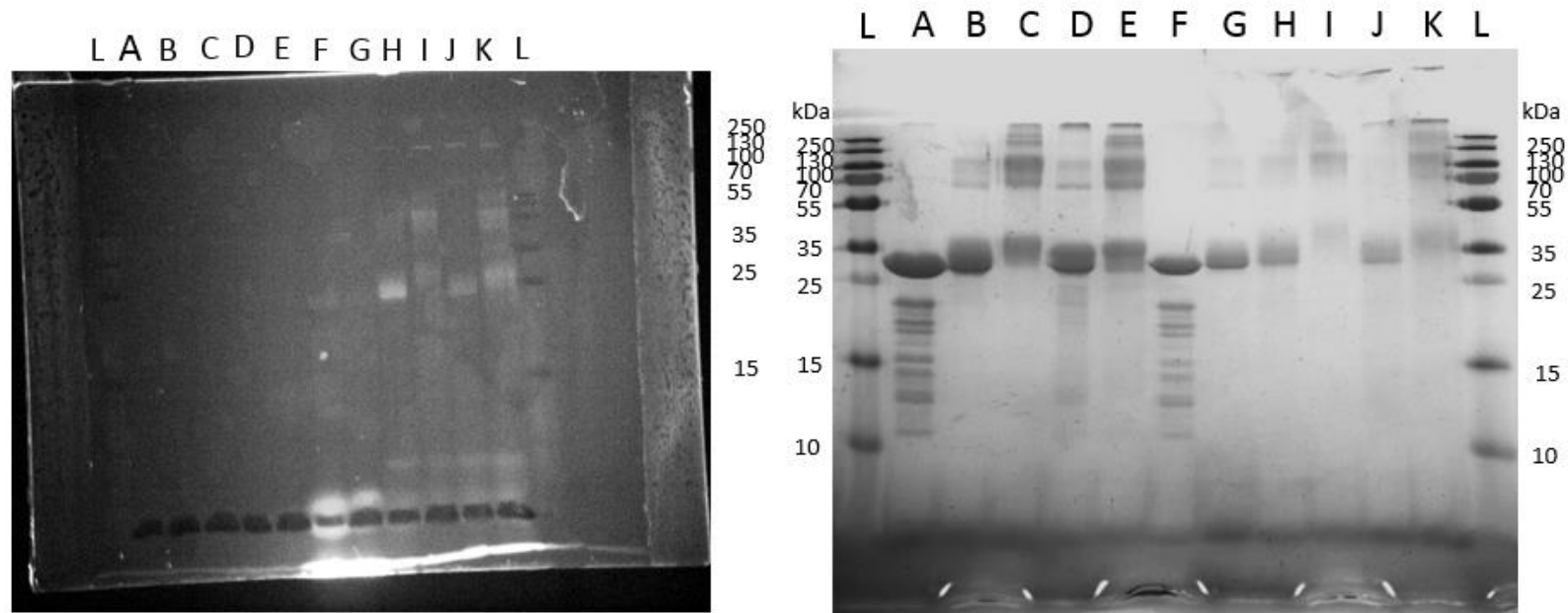


Figure 67: SDS PAGE images of 1 mL scale PTAD conjugation under different solvent and buffer conditions. Left: un-stained UV-light exposed SDS PAGE gel. Right: The same SDS-PAGE gel. L = Protein ladder, A = 1 mg/mL NT2RepCT control, B = NT2RepCT PTAD-N<sub>3</sub> (Na Phosphate + DMF), C = NT2RepCT PTAD-N<sub>3</sub> (Na Phosphate + ACN), D = NT2RepCT PTAD-N<sub>3</sub> (Tris + DMF), E = NT2RepCT PTAD-N<sub>3</sub> (Tris + ACN), F = NT2RepCT + FAM alkyne control, G = NT2RepCT PTAD-N<sub>3</sub> (Na/P + DMF) + FAM alkyne (no copper in CuAAC) control, H = NT2RepCT PTAD-N<sub>3</sub> (Na/P + DMF) + FAM alkyne CuAAC, I = NT2RepCT PTAD-N<sub>3</sub> (Na/P + ACN) + FAM alkyne CuAAC, J = NT2RepCT PTAD-N<sub>3</sub> (Tris + DMF) + FAM alkyne CuAAC, K = NT2RepCT PTAD-N<sub>3</sub> (Tris + ACN) + FAM alkyne CuAAC.

### 7.3.5. *In vitro* release of rhodamine B from hydrogels

The release of rhodamine B from MQ 37 T and CAPS10 hydrogels was monitored in PBS pH 5.645 and 7.4. The standard curves used to calculate concentration of rhodamine B from the sample aliquots (Figure 68) had a fairly low  $R^2$  of 0.9821-0.9859 and this was likely because of the maximum relative fluorescence intensity (RFU) measurable being reached at the highest concentration standard, leading to a non-linear response. However, all the measured RFU values for the samples were well within the standard curve concentration boundaries, with the highest RFU measured around 35,000 and the lowest 3,000 therefore, the standard curves were acceptable.

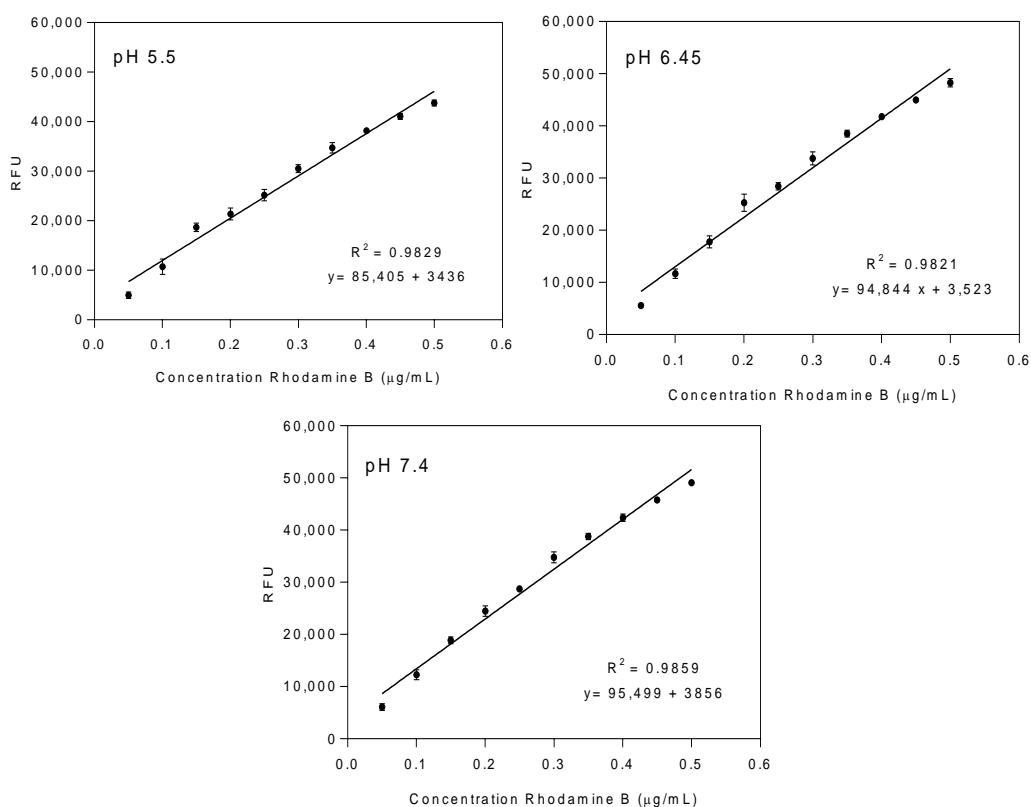


Figure 68: Standard curve relating fluorescence to concentration of rhodamine B in PBS pH 5.5, pH 6.45 and pH 7.4. Mean  $\pm$  SD (n=3).

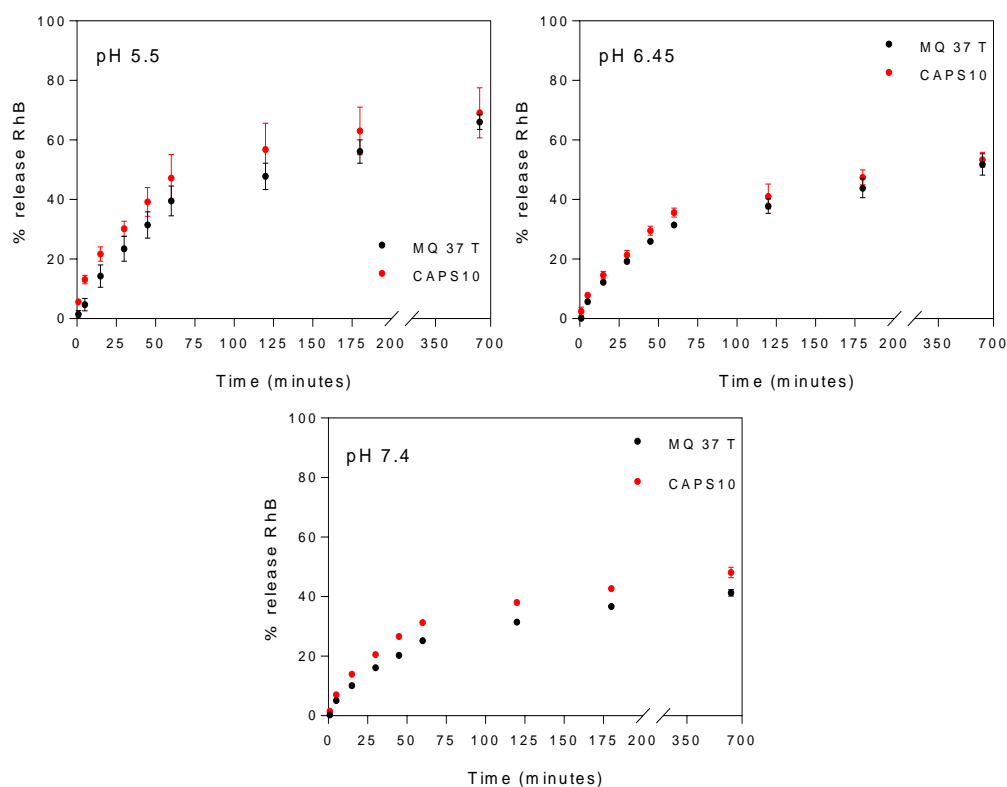


Figure 69: pH dependent cumulative release (%) of rhodamine B (RhB) from NT2RepCT hydrogels *in vitro*. MQ 37 T (black circles) and CAPS10 (red circles) hydrogels in PBS pH 5, 6.45 or 7.4. Mean  $\pm$  SD (n=3)

Rhodamine B was released from MQ 37 T and CAPS10 hydrogels at the 3 PBS pH investigated (Figure 69). In all cases the release profile was biphasic with initial burst release up to 50 minutes, followed by slower release for the duration of the release assay. The cumulative percentage of loaded rhodamine B released at 10.5 hours was highest in PBS pH 5.5 at  $67.0 \pm 2.6\%$  for MQ 37 T hydrogels and  $69.1 \pm 8.4\%$  for CAPS10 hydrogels. The cumulative release decreased with increasing PBS pH. After 10.5 hours in PBS pH 6.45, MQ 37 T released  $51.8 \pm 3.4\%$  whereas CAPS10 released  $53.3 \pm 2.5\%$  of loaded RhB. At pH 7.4 MQ 37 T had released  $41.3 \pm 1.1\%$  and CAPS10 had released  $48.1 \pm 1.7\%$  at 10.5 hours of loaded RhB. At all PBS pH, CAPS10 hydrogels released more RhB than MQ 37 T but there was only a significant increase at pH 7.4 (Table 14).

Table 14: Maximum percentage release of loaded rhodamine B (RhB) from MQ 37 T and CAPS10 hydrogels after 10.5 hours in PBS pH 5.5, 6.45 or 7.4. Averages (n=3) ± SD. Unpaired students t-test between MQ 37 T and CAPS10 at pH 7.4 \*\* P<0.01.

Hydrogel	PBS pH	Percentage release loaded	
		RhB at 10.5 hours	
		AVG	SD
MQ 37 T	5.5	67.0	2.6
	6.45	51.8	3.4
	7.4	41.3	1.1
CAPS10	5.5	69.1	8.4
	6.45	53.3	2.5
	7.4	48.1 **	1.7

To investigate the release profile four distinct mathematical models were used. Zero order, First order, the Higuchi equation and the Korsmeyers-Peppas equation. The data was fit to the 4 models and the R<sup>2</sup> values were compared (Table 15). The lowest R<sup>2</sup> was seen for first order release at 0.3154-0.5960. Zero order release R<sup>2</sup> was 0.8218-0.8545 and for the Higuchi equation R<sup>2</sup> was 0.9662-0.9816. For the Korsmeyer-Peppas equation R<sup>2</sup> was >0.98. The Korsmeyer-Peppas equation was taken forward due to the slightly higher R<sup>2</sup>. The kinetic rate constant  $k$  (min<sup>-1</sup>) and diffusivity exponent  $n$  were calculated for each hydrogel and PBS pH (Table 16). The calculated kinetic rate constant was larger for CAPS10 hydrogels at all PBS pH than MQ 37 T hydrogels and the release rate fell with increasing pH. The diffusivity exponent  $n$  was <0.5 for all hydrogels apart from MQ 37 T hydrogel at PBS pH 5 where it was 0.51.

Table 15: R<sup>2</sup> values for each mathematical model of *In vitro* rhodamine B release from MQ and CAPS10 hydrogels at 3 PBS pH.

Hydrogel	PBS pH	Zero order (R <sup>2</sup> )	First order (R <sup>2</sup> )	Higuchi (R <sup>2</sup> )	Korsmeyer-Peppas (R <sup>2</sup> )
<b>MQ 37 T</b>	5.5	0.8545	0.5189	0.9745	0.9863
	6.45	0.8356	0.3154	0.9703	0.9864
	7.4	0.8600	0.4047	0.9816	0.9910
<b>CAPS10</b>	5.5	0.8371	0.5960	0.9706	0.9931
	6.45	0.8265	0.5347	0.9633	0.986
	7.4	0.8218	0.4889	0.9662	0.9884

Table 16: Calculated kinetic rate constant *k* and diffusivity exponent *n* of *in vitro* release of rhodamine B from MQ and CAPS10 hydrogels at 3 PBS pH values using the Korsmeyers-Peppas mathematical model.

Hydrogel	PBS pH	<i>k</i> (min <sup>-1</sup> )	<i>n</i>
<b>MQ 37 T</b>	5.5	4.13	0.51
	6.45	3.73	0.48
	7.4	2.97	0.49
<b>CAPS10</b>	5.5	6.64	0.45
	6.45	4.94	0.44
	7.4	4.54	0.44

### 7.3.6. *In vitro* release of fluorescein from encapsulated and conjugated NT2RepCT hydrogels

Fluorescein alkyne (FAM alkyne) was incorporated into NT2RepCT MQ or CAPS10 hydrogels via a covalent bond or via incorporation/encapsulation in the hydrogel

network via non-covalent interactions. Since the amount of FAM alkyne covalently bound to NT2RepCT was unknown, controls containing 0.65  $\mu\text{g}$  FAM alkyne were created. Presence of FAM alkyne was visible with a colour change and fluorescence under UV-light in FAM-PTAD hydrogels cast in 1 mL syringe moulds (Figure 70).

A standard curve including ten FAM alkyne concentrations (0.5  $\mu\text{g}/\text{mL}$  to 0.2  $\mu\text{g}/\text{mL}$ ) was created (Figure 71). The  $R^2$  of the standard curve was 0.9947 and all RFU measured in the samples were within the standard curve.



Figure 70: PTAD-FAM MQ hydrogel (50  $\mu\text{L}$  1  $\text{mg}/\text{mL}$  NT2RepCT PTAD FAM) + 450  $\mu\text{L}$  26.7  $\text{mg}/\text{mL}$  NT2RepCT to make 24  $\text{mg}/\text{mL}$ . A) NT2RepCT-PTAD-FAM hydrogel (MQ) white light on top of striped background. B) NT2RepCT-PTAD-FAM hydrogel (MQ) white light on top of black background. C) NT2RepCT-PTAD-FAM hydrogel (MQ) UV light on top of black background showing fluorescence. Scale bar = 0.5 cm

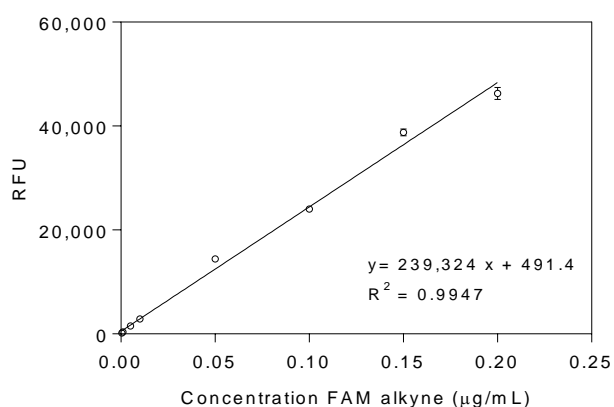


Figure 71: Standard curve relating fluorescence to concentration of FAM alkyne in PBS pH 7. Mean  $\pm$  SD (n=3). Equation of line  $y=239,324 x + 419.4$ ,  $R^2=0.9947$ .

The hydrogels containing non-covalently bound FAM alkyne (FAM MQ and FAM CAPS10) showed an initial burst release followed by a slower rate of release over time (Figure 72). FAM MQ released more FAM alkyne than FAM CAPS10 at every time point and overall released significantly more with  $35.0 \pm 6.6\%$  and  $21.4 \pm 1.4\%$  loaded FAM alkyne released respectively after 1320 minutes (22 hours). Release of FAM alkyne from FAM MQ showed greater standard deviation compared to FAM CAPS10. The PTAD-FAM MQ and PTAD-FAM CAPS10 hydrogels cumulative FAM alkyne release ( $\mu\text{g}$ ), showed initial burst release, followed by a slower rate of release throughout the rest of the experiment (Figure 73).

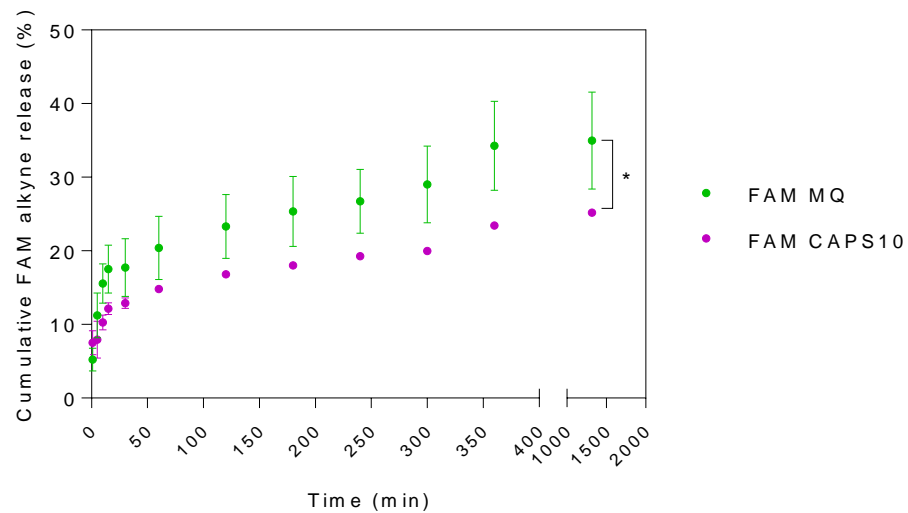


Figure 72: Cumulative release (%) of FAM from NT2RepCT hydrogels over time. FAM MQ (green symbols) and FAM CAPS10 (purple symbols) contained  $0.65 \mu\text{g}$  FAM, encapsulated within the hydrogel network, non-covalently linked. Mean  $\pm$  SD (n=5). Unpaired students t-test. \*  $P < 0.05$ .

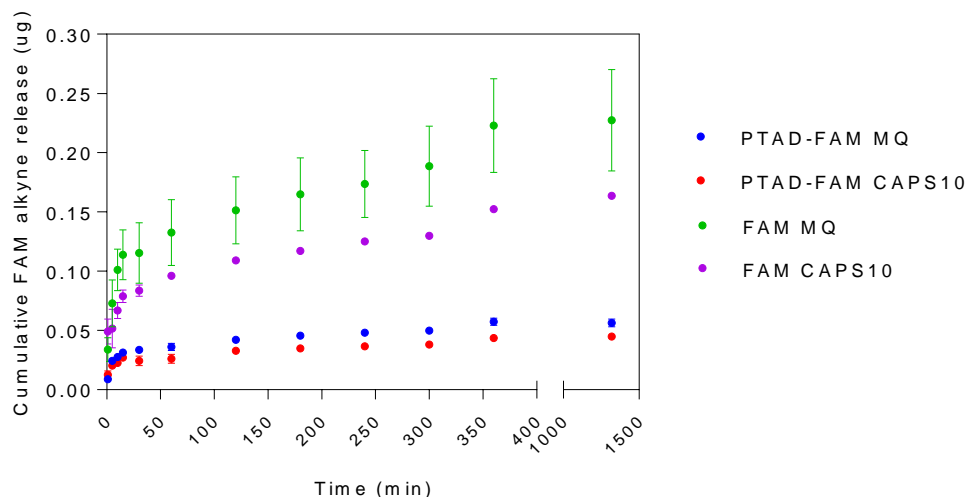


Figure 73: Cumulative release of FAM alkyne from NT2RepCT hydrogels over time ( $\mu\text{g}$ ). PTAD-FAM MQ (blue symbols) and PTAD-FAM CAPS10 (red symbols) contained covalently linked FAM alkyne via PTAD conjugation to tyrosine residues. FAM MQ (green symbols) and FAM CAPS10 (purple symbols) contained  $0.65 \mu\text{g}$  FAM alkyne, encapsulated within the hydrogel network, non-covalently linked. Mean  $\pm$  SD (n=5)

More FAM alkyne was released from PTAD-FAM MQ than PTAD-FAM CAPS10 throughout the experiment with  $0.056 \pm 0.003 \mu\text{g}$  and  $0.045 \pm 0.002 \mu\text{g}$  FAM alkyne released respectively after 1320 minutes or 22 hours (Table 17). Compared to the hydrogels containing free FAM alkyne, FAM MQ and FAM CAPS10, the release of FAM alkyne from PTAD-FAM MQ and PTAD-FAM CAPS10 was much reduced with a shallower gradient and less FAM alkyne released at 1320 minutes.

Kinetic modelling of the release of FAM alkyne from FAM MQ, FAM CAPS10, PTAD-FAM MQ and PTAD-FAM CAPS10 was performed as previously described (Section 7.3.5). The model that gave the highest  $R^2$  was the Korsmeyer-Peppas equation with the Higuchi equation and Zero order calculated as the next highest  $R^2$ . FAM alkyne release did not follow first order kinetic release as can be seen by the low  $R^2$  (Table

18). The Korsmeyer-Peppas equation rate constant  $k$  ( $\text{min}^{-1}$ ) and diffusion exponent  $n$  were calculated (Table 19).

Table 17: Cumulative amount of FAM released at 1320 minutes for from PTAD FAM MQ, PTAD-FAM CAPS10, FAM MQ and FAM CAPS10 in  $\mu\text{g}$  and as a percentage of loaded 0.65  $\mu\text{g}$  FAM for MQ FAM and FAM CAPS10. Average  $\pm$  SD (n=5).

	FAM released at 1320 min		FAM released after a 1320 min	
	( $\mu\text{g}$ )		(% of loaded 0.65 $\mu\text{g}$ )	
	AVG	SD	AVG	SD
<b>PTAD-FAM MQ</b>	0.056	0.003	-	-
<b>PTAD-FAM CAPS10</b>	0.045	0.002	-	-
<b>FAM MQ</b>	0.227	0.043	35.0	6.6
<b>FAM CAPS10</b>	0.166	0.003	21.4	1.4

Table 18: Coefficient of determination ( $R^2$ ) of the 4 models of drug release, zero order release, first order release, the Higuchi equation and the Korsmeyer-Peppas equation of FAM release from PTAD FAM MQ, PTAD-FAM CAPS10, FAM MQ and FAM CAPS10 hydrogels.

Hydrogel	$R^2$			
	Zero order	First order	Higuchi	Korsmeyer-Peppas
<b>PTAD-FAM MQ</b>	0.782	0.513	0.715	0.975
<b>PTAD-FAM CAPS10</b>	0.845	0.69	0.795	0.976
<b>FAM MQ</b>	0.827	0.577	0.787	0.975
<b>FAM CAPS10</b>	0.885	0.765	0.857	0.969

Table 19: Korsmeyer-Peppas rate constant  $k$  ( $\text{min}^{-1}$ ) and diffusion exponent  $n$  calculated for release of FAM from PTAD-FAM MQ, PTAD-FAM CAPS10, FAM MQ and FAM CAPS10 hydrogels.

Hydrogel	$k$ ( $\text{min}^{-1}$ )	$n$
PTAD-FAM MQ	2.22	0.17
PTAD-FAM CAPS10	2.41	0.21
FAM MQ	7.96	0.23
FAM CAPS10	6.48	0.20

## 7.4. Discussion of NT2RepCT hydrogel drug delivery systems

### 7.4.1. Overview

The aim of this chapter was to determine whether MQ 37 T and CAPS10 hydrogels could be used as a drug delivery system by exploring two types of drug release models (entrapment and conjugation by covalent attachment). By investigating *in vitro* release of a hydrophilic model compound, rhodamine B, it was shown that release was diffusion driven and pH dependent. Conjugation of FAM alkyne via PTADs to NT2RepCT tyrosine residues was examined and was found to follow a different release profile compared to unconjugated. The hydrogel's viscosity response with increasing shear stress was investigated and it was found that MQ 37 T and CAPS10 were shear-thinning and injectable and their porous structure was altered after injection.

### 7.4.2. Injectable hydrogels

The gelation time of MQ 37 T and CAPS10 is too slow at >2 hours to be used for *in situ* gelation of an injectable pre-gel solution, not to mention the inhibition of gelation by DMEM and PBS. Therefore, MQ 37 T and CAPS10 hydrogels, would need to be injected in the hydrogel form. To investigate the possibility of this, MQ 37 T and CAPS10 hydrogels were formed in a syringe with incubation at 37 °C overnight and

were extruded through a 16 G needle onto a Petri dish (Figure 62). The extruded shape indicates that both MQ 37 T and CAPS10 rapidly recovered their elastic modulus after the increased shear force within the extrusion. This indicates the possibility that these hydrogels could be 3D extruded printed, like eADF4(C16) and eMaSp1s recombinant spider silk hydrogels<sup>140</sup>, but with the added benefit of high yield expression and purification of soluble NT2RepCT. MQ 37 T and CAPS10 were injectable although to avoid patient discomfort and damage to surrounding tissues, an injection force of 10-20 N is required<sup>226</sup>. Further work is necessary to understand the change in mechanical properties during and after injection or shear force. Both pre-formed MQ and CAPS10 hydrogels were shear-thinning and showed non-Newtonian behavior with decreasing viscosity in response to increasing shear rate (Figure 63). This allowed the hydrogel to be extruded through the narrow opening of the needle because it had become sol.

Like the physically crosslinked MQ 37 T and CAPS10 hydrogels, physically crosslinked hydrogels made from silk fibroin show shear-thinning behaviour<sup>1</sup> as does natural spider silk dope<sup>13</sup> and NT2RepCT at dope concentrations of 500 mg/mL<sup>132</sup>.

In the shear-thinning experiment, MQ 37 T and CAPS10 hydrogels were swollen in PBS pH 7.2 for 24 hours to ensure equilibrium swelling but in the extrusion experiment the hydrogels were not swollen. It would be interesting to investigate the shear-thinning behaviour of the unswollen MQ 37 T and CAPS10 hydrogels to understand the effect of PBS pH 7.2 on the hydrogel's material properties.

After injection both non-crosslinked MQ 37 T and CAPS10 hydrogels showed textured morphologies with granulation. This could be fibrils induced by shear force of injection that had collapsed in the SEM plunge freezing and lyophilisation sample preparation process. The angular pores in CAPS10 syringe suggests inefficient freezing and the formation of crystalline ice. No porous structure was seen in no GA MQ 37 T syringe but there was more extensive granular texture. Fibre formation in NT2RepCT

occurs at acidic pH<sup>2</sup> which could explain this increased granulation if the texture seen is collapsed fibrils. The 1 % (v/v) GA crosslinked extruded MQ 37 T and CAPS10 hydrogels did not show granulated texture and instead showed increased lamellar structures and extensive fibril and pore structures. This was more extensive in MQ 37 T 1GA syringe hydrogels. The introduction of shear force from injection led to conditions that promote fibril formation and possibly larger scale fibre formation, particularly in MQ 37 T 1GA syringe. Compared to the non-extruded MQ 37 T and CAPS10 hydrogels seen in Chapter 5 (Figure 43) there are clear differences in morphology of the extruded hydrogels. This suggests a structural change is occurring during injection which requires further investigation, since this change is likely irreversible. Spider silk fibres are notoriously difficult if not impossible to dissolve and this could be the case with NT2RepCT fibres.

Understanding of how quickly the elastic modulus of MQ 37 T and CAPS10 hydrogel recovers after deformation due to shear is needed. It is expected that upon application of shear force the storage/elastic modulus will rapidly fall as the hydrogel undergoes shear-thinning but after removal of the shear force, the storage/elastic modulus should rapidly recover to pre-shear levels. This is the case for eADF4(C16) and eMaSp1 shear thinning hydrogels<sup>140</sup> and is an important behavior to study for injectable hydrogels<sup>153</sup>. If shear force introduces fibril formation within the NT2RepCT hydrogels there is potential for the recovered elastic modulus to be higher than pre-shear.

### **7.4.3. PTAD conjugation**

The approach used by D. Harvey *et al.*<sup>91</sup> in which all methionine residues of the recombinant spidroin 4RepCT were replaced by a methionine synthetic analogue L-azidohomoalanine providing functional handles for conjugation, is not applicable for the miniature spidroin NT2RepCT. NT2RepCT contains more methionine residues than TRX-4RepCT and 4RepCT, all of which are found in the N terminus (Figure 74).

Incorporation of 11 L-azidohomoalanine residues would affect NT2RepCT protein folding and potentially fibre formation. Although not all the methionine residues would be visible on the surface of the protein and accessible for conjugation. Additionally, this could affect NT2RepCT expression yield due to the need for *E. coli* growth in M9 minimal media.

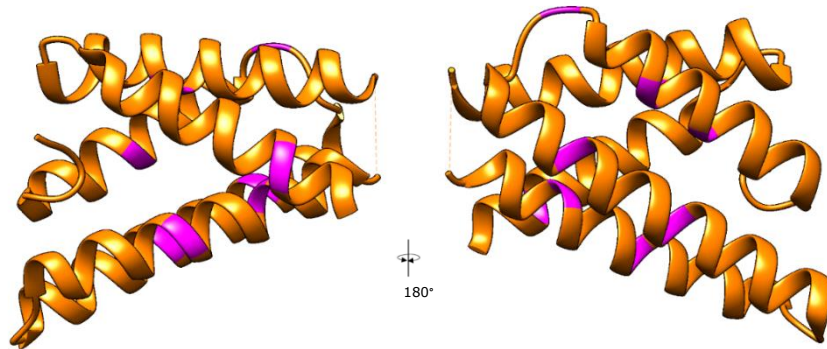


Figure 74: NT2RepCT N-terminus with 11 methionine residues highlighted in pink. 180° rotation about the y axis. NT2RepCT contains this amino acid sequence. Full NT2RepCT sequence can be found in General Methods. (*E. australis* MaSp1 NT. PDB 3LR2)

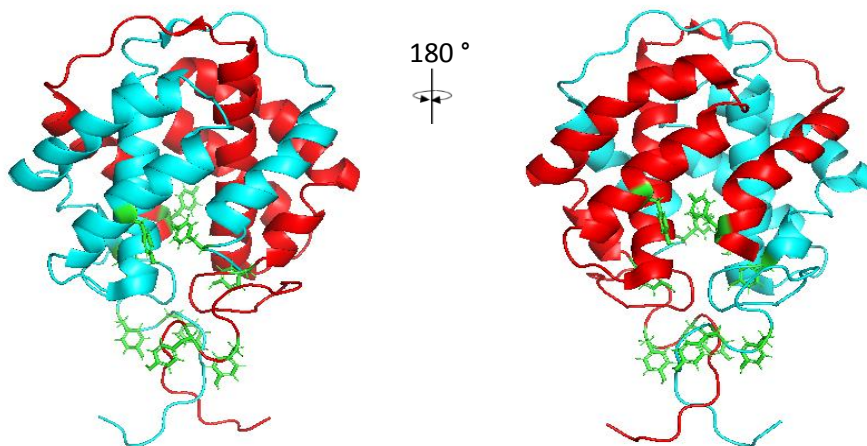


Figure 75: NT2RepCT C terminal dimer Each monomer subunit in cyan or red. Tyrosine residues in green. Rotation of 180° about the y axis is shown. (*A. ventricosus* MiSp1 CT PDB: 2mfz).

Therefore, a different approach was needed for adding functionality to NT2RepCT. Since NT2RepCT expresses in extremely high yields (>300 mg/L LB media shake flask culture), post-purification modification targeting amino acid side chains so as not to alter the peptide sequence was preferable. NT2RepCT contains no cysteine residues so typical maleimide<sup>227</sup> bioconjugation and other cysteine modifications<sup>228</sup> were not an option. However, cysteine conjugations are not recommended in spidroins due to the structural significance of the highly conserved di-sulfide bridge in many dragline spidroin C terminal domains<sup>229</sup>. NT2RepCT has nine tyrosine residues, four in the repetitive region and five in the C terminus (Figure 75). Tyrosine residues can be conjugated with PTAD azide (4-(4-(2-azidoethoxy)phenyl)-1,2,4-triazolidine-3,5-dione) under mild conditions, adding a functional handle<sup>230</sup> which can then be conjugated to fluorescein alkyne using click chemistry (Figure 76-Figure 77). The reaction between the phenol R group of tyrosine and PTAD could occur via several reaction mechanisms depending on reaction conditions which can be found described by D. Kaiser *et al*<sup>231</sup>. FAM alkyne was used due to ease of availability and as a model. However, other molecules containing an alkyne might be clicked onto NT2RepCT-PTAD-N<sub>3</sub> instead. Cyclic arginine-glycine-aspartate peptide (cyclic-RGD)<sup>78</sup> was clicked to 4RepCT<sup>3Aha</sup> with strain promoted alkyne-azide cycloaddition (SPAAC) to improve human mesenchymal stem cell adhesion<sup>78</sup> and the antibiotic levofloxacin was clicked to 4RepCT<sup>3Aha</sup> using CuAAC<sup>91</sup> to add antibacterial functionality to the material. PTADs have been used to impart functionality to biomaterials such as <sup>18</sup>F for radiofluorination<sup>232</sup>. PTADS were also used to create an elastin-like protein (ELP) chemically crosslinked hydrogel through combining PTAD azide functionalized ELP with cyclooctyne functionalized ELP and using SPAAC to form crosslinks<sup>230</sup>. Use of PTADs is relatively economical with PTAD azide costing £3.44/mg (Sigma Aldrich), has quick reaction times, is easily purified and can be performed in aqueous environments.

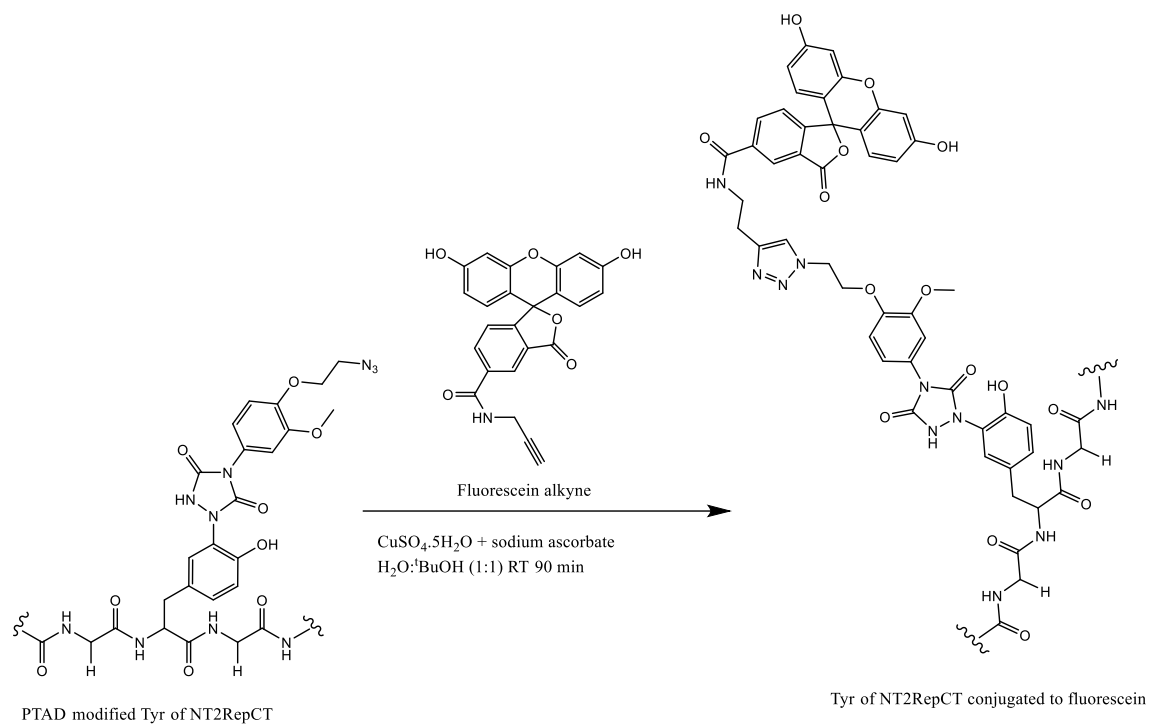


Figure 76: Conjugation of FAM-alkyne (Fluorescein alkyne) with NT2RepCT-PTAD N<sub>3</sub> via copper catalyzed azide-alkyne cycloaddition (CuAAC)



the expected molecular weight was shifted by bulging of the band of interest. However, this was an artefact of the SDS-PAGE gel since the same effect was seen at the dye front. Un-bound FAM alkyne migrated with the dye front in all samples containing FAM alkyne, including in the successful CuAAC reactions suggesting the CuAAC reactions contained an excess of FAM alkyne or there was incomplete reaction. However, since there were fluorescent protein bands in the CuAAC reactions it can be concluded that all PTAD conjugation reaction conditions went on to produce covalently bound FAM alkyne in the CuAAC reactions. The PTAD conjugation reactions containing acetonitrile (Figure 67 lanes C and E) created more higher weight oligomers of NT2RepCT compared to dry DMF (Figure 67 lanes B and D), which was carried through in the CuAAC reaction with FAM alkyne, although the protein band was smaller than DMF suggesting either protein loss or a greater shift to oligomers. Additionally, the protein band mid-point of the NT2RepCT-PTAD-N<sub>3</sub> monomer was higher molecular weight with acetonitrile than dry DMF possibly indicating a larger number of tyrosine residues reacted with the PTAD azide. These results taken together indicate successful replication of work published by H. Ban *et. al*<sup>224</sup> with small (89.5 μL) reaction volumes, dry DMF and 100 mM Na Phosphate pH 7.5 and removal of unreacted components with Zeba™ spin desalting columns. Additionally, the conjugation was successful at larger volumes (1 mL) using acetonitrile and 20 mM Tris pH 8 and using dialysis to remove un-reacted components PTAD reaction components instead of Zebaspin™ columns.

#### **7.4.4. *In vitro* Rhodamine B release**

The fluorescent dye rhodamine B (RhB) was chosen as a model drug surrogate for the *in vitro* release assay as it is small and hydrophilic. RhB is a commonly used model drug surrogate<sup>215,222,233</sup> due to its ready availability and strong fluorescent signals in aqueous environments. This allows monitoring of RhB release by fluorescence

microscopy from a hydrogel. The RhB release assay described here was based on work published by F. Luo *et al.*<sup>130</sup>. In the published study, 0.05 mg/mL RhB was used per 100  $\mu$ L 16.7 % (w/v) NcCT hydrogel. The hydrogel NcCT was formed, from a recombinant spidroin based on CT domain from MaSp1 of *Nephila clavipes*. NcCT gelation was induced by 37 °C incubation overnight. However, compared to NT2RepCT NcCT does not contain the repetitive domain or non-repetitive NT. Furthermore, NT2RepCT is very hydrophilic and pH responsive spidroin<sup>2</sup>. Release of RhB in the published study by F. Luo *et al.* was monitored in PBS at pH 5.0, 6.0 and 7.2 with a dissolution volume of 200  $\mu$ L. Furthermore, the hydrogels in the study were formed in a 96 well plate whereas NT2RepCT hydrogels were formed in a 24 well plate and therefore they had different morphologies. Comparing the *in vitro* RhB release assay results from NT2RepCT hydrogels MQ 37 T and CAPS10 and NcCT hydrogels, both showed pH responsive release with differing cumulative percentage RhB released throughout the assay at the 3 PBS pH. Interestingly, NT2RepCT hydrogels had the opposite pH response to NcCT hydrogels with release of rhodamine B decreasing as pH increased. Whereas, NcCT hydrogels showed increasing rhodamine B release with increasing PBS pH. RhB fluorescence is highest at acidic pH and decreases towards neutral pH<sup>234</sup>. However, in this study three standard lines were created at the three PBS pH to account for this difference in fluorescence intensity. The pH values were chosen for two reasons: a) at pH below 5.5, NT2RepCT changes conformation to elicit fibre formation, b) pH 6.45 and pH 7.4 represent different pH in different organs in the body.

The pH dependent release might be explained by the conformation change that NT2RepCT undertakes at pH 5.5<sup>2</sup> and below, releasing more RhB from the network and by the pH moving closer to NT2RepCT PI of 4.26, leading to reduced net charge and reduced interaction with RhB. Between the two hydrogels, CAPS10 released more RhB

than MQ 37 T with a significant increase at pH 7.4. When swollen in PBS at pH 5, 6.45 and 7.6, MQ 37 T swells significantly more than CAPS10 and one would infer that this would lead to increased RhB release. However, ionic shielding in CAPS10 by PBS leads to reduced electrostatic repulsion and therefore reduced net charge. This means there was less interaction between NT2RepCT and RhB in CAPS10 than MQ 37 T in PBS pH 7.4 leading to increased drug release.

As with NcCT, 100 % RhB release did not occur from MQ 37 T and CAPS10 hydrogels during the duration of the experiment. This was likely a result of interactions between RhB and NT2RepCT which were strengthened with increasing pH due to an increase in net negative charge. The release of RhB from MQ 37 T and CAPS10 hydrogels might increase over a longer time period than 10.5 hours. In comparison, maximal release from NcCT hydrogels was achieved after 12 hours at ~50 % and did not increase up to 36 hours which was the final time point. The authors suggested that release of RhB would likely increase to 100 % as the hydrogel was degraded, if used *in vivo*<sup>130</sup>. An investigation of the biodegradation of NT2RepCT hydrogels in simulated *in vivo* conditions *in vitro* with protease solution is required to determine whether 100 % release could occur.

Further work is required to investigate the effect of acidic and alkaline pH on model drug release and to see if the drug release can be further tuned and controlled. Additionally, PBS is a simple system and does not reflect the complexities of *in vivo* conditions<sup>235</sup>. Furthermore, the hydrogels and solution were static with no mixing or stirring which would occur *in vivo* which can affect drug release kinetics.

#### **7.4.5. *In vitro* FAM release**

Conjugation of a drug to the hydrogel network via a covalent bond seeks to increase the duration of release and control the release rate compared to a drug that is simply encapsulated in the network. Since the number of successful FAM alkyne to PTAD

conjugations or number of PTAD to tyrosine residue conjugations for NT2RepCT-PTAD was unknown, a low concentration was chosen for the hydrogels containing FAM alkyne by encapsulation with no covalent bonds. Therefore, the controls of free, encapsulated FAM alkyne hydrogels (FAM MQ and FAM CAPS10) contained 0.65  $\mu\text{g}$  FAM alkyne/gel. Which was equivalent to one FAM alkyne molecule for every 2 molecules NT2RepCT with one PTAD- $\text{N}_3$ . This was calculated by using molar ratios of the PTAD-FAM MQ and PTAD-FAM CAPS10 hydrogels which were prepared containing 100  $\mu\text{L}$  1 mg/mL NT2RepCT-PTAD-FAM. FAM alkyne and not FAM was used in the 'free' encapsulated hydrogels for continuity and to account for the potential differences the alkyne could contribute in interactions between NT2RepCT and fluorescein.

1.) NT2RepCT PTAD-FAM MQ and PTAD-FAM-CAPS10 samples:

100  $\mu\text{L}$  of 1 mg/mL NT2RepCT-PTAD-FAM added to 450  $\mu\text{L}$  26.7 mg/mL NT2RepCT to make 24 mg/mL NT2RepCT total, therefore 0.1 mg NT2RepCT-PTAD-FAM per 100  $\mu\text{L}$  hydrogel. The molecular weight of NT2RepCT is 33,278  $\text{g mol}^{-1}$  and the molecular weight of PTAD azide is 262.22  $\text{g mol}^{-1}$ .

$$\frac{0.1 \times 10^{-3} \text{g}}{33,278 \text{ g mol}^{-1} + 262.22 \text{ g mol}^{-1}} = 7.15 \times 10^{-8} \text{ moles} \times 6.02 \times 10^{23}$$

$$= 1.79 \times 10^{15} \text{ molecules NT2RepCTPTAD/gel}$$

2.) FAM MQ and FAM CAPS10 hydrogels containing 0.65  $\mu\text{g}$  FAM alkyne per 100  $\mu\text{L}$  hydrogel. The molecular weight of FAM alkyne is 413.38  $\text{g mol}^{-1}$ .

$$\frac{0.65 \times 10^{-6} \text{g}}{413.38 \text{ g mol}^{-1}} = 1.57 \times 10^{-9} \text{ moles} \times 6.02 \times 10^{23}$$

$$= 9.47 \times 10^{14} \text{ molecules FAM alkyne/gel}$$

3.) Calculating the ratio between NT2RepCT-PTAD and FAM alkyne.:

$$1.59 \times 10^{15} \text{ molecules NT2RepCTPTAD} : 9.47 \times 10^{14} \text{ molecules FAM alkyne}$$

$$= 1.69 \text{ molecules NT2RepCTPTAD} : 1 \text{ molecule FAM alkyne}$$

4.) Mass FAM alkyne (mg) needed for 1 successful PTAD-FAM conjugation based on number of molecules of NT2RepCT-PTAD from 1.)

$$\frac{1.79 \times 10^{15} \text{ molecules NT2RepCTPTAD}}{6.02 \times 10^{23}}$$

$$= 2.97 \times 10^{-9} \text{ moles} \times 413.38 \text{ gmol}^{-1}$$

$$= 1.22 \times 10^{-6} \text{ g} = 1.22 \text{ } \mu\text{g FAM alkyne}$$

These calculations assume 1 successful PTAD conjugation to 1 tyrosine residue on NT2RepCT.

However, 0.65  $\mu\text{g}$  FAM alkyne per hydrogel is half of 1 successful conjugation (1.22  $\mu\text{g}$  FAM alkyne per hydrogel). This means that whatever the conjugation state of the PTAD-FAM MQ and PTAD-FAM CAPS10 hydrogels, less FAM alkyne was released during the experiment than the 0.65  $\mu\text{g}$  FAM alkyne control hydrogels FAM MQ and FAM CAPS10. However, it is possible that the amount of FAM alkyne in the PTAD-FAM MQ and PTAD-FAM CAPS10 hydrogels is even less than 0.65  $\mu\text{g}$  and this could explain the lower rate and level of release throughout the drug release assay. Therefore, the results of this release assay should be taken with caution and do not conclusively show that the release rate is reduced or that release is controlled with covalent bonding via PTADs. Mass spectrometry is required to assess the success of the PTAD conjugation and the CuAAC reaction to conjugate FAM alkyne to NT2RepCT.

Examining the hydrogels that contained encapsulated and free FAM alkyne, FAM MQ and FAM CAPS10, during the release assay time (22h) only  $35.0 \pm 6.6 \%$  and  $21.4 \pm 1.4 \%$  loaded FAM alkyne were released respectively (Table 17) and (Figure 72). This is less release in a longer duration compared to the release of RhB from CAPS10 in PBS pH 7.4, which released  $\sim 67 \%$  after 10.5 hours. However, although RhB and FAM alkyne have similar structures (Figure 78), the RhB release experiment had a larger

dissolution buffer volume (1 mL compared to 250  $\mu$ L) and the hydrogels were loaded with more RhB than FAM alkyne (5  $\mu$ g RhB compared to 0.65  $\mu$ g FAM alkyne). This can increase release rate<sup>218,128</sup>.

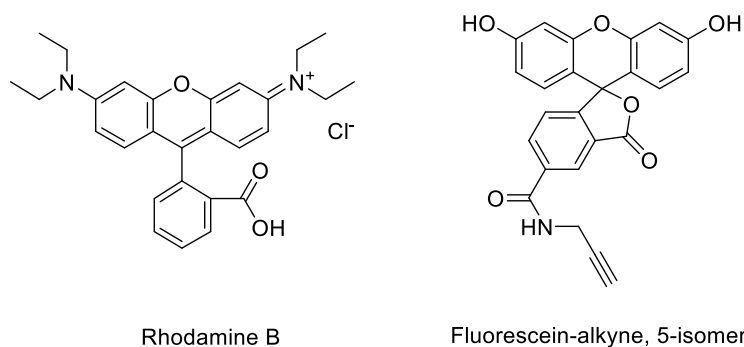


Figure 78: Rhodamine B (RhB) and FAM alkyne structure

Since FAM MQ released more FAM alkyne than FAM CAPS10 hydrogel this means that FAM alkyne had stronger interactions that slowed rate of release with FAM alkyne from CAPS10. Therefore, unlike RhB release which showed increased release from CAPS10 which was not expected from the swelling results, FAM alkyne release follows the swelling results in PBS. This likely means that there is less interaction between NT2RepCT and FAM alkyne than between NT2RepCT and RhB or that the interactions are less electrostatic in nature. Further work is needed to understand the interactions between model drug surrogates and NT2RepCT with respect to pH and protein secondary structure.

Release of FAM alkyne from FAM-MQ showed greater standard deviation than from FAM-CAPS10. This is likely related to the lower Young's modulus and elastic modulus leading to erosion or damage to the hydrogel with repeated pipetting to remove aliquots and replace with fresh media. During swelling experiments, the MQ 37 T hydrogels were extremely soft and prone to breakage. The initial burst release profile was likely caused by excess FAM alkyne present which had not covalently bound to

the PTAD azide on NT2RepCT during the CuAAC reaction, leading to free FAM alkyne rapidly diffusing out of the hydrogels. This was followed by minimal further diffusion of FAM alkyne out of the hydrogel due to most of the remaining FAM alkyne being covalently attached to NT2RepCT. Excess, unbound FAM alkyne was seen in SDS PAGE (Figure 66-Figure 67). Additional wash steps of the hydrogel could minimize this effect.

#### **7.4.6. Kinetic modelling**

The release of the model drugs RhB and FAM alkyne were fitted to four distinct mathematical models, zero order release, first order release, the Higuchi equation and the Korsmeyer-Peppas equation. The goodness of fit was assessed by the coefficient of determination  $R^2$ . All models make assumptions and have limitations and in complex cases such as hydrogels there are many factors governing release such as, interactions between the hydrogel and the drug, the presence of a large amount of water and swelling of the hydrogel. Additionally, models assume certain conditions such as a perfect sink for the drug to be released into, assumptions about the geometry of the drug delivery system, constant diffusivity of the drug and initial uniform drug concentrations throughout the system<sup>236</sup>. In the case of the Higuchi and Korsmeyers-Peppas equation these assume either a 2D film or an infinite length cylinder and no swelling. Furthermore, both MQ 37 T and CAPS10 hydrogels swell in PBS and this likely contributes to drug release. More informative and complex solutions involve use of neural networks or multi-component systems which assess movement of water, interactions between drug molecules and the hydrogel and the influence of swelling to model drug release. Unfortunately, that is out of the scope of this thesis and therefore, with caution, single component models which only consider drug mass transport using kinetic models have been used.

Zero order kinetics describes constant release, where the amount of drug released per unit time is the same throughout the process and is independent of concentration.

Zero order kinetics have been seen in hydrogels that rely on drug loss by surface erosion<sup>217</sup>. First order release describes a system where the same percentage of the loaded drug is released per unit time and depends on concentration. The *in vitro* RhB and FAM alkyne release data did not fit well to either of these kinetic models with R<sup>2</sup> ranging from 0.82-0.88 for zero order and 0.31-0.76 for first order. Interestingly, the kinetic modelling for both RhB release and FAM alkyne release had largest R<sup>2</sup> values with the Korsmeyer-Peppas equation, although RhB release also fit well to the Higuchi equation which FAM alkyne release did not. The rate constant  $k$  of FAM alkyne release was similar for MQ FAM and MQ CAPS10 at 6.48 min<sup>-1</sup> and 7.96 min<sup>-1</sup> respectively. Whereas, at pH 7.2 the rate constant  $k$  of RhB release was 4.13 min<sup>-1</sup> from MQ hydrogels but 6.64 min<sup>-1</sup> from CAPS10 hydrogels. Additionally, the diffusivity exponent was closer to 0.5 indicating Fickian diffusion of Rhodamine B but lower at 0.2 indicating either more quasi-Fickian diffusion or less applicability to the Korsmeyer-Peppas model. This suggests diffusional release with minimal contribution from swelling. However, it should be considered that the hydrogels used in the FAM alkyne release assay were cast in wells of 96 well plate and were therefore more cylindrical than the hydrogels in the RhB release assay which were ring shapes, in addition to the differences in dissolution buffer volume.

As expected, the rate constant was greater for FAM MQ and CAPS10 than PTAD-FAM MQ and PTAD-FAM CAPS10 due to FAM alkyne being encapsulated in the system rather than covalently bound to NT2RepCT. The diffusivity exponent  $n$  was similar for both the free FAM hydrogels and the PTAD conjugated hydrogels at  $\sim 0.2$  indicating purely diffusional release.

## 7.5. Summary

The transparent NT2RepCT hydrogels MQ 37 T and CAPS10 were formed in a syringe and were extruded out of a 16 G needle and retained their extruded shape. Injectable hydrogels are useful in drug delivery or medical purposes as there is no surgery required to implant into the body. It was found that MQ 37 T and CAPS10 were shear-thinning with non-Newtonian properties. This is a very promising result and opens possibilities for 3D printing and drug delivery.

Drug release experiments of the model drug surrogate Rhodamine B (RhB) was found to be pH responsive from MQ 37 T and CAPS10. The maximum cumulatively released RhB decreased as pH increased from 5.5 to 7.2. Stimulus responsive hydrogels are incredibly useful for targeted drug release and this initial result is proof of concept that NT2RepCT hydrogels could be used in this field. Additionally, at pH 7.2 it was found that CAPS10 released significantly more RhB than MQ 37 T. The release data was fitted to four kinetic release models and was found to be diffusional by the Korsmeyers-Peppas kinetic model.

Tyrosine residues in NT2RepCT were exploited as functional handles by reaction with PTAD-N<sub>3</sub>. CuAAC was used to covalently bond FAM alkyne to the added azide moiety. It was found that in both dry DMF and acetonitrile, at 1 mL scale this conjugation was successful as judged by SDS-PAGE. This is the first time a functional handle has been added to NT2RepCT, although confirmation with mass spectrometry is required.

The release rate of FAM alkyne was reduced and controlled in MQ 37 T and CAPS10 hydrogels containing covalently linked FAM alkyne. Hydrogels containing physically entrapped 'free' FAM alkyne had increased release kinetics, illustrating how hydrogels can be altered for different drug delivery applications.

This chapter demonstrates proof of concept that NT2RepCT hydrogels can be used for injectable drug delivery, that are not only stimulus responsive but can have controlled release rates through covalent bonds between the protein and the drug.

## 8. Project conclusions

To contribute to the growing need for new xeno-free materials to form biomaterials for controlled drug delivery, protein hydrogels were formed from the recombinant miniature spidroin NT2RepCT. Self-assembling, natural and physically crosslinked hydrogels were formed in various buffers by thermal gelation at 37 °C or 40 °C. These hydrogels were characterised by a variety of techniques to understand the factors affecting gelation, how this can be controlled and the hydrogel's feasibility as a controlled drug delivery system.

Results showed that pH of gelation was a critical factor due to the pH sensitive NT2RepCT protein secondary structure changes and charge state. Additionally, it was found that presence of metal cations or cell culture appropriate medium such as DMEM or PBS inhibited hydrogel formation.

In pure MQ water or at pH 10, transparent, highly swelling and non-dissociating NT2RepCT protein hydrogels were formed. These were called MQ 37 T and CAPS10. Hydrogels formed in impure MQ water, at pH 7 or buffers not able to maintain pH 10 were opaque, with minimal swelling and dissociation in DMEM or PBS at 37 °C. These were opaque hydrogels called MQ 37 O, MQ 40 O, t7 37 O, t7 40 O, t10 37 O and t10 40 O.

It was found that there was a correlation between high light transmittance and high swelling ratios due to increased electrostatic repulsion within the hydrogel. Furthermore, the swelling behaviour of the hydrogels in pure MQ water or DMEM could be controlled by the gelation conditions demonstrating the tunable properties

of NT2RepCT protein hydrogels. Chemical crosslinking of the opaque hydrogels with glutaraldehyde (GA) prevented dissociation and led to increased swelling compared to the non-crosslinked.

An examination of pore morphology by SEM indicated extensive, inter-connected porous networks throughout the hydrogels. However, the SEM, cryo-SEM and eSEM sample preparation was found to be critical to minimise crystalline ice formation and artefacts which could provide inaccurate pore sizes. Furthermore, chemical crosslinking with glutaraldehyde (GA) of the formed hydrogels was necessary to minimize pore collapse and preserve hydrogel architecture in the SEM analysis as non-crosslinked hydrogels showed extensive ice formation and minimal pores. The transparent hydrogels MQ 37 T and CAPS10 were found to have a higher porosity and contained nano-fibrils within the pores compared to the opaque hydrogels MQ 37 O, t10 37 O and t10 40 O which contained no fibrils. However, the influence of GA crosslinking changing aspects of the hydrogel morphology cannot be ruled out as the reason for this result.

Stiffness was found to be improved at alkaline pH of gelation in both the opaque and transparent hydrogels. Additionally, GA crosslinking increased the opaque hydrogel stiffness and material handling capabilities. However, due to the need for chemical crosslinking the opaque hydrogels were not carried forward in this research as GA is toxic and difficult to remove.

The rheological properties of the transparent hydrogels MQ 37 T and CAPS10 were found to be viscoelastic. The hydrogels were stable up to 10 % strain as determined by the LVE region with CAPS10 moduli greater than MQ 37 T moduli. Both MQ 37 T and CAPS10 hydrogels had the same moduli dependence with increasing frequency. Both MQ 37 T and CAPS10 were shear-thinning and injectable, retaining their extruded shape. It was found that the introduction of shear-force from injection-initiated fibril

formation with a clear difference in morphology between the non-injected and the injected as assessed by SEM.

MQ 37 T and CAPS10 loaded with the model drug surrogate Rhodamine B showed pH dependent, diffusional based release. Rhodamine B release was lowest at neutral pH and increased with increasing acidity. A functional handle was added to tyrosine residues using PTAD-azide under physiological conditions. Then, CuAAC was used to conjugate FAM alkyne to the NT2RepCT-PTAD azide. The release of FAM alkyne was controlled in both MQ 37 T and CAPS10 hydrogels when FAM alkyne was covalently conjugated compared to non-conjugated.

Thus, NT2RepCT can be formed into protein hydrogels with tunable characteristics suitable for injectable, controlled drug delivery.

## 9. Future work

In this research project, the recombinant spidroin NT2RepCT was formed into protein hydrogels which showed tunable properties. The hydrogels were shown to be suitable for injectable drug delivery. Since NT2RepCT is a very new protein (first reported in 2017), there are many opportunities for this exciting spidroin. Furthermore, the protein hydrogels described here are not fully characterised and there are many questions remaining about their formation and behaviours. Therefore, some suggestions for improving the current study and opportunities for future endeavors are described below.

The CD study examining NT2RepCT protein secondary structure was only performed in temperature ramp mode between 7-74 °c with minimal time at each temperature. To further understand the mechanisms involved in gelation, NT2RepCT protein secondary structure should be monitored at the three established gelation conditions of MQ water, pH 7 and pH 10 at 37 °C for the duration of gelation. This would inform

to the extent of these changes and offer some insight into how important these changes are for hydrogel formation. Additionally, the reversibility of NT2RepCT temperature induced secondary structure conformation change in MQ water should be determined as it was for pH 7 and pH 10 in this study.

The behaviour of NT2RepCT in acidic, buffered conditions and its effect on hydrogel formation should be investigated. At pH 5.5 and below NT2RepCT forms fibres due to shear force, NT dimerization and CT unfolding to  $\beta$ -amyloid like fibrils. One would expect that a hydrogel formed in buffered acidic conditions would contain extensive nano-fibres that could improve the stiffness, strength and other material properties.

Although some research into the minimum concentration for hydrogel formation was performed in this study the results were variable and incomplete. An investigation into how NT2RepCT concentration affects gelation kinetics, hydrogel formation and material properties should be performed. It is expected that increasing concentration would reduce gelation time, swelling ratios and increase the stiffness and moduli.

Natural spider silk is non-immunogenic and various recombinant spidroins have been shown to induce low inflammation and immune response *in vitro* and *in vivo*. However, the specific immune response of NT2RepCT should be assessed in soluble form, as fibres and as hydrogels to ensure biomaterials formed from it are safe for use in biomedical settings.

Further work on the swelling behaviour of the NT2RepCT hydrogels would be useful to determine whether this behaviour is pH dependent. For example, reduced swelling at acidic pH but increased at neutral or alkaline pH opens possibilities of stimulus responsive 'smart' hydrogels. Since NT2RepCT is pH responsive it would be expected that some pH dependent swelling behaviour would be seen in addition to the differences in swelling in MQ water compared to PBS/DMEM as demonstrated in this study.

The capability for NT2RepCT hydrogels to support cell attachment, growth and survival is an important area of interest given the limited opportunities in the present research for cell culture. The bioactive properties of NT2RepCT can be improved by addition of RGD integrin recognition sites via tyrosine PTAD conjugation. Furthermore, if NT2RepCT can support cell growth then there are possibilities of producing drug loaded hydrogels which could be implanted long term. Following on from this endeavor, the biodegradation of NT2RepCT in various forms should be examined to assess the shelf life of these biomaterials.

## References

- (1) Holland, C.; Numata, K.; Rnjak-Kovacina, J.; Seib, F. P. The Biomedical Use of Silk: Past, Present, Future. *Adv. Healthc. Mater.* **2019**, *8* (1), 1800465. <https://doi.org/10.1002/adhm.201800465>.
- (2) Andersson, M.; Jia, Q.; Abella, A.; Lee, X. Y.; Landreh, M.; Purhonen, P.; Hebert, H.; Tenje, M.; Robinson, C. V.; Meng, Q.; et al. Biomimetic Spinning of Artificial Spider Silk from a Chimeric Minispidroin. *Nat. Chem. Biol.* **2017**, *13* (3), 262–264. <https://doi.org/10.1038/nchembio.2269>.
- (3) Ahmed, E. M. Hydrogel: Preparation, Characterization, and Applications: A Review. *J. Adv. Res.* **2015**, *6* (2), 105–121. <https://doi.org/10.1016/j.jare.2013.07.006>.
- (4) Hassanbhai, Ammar Mansoor; Lau, Chau Sang; Wen, Feng; Jayaraman, Praveena; Goh, Bee Tin; Yu, Na; Teoh, S.-H. In Vivo Immune Responses of Cross-Linked Electrospun Tilapia Collagen Membrane. *Tissue Eng. Part A* **2017**, *23* (5), 1110–1120. <https://doi.org/10.1089/ten.tea.2016.0504>.
- (5) Tokareva, O.; Jacobsen, M.; Buehler, M.; Wong, J.; Kaplan, D. L. Structure-Function-Property-Design Interplay in Biopolymers: Spider Silk. *Acta Biomater.* **2014**, *10* (4), 1612–1626. <https://doi.org/10.1016/j.actbio.2013.08.020>.
- (6) Andersson, M.; Johansson, J.; Rising, A. Silk Spinning in Silkworms and Spiders. *Int. J. Mol. Sci.* **2016**, *17* (8), 1–14. <https://doi.org/10.3390/ijms17081290>.
- (7) Walker, A. A.; Church, J. S.; Woodhead, A. L.; Sutherland, T. D. Silver Fish Silk Is Formed by Entanglement of Randomly Coiled Protein Chains. *Insect Biochem. Mol. Biol.* **2013**, *43* (7), 572–579. <https://doi.org/10.1016/j.ibmb.2013.03.014>.
- (8) Campbell, P. M.; Trueman, H. E.; Zhang, Q.; Kojima, K.; Kameda, T.; Sutherland, T. D. Cross-Linking in the Silks of Bees, Ants and Hornets. *Insect Biochem. Mol. Biol.* **2014**, *48*, 40–50. <https://doi.org/10.1016/j.ibmb.2014.02.009>.
- (9) Nudelman, F.; Chen, H. H.; Goldberg, H. A. Spiers Memorial Lecture Lessons from Biomineralization : Comparing the Growth Strategies of Mollusc Shell Prismatic and Nacreous Layers in *Atrina Rigida*. *Faraday Discuss.* **2007**, *136*, 9–25. <https://doi.org/10.1039/b704418f>.
- (10) Liu, J.; Guo, D.; Zhou, Y.; Wu, Z.; Li, W.; Zhao, F.; Zheng, X. Identification of Ancient Textiles from Yingpan, Xinjiang, by Multiple Analytical Techniques. *J. Archaeol. Sci.* **2011**, *38* (7), 1763–1770. <https://doi.org/10.1016/j.jas.2011.03.017>.
- (11) Griggs, J. On the Silk Road. *New Sci.* **2012**, *213* (2850), 36–39. [https://doi.org/https://doi.org/10.1016/S0262-4079\(12\)60307-8](https://doi.org/https://doi.org/10.1016/S0262-4079(12)60307-8).
- (12) Lefèvre, T.; Auger, M. Spider Silk as a Blueprint for Greener Materials: A Review. *Int. Mater. Rev.* **2016**, *61* (2), 127–153. <https://doi.org/10.1080/09506608.2016.1148894>.

- (13) Vollrath, F.; Knight, D. P. Liquid Crystalline Spinning of Spider Silk. *Nature* **2001**, *410* (6828), 541–548. <https://doi.org/10.1038/35069000>.
- (14) Gerritsen, V. B. The Tiptoe of an Airbus. *Protein Spotlight* **2002**, *24*, 1–2.
- (15) Hsia, Y.; Gnesa, E.; Jeffery, F.; Tang, S.; Vierra, C. Spider Silk Composites and Applications. In *Metal, Ceramic and Polymeric Composites for Various Uses*; Cuppoletti, J., Ed.; 2011; pp 303–324.
- (16) Bon, M. A Discourse upon the Usefulness of the Silk of Spiders. *Philos. Trans.* **1710**, *27*, 2–16.
- (17) Forrest, R. D. Early History of Wound Treatment. *J. R. Soc. Med.* **1982**, *75* (3), 198–205.
- (18) Omenetto, F. G.; Kaplan, D. L. New Opportunities for an Ancient Material. *Science* (80-. ). **2010**, *329* (5991), 528–531. <https://doi.org/10.1126/science.1188936>.
- (19) Vollrath, F.; Barth, P.; Basedow, A.; Engström, W.; List, H. Local Tolerance to Spider Silks and Protein Polymers in Vivo. *In Vivo (Brooklyn)*. **2002**, *16* (4), 229–234.
- (20) Heim, M.; Keerl, D.; Scheibel, T. Spider Silk: From Soluble Protein to Extraordinary Fiber. *Angew. Chemie - Int. Ed.* **2009**, *48* (20), 3584–3596. <https://doi.org/10.1002/anie.200803341>.
- (21) Römer, L.; Scheibel, T. The Elaborate Structure of Spider Silk: Structure and Function of a Natural High Performance Fiber. *Prion* **2008**, *2* (4), 154–161. <https://doi.org/10.4161/pri.2.4.7490>.
- (22) Sponner, A.; Schlott, B.; Vollrath, F.; Unger, E.; Grosse, F.; Weisshart, K. Characterization of the Protein Components of Nephila Clavipes Dragline Silk. *Biochemistry* **2005**, *44* (12), 4727–4736.
- (23) Jackson, C.; Brien, J. P. O. Molecular Weight Distribution of Nephila Clavipes Dragline Silk. *Macromolecules* **1995**, *28* (17), 5975–5977.
- (24) Lewis, R. V. Spider Silk : Ancient Ideas for New Biomaterials. *Chem. Rev.* **2006**, *106* (9), 3762–3774. <https://doi.org/10.1021/cr010194g>.
- (25) Hinman, M. B.; Lewis, R. V. Isolation of a Clone Encoding a Second Dragline Silk Fibroin. *J. Biol. Chem.* **1992**, *267* (21), 19320–19324.
- (26) Hagn, F.; Eisoldt, L.; Hardy, J. G.; Vendrely, C.; Coles, M.; Scheibel, T.; Kessler, H. A Conserved Spider Silk Domain Acts as a Molecular Switch That Controls Fibre Assembly. *Nature* **2010**, *465* (7295), 239–242. <https://doi.org/10.1038/nature08936>.
- (27) Rammensee, S.; Slotta, U.; Scheibel, T.; Bausch, A. R. Assembly Mechanism of Recombinant Spider Silk Proteins. *Proc. Natl. Acad. Sci. U. S. A.* **2008**, *105* (18), 6590–6595. <https://doi.org/10.1073/pnas.0709246105>.
- (28) Rising, A.; Johansson, J. Toward Spinning Artificial Spider Silk. *Nat. Chem. Biol.* **2015**, *11* (5), 309–315. <https://doi.org/10.1038/nchembio.1789>.

- (29) Guinea, G. V.; Elices, M.; Plaza, G. R.; Perea, G. B.; Daza, R.; Riekkel, C.; Agulló-Rueda, F.; Hayashi, C.; Zhao, Y.; Pérez-Rigueiro, J. Minor Ampullate Silks from *Nephila* and *Argiope* Spiders: Tensile Properties and Microstructural Characterization. *Biomacromolecules* **2012**, *13* (7), 2087–2098. <https://doi.org/10.1021/bm3004644>.
- (30) Scheibel, T. Spider Silks: Recombinant Synthesis, Assembly, Spinning, and Engineering of Synthetic Proteins. *Microb. Cell Fact.* **2004**, *3* (1), 14. <https://doi.org/10.1186/1475-2859-3-14>.
- (31) Jenkins, J. E.; Creager, M. S.; Lewis, R. V.; Holland, G. P.; Yarger, J. L. Quantitative Correlation between the Protein Primary Sequences and Secondary Structures in Spider Dragline Silks. *Biomacromolecules* **2010**, *11* (1), 192–200. <https://doi.org/10.1021/bm9010672>.
- (32) Challis, R. J.; Goodacre, S. L.; Hewitt, G. M. Evolution of Spider Silks: Conservation and Diversification of the C-Terminus. *Insect Mol. Biol.* **2006**, *15* (1), 45–56. <https://doi.org/10.1111/j.1365-2583.2005.00606.x>.
- (33) Hayashi, C. Y.; Shipley, N. H.; Lewis, R. V. Hypotheses That Correlate the Sequence, Structure, and Mechanical Properties of Spider Silk Proteins. *Int. J. Biol. Macromol.* **1999**, *24* (2–3), 271–275. [https://doi.org/10.1016/S0141-8130\(98\)00089-0](https://doi.org/10.1016/S0141-8130(98)00089-0).
- (34) Jaudzems, K.; Askarieh, G.; Landreh, M.; Nordling, K.; Hedhammar, M.; Jörnvall, H.; Rising, A.; Knight, S. D.; Johansson, J. PH-Dependent Dimerization of Spider Silk N-Terminal Domain Requires Relocation of a Wedged Tryptophan Side Chain. *J. Mol. Biol.* **2012**, *422* (4), 477–487. <https://doi.org/10.1016/j.jmb.2012.06.004>.
- (35) Andersson, M.; Chen, G.; Otikovs, M.; Landreh, M.; Nordling, K.; Kronqvist, N.; Westermarck, P.; Jörnvall, H.; Knight, S.; Ridderstråle, Y.; et al. Carbonic Anhydrase Generates CO<sub>2</sub> and H<sup>+</sup> That Drive Spider Silk Formation Via Opposite Effects on the Terminal Domains. *PLoS Biol.* **2014**, *12* (8), 1–14. <https://doi.org/10.1371/journal.pbio.1001921>.
- (36) Askarieh, G.; Hedhammar, M.; Nordling, K.; Saenz, A.; Casals, C.; Rising, A.; Johansson, J.; Knight, S. D. Self-Assembly of Spider Silk Proteins Is Controlled by a PH-Sensitive Relay. *Nature* **2010**, *465* (7295), 236–239. <https://doi.org/10.1038/nature08962>.
- (37) Landreh, M.; Askarieh, G.; Nordling, K.; Hedhammar, M.; Rising, A.; Casals, C.; Astorga-Wells, J.; Alvelius, G.; Knight, S. D.; Johansson, J.; et al. A PH-Dependent Dimer Lock in Spider Silk Protein. *J. Mol. Biol.* **2010**, *404* (2), 328–336. <https://doi.org/10.1016/j.jmb.2010.09.054>.
- (38) Gaines, W. A.; Sehorn, M. G.; Marcotte, W. R. Spidroin N-Terminal Domain Promotes a PH-Dependent Association of Silk Proteins during Self-Assembly. *J. Biol. Chem.* **2010**, *285* (52), 40745–40753. <https://doi.org/10.1074/jbc.M110.163121>.

- (39) Kronqvist, N.; Otikovs, M.; Chmyrov, V.; Chen, G.; Andersson, M.; Nordling, K.; Landreh, M.; Sarr, M.; Jörnvall, H.; Wennmalm, S.; et al. Sequential PH-Driven Dimerization and Stabilization of the N-Terminal Domain Enables Rapid Spider Silk Formation. *Nat. Commun.* **2014**, *5* (2014), 3254. <https://doi.org/10.1038/ncomms4254>.
- (40) Hijirida, D. H.; Do, K. G.; Michal, C.; Wong, S.; Zax, D.; Jelinski, L. W. <sup>13</sup>C NMR of Nephila Clavipes Major Ampullate Silk Gland. *Biophys. J.* **1996**, *71* (6), 3442–3447. [https://doi.org/10.1016/S0006-3495\(96\)79539-5](https://doi.org/10.1016/S0006-3495(96)79539-5).
- (41) Finnigan, W.; Roberts, A. D.; Ligorio, C.; Scrutton, N. S.; Breitling, R.; Blaker, J. J.; Takano, E. The Effect of Terminal Globular Domains on the Response of Recombinant Mini - Spidroins to Fiber Spinning Triggers. *Sci. Rep.* **2020**, *10* (1), 1–13. <https://doi.org/10.1038/s41598-020-67703-1>.
- (42) Eisoldt, L.; Thamm, C.; Scheibel, T. The Role of Terminal Domains during Storage and Assembly of Spider Silk Proteins. *Biopolymers* **2011**, *97* (6), 355–361. <https://doi.org/10.1002/bip.22006>.
- (43) Vollrath, F.; Knight, D. P.; Hu, X. W. Silk Production in a Spider Involves Acid Bath Treatment. *Proc. R. Soc. London Ser. B* **1998**, *265*, 817–820.
- (44) Knight, D. P.; Vollrath, F. Changes in Element Composition along the Spinning Duct in a Nephila Spider. *Naturwissenschaften* **2001**, *88* (4), 179–182. <https://doi.org/10.1007/s001140100220>.
- (45) Dicko, C.; Kenney, J. M.; Knight, D.; Vollrath, F. Transition to a B-Sheet-Rich Structure in Spidroin in Vitro: The Effects of PH and Cations. *Biochemistry* **2004**, *43* (44), 14080–14087. <https://doi.org/10.1021/bi0483413>.
- (46) Hagn, F.; Thamm, C.; Scheibel, T.; Kessler, H. PH-Dependent Dimerization and Salt-Dependent Stabilization of the N-Terminal Domain of Spider Dragline Silk - Implications for Fiber Formation. *Angew. Chemie - Int. Ed.* **2011**, *50* (1), 310–313. <https://doi.org/10.1002/anie.201003795>.
- (47) Rockwood, D. N.; Preda, R. C.; Yücel, T.; Wang, X.; Lovett, M. L.; Kaplan, D. L. Materials Fabrication from Bombyx Mori Silk Fibroin. *Nat. Protoc.* **2011**, *6* (10), 1612–1631. <https://doi.org/10.1038/nprot.2011.379>.
- (48) Asakura, T.; Okushita, K.; Williamson, M. P. Analysis of the Structure of Bombyx Mori Silk Fibroin by NMR. *Macromolecules* **2015**, *48* (8), 2345–2357. <https://doi.org/10.1021/acs.macromol.5b00160>.
- (49) Panilaitis, B.; Altman, G. H.; Chen, J.; Jin, H. J.; Karageorgiou, V.; Kaplan, D. L. Macrophage Responses to Silk. *Biomaterials* **2003**, *24* (18), 3079–3085. [https://doi.org/10.1016/S0142-9612\(03\)00158-3](https://doi.org/10.1016/S0142-9612(03)00158-3).
- (50) Wang, X.; Qiu, Y.; Carr, A. J. Optimization of the Silk Scaffold Sericin Removal Process for Retention of Silk Fibroin Protein Structure and Mechanical. *Biomed. Mater.* **2010**, *5* (3), 35008–35020. <https://doi.org/10.1088/1748-6041/5/3/035008>.

- (51) Thurber, A. E.; Omenetto, F. G.; Kaplan, D. L. In Vivo Bioresponses to Silk Proteins. *Biomaterials* **2015**, *71*, 145–157. <https://doi.org/10.1016/j.biomaterials.2015.08.039>.
- (52) Fredriksson, C.; Hedhammar, M.; Feinstein, R.; Nordling, K.; Kratz, G.; Johansson, J.; Huss, F.; Rising, A. Tissue Response to Subcutaneously Implanted Recombinant Spider Silk: An in Vivo Study. *Materials (Basel)*. **2009**, *2* (4), 1908–1922. <https://doi.org/10.3390/ma2041908>.
- (53) Radtke, C.; Allmeling, C.; Waldmann, K. H.; Reimers, K.; Thies, K.; Schenk, H. C.; Hillmer, A.; Guggenheim, M.; Brandes, G.; Vogt, P. M. Spider Silk Constructs Enhance Axonal Regeneration and Remyelination in Long Nerve Defects in Sheep. *PLoS One* **2011**, *6* (2). <https://doi.org/10.1371/journal.pone.0016990>.
- (54) Liebsch, C.; Bucan, V.; Menger, B.; Köhne, F.; Waldmann, K.; Vaslaitis, D.; Vogt, P. M.; Strauss, S.; Kuhbier, J. W. Preliminary Investigations of Spider Silk in Wounds in Vivo — Implications for an Innovative Wound Dressing. *Burns* **2018**, *44* (7), 1829–1838. <https://doi.org/10.1016/j.burns.2018.03.016>.
- (55) Wright, S.; Goodacre, S. L. Evidence for Antimicrobial Activity Associated with Common House Spider Silk. *BMC Res. Notes* **2012**, *5* (1), 326. <https://doi.org/10.1186/1756-0500-5-326>.
- (56) Huemmerich, D.; Scheibel, T.; Vollrath, F.; Cohen, S.; Gat, U.; Ittah, S. Novel Assembly Properties of Recombinant Spider Dragline Silk Proteins. *Curr. Biol.* **2004**, *14* (22), 2070–2074. <https://doi.org/10.1016/j>.
- (57) Fahnestock, S. R.; Bedzyk, L. A. Production of Synthetic Spider Dragline Silk Protein in *Pichia Pastoris*. *Appl. Microbiol. Biotechnol.* **1997**, *47* (1), 33–39. <https://doi.org/10.1007/s002530050884>.
- (58) Scheller, J.; Gührs, K.; Grosse, F.; Conrad, U. Production of Spider Silk Proteins in Tobacco and Potato. *Nat. Biotechnol.* **2001**, *19* (June), 573–577. <https://doi.org/https://doi.org/10.1038/89335>.
- (59) Widmaier, D. M.; Tullman-ercek, D.; Mirsky, E. A.; Hill, R.; Govindarajan, S.; Minshull, J.; Voigt, C. A. Engineering the Salmonella Type III Secretion System to Export Spider Silk Monomers. *Mol. Syst. Biol.* **2009**, *5* (309), 1–9. <https://doi.org/10.1038/msb.2009.62>.
- (60) Lazaris, A.; Arcidiacono, S.; Huang, Y.; Zhou, J.-F.; Duguay, F.; Chretien, N.; Welsh, E. A.; Soares, J. W.; Karatzas, C. N. Spider Silk Fibres Spun from Soluble Recombinant Silk Produced in Mammalian Cells. *Science (80-. )*. **2002**, *295* (5554), 472–476. <https://doi.org/10.1126/science.1065780>.
- (61) Wen, H.; Lan, X.; Zhang, Y.; Zhao, T.; Wang, Y.; Kajiura, Z.; Nakagaki, M. Transgenic Silkworms ( *Bombyx Mori* ) Produce Recombinant Spider Dragline Silk in Cocoons. *Mol. Biol. Rep.* **2010**, *37* (4), 1815–1821. <https://doi.org/10.1007/s11033-009-9615-2>.
- (62) Xu, H.-T.; Fan, B.-L.; Yu, S.-Y.; Huang, Y.-H.; Zhao, Z.-H.; Lian, Z.-X.; Dai, Y.-P.; Wang, L.-L.; Liu, Z.-L.; Fei, J.; et al. Construct Synthetic Gene Encoding Artificial Spider Dragline Silk Protein and Its Expression in Milk of Transgenic Mice. *Anim. iBotechnology* **2007**, *18* (1), 1–12. <https://doi.org/10.1080/10495390601091024>.

- (63) An, B.; Tang-Schomer, M. D.; Huang, W.; He, J.; Jones, J. A.; Lewis, R. V.; Kaplan, D. L. Physical and Biological Regulation of Neuron Regenerative Growth and Network Formation on Recombinant Dragline Silks. *Biomaterials* **2015**, *48*, 137–146. <https://doi.org/10.1016/j.biomaterials.2015.01.044>.
- (64) Rosano, G. L.; Ceccarelli, E. A. Recombinant Protein Expression in Escherichia Coli: Advances and Challenges. *Front. Microbiol.* **2014**, *5* (172), 1–17. <https://doi.org/10.3389/fmicb.2014.00172>.
- (65) Wong, S.-L. Advances in the Use of Bacillus Subtilis for the Expression and Secretion of Heterologous Proteins. *Curr. Opin. Biotechnol.* **1995**, *6* (5), 517–522. [https://doi.org/10.1016/0958-1669\(95\)80085-9](https://doi.org/10.1016/0958-1669(95)80085-9).
- (66) Petsch, D.; Anspach, F. B. Endotoxin Removal from Protein Solutions. *J. Biotechnol.* **2000**, *76* (2), 97–119. [https://doi.org/10.1016/s0168-1656\(99\)00185-6](https://doi.org/10.1016/s0168-1656(99)00185-6).
- (67) Hedhammar, M. Y.; Bramfeldt, H.; Baris, T.; Widhe, M.; Askarieh, G.; Nordling, K.; Aulock, S. Von; Johansson, J. Sterilized Recombinant Spider Silk Fibres of Low Pyrogenicity. *Biomacromolecules* **2010**, *11* (4), 953–959. <https://doi.org/10.1021/bm9014039>.
- (68) Reichelt, P.; Schwarz, C.; Donzeau, M. Single Step Protocol to Purify Recombinant Proteins with Low Endotoxin Contents. *Protein Expr. Purif.* **2006**, *46* (2), 483–488. <https://doi.org/10.1016/j.pep.2005.09.027>.
- (69) Fahnestock, S. .; Irwin, S. . Synthetic Spider Dragline Silk Proteins and Their Production in Escherichia Coli. *Appl. Microbiol. Biotechnol.* **1997**, *1* (47), 23–32.
- (70) Ayoub, N. A.; Garb, J. E.; Tinghitella, R. M.; Collin, M. A.; Hayashi, C. Y. Blueprint for a High-Performance Biomaterial: Full-Length Spider Dragline Silk Genes. *PLoS One* **2007**, *2* (6), e514. <https://doi.org/10.1371/journal.pone.0000514>.
- (71) Arcidiacono, S.; Mello, C.; Kaplan, D.; Cheley, S.; Bayley, H. Purification and Characterization of Recombinant Spider Silk Expressed in Escherichia Coli. *Appl. Microbiol. Biotechnol.* **1998**, *1* (49), 31–38. <https://doi.org/https://doi.org/10.1007/s002530051133>.
- (72) Xia, X.; Qian, Z.; Seok, C.; Hwan, Y.; Kaplan, D. L.; Yup, S. Native-Sized Recombinant Spider Silk Protein Produced in Metabolically Engineered Escherichia Coli Results in a Strong Fiber. *PNAS* **2010**, *107* (32), 14059–14063. <https://doi.org/10.1073/pnas.1003366107>.
- (73) Bowen, C. H.; Dai, B.; Sargent, C. J.; Bai, W.; Ladiwala, P.; Feng, H.; Huang, W.; Kaplan, D. L.; Galazka, J. M.; Zhang, F. Recombinant Spidroins Fully Replicate Primary Mechanical Properties of Natural Spider Silk. *Biomacromolecules* **2018**, *19* (9), 3853–3860. <https://doi.org/10.1021/acs.biomac.8b00980>.
- (74) Jansson, R.; Lau, C. H.; Ishida, T.; Ramström, M.; Sandgren, M.; Hedhammar, M. Functionalized Silk Assembled from a Recombinant Spider Silk Fusion Protein (Z-4RepCT) Produced in the Methylotrophic Yeast Pichia Pastoris. *Biotechnol. J.* **2016**, *11* (5), 687–699. <https://doi.org/10.1002/biot.201500412>.

- (75) Block, H.; Maertens, B.; Spriestersbach, A.; Brinker, N.; Kubicek, J.; Fabis, R. Immobilized-Metal Affinity Chromatography ( IMAC ): A Review. *Methods Enzymol.* **2009**, *463* (09), 439–473.  
[https://doi.org/10.1016/S0076-6879\(09\)63027-5](https://doi.org/10.1016/S0076-6879(09)63027-5).
- (76) Schacht, K.; Jüngst, T.; Schweinlin, M.; Ewald, A.; Groll, J.; Scheibel, T. Biofabrication of Cell-Loaded 3D Spider Silk Constructs. *Angew. Chemie - Int. Ed.* **2015**, *54* (9), 2816–2820.  
<https://doi.org/10.1002/anie.201409846>.
- (77) Wohlrab, S.; Müller, S.; Schmidt, A.; Neubauer, S.; Kessler, H.; Leal-Egaña, A.; Scheibel, T. Cell Adhesion and Proliferation on RGD-Modified Recombinant Spider Silk Proteins. *Biomaterials* **2012**, *33* (28), 6650–6659.  
<https://doi.org/10.1016/j.biomaterials.2012.05.069>.
- (78) Harvey, D.; Bray, G.; Zamberlan, F.; Amer, M.; Goodacre, S. L.; Thomas, N. R. Cyclo ( RGDfK ) Functionalized Spider Silk Cell Scaffolds : Significantly Improved Performance in Just One Click. *Macromol. Biosci.* **2020**, *20* (12), 2000255.  
<https://doi.org/10.1002/mabi.202000255>.
- (79) Huemmerich, D.; Helsen, C. W.; Quedzuweit, S.; Oschmann, J.; Rudolph, R.; Scheibel, T. Primary Structure Elements of Spider Dragline Silks and Their Contribution to Protein Solubility. *Biochemistry* **2004**, *43* (42), 13604–13612.  
<https://doi.org/10.1021/bi048983q>.
- (80) Hedhammar, M.; Rising, A.; Grip, S.; Martinez, A. S.; Nordling, K.; Casals, C.; Stark, M.; Johansson, J. Structural Properties of Recombinant Nonrepetitive and Repetitive Parts of Major Ampullate Spidroin 1 from *Euprosthenoops Australis*: Implications for Fiber Formation. *Biochemistry* **2008**, *47* (11), 3407–3417.  
<https://doi.org/10.1021/bi702432y>.
- (81) Qian, Z. G.; Zhou, M. L.; Song, W. W.; Xia, X. X. Dual Thermosensitive Hydrogels Assembled from the Conserved C-Terminal Domain of Spider Dragline Silk. *Biomacromolecules* **2015**, *16* (11), 3704–3711. <https://doi.org/10.1021/acs.biomac.5b01231>.
- (82) Kronqvist, N.; Chen, G.; Aleksis, R.; Purhonen, P.; Hebert, H. A Spidroin-Derived Solubility Tag Enables Controlled Aggregation of a Designed Amyloid Protein. *FEBS J.* **2018**, *285* (10), 1873–1885.  
<https://doi.org/10.1111/febs.14451>.
- (83) Salehi, S.; Koeck, K.; Scheibel, T. Spider Silk for Tissue Engineering Applications. *Molecules* **2020**, *25* (3), 737.  
<https://doi.org/https://doi.org/10.3390/molecules25030737>.
- (84) Humenik, M.; Mohrand, M.; Scheibel, T. Self-Assembly of Spider Silk-Fusion Proteins Comprising Enzymatic and Fluorescence Activity. *Bioconjug. Chem.* **2018**, *29* (4), 898–904.  
<https://doi.org/10.1021/acs.bioconjchem.7b00759>.
- (85) Müller-Herrmann, S.; Scheibel, T. Enzymatic Degradation of Films, Particles, and Nonwoven Meshes Made of a Recombinant Spider Silk Protein. *ACS Biomater. Sci. Eng.* **2015**, *1* (4), 247–259.  
<https://doi.org/10.1021/ab500147u>.

- (86) Kumari, S.; Bargel, H.; Anby, M. U.; Lafargue, D.; Scheibel, T. Recombinant Spider Silk Hydrogels for Sustained Release of Biologicals. *ACS Biomater. Sci. Eng.* **2018**, *4* (5), 1750–1759. <https://doi.org/10.1021/acsbiomaterials.8b00382>.
- (87) DeSimone, E.; Aigner, T. B.; Humenik, M.; Lang, G.; Scheibel, T. Aqueous Electrospinning of Recombinant Spider Silk Proteins. *Mater. Sci. Eng. C* **2020**, *106* (June 2019), 110145. <https://doi.org/10.1016/j.msec.2019.110145>.
- (88) Agostini, E.; Winter, G.; Engert, J. Water-Based Preparation of Spider Silk Films as Drug Delivery Matrices. *J. Control. Release* **2015**, *213*, 134–141. <https://doi.org/10.1016/j.jconrel.2015.06.025>.
- (89) Seijsing, F.; Nilebäck, L.; Öhman, O.; Pasupuleti, R.; Ståhl, C.; Seijsing, J.; Hedhammar, M. Recombinant Spider Silk Coatings Functionalized with Enzymes Targeting Bacteria and Biofilms. *Microbiologyopen* **2020**, *9* (4), 1–10. <https://doi.org/10.1002/mbo3.993>.
- (90) Nilebäck, L.; Chouhan, D.; Jansson, R.; Widhe, M.; Mandal, B. B.; Hedhammar, M. Silk-Silk Interactions between Silkworm Fibroin and Recombinant Spider Silk Fusion Proteins Enable the Construction of Bioactive Materials. *ACS Appl. Mater. Interfaces* **2017**, *9* (37), 31634–31644. <https://doi.org/10.1021/acsami.7b10874>.
- (91) Harvey, D.; Bardelang, P.; Goodacre, S. L.; Cockayne, A.; Thomas, N. R. Antibiotic Spider Silk: Site-Specific Functionalization of Recombinant Spider Silk Using “Click” Chemistry. *Adv. Mater.* **2017**, *29* (10), 1604245. <https://doi.org/10.1002/adma.201604245>.
- (92) Johansson, U.; Ria, M.; Karin, Å.; Shalaly, N. D. Pancreatic Islet Survival and Engraftment Is Promoted by Culture on Functionalized Spider Silk Matrices. *PLoS One* **2015**, *10* (6), 1–21. <https://doi.org/10.1371/journal.pone.0130169>.
- (93) Widhe, M.; Hedhammar, M. Recombinant Spider Silk Functionalized Silkworm Silk Matrices as Potential Bioactive Wound Dressings and Skin Grafts. *ACS Appl. Mater. Interfaces* **2018**, No. 10, 23560–23572. <https://doi.org/10.1021/acsami.8b05853>.
- (94) Lewicka, M.; Rebellato, P.; Lewicki, J.; Uhlén, P.; Rising, A.; Hardy, J. G. Recombinant Spider Silk Protein Matrices Facilitate Differentiation of Neural Stem Cells Into Mature and Functional Neurons. *Front. Mater.* **2021**, *7*, 1–9. <https://doi.org/10.3389/fmats.2020.560372>.
- (95) Gomes, S.; Gallego-Llamas, J.; Leonor, I. B.; Mano, J. F.; Reis, R. L.; Kaplan, D. L. Biological Responses to Spider Silk-Antibiotic Fusion Protein. *J. Tissue Eng. Regen. Med.* **2012**, *6* (5), 356–368. <https://doi.org/10.1002/term.437>.
- (96) Lee, K. S.; Kim, B. Y.; Kim, D. H.; Jin, B. R. Recombinant Spider Silk Fibroin Protein Produces a Non-Cytotoxic and Non-Inflammatory Response. *J. Asia. Pac. Entomol.* **2016**, *19* (4), 1015–1018. <https://doi.org/10.1016/j.aspen.2016.09.004>.

- (97) Zeplin, P. H.; Maksimovikj, N. C.; Jordan, M. C.; Nickel, J.; Lang, G.; Leimer, A. H.; Römer, L.; Scheibel, T. Spider Silk Coatings as a Bioshield to Reduce Periprosthetic Fibrous Capsule Formation. *Adv. Drug Deliv. Rev.* **2014**, *24* (18), 2658–2666. <https://doi.org/10.1002/adfm.201302813>.
- (98) Caló, E.; Khutoryanskiy, V. V. Biomedical Applications of Hydrogels: A Review of Patents and Commercial Products. *Eur. Polym. J.* **2015**, *65*, 252–267. <https://doi.org/10.1016/j.eurpolymj.2014.11.024>.
- (99) Fu, S.; Guo, G.; Gong, C.; Zeng, S.; Liang, H.; Luo, F.; Zhang, X.; Zhao, X.; Wei, Y.; Qian, Z. Injectable Biodegradable Thermosensitive Hydrogel Composite for Orthopedic Tissue Engineering. 1. Preparation and Characterization of Nanohydroxyapatite/Poly(Ethylene Glycol)–Poly( $\epsilon$ -Caprolactone)–Poly(Ethylene Glycol) Hydrogel Nanocomposites. *J. Phys. Chem. B* **2009**, *113* (52), 16518–16525. <https://doi.org/https://doi.org/10.1021/jp907974d>.
- (100) Ossipov, D. A.; Brännvall, K.; Forsberg-Nilsson, K.; Hilborn, J. Formation of the First Injectable Poly (Vinyl Alcohol) Hydrogel by Mixing of Functional PVA Precursors. *J. Appl. Polym. Sci.* **2007**, *106* (1), 60–70. <https://doi.org/10.1002/app.26455>.
- (101) Reid, B.; Gibson, M.; Singh, A.; Taube, J.; Furlong, C.; Elisseff, J. PEG Hydrogel Degradation and the Role of the Surrounding Tissue Environment. *J. Tissue Eng. Regen. Med.* **2016**, *9* (3), 315–318. <https://doi.org/10.1002/term.1688.PEG>.
- (102) Hillel, A. T.; Unterman, S.; Nahas, Z.; Reid, B.; Jeannine, M.; Axelman, J.; Chae, J. J.; Guo, Q.; Trow, R.; Hou, Z.; et al. Photoactivated Composite Biomaterial for Soft Tissue Restoration in Rodents and in Humans. *Sci. Transl. Med.* **2015**, *3* (93), 93ra67. <https://doi.org/10.1126/scitranslmed.3002331.Photoactivated>.
- (103) Vedadghavami, A.; Minooei, F.; Mohammadi, M. H.; Khetani, S.; Rezaei Kolahchi, A.; Mashayekhan, S.; Sanati-Nezhad, A. Manufacturing of Hydrogel Biomaterials with Controlled Mechanical Properties for Tissue Engineering Applications. *Acta Biomater.* **2017**, *62*, 42–63. <https://doi.org/10.1016/j.actbio.2017.07.028>.
- (104) Zhu, J.; Marchant, R. E. Design Properties of Hydrogel Tissue-Engineering Scaffolds. *Expert Rev. Med. Devices* **2011**, *8* (5), 607–626. <https://doi.org/10.1586/erd.11.27>.
- (105) Yang, B.; Gong, C. Y.; Qian, Z. Y.; Zhao, X.; Li, Z. Y.; Qi, X. R.; Zhou, S. T.; Zhong, Q.; Luo, F.; Wei, Y. Q. Prevention of Post-Surgical Abdominal Adhesions by a Novel Biodegradable Thermosensitive PECE Hydrogel. *BMC Biotechnol.* **2010**, *10* (65), 65. <https://doi.org/10.1186/1472-6750-10-65>.
- (106) Shi, K.; Xue, B.; Liao, J.; Qu, Y.; Qian, Z. Polymeric Hydrogels for Post-Operative Adhesion Prevention: A Review. *Mater. Express* **2017**, *7* (6), 417–438. <https://doi.org/10.1166/mex.2017.1403>.
- (107) Hern, D. L.; Hubbell, J. A. Incorporation of Adhesion Peptides into Nonadhesive Hydrogels Useful for Tissue Resurfacing. *J. Biomed. Mater. Res.* **1998**, *39* (2), 266–276. [https://doi.org/10.1002/\(SICI\)1097-4636\(199802\)39:2<266::AID-JBM14>3.0.CO;2-B](https://doi.org/10.1002/(SICI)1097-4636(199802)39:2<266::AID-JBM14>3.0.CO;2-B).

- (108) Zhu, J. Bioactive Modification of Poly(Ethylene Glycol) Hydrogels for Tissue Engineering. *Biomaterials* **2010**, *31* (17), 4639–4656. <https://doi.org/10.1016/j.biomaterials.2010.02.044>.
- (109) Drury, J. L.; Mooney, D. J. Hydrogels for Tissue Engineering: Scaffold Design Variables and Applications. *Biomaterials* **2003**, *24* (24), 4337–4351. [https://doi.org/10.1016/S0142-9612\(03\)00340-5](https://doi.org/10.1016/S0142-9612(03)00340-5).
- (110) Partlow, B. P.; Hanna, C. W.; Rnjak-kovacina, J.; Moreau, J. E.; Matthew, B.; Burke, K. A.; Marelli, B.; Mitropoulos, A. N.; Fiorenzo, G.; Kaplan, D. L. Highly Tunable Elastomeric Silk Biomaterials. *Adv. Funct. Mater.* **2015**, *24* (29), 4615–4624. <https://doi.org/10.1002/adfm.201400526>.
- (111) Floren, M.; Migliaresi, C.; Motta, A. Processing Techniques and Applications of Silk Hydrogels in Bioengineering. *J. Funct. Biomater.* **2016**, *7* (3), 26. <https://doi.org/10.3390/jfb7030026>.
- (112) Schacht, K.; Scheibel, T. Controlled Hydrogel Formation of a Recombinant Spider Silk Protein. *Biomacromolecules* **2011**, *12* (7), 2488–2495. <https://doi.org/10.1021/bm200154k>.
- (113) Farjami, T.; Madadlou, A. Fabrication Methods of Biopolymeric Microgels and Microgel-Based Hydrogels. *Food Hydrocoll.* **2017**, *62*, 262–272. <https://doi.org/10.1016/j.foodhyd.2016.08.017>.
- (114) Oryan, A.; Kamali, A.; Moshiri, A.; Baharvand, H.; Daemi, H. Chemical Crosslinking of Biopolymeric Scaffolds : Current Knowledge and Future Directions of Crosslinked Engineered Bone Scaffolds. *Int. J. Biol. Macromol.* **2018**, *107* (A), 678–688. <https://doi.org/10.1016/j.ijbiomac.2017.08.184>.
- (115) Hasturk, O.; Jordan, K. E.; Choi, J.; Kaplan, D. L. Enzymatically Crosslinked Silk and Silk-Gelatin Hydrogels with Tunable Gelation Kinetics , Mechanical Properties and Bioactivity for Cell Culture and Encapsulation. *Biomaterials* **2020**, *232* (December 2019), 119720. <https://doi.org/10.1016/j.biomaterials.2019.119720>.
- (116) Kim, H. H.; Song, D. W.; Kim, M. J.; Ryu, S. J.; Um, I. C.; Ki, C. S.; Park, Y. H. Effect of Silk Fibroin Molecular Weight on Physical Property of Silk Hydrogel. *Polymer (Guildf)*. **2016**, *90*, 26–33. <https://doi.org/10.1016/j.polymer.2016.02.054>.
- (117) Li, H.; Chen, X. D.; Mercadé-Prieto, R. Elastic Modulus and Equilibrium Swelling of Stranded and Particulate Protein Hydrogels at Acid PH. *Food Hydrocoll.* **2017**, *71*, 168–175. <https://doi.org/10.1016/j.foodhyd.2017.05.008>.
- (118) Choi, J.; McGill, M.; Raia, N. R.; Hasturk, O.; Kaplan, D. L. Silk Hydrogels Crosslinked by the Fenton Reaction. *Adv. Healthc. Mater.* **2019**, *1900644*, 1900644. <https://doi.org/10.1002/adhm.201900644>.
- (119) Matsumoto, A.; Chen, J.; Collette, A. L.; Kim, U. J.; Altman, G. H.; Cebe, P.; Kaplan, D. L. Mechanisms of Silk Fibroin Sol-Gel Transitions. *J. Phys. Chem. B* **2006**, *110* (43), 21630–21638. <https://doi.org/10.1021/jp056350v>.

- (120) Wu, J.; Li, P.; Dong, C.; Jiang, H.; Xue, B.; Gao, X.; Qin, M.; Wang, W.; Chen, B.; Cao, Y. Rationally Designed Synthetic Protein Hydrogels with Predictable Mechanical Properties. *Nat. Commun.* **2018**, *9* (620), 1–11. <https://doi.org/10.1038/s41467-018-02917-6>.
- (121) Navarra, G.; Peres, C.; Contardi, M.; Picone, P.; San Biagio, P. L.; Di Carlo, M.; Giacomazza, D.; Militello, V. Heat- and PH-Induced BSA Conformational Changes, Hydrogel Formation and Application as 3D Cell Scaffold. *Arch. Biochem. Biophys.* **2016**, *606*, 134–142. <https://doi.org/10.1016/j.abb.2016.07.020>.
- (122) Kapoor, S.; Kundu, S. C. Silk Protein-Based Hydrogels: Promising Advanced Materials for Biomedical Applications. *Acta Biomater.* **2016**, *31*, 17–32. <https://doi.org/10.1016/j.actbio.2015.11.034>.
- (123) Yucel, T.; Cebe, P.; Kaplan, D. L. Vortex-Induced Injectable Silk Fibroin Hydrogels. *Biophys. J.* **2009**, *97* (7), 2044–2050. <https://doi.org/10.1016/j.bpj.2009.07.028>.
- (124) Bai, S.; Zhang, X.; Lu, Q.; Sheng, W.; Liu, L.; Dong, B.; Kaplan, D. L. Reversible Hydrogel – Solution System of Silk with High B-Sheet Content. *Biomacromolecules* **2014**, *15* (8), 3044–3051. <https://doi.org/https://doi.org/10.1021/bm500662z>.
- (125) Wang, X.; Kluge, J. A.; Leisk, G. G.; Kaplan, D. L. Sonication-Induced Gelation of Silk Fibroin for Cell Encapsulation. *Biomaterials* **2008**, *29* (8), 1054–1064. <https://doi.org/10.1016/j.biomaterials.2007.11.003>.
- (126) Hopkins, A. M.; De Laporte, L.; Tortelli, F.; Spedden, E.; Staii, C.; Atherton, T. J.; Hubbell, J. A.; Kaplan, D. L. Silk Hydrogels as Soft Substrates for Neural Tissue Engineering. *Adv. Funct. Mater.* **2013**, *23* (41), 5140–5149. <https://doi.org/10.1002/adfm.201300435>.
- (127) Kim, U.; Park, J.; Li, C.; Jin, H.; Valluzzi, R.; Kaplan, D. L. Structure and Properties of Silk Hydrogels. *Bio Macromol.* **2004**, *5* (3), 786–792. <https://doi.org/https://doi.org/10.1021/bm0345460>.
- (128) Fang, J.; Zhang, X.; Cai, Y.; Wei, Y. Small Globular Protein Motif Forms Particulate Hydrogel under Various Ph Conditions. *Biomacromolecules* **2011**, *12* (5), 1578–1584. <https://doi.org/10.1021/bm101571r>.
- (129) Rammensee, S.; Huemmerich, D.; Hermanson, K. D.; Scheibel, T.; Bausch, A. R. Rheological Characterization of Hydrogels Formed by Recombinantly Produced Spider Silk. *Appl. Phys. A* **2005**, *82* (2), 261–264. <https://doi.org/10.1007/s00339-005-3431-x>.
- (130) Luo, F.; Qian, Z. G.; Xia, X. X. Responsive Protein Hydrogels Assembled from Spider Silk Carboxyl-Terminal Domain and Resilin Copolymers. *Polymers (Basel)*. **2018**, *10* (8). <https://doi.org/10.3390/polym10080915>.
- (131) XIAOXIA, X.; QIN, K.; ZHIGANG, Q.; ZHOU, M.; SONG, W. Thermosensitive Hydrogel Based on Spider Silk Protein. CN105031723 (A), 2015.

- (132) Arndt, T.; Laity, P. R.; Johansson, J.; Holland, C.; Rising, A. Native-like Flow Properties of an Artificial Spider Silk Dope. *ACS Biomater. Sci. Eng.* **2021**, *7* (2), 0–9. <https://doi.org/10.1021/acsbomaterials.0c01308>.
- (133) Landreh, M.; Andersson, M.; Marklund, E. G.; Jia, Q.; Meng, Q.; Johansson, J.; Robinson, C. V.; Rising, A. Mass Spectrometry Captures Structural Intermediates in Protein Fiber Self-Assembly. *Chem. Commun.* **2017**, *53* (23), 3319–3322. <https://doi.org/10.1039/C7CC00307B>.
- (134) Greenfield, N. J. Using Circular Dichroism Spectra to Estimate Protein Secondary Structure. *Nat. Protoc.* **2007**, *1* (6), 2876–2890. <https://doi.org/10.1038/nprot.2006.202>.
- (135) Kleinman, H. K.; Martin, G. R. Matrigel: Basement Membrane Matrix with Biological Activity. *Semin. Cancer Biol.* **2005**, *15* (5 SPEC. ISS.), 378–386. <https://doi.org/10.1016/j.semcancer.2005.05.004>.
- (136) Benton, G.; Arnaoutova, I.; George, J.; Kleinman, H. K.; Koblinski, J. Matrigel: From Discovery and ECM Mimicry to Assays and Models for Cancer Research. *Adv. Drug Deliv. Rev.* **2014**, *79*, 3–18. <https://doi.org/10.1016/j.addr.2014.06.005>.
- (137) Antoine, E. E.; Vlachos, P. P.; Rylander, M. N. Review of Collagen I Hydrogels for Bioengineered Tissue Microenvironments: Characterization of Mechanics, Structure, and Transport. *Tissue Eng. - Part B Rev.* **2014**, *20* (6), 683–696. <https://doi.org/10.1089/ten.teb.2014.0086>.
- (138) Raghavan, S.; Chipiano, B. Chapter 8: Phase Diagrams Using Tabletop Rheology and Calorimetry. In *Molecular Gels*; Springer science & business media: Berlin, Germany, 2006; pp 241–252. [https://doi.org/10.1007/1-4020-3689-2\\_9](https://doi.org/10.1007/1-4020-3689-2_9).
- (139) Zuidema, J. M.; Rivet, C. J.; Gilbert, R. J.; Morrison, F. A. A Protocol for Rheological Characterization of Hydrogels for Tissue Engineering Strategies. *J. Biomed. Mater. Res. - Part B Appl. Biomater.* **2014**, *102* (5), 1063–1073. <https://doi.org/10.1002/jbm.b.33088>.
- (140) Thamm, C.; DeSimone, E.; Scheibel, T. Characterization of Hydrogels Made of a Novel Spider Silk Protein EMaSp1s and Evaluation for 3D Printing. *Macromol. Biosci.* **2017**, *1700141*, 1700141. <https://doi.org/10.1002/mabi.201700141>.
- (141) Ball, P.; Hallsworth, J. E. Water Structure and Chaotropicity: Their Uses, Abuses and Biological Implications. *Phys. Chem. Chem. Phys.* **2015**, *17* (13), 8297–8305. <https://doi.org/10.1039/c4cp04564e>.
- (142) DeSimone, E.; Schacht, K.; Scheibel, T. Cations Influence the Cross-Linking of Hydrogels Made of Recombinant, Polyanionic Spider Silk Proteins. *Mater. Lett.* **2016**, *183*, 101–104. <https://doi.org/10.1016/j.matlet.2016.07.044>.
- (143) El-Harakany, A.A.; Abdel Halima, F.M. and Barakat, A. . Dissociation Constants and Related Thermodynamic Quantities of the Protonated Acid Form of Tris-(Hydroxymethyl)-Aminomethane in Mixtures of 2-Methoxyethanol and Water at Different Temperatures. *J. Electroanal. Chem. Interfacial Electrochem.* **1984**, *162* (1–2), 285–305. [https://doi.org/https://doi.org/10.1016/S0022-0728\(84\)80171-0](https://doi.org/https://doi.org/10.1016/S0022-0728(84)80171-0).

- (144) Xie, C.; Tian, T.; Yu, S.; Li, L. PH-Sensitive Hydrogel Based on Carboxymethyl Chitosan / Sodium Alginate and Its Application for Drug Delivery. *J. Appl. Polym. Sci.* **2018**, *136*, 46911. <https://doi.org/10.1002/app.46911>.
- (145) Lv, Q.; Hu, K.; Feng, Q.; Cui, F. Fibroin/Collagen Hybrid Hydrogels with Crosslinking Method: Preparation, Properties, and Cytocompatibility. *J. Biomed. Mater. Res. Part A* **2007**, *84A* (1), 198–207. <https://doi.org/10.1002/jbm.a>.
- (146) Sanchez-Ferrero, A.; Mata, A.; Mateos-Timoneda, M. A.; Rodríguez-Cabello, J. C.; Alonso, M.; Planell, J.; Enge, E. Biomaterials Development of Tailored and Self-Mineralizing Citric Acid-Crosslinked Hydrogels for in Situ Bone Regeneration. *Biomaterials* **2015**, *68*, 42–53. <https://doi.org/10.1016/j.biomaterials.2015.07.062>.
- (147) Bragg, J. C.; Kweon, H.; Jo, Y.; Lee, K. G.; Lin, C.-C. In Situ Formation of Silk-Gelatin Hybrid Hydrogels for Affinity-Based Growth Factor Sequestration and Release. *RSC Adv.* **2016**, *6* (115), 114353–114360. <https://doi.org/10.1039/C6RA22908E>.
- (148) Gilarska, A.; Ł, J. L.-; Horak, W.; Nowakowska, M. Collagen / Chitosan / Hyaluronic Acid – Based Injectable Hydrogels for Tissue Engineering Applications – Design , Physicochemical and Biological Characterization. *Colloids Surfaces B Biointerfaces* **2018**, *170* (June), 152–162. <https://doi.org/10.1016/j.colsurfb.2018.06.004>.
- (149) Hafner, K.; Montag, D.; Maeser, H.; Peng, C.; Marcotte, W. R.; Dean, D.; Kennedy, M. S. Evaluating Adhesion and Alignment of Dental Pulp Stem Cells to a Spider Silk Substrate for Tissue Engineering Applications. *Mater. Sci. Eng. C* **2017**, *81*, 104–112. <https://doi.org/10.1016/j.msec.2017.07.019>.
- (150) Wu, X.; Black, L.; Santacana-laffitte, G.; Patrick, C. W. Preparation and Assessment of Glutaraldehyde-Crosslinked Collagen – Chitosan Hydrogels for Adipose Tissue Engineering. *J. Biomed. Mater. Res. Part A* **2007**, *81* (1), 59–65. <https://doi.org/10.1002/jbm.a>.
- (151) Tian, Z.; Liu, W.; Li, G. The Microstructure and Stability of Collagen Hydrogel Cross-Linked by Glutaraldehyde. *Polym. Degrad. Stab.* **2016**, *130*, 264–270. <https://doi.org/10.1016/j.polymdegradstab.2016.06.015>.
- (152) Azab, A. K.; Orkin, B.; Doviner, V.; Nissan, A.; Klein, M.; Srebnik, M.; Rubinstein, A. Crosslinked Chitosan Implants as Potential Degradable Devices for Brachytherapy: In Vitro and in Vivo Analysis. *J. Control. Release* **2006**, *111* (3), 281–289. <https://doi.org/10.1016/j.jconrel.2005.12.014>.
- (153) Koetting, M. C.; Peters, J. T.; Steichen, S. D.; Peppas, N. A. Stimulus-Responsive Hydrogels: Theory, Modern Advances, and Applications. *Mater. Sci. Eng. R Reports* **2015**, *93*, 1–49. <https://doi.org/10.1016/j.mser.2015.04.001>.
- (154) Peppas, N. A.; Bures, P.; Leobandung, W.; Ichikawa, H. Hydrogels in Pharmaceutical Formulations. *Eur. J. Pharm. Biopharm.* **2000**, *50* (1), 27–46. [https://doi.org/10.1016/S0939-6411\(00\)00090-4](https://doi.org/10.1016/S0939-6411(00)00090-4).

- (155) Kamata, H.; Akagi, Y.; Kayasuga-Kariya, Y.; Chung, U. Il; Sakai, T. "Nonswellable" Hydrogel without Mechanical Hysteresis. *Science* (80- . ). **2014**, 343 (6173), 873–875. <https://doi.org/10.1126/science.1247811>.
- (156) Kaberova, Zhansaya Karpushkin, Evgeny Nevoralová, M.; Vetrík, M.; Šlouf, M.; Dušková-Smrčková, M. Microscopic Structure of Swollen Hydrogels by Scanning Electron and Light Microscopies: Artifacts and Reality. *Polymers (Basel)*. **2020**, 12 (3), 578. <https://doi.org/10.3390/polym12030578>.
- (157) Raghuwanshi, V. S.; Garnier, G. Characterisation of Hydrogels: Linking the Nano to the Microscale. *Adv. Colloid Interface Sci.* **2019**, 274, 102044. <https://doi.org/10.1016/j.cis.2019.102044>.
- (158) Aston, R.; Sewell, K.; Klein, T.; Lawrie, G.; Grøndahl, L. Evaluation of the Impact of Freezing Preparation Techniques on the Characterisation of Alginate Hydrogels by Cryo-SEM. *Eur. Polym. J.* **2016**, 82, 1–15. <https://doi.org/10.1016/j.eurpolymj.2016.06.025>.
- (159) Parmenter, C.; Baki, A.; Shakesheff, K. M. The Application of Cryogenic Focused Ion Beam Scanning Electron Microscopy to Hydrogel Characterization. *Microsc. Microanal.* **2016**, 22 (S3), 192–193. <https://doi.org/10.1017/S1431927616001811>.
- (160) Gontier, E.; Ibarboure, E.; Payr, B.; Meins, L.; Schatz, C. Insights into Carbopol Gel Formulations: Microscopy Analysis of the Microstructure and the Influence of Polyol Additives. *J. Appl. Polym. Sci.* **2015**, 132 (46), 1–7. <https://doi.org/10.1002/app.42761>.
- (161) Hayles, M. .; De Winter, D. A. . An Introduction to Cryo-FIB-SEM Cross-Sectioning of Frozen, Hydrated Life Science Samples. *J. Microsc.* **2021**, 281 (2), 138–156. <https://doi.org/10.1111/jmi.12951>.
- (162) Kizilyaprak, C.; Daraspe, J.; Humbel, B. M. Focused Ion Beam Scanning Electron Microscopy in Biology. *J. Microsc.* **2014**, 254 (3), 109–114. <https://doi.org/10.1111/jmi.12127>.
- (163) Chen, Y.; Dai, X.; Huang, L.; Sun, Y.; Chan, H. N.; Shen, B.; Zeng, X.; Wu, Z.; Hsing, I. M.; Guo, Z.; et al. A Universal and Facile Approach for the Formation of a Protein Hydrogel for 3D Cell Encapsulation. *Adv. Funct. Mater.* **2015**, 25 (39), 6189–6198. <https://doi.org/10.1002/adfm.201502942>.
- (164) Vetráková, L.; Neděla, V.; Runštuk, J.; Tihlaříková, E.; Heger, D. Dynamical In-Situ Observation of the Lyophilization and Vacuum-Drying Processes of a Model Biopharmaceutical System by an Environmental Scanning Electron Microscope. *Int. J. Pharm.* **2020**, 585 (May), 119448. <https://doi.org/10.1016/j.ijpharm.2020.119448>.
- (165) Wine, Y.; Cohen-hadar, N.; Freeman, A.; Frolow, F. Elucidation of the Mechanism and End Products of Glutaraldehyde Crosslinking Reaction by X-Ray Structure Analysis. *Biotechnol. Bioeng.* **2007**, 98 (3), 711–718. <https://doi.org/10.1002/bit.21459>.

- (166) Migneault, I.; Dartiguenave, C.; Bertrand, M. J.; Waldron, K. C. Glutaraldehyde: Behavior in Aqueous Solution, Reaction with Proteins, and Application to Enzyme Crosslinking. *Biotechniques* **2004**, *37* (5), 798–802. <https://doi.org/https://doi.org/10.2144/04375RV01>.
- (167) Salem, M.; Mauguen, Y.; Prange, T. Revisiting Glutaraldehyde Cross-Linking : The Case of the Arg – Lys Intermolecular Doublet. *Acta Crystallogr. Sect. F Struct. Biol. Cryst. Commun.* **2010**, *66* (Pt 3), 225–228. <https://doi.org/10.1107/S1744309109054037>.
- (168) Farrell, K.; Joshi, J.; Kothapalli, C. R. Injectable Uncrosslinked Biomimetic Hydrogels as Candidate Scaffolds for Neural Stem Cell Delivery. *J. Biomed. Mater. Res. - Part A* **2017**, *105* (3), 790–805. <https://doi.org/10.1002/jbm.a.35956>.
- (169) Gao, Y.; Kong, W.; Li, B.; Ni, Y.; Yuan, T.; Guo, L.; Lin, H.; Fan, H.; Fan, Y.; Zhang, X. Fabrication and Characterization of Collagen-Based Injectable and Self-Crosslinkable Hydrogels for Cell Encapsulation. *Colloids Surfaces B Biointerfaces* **2018**, *167*, 448–456. <https://doi.org/10.1016/j.colsurfb.2018.04.009>.
- (170) Reese, S. P.; Farhang, N.; Poulson, R.; Parkman, G.; Weiss, J. A. Nanoscale Imaging of Collagen Gels with Focused Ion Beam Milling and Scanning Electron Microscopy. *Biophys. J.* **2016**, *111* (8), 1797–1804. <https://doi.org/10.1016/j.bpj.2016.08.039>.
- (171) Efthymiou, C.; Williams, M. A. K.; McGrath, K. M. Revealing the Structure of High-Water Content Biopolymer Networks: Diminishing Freezing Artefacts in Cryo-SEM Images. *Food Hydrocoll.* **2017**, *73*, 203–212. <https://doi.org/10.1016/j.foodhyd.2017.06.040>.
- (172) Jacobsen, S.; Scherer, G. W.; Schulson, E. M. Cement and Concrete Research Concrete – Ice Abrasion Mechanics. *Cem. Concr. Res.* **2015**, *73*, 79–95. <https://doi.org/10.1016/j.cemconres.2015.01.001>.
- (173) Ua, F.; Santana, B. P.; Nedel, F.; O, C. P.; Silva, R. M. E.; Fernandes, A.; Silva, D. A.; Avio, F. L.; Demarco, F. Comparing Different Methods to Fix and to Dehydrate Cells on Alginate Hydrogel Scaffolds Using Scanning Electron Microscopy. *Microsc. Res. Tech.* **2015**, *78* (7), 553–561. <https://doi.org/10.1002/jemt.22508>.
- (174) Zhang, D.; Peng, H.; Sun, B.; Lyu, S. High Water Content Silk Protein-Based Hydrogels with Tunable Elasticity Fabricated via a Ru ( II ) Mediated Photochemical Cross-Linking Method. *Fibres Polym.* **2017**, *18* (10), 1831–1840. <https://doi.org/10.1007/s12221-017-7463-6>.
- (175) Cao, M.; Wang, Y.; Hu, X.; Gong, H.; Li, R.; Cox, H.; Zhang, J.; Waigh, T. A.; Xu, H.; Lu, J. R. Reversible Thermoresponsive Peptide – PNIPAM Hydrogels for Controlled Drug Delivery. *Biomacromolecules* **2019**, *20* (9), 3601–3610. <https://doi.org/10.1021/acs.biomac.9b01009>.

- (176) Gustafsson, L.; Tasiopoulos, C. P.; Jansson, R.; Kwick, M.; Duursma, T.; Gasser, T. C.; Wijngaart, W. Van Der. Recombinant Spider Silk Forms Tough and Elastic Nanomembranes That Are Protein-Permeable and Support Cell Attachment and Growth. *Adv. Funct. Mater.* **2020**, 2002982 (30), 1–9. <https://doi.org/10.1002/adfm.202002982>.
- (177) Kwick, M.; Tasiopoulos, C. P.; Barth, A.; Söderberg, L. D.; Lundell, F.; Hedhammar, M. Cyclic Expansion / Compression of the Air – Liquid Interface as a Simple Method to Produce Silk Fibres. *Macromol. Biosci.* **2020**, 2000227, 1–9. <https://doi.org/10.1002/mabi.202000227>.
- (178) Discher, D. E.; Janmey, P.; Wang, Y. Tissue Cells Feel and Respond to the Stiffness of Their Substrate. *Science (80-. )*. **2005**, 310 (5751), 1139–1144. <https://doi.org/10.1126/science.1116995>.
- (179) Huebsch, N. Translational Mechanobiology: Designing Synthetic Hydrogel Matrices for Improved in Vitro Models and Cell-Based Therapies. *Acta Biomater.* **2019**, 94 (August 2019), 97–111. <https://doi.org/10.1016/j.actbio.2019.05.055>.
- (180) Trappmann, B.; Chen, C. S. How Cells Sense Extracellular Matrix Stiffness: A Material’s Perspective. *Curr. Opin. Biotechnol.* **2013**, 24 (5), 948–953. <https://doi.org/10.1016/j.copbio.2013.03.020>.
- (181) Engler, A. J.; Sen, S.; Sweeney, H. L.; Discher, D. E. Matrix Elasticity Directs Stem Cell Lineage Specification. *Cell* **2006**, 126 (4), 677–689. <https://doi.org/10.1016/j.cell.2006.06.044>.
- (182) Peyton, S. R.; Raub, C. B.; Keschrums, V. P.; Putnam, A. J. The Use of Poly ( Ethylene Glycol ) Hydrogels to Investigate the Impact of ECM Chemistry and Mechanics on Smooth Muscle Cells. *Biomaterials* **2006**, 27 (28), 4881–4893. <https://doi.org/10.1016/j.biomaterials.2006.05.012>.
- (183) Zhang, J.; Yang, Z.; Li, C.; Dou, Y.; Li, Y.; Thote, T.; Wang, D.; Ge, Z. Cells Behave Distinctly within Sponges and Hydrogels Due to Differences of Internal Structure. *Tissue Eng. Part A* **2013**, 19 (19–20), 2166–2175. <https://doi.org/10.1089/ten.TEA.2012.0393>.
- (184) Scott, J. B.; Afshari, M.; Kotek, R.; Saul, J. M. The Promotion of Axon Extension in Vitro Using Polymer-Templated Fibrin Scaffolds. *Biomaterials* **2011**, 32 (21), 4830–4839. <https://doi.org/10.1016/j.biomaterials.2011.03.037>.
- (185) Lee, D.; Zhang, H.; Ryu, S. *Elastic Modulus Measurement of Hydrogels*. In: Mondal M. (Eds) *Cellulose-Based Superabsorbent Hydrogels. Polymers and Polymeric Composites: A Reference Series*; Springer, Cham, 2018. [https://doi.org/https://doi.org/10.1007/978-3-319-76573-0\\_60-1](https://doi.org/https://doi.org/10.1007/978-3-319-76573-0_60-1).
- (186) Wang, P.; Todai, M.; Nakano, T. B Titanium Single Crystal with Bone-like Elastic Modulus and Large Crystallographic Elastic Anisotropy. *J. Alloys Compd.* **2019**, 782, 667–671. <https://doi.org/10.1016/j.jallcom.2018.12.236>.
- (187) Levental, I.; Georges, C.; Janmey, P. A. Soft Biological Materials and Their Impact on Cell Function. *Soft Matter* **2007**, No. 3, 299–306. <https://doi.org/10.1039/b610522j>.

- (188) Aigner, T. B.; DeSimone, E.; Scheibel, T. Biomedical Applications of Recombinant Silk-Based Materials. *Adv. Mater.* **2018**, *30* (19), 1–28. <https://doi.org/10.1002/adma.201704636>.
- (189) Oyen, M. L. Mechanical Characterisation of Hydrogel Materials. *Int. Mater. Rev.* **2014**, *59* (1), 44–59. <https://doi.org/10.1179/1743280413Y.0000000022>.
- (190) Browning, M. B.; Wilems, T.; Hahn, M. Compositional Control of Poly ( Ethylene Glycol ) Hydrogel Modulus Independent of Mesh Size. *J. Biomed. Mater. Res. Part A* **2011**, *98 A* (2), 268–273. <https://doi.org/10.1002/jbm.a.33109>.
- (191) Alexander, A.; Khan, J.; Saraf, S.; Saraf, S. Polyethylene Glycol ( PEG )– Poly ( N-Isopropylacrylamide ) ( PNIPAAm ) Based Thermosensitive Injectable Hydrogels for Biomedical Applications. *Eur. J. Pharm. Biopharm.* **2014**, *88* (3), 575–585. <https://doi.org/10.1016/j.ejpb.2014.07.005>.
- (192) Griffin, M. F.; Leung, B. C.; Premakumar, Y.; Szarko, M.; Butler, P. E. Comparison of the Mechanical Properties of Different Skin Sites for Auricular and Nasal Reconstruction. *J. Otolaryngol. - Head Neck Surg.* **2017**, *46* (1), 33–36. <https://doi.org/10.1186/s40463-017-0210-6>.
- (193) Berry, M. F.; Engler, A. J.; Woo, Y. J.; Pirolli, T. J.; Bish, L. T.; Jayasankar, V.; Morine, K. J.; Gardner, T. J.; Discher, D. E.; Sweeney, H. L.; et al. Mesenchymal Stem Cell Injection after Myocardial Infarction Improves Myocardial Compliance. *Am. J. Physiol. Heart Circ. Physiol.* **2006**, *290* (6), H2196–H2203. <https://doi.org/10.1152/ajpheart.01017.2005>.
- (194) Soofi, S. S.; Last, J. A.; Liliensiek, S. J.; Nealey, P. F.; Murphy, C. J. The Elastic Modulus of Matrigel as Determined by Atomic Force Microscopy. *J. Struct. Biol.* **2015**, *167* (3), 216–219. <https://doi.org/10.1016/j.jsb.2009.05.005>.
- (195) Baek, K.; Clay, N. E.; Qin, E. C.; Sullivan, K. M.; Kim, D. H.; Kong, H. In Situ Assembly of the Collagen-Polyacrylamide Interpenetrating Network Hydrogel: Enabling Decoupled Control of Stiffness and Degree of Swelling. *Eur. Polym. J.* **2015**, *72*, 413–422. <https://doi.org/10.1016/j.eurpolymj.2015.07.044>.
- (196) Zerpa, A.; Pakzad, L.; Fatehi, P. Hardwood Kraft Lignin-Based Hydrogels: Production and Performance. *ACS Omega* **2018**, *3* (July), 8233–8242. <https://doi.org/10.1021/acsomega.8b01176>.
- (197) Solar, C.; Palacio, D.; Sánchez, S.; Urbano, B. F. Oscillatory Strain Sweeps of Hydrogels from Methacrylated Alginate Macromonomers: Assessment of Synthesis and Acquisition Variables. *J. Chil. Chem. Soc.* **2019**, *3*, 1–5. <https://doi.org/10.4067/S0717-97072019000304542>.
- (198) Chouhan, D.; Lohe, T. u.; Samudrala, P. K.; Mandal, B. B. In Situ Forming Injectable Silk Fibroin Hydrogel Promotes Skin Regeneration in Full Thickness Burn Wounds. *Adv. Healthc. Mater.* **2018**, *7* (24). <https://doi.org/10.1002/adhm.201801092>.
- (199) Rizzo, F.; Kehr, N. S. Recent Advances in Injectable Hydrogels for Controlled and Local Drug Delivery. *Adv. Healthc. Mater.* **2021**, *2001341* (6), 1–26. <https://doi.org/10.1002/adhm.202001341>.

- (200) Matter, S.; Guvendiren, M.; Lu, H. D.; Burdick, J. A. Shear-Thinning Hydrogels for Biomedical Applications. *Soft Matter* **2012**, *2* (8), 260–272. <https://doi.org/10.1039/c1sm06513k>.
- (201) Florczak, A.; Mackiewicz, A.; Dams-kozlowska, H. Functionalized Spider Silk Spheres As Drug Carriers for Targeted Cancer Therapy. *Bio Macromol.* **2014**, *15* (8), 2971–2981. <https://doi.org/10.1021/bm500591p>.
- (202) Jastrzebska, K.; Felcyn, E.; Kozak, M.; Szybowicz, M.; Buchwald, T.; Pietralik, Z.; Jesionowski, T.; Mackiewicz, A.; Dams-Kozłowska, H. The Method of Purifying Bioengineered Spider Silk Determines the Silk Sphere Properties. *Sci. Rep.* **2016**, *6* (May), 1–15. <https://doi.org/10.1038/srep28106>.
- (203) Yang, G.; Liu, Y.; Jin, S.; Zhao, C. Development of Core-Shell Nanoparticle Drug Delivery Systems Based on Biomimetic Mineralization. *ChemBioChem* **2020**, *21* (50), 2871–2879. <https://doi.org/10.1002/cbic.202000105>.
- (204) Svagan, A. J.; Benjamins, J.; Al-ansari, Z.; Bar, D.; Müllertz, A.; Wågberg, L.; Löbmann, K. Solid Cellulose Nano Fiber Based Foams – Towards Facile Design of Sustained Drug Delivery Systems. *J. Control. Release* **2016**, *244* (Part A), 74–82. <https://doi.org/10.1016/j.jconrel.2016.11.009>.
- (205) Xi, H.; Zhao, H. Silk Fibroin Coaxial Bead-on-String Fiber Materials and Their Drug Release Behaviors in Different PH. *J. Mater. Sci.* **2019**, *54* (5), 4246–4258. <https://doi.org/10.1007/s10853-018-3137-z>.
- (206) He, Z.; Wang, B.; Hu, C.; Zhao, J. An Overview of Hydrogel-Based Intra-Articular Drug Delivery for the Treatment of Osteoarthritis. *Colloids Surfaces B Biointerfaces* **2017**, *154*, 33–39. <https://doi.org/10.1016/j.colsurfb.2017.03.003>.
- (207) Reig-vano, B.; Tylkowski, B.; Montané, X.; Giamberini, M. Alginate-Based Hydrogels for Cancer Therapy and Research. *Int. J. Biol. Macromol.* **2021**, *170*, 424–436. <https://doi.org/10.1016/j.ijbiomac.2020.12.161>.
- (208) Gibbs, D. M. R.; Black, C. R. M.; Dawson, J. I.; Oreffo, R. O. C. A Review of Hydrogel Use in Fracture Healing and Bone Regeneration. *J. Tissue Eng. Regen. Med.* **2016**, *10* (3), 187–198. <https://doi.org/10.1002/term>.
- (209) Gyles, D. A.; Castro, L. D.; Silva, J. O. C.; Ribeiro-Costa, R. M. A Review of the Designs and Prominent Biomedical Advances of Natural and Synthetic Hydrogel Formulations. *Eur. Polym. J.* **2017**, *88* (01), 373–392. <https://doi.org/10.1016/j.eurpolymj.2017.01.027>.
- (210) Vashist, A.; Kaushik, A.; Vashist, A.; Jayant, D.; Tomitaka, A. Recent Trends on Hydrogel Based Drug Delivery Systems for Infectious Diseases. *Biomater. Sci.* **2016**, *4* (11), 1535–1553. <https://doi.org/10.1039/c6bm00276e>.
- (211) Al-kinani, A. A.; Zidan, G.; Elsaid, N.; Seyfoddin, A.; Alani, A. W. G.; Alany, R. G. Ophthalmic Gels: Past , Present and Future. *Adv. Drug Deliv. Rev.* **2018**, *126*, 113–126. <https://doi.org/10.1016/j.addr.2017.12.017>.

- (212) Gupta, A.; Kowalczyk, M.; Heaselgrave, W.; Britland, S. T. The Production and Application of Hydrogels for Wound Management: A Review. *Eur. Polym. J.* **2019**, *111*, 134–151. <https://doi.org/10.1016/j.eurpolymj.2018.12.019>.
- (213) Cascone, S.; Lamberti, G. Hydrogel-Based Commercial Products for Biomedical Applications : A Review. *Int. J. Pharm.* **2020**, *573*, 118803. <https://doi.org/10.1016/j.ijpharm.2019.118803>.
- (214) Huang, X.; Brazel, C. S. On the Importance and Mechanisms of Burst Release in Matrix-Controlled Drug Delivery Systems. *J. Control. Release* **2001**, *73* (2–3), 121–136. [https://doi.org/10.1016/S0168-3659\(01\)00248-6](https://doi.org/10.1016/S0168-3659(01)00248-6).
- (215) Numata, K.; Yamazaki, S.; Naga, N. Biocompatible and Biodegradable Dual-Drug Release System Based on Silk Hydrogel Containing Silk Nanoparticles. *Bio Macromol.* **2012**, *13* (5), 1383–1389.
- (216) Hoare, T. R.; Kohane, D. S. Hydrogels in Drug Delivery: Progress and Challenges. *Polymer (Guildf)*. **2008**, *49* (8), 1993–2007. <https://doi.org/10.1016/j.polymer.2008.01.027>.
- (217) Li, J.; Mooney, D. J. Designing Hydrogels for Controlled Drug Delivery. *Nat. Rev. Mater.* **2016**, *1* (12), 1–38. <https://doi.org/10.1038/natrevmats.2016.71>.Designing.
- (218) Fredenberg, S.; Wahlgren, M.; Reslow, M.; Axelsson, A. The Mechanisms of Drug Release in Poly ( Lactic-Co-Glycolic Acid ) - Based Drug Delivery Systems — A Review. *Int. J. Pharm.* **2011**, *415* (1–2), 34–52. <https://doi.org/10.1016/j.ijpharm.2011.05.049>.
- (219) Behavior, D.; Guo, J.; Pan, S.; Yin, X.; He, Y.; Li, T.; Wang, R. PH-Sensitive Keratin-Based Polymer Hydrogel and Its Controllable. *J. Appl. Polym. Sci.* **2014**, *132* (9), 1–8. <https://doi.org/10.1002/app.41572>.
- (220) Arbade, G. K.; Jaiswal, M.; Dinda, A. K.; Bawa, P.; Pillay, V.; Gupta, P.; Purwar, R. Regulating Drug Release from PH- and Temperature-Responsive Electrospun CTS-g-PNIPAAm / Poly ( Ethylene Oxide ) Hydrogel Nanofibres. *Biomed. Mater.* **2014**, *9* (5), 055001. <https://doi.org/10.1088/1748-6041/9/5/055001>.
- (221) Macaya, D.; Spector, M. Injectable Hydrogel Materials for Spinal Cord Regeneration: A Review. *Biomed. Mater.* **2012**, *7* (1), 012001. <https://doi.org/10.1088/1748-6041/7/1/012001>.
- (222) Gong, C.; Shan, M.; Li, B.; Wu, G. Injectable Dual Redox Responsive Diselenide-Containing Poly(Ethylene Glycol) Hydrogel. *J. Biomed. Mater. Res. - Part A* **2017**, *105* (9), 2451–2460. <https://doi.org/10.1002/jbm.a.36103>.
- (223) Bhattarai, N.; Gunn, J.; Zhang, M. Chitosan-Based Hydrogels for Controlled, Localized Drug Delivery. *Adv. Drug Deliv. Rev.* **2010**, *62* (1), 83–99. <https://doi.org/10.1016/j.addr.2009.07.019>.
- (224) Ban, H.; Nagano, M.; Gavriyuk, J.; Hakamata, W.; Inokuma, T.; Barbas, C. F. Facile and Stable Linkages through Tyrosine: Bioconjugation Strategies with the Tyrosine-Click Reaction. *Bioconjug. Chem.* **2013**, *24* (4), 520–532. <https://doi.org/10.1021/bc300665t>.

- (225) Lobo, M. S.; Costa, P. Modeling and Comparison of Dissolution Profiles. *Pharm. Sci.* **2001**, *13*, 123–133.  
[https://doi.org/https://doi.org/10.1016/S0928-0987\(01\)00095-1](https://doi.org/https://doi.org/10.1016/S0928-0987(01)00095-1).
- (226) Brown, J. E.; Partlow, B. P.; Berman, A. M.; House, M. D.; Kaplan, D. L. Injectable Silk-Based Biomaterials for Cervical Tissue Augmentation: An In Vitro Study. *Am. J. Obstet. Gynecol.* **2016**, *214* (1), 118.e1-118.e9.  
<https://doi.org/10.1016/j.surg.2015.03.052>.Rate.
- (227) Ravasco, J. M. J. M.; Faustino, H. Ø.; Trindade, A.; Gois, P. M. P. Bioconjugation with Maleimides: A Useful Tool for Chemical Biology. *Chem. A Eur. J. Rev.* **2019**, *25* (1), 43–59.  
<https://doi.org/10.1002/chem.201803174>.
- (228) Choi, H.; Kim, M.; Jang, J.; Hong, S. Visible-Light-Induced Cysteine-Specific Bioconjugation: Biocompatible Thiol – Ene Click Chemistry Angewandte. *Angew. Chemie (International ed.)* **2020**, *59* (50), 22514–22522. <https://doi.org/10.1002/anie.202010217>.
- (229) Ittah, S.; Michaeli, A.; Goldblum, A.; Gat, U. A Model for the Structure of the C-Terminal Domain of Dragline Spider Silk and the Role of Its Conserved Cysteine. *Biomacromolecules* **2007**, *8*, 2768–2773. <https://doi.org/10.1021/bm7004559>.
- (230) Madl, C. M.; Heilshorn, S. C. Tyrosine-Selective Functionalization for Bio-Orthogonal Cross-Linking of Engineered Protein Hydrogels. *Bioconjug. Chem.* **2017**, *28* (3), 724–730.  
<https://doi.org/10.1021/acs.bioconjchem.6b00720>.
- (231) Kaiser, D.; Winne, J. M.; Ortiz-soto, M. E.; Seibel, J.; Le, T. A.; Engels, B. Mechanistical Insights into the Bioconjugation Reaction of Triazolinediones with Tyrosine. *J. Inorg. Chem.* **2018**, *83*, 10248–10260. <https://doi.org/10.1021/acs.joc.8b01445>.
- (232) Al-momani, E.; Israel, I.; Buck, A. K.; Samnick, S. Improved Synthesis of [18 F] FS-PTAD as a New Tyrosine-Specific Prosthetic Group for Radio Fluorination of Biomolecules. *Appl. Radiat. Isot.* **2015**, *104*, 136–142.  
<https://doi.org/10.1016/j.apradiso.2015.06.021>.
- (233) Kasko, A. M.; Griffin, D. R. Photoselective Delivery of Model Therapeutics from Hydrogels. *ACS Macro Lett.* **2012**, *1*, 1330–1334.  
<https://doi.org/10.1021/mz300366s>.
- (234) Lv, H.; Huang, S.; Zhao, B.; Miao, J. A New Rhodamine B-Based Lysosomal PH Fluorescent Indicator. *Anal. Chim. Acta* **2013**, *788*, 177–182. <https://doi.org/10.1016/j.aca.2013.06.038>.
- (235) Vigata, M.; Meinert, C.; Hutmacher, D. W.; Bock, N. Hydrogels as Drug Delivery Systems: A Review of Current Characterization and Evaluation Techniques. *Pharmaceutics* **2020**, *12* (12), 1188.
- (236) Caccavo, D. An Overview on the Mathematical Modeling of Hydrogels' Behavior for Drug Delivery Systems. *Int. J. Pharm.* **2019**, *560* (December 2018), 175–190.  
<https://doi.org/10.1016/j.ijpharm.2019.01.076>.

# Appendix

## 1.1. Incorporation of TEV protease site into NT2RepCT

### 1.1.1. Primers

A TEV protease site was inserted into the gene encoding NT2RepCT in the pET22b plasmid. The sequence was to be inserted between the hexa-histidine purification tag and the NT of NT2RepCT. This would allow easy removal of the purification tag from the protein since histidine tags can chelate heavy metals which could cause toxicity problems *in vivo*. The amino acid sequence recognized by TEV protease is ENLYFQS. Primers were designed and ordered from Sigma Aldrich utilizing their Q5 mutagenesis primer design software. Sequence added: GAAAATTTATACTTTCAGTCT

Forward primer: `CTTTCAGTCTATGTCGCACACCACCCCA`

Reverse primer: `TATAAATTTTCGTGATGATGGTGATGATGACCC`

### 1.1.2. Q5 PCR mutagenesis reaction and amplification

Each reaction contained:

- 1  $\mu\text{L}$  20 ng/ $\mu\text{L}$  NT2RepCT Pet22b template
- 1.25  $\mu\text{L}$  Forward primer (10  $\mu\text{M}$ )
- 1.25  $\mu\text{L}$  Reverse primer (10  $\mu\text{M}$ )
- 12.5  $\mu\text{L}$  2x Q5 mix
- 9  $\mu\text{L}$  nuclease free water

Initial denaturation:

98 °C 30 s

35 cycles of:

98 °C 30 s

68 °C 30 s

72 °C 3 minutes

Final extension:

72 °C 2 minutes

Hold:

4 °C

The Q5 PCR product was run on a 1 % (w/v) Agarose (EtBr) gel at 100 V for 30 minutes. A bright band at ~6 kDa was seen indicating that the Q5 PCR product was formed. There were some non-specific binding bands at the bottom of the gel

indicating incomplete PCR reaction. Increasing the annealing temperature might reduce this as this residue (primers etc) can interfere with the KLD reaction.

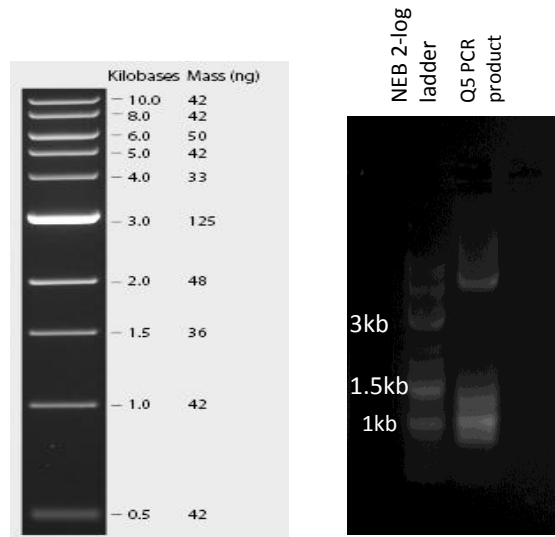


Figure 79: 1% agarose (EtBr) gel of Q5 PCR product before KLD reaction. NT2RepCT Pet22b plasmid is ~ 6 kDa

### 1.1.3. KLD reaction

The KLD reaction was performed at 20 °C for 4 hours before transforming into NEB5 $\alpha$  chemically competent cells and plating 60  $\mu$ L recovered cells onto an ampicillin (100 mg/mL) LB agar plate in 37 °C plate incubator for 16 hours. KLD reaction performed with:

- 1  $\mu$ L Q5 PCR product
- 3  $\mu$ L nuclease free water
- 5  $\mu$ L KLD reaction buffer (2x)
- 1  $\mu$ L KLD enzyme mix (10x)

### 1.1.4. Plasmid purification of transformed NEB5 $\alpha$

Six separate and distinct colonies of NEB5 $\alpha$  transformed with NT2RepCT Tev (Q5 mutagenesis product) were picked and labelled A to E. Each colony was used to inoculate 10 mL of sterile LB media with 100  $\mu$ g/mL ampicillin. These cultures were grown for 16 hours at 37 °C at 180 rpm shaking and a Promega Wizard SV miniprep kit

was used to purify the pEt22b plasmid. 30 µL nuclease free water was used to elute the plasmid from the column and the concentrations ranged from 80-150 ng/µL.

Sequencing of the plasmids was performed by Source Bioscience in Nottingham using their provided T7 forward and reverse primers. Only plasmids A-E were sent for sequencing.

#### **1.1.5. Sequencing results**

Of the six purified plasmids sent for sequencing plasmid B & C were successful but with poor signal to noise ratio. Colony E successfully contained the expected TEV protease cleavage site mutation with good signal to noise ratio. Colony E was taken forward to transformation and expression of TEV NT2RepCT.

#### **1.1.6. Transformation and test expression of TEV NT2RepCT**

Colony E was used to transform *E. coli* BL21 Rosetta (DE3) and plated onto ampicillin resistant plates. Four colonies were picked and used for small scale expression test. Four starter cultures of 5 mL LB containing 100 µg/mL ampicillin) were inoculated with each picked colony and incubated at 37 °C at 180 rpm for 16 hours. Flasks containing 50 mL sterile LB broth containing 100 µg/mL ampicillin were inoculated with 0.5 mL starter culture and incubated at 37 at 180 rpm for 3.5 hours until  $OD_{595} = 0.7$ . The 50 mL LB media was then split and half was induced with 1 mM IPTG and was incubated for 3 hours at 37 °C 180 rpm and the other half was not induced and incubated for 3 hours at 37 °C 180 rpm. A certain volume of media was taken from each flask by dividing 1000 µL by the optical density at 595 nm. Calculated by the following equation:

$$Volume (\mu L) = \frac{1000 \mu L}{OD_{595}}$$

The volume was transferred into a 1.5 mL Eppendorf and the cells were pelleted at 13,000 x g for 1 minute. For the pellets taken from the induced flasks the supernatant was removed, and the cell pellet frozen at -20 °C for 16 hours. The pellet was then

thawed and cells were lysed by addition of 200  $\mu$ L CellLytic (Sigma), 1  $\mu$ L lysozyme (50mg/ml), 0.5  $\mu$ L Benzonase, 3  $\mu$ L 1M  $MgCl_2$  per sample and the pellet was resuspended by pipetting. The sample was then centrifuged at 13,000 x g for 10 minutes. The supernatant was then transferred into a new 1.5 mL Eppendorf which is referred to herein as the soluble sample. The remaining pellet was resuspended in 200  $\mu$ L 20 mM tris pH 8 and is referred to herein as the insoluble sample. For cell pellets taken from the uninduced flasks, the pellet was lysed by addition of 200  $\mu$ L CellLytic (Sigma), 1 $\mu$ L lysozyme (50mg/ml), 1 $\mu$ L DNase (14,6u/ $\mu$ L), 3 $\mu$ L 1M  $MgCl_2$  and resuspended by pipetting. To all tubes, induced soluble, induced insoluble or uninduced, 100  $\mu$ L SDS PAGE loading buffer was added and the samples were boiled at 95  $^{\circ}$ C for 5 minutes. To a 15 % SDS PAGE gel, 12  $\mu$ L each sample was added to each well (Figure 80).

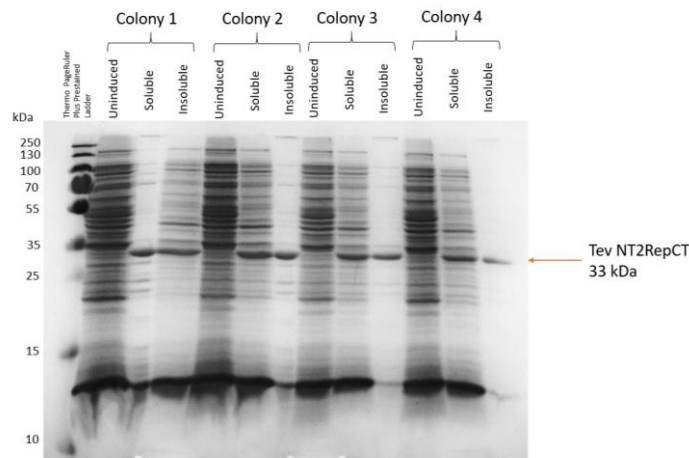


Figure 80: SDS PAGE results of test expression of 4 colonies of BL21 Rosetta (DE3) transformed with TEV NT2RepCT pET22b plasmid.

The expression of TEV NT2RepCT was split equally across the induced soluble and insoluble fraction. This split also occurs in NT2RepCT but to a lesser degree. Since this expression test was 37  $^{\circ}$ C growth and 37  $^{\circ}$ C induction this is not the same conditions as usual NT2RepCT expression (30  $^{\circ}$ C growth and 20  $^{\circ}$ C induction). Therefore,

expression can be improved by the lower temperatures of the usual NT2RepCT expression.

### 1.1.7. 1L scale expression and purification of TEV NT2RepCT

TEV NT2RepCT was expressed and purified using the same protocol as described for NT2RepCT. (Section 3.1). High expression of TEV NT2RepCT was seen with the main bulk of protein eluting in the 30 % Buffer B step (Figure 81). No protein was eluted in the flow through indicating efficient binding to the Nickel affinity HiTrap column. Fractions of interest were visualized with SDS PAGE with the expected TEV NT2RepCT protein band migrating to 34 kDa (Figure 81).

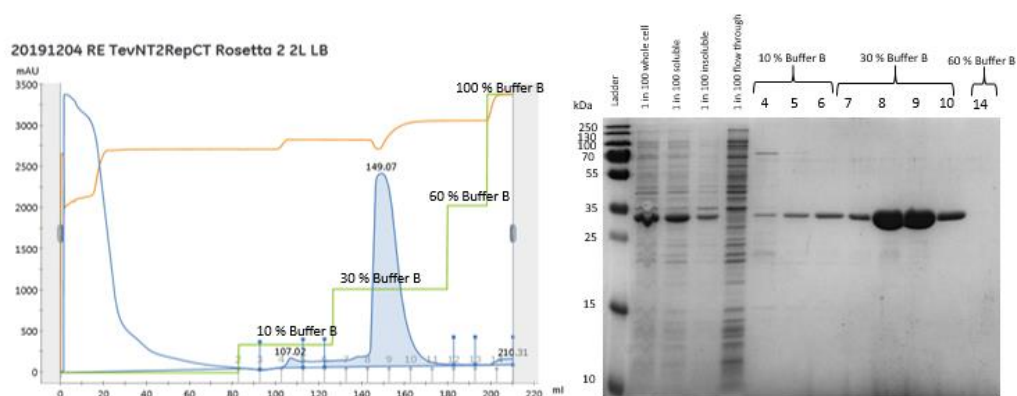


Figure 81: (Left) Purification trace of 2L LB containing BL21 Rosetta (DE3) TEV NT2RepCT. (Right) SDS-PAGE analysis of TEV NT2RepCT expression and purification from trace. 1 in 10 dilutions of fractions of interest used.